Journal of
Mechanics of Materials and Structures

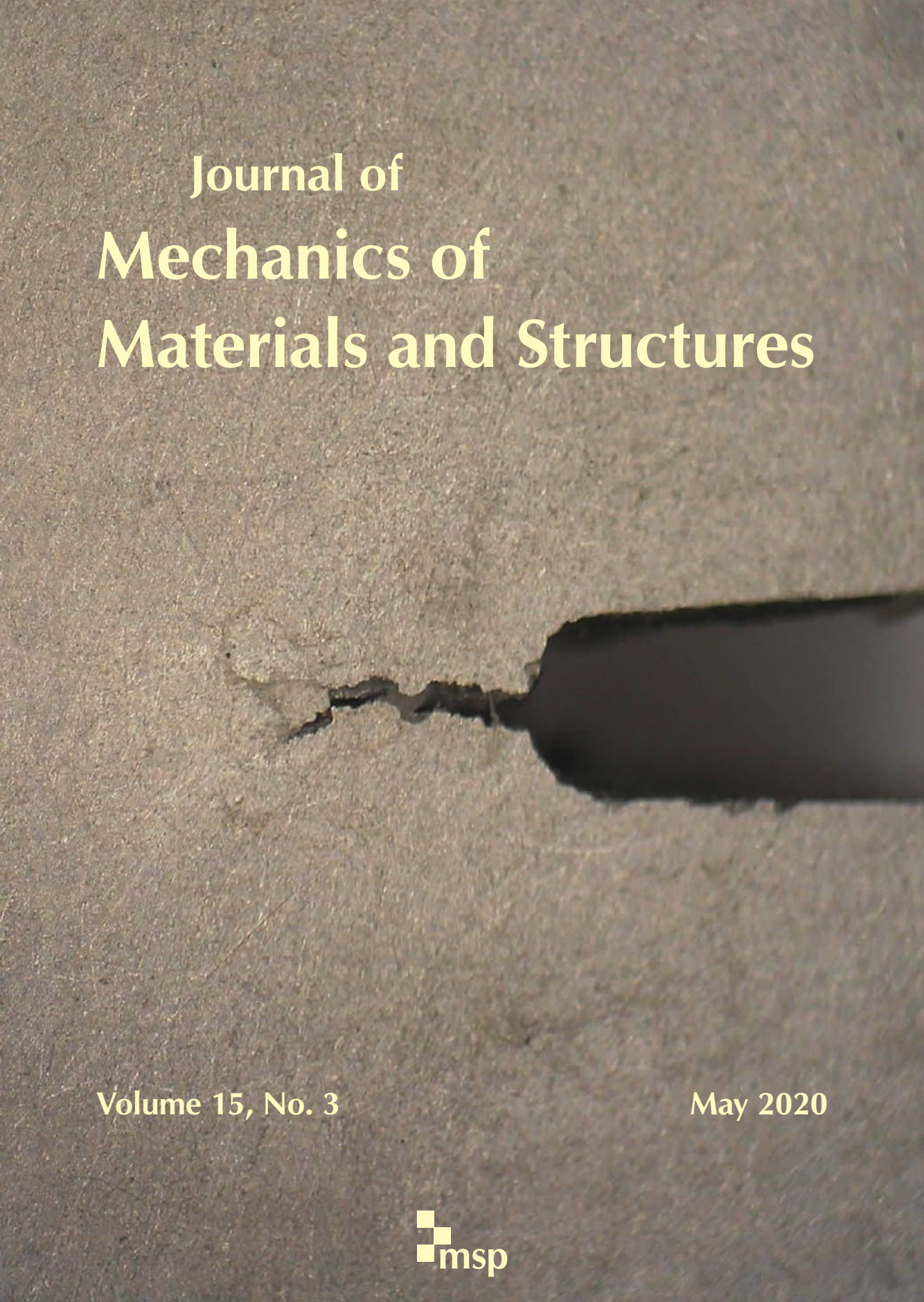

Volume 15, No. 3 May 2020

msp

JOURNAL OF MECHANICS OF MATERIALS AND STRUCTURES

msp.org/jomms

Founded by Charles R. Steele and Marie-Louise Steele

See msp.org/jomms for submission guidelines.

JoMMS (ISSN 1559-3959) at Mathematical Sciences Publishers, 798 Evans Hall #6840, c/o University of California, Berkeley, CA 94720-3840, is published in 10 issues a year. The subscription price for 2020 is US $660/year for the electronic version, and $830/year (+$60, if shipping outside the US) for print and electronic. Subscriptions, requests for back issues, and changes of address should be sent to MSP.

JoMMS peer-review and production is managed by EditFLOW® from Mathematical Sciences Publishers.

PUBLISHED BY

mathematical sciences publishers

nonprofit scientific publishing

http://msp.org/

JOURNAL OF MECHANICS OF MATERIALS AND STRUCTURES
Vol. 15, No. 3, 2020
https://doi.org/10.2140/jomms.2020.15.291

3D PHASE-EVOLUTION-BASED THERMOMECHANICAL CONSTITUTIVE MODEL OF SHAPE MEMORY POLYMER WITH FINITE ELEMENT IMPLEMENTATION

YUNXIN LI, RUOXUAN LIU, ZISHUN LIU AND SOMSAK SWADDIWUDHIPONG

Shape memory polymers (SMPs) are a class of smart materials which can undergo transition between two different states (temporary shape and permanent state) induced by external stimuli, such as temperature, light etc. In order to study the deformation behavior of this fast-developing SMP structures, the key points are formulating suitable theoretical constitutive models to correctly reflect the material behavior and developing appropriate numerical simulation techniques to handle complex structures. In this paper, we proposed a three-dimensional (3D) thermomechanical constitutive model of SMPs and its implementation as a user material subroutine, UMAT, in a finite element package ABAQUS. The shape memory effects of the SMPs under three different loading patterns are simulated by the proposed approach and the acquired numerical results are compared with theoretical computational results and available experimental data. They agree reasonably well. Two SMP structural examples are presented to demonstrate the feasibility of the proposed approach. The exercises involve the analyses of (i) an intelligent hexachiral deployable structure and (ii) a 3D self-folding structure achieved through a 2D plate.

1. Introduction

Shape memory polymers (SMPs) are soft and intelligent materials that can recover their permanent configuration from a temporary deformed shape upon the application of stimuli, such as, temperature, water, light and electricity [Li et al. 2015; Zheng et al. 2018; Conti et al. 2007; Huang et al. 2005; Lendlein et al. 2005; Qi and Dunn 2010]. SMPs have several advantages over the traditional shape memory materials (*e.g.* shape memory alloys) as SMPs are biodegradable, biocompatible, light weight, low cost and able to render large deformation [Baghani et al. 2012; Hager et al. 2015; Leng et al. 2009] and hence SMPs have great potential applications in various fields, such as, aerospace structures [Behl et al. 2010; Hu et al. 2012], functional textiles [Castano and Flatau 2014; Hu and Chen 2010], biomedicine [Lendlein et al. 2010; Yakacki and Gall 2009; Liu et al. 2019b], self-healing materials [Luo and Mather 2013; Shojaei and Li 2014; Shojaei et al. 2013] and pattern transformations [He et al. 2015; Liu et al. 2015].

The diverse applications and benefits of SMPs in various fields, especially those of critical importance, have stimulated a great progress in theoretical [Pan et al. 2018], numerical [Pan et al. 2019; Li et al. 2018; Eskandari et al. 2018; Valizadeh et al. 2018] and experimental studies [Liu et al. 2019a] of these materials on their deformation mechanism. The experimental approach is essential but normally costly and time

Zishun Liu is the corresponding author.
Keywords: shape memory polymer, constitutive model, finite element method.

consuming. On the contrary, once the material parameters are evaluated from test data, the theoretical and numerical studies provide comprehensive descriptions and predictions of the mechanical behavior of SMPs with substantially less cost and time. The theory describing SMPs dated back more than two decades ago [Huang et al. 2020]. Tobushi et al. [1997] recommended a viscoelastic modeling approach for SMPs in 1997. They developed a one-dimensional rheological model that qualitatively describes the shape memory process by introducing an irreversible slip element in traditional spring-damper system. Based on the above approach, Lin and Chen [1999] proposed another viscoelastic model to predict the shape memory effect and rate-dependent behavior of polyurethanes. Diani et al. [2006] explored a three-dimensional (3D) viscoelastic constitutive model that was thermodynamically motivated. Though the model is able to capture some key features of shape memory behavior, it is incapable of predicting the details of response in thermodynamic cycle. To cater for the time-dependent and temperature-dependent characteristics of the amorphous SMPs, Nguyen et al. [2008] developed a thermo-viscoelastic constitutive model which considered structural and stress relaxation as the primary molecular mechanisms of the shape memory effect and its time-dependency. Srivastava et al. [2010] established a thermo-mechanically coupled large-deformation constitutive model and determined the model parameters using stress-strain experimental data. The model is able to predict the shape memory behavior of the SMPs with satisfactory results. Yu et al. [2014] introduced a 3D viscoelastic model which combined a spring element and several Maxwell elements in parallel fashion to represent different active relaxation mechanisms in SMPs. Based on multiplicative decompositions of the deformation gradient, Li et al. [2017a] proposed a novel viscoelastic constitutive model for SMPs. To reduce the parameters of describing SMP constitutive model, the fractional order models are proposed. Fang et al. [2018] developed a multi-branch thermoviscoelastic model which was valid for multi-shape memory effect of SMP by introducing the shift factor. Pan and Liu [2018] presented a new fractional viscoelastic constitutive model for SMPs to describe the phase transition phenomenon of SMPs with various constitutive components defined around the glass transition temperature. All these two models reduced considerably the number of material parameters required to describe the phase transition phenomenon of SMPs. The phenomenological phase transition modeling of SMPs was introduced in [Liu et al. 2006], which considered SMPs as a mixture of different phases that are interchangeable depending on the heat stimulus. Based on that work, many comprehensive phenomenological models of SMPs were formulated and presented in [Baghani et al. 2014; Chen and Lagoudas 2008a; Chen and Lagoudas 2008b; Gilormini and Diani 2012; Gu et al. 2015; Li et al. 2017b; Li and Liu 2018; Moon et al. 2015; Qi et al. 2008; Volk et al. 2010; Yang and Li 2015].

Numerical approach has also been applied to study the thermomechanical behavior of SMPs. Qi et al. [2008] implemented a 3D model into ABAQUS user material subroutine (UMAT) for amorphous SMPs. Reese et al. [2010] formulated a new model in a micromechanical as well as a macro-mechanical format and implemented this model into software “FEAP” (a finite element analysis program originated by researchers at the University of California, Berkeley). The generalized Maxwell model and WLF equation which are available in ABAQUS were adopted by Diani et al. [2012] to model SMP materials. Baghani et al. [2012] employed the finite element method (FEM) for SMPs to study 3D shape memory beams and medical stents while Tian and Venkatesh [2013] implemented the FEM for indentation of SMPs. The FEM was also adopted by Li et al. [2015] to conduct the thermomechanical behavior analysis of polyurethane. Recently, Pieczyska et al. [2017] developed the FEM in AceGen/AceFEM environment to simulate the cyclic tensile tests of SMPs.

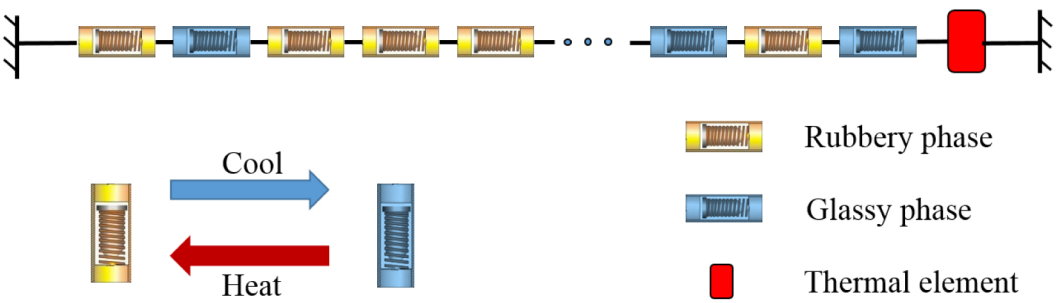

Figure 1. Schematic illustration of phase-evolution-based thermomechanical constitutive model reflecting process of phase transition between yellow rubbery phase and glassy phase in pewter.

In 2017, we introduced a phase-evolution-based thermomechanical constitutive model which can capture the shape memory effect of amorphous SMPs [2017b]. However, the model is of just a one-dimensional (1D) framework and hence is not able to trace and evaluate the deformation behavior of complex SMP structures. The present article extends the 1D SMP constitutive model into a 3D platform with an implementation as a UMAT subroutine in the finite element package ABAQUS. This enables us to apply the proposed constitutive model to simulate the deformation behavior of any complex SMP structures effectively and conveniently.

The paper is organized as follows. In Section 2, we re-introduce briefly a 1D phase-evolution-based thermomechanical constitutive model for SMPs. The 1D constitutive model is extended to a 3D form and then implemented in ABAQUS in Section 3. The detailed formulations and procedural considerations associated with FEM are provided in this section. Section 4 involves the verifications of both theoretical considerations and numerical implementation through the comparison of numerical solutions with theoretical computational results and available experimental data. Reasonably good agreement is observed. The proposed 3D constitutive model for SMPs with FEM implementation is applied to analyze two complex SMP structures and the outcomes are reported in Section 5. Finally, the concluding remarks are given in Section 6.

2. Constitutive model for SMPs

Prior to the presentation of a 3D phase-evolution-based thermomechanical constitutive model formulation in Section 3, a 1D development that has been elaborated earlier by Li et al. [2017b] is briefly described in this section.

2.1. ***General description of the constitutive model.*** In this approach, SMPs are considered as a mixture of the yellow rubbery phase regions and the glassy phase regions in pewter color as shown in Figure 1. The volume fraction of each of the former is $\Delta\gamma_r^j$ and the latter as $\Delta\gamma_g^j$, where the total sum is unity, i.e., $\Sigma\Delta\gamma_g^j + \Sigma\Delta\gamma_r^j = 1$. The total strain of the adopted model including that of thermal effect is expressed as

$$\varepsilon_{\text{total}} = \Sigma\Delta\gamma_r^j \varepsilon_{\text{rubbery}}^j + \Sigma\Delta\gamma_g^j \varepsilon_{\text{glassy}}^j + \varepsilon_T \tag{1}$$

where ε_T is the thermal strain, $\varepsilon^j_{\text{rubbery}}$ and $\varepsilon^j_{\text{glassy}}$ are strains in any j-th rubbery and any j-th glassy phase regions, respectively.

These two kinds of springs which represent two different phases (yellow for rubbery phase and pewter for glassy phase) are interchangeable governed by the variation of temperature. As the temperature decreases, certain rubbery phase regions will be transformed into those of the glassy phase where part of their deformations are frozen. In the newly formed glassy phase regions, the frozen strain and residual mechanical strain are denoted by $\varepsilon_{\text{frozen}}$ and $\varepsilon_{g\text{-mechanics}}$, respectively. Li et al. [2017b] defined the frozen strain $\varepsilon_{\text{frozen}}$ as

$$\varepsilon_{\text{frozen}} = \varepsilon_{r\text{-mechanics}} - f(T)\varepsilon_{r\text{-mechanics}} \tag{2}$$

where $\varepsilon_{r\text{-mechanics}}$ is the mechanical strain in the corresponding previous rubbery phase regions. $f(T)$ is the ratio of the mechanical strains corresponding to the two transformed phase regions, i.e., $f(T) = \varepsilon_{g\text{-mechanics}}/\varepsilon_{r\text{-mechanics}}$. $f(T)$ is calibrated based on experimental data.

At the increase in temperature, the transition glassy phase regions are reverted back to those of the rubbery phase while the frozen strain is released, leaving only the mechanical strain $\varepsilon_{r\text{-mechanics}}$ in the rubbery phase regions. The strains in the glassy phase regions comprise both the mechanical strain $\varepsilon_{g\text{-mechanics}}$ and the frozen strain $\varepsilon_{\text{frozen}}$. Hence, the total strain in Eq. (1) at the latter stage can be written as

$$\varepsilon_{\text{total}} = \Sigma\Delta\gamma_r^j\varepsilon^j_{r\text{-mechanics}} + \Sigma\Delta\gamma_g^j\left(\varepsilon^j_{g\text{-mechanics}} + \varepsilon^j_{\text{frozen}}\right) + \varepsilon_T \tag{3}$$

The stress in each phase region is described by Hooke's law as stipulated in Eqs. (4) and (5):

$$\sigma_r^j = E_r\varepsilon^j_{r\text{-mechanics}}, \tag{4}$$

$$\sigma_g^j = E_g\varepsilon^j_{g\text{-mechanics}}, \tag{5}$$

where E_r and E_g are the Young's moduli of the rubbery and glassy phase regions, respectively.

All spring elements shown in Figure 1 are in series and hence the stress in any phase region is the same and equals the total stress, namely,

$$\sigma_{\text{total}} = \sigma_r^j = \sigma_g^j \tag{6}$$

As the mechanical strain of any j-th rubbery phase region remains unchanged, we have $\varepsilon^j_{r\text{-mechanics}} = \varepsilon_{r\text{-mechanics}}$. This is similarly true for the mechanical strain of any j-th glassy phase region and hence we also have $\varepsilon^j_{g\text{-mechanics}} = \varepsilon_{g\text{-mechanics}}$. Substituting these 2 identities into Eq. (3), the total strain becomes

$$\varepsilon_{\text{total}} = (1-\gamma)\varepsilon_{r\text{-mechanics}} + \gamma\varepsilon_{g\text{-mechanics}} + \varepsilon_f + \varepsilon_T \tag{7}$$

In Eq. (7), $\gamma = \Sigma\Delta\gamma_g^j$ denotes the fraction of the glassy phase and hence the fraction of the rubbery phase is $1-\gamma = \Sigma\Delta\gamma_r^j$. The total frozen strain in SMPs is then represented by the expression, $\varepsilon_f = \Sigma\Delta\gamma_g^j\varepsilon^j_{\text{frozen}}$.

2.2. ***Governing equation of shape memory effect.*** An incremental approach is adopted to establish the governing equations of SMP model covering the continuous phase transition processes. During the cooling period, the temperature decreases from a high temperature T_h to a low value of T_l. The temperature interval of interest $[T_h, T_l]$ is divided into numerous small increments. For a generic advancement of

temperature $[T_{\text{cool}}^{n-1}, T_{\text{cool}}^{n}]$, the stress and strain are denoted by superscript n-1 at temperature T_{cool}^{n-1} and that of n at temperature T_{cool}^{n}, respectively.

When temperature drops from T_{cool}^{n-1} to T_{cool}^{n}, certain portions of the rubbery phase regions of $(\Delta\gamma^n)$ are transformed into those of the glassy phase and parts of deformations $(\varepsilon_{\text{frozen}}^{n})$ are frozen. The total frozen strain ε_f^n at T_{cool}^{n} is

$$\varepsilon_f^n = \sum_{j=1}^{n} \Delta\gamma_g^j \varepsilon_{\text{frozen}}^j = \varepsilon_f^{n-1} + \Delta\gamma^n \varepsilon_{\text{frozen}}^n \tag{8}$$

where $\varepsilon_f^{n-1} = \sum_{j=1}^{n-1} \Delta\gamma^j \varepsilon_{\text{frozen}}^j$ is the total frozen strain at temperature T_{cool}^{n-1}.

Substituting Eq. (2) into Eq. (8) yields

$$\varepsilon_f^n = \varepsilon_f^{n-1} + \Delta\gamma^n (1 - f(T))\varepsilon_{r\text{-mechanics}}^n \,. \tag{9}$$

Here $\varepsilon_f^n - \varepsilon_f^{n-1} = \Delta\varepsilon_f^n$ is the small increment of total frozen strain. Inserting Eq. (4)–Eq. (7) into Eq. (9), we obtain the expressions for σ_{total}^n and $\Delta\varepsilon_f^n$ at T_{cool}^{n} as given by

$$\sigma_{\text{total}}^n = \frac{\varepsilon_{\text{total}}^n - \varepsilon_f^n - \varepsilon_T^n}{\dfrac{\gamma^n}{E_g} + \dfrac{1-\gamma^n}{E_r}}, \tag{10}$$

$$\Delta\varepsilon_f^n = \Delta\gamma^n [1 - f(T)] \frac{\varepsilon_{\text{total}}^{n-1} - \varepsilon_f^{n-1} - \varepsilon_T^{n-1}}{E_r\left(\dfrac{\gamma^{n-1}}{E_g} + \dfrac{1-\gamma^{n-1}}{E_r}\right)}. \tag{11}$$

Expressing Eq. (11) in differential form, the governing equations of shape memory effect can be written collectively in general form as

$$\begin{cases} \sigma_{\text{total}} = \dfrac{\varepsilon_{\text{total}} - \varepsilon_f - \varepsilon_T}{\dfrac{\gamma}{E_g} + \dfrac{1-\gamma}{E_r}}, \\ \dfrac{d\varepsilon_f}{dT} = \dfrac{d\gamma}{dT}[1 - f(T)] \dfrac{\varepsilon_{\text{total}} - \varepsilon_f - \varepsilon_T}{E_r\left(\dfrac{\gamma}{E_g} + \dfrac{1-\gamma}{E_r}\right)}. \end{cases} \tag{12}$$

2.3. ***Thermal deformation.*** The thermal strain ε_T is

$$\varepsilon_T = \int_{T_0}^{T} \alpha dT \tag{13}$$

where α is the coefficient of thermal expansion (CTE) and T_0 is the reference temperature.

3. Finite element approach

3.1. ***3D form of constitutive model.*** To apply the proposed constitutive relationship into finite element computation, the constitutive model of 1D form must be generalized into 3D form [Lucchesi et al. 2019]. Therefore, we extend the previous SMP constitutive model into a 3D form and implement the latter in a

finite element package ABAQUS through its UMAT subroutine. For a 3D isotropic solid, the total strain and the total stress can be rewritten as follows:

$$\varepsilon_{ij}^{\text{total}} = (1-\gamma)\varepsilon_{ij}^{r\text{-mechanics}} + \gamma\varepsilon_{ij}^{g\text{-mechanics}} + \varepsilon_{ij}^{f} + \varepsilon_{ij}^{T} \quad i, j = x, y, z \tag{14}$$

$$\sigma_{ij}^{\text{total}} = \sigma_{ij}^{r} = \sigma_{ij}^{g} \quad i, j = x, y, z \tag{15}$$

The one-dimensional (1D) governing equation (Eq. (4)) of the rubbery phase element can be generalized into a 3D form as shown in Eq. (16) and Eq. (17).

$$\sigma_{xx}^{r} = \lambda_r \varepsilon_V^{r\text{-mechanics}} + 2\mu_r \varepsilon_{xx}^{r\text{-mechanics}}, \quad \text{etc.} \tag{16}$$

$$\sigma_{xy}^{r} = 2\mu_r \varepsilon_{xy}^{r\text{-mechanics}}, \quad \text{etc.} \tag{17}$$

where $\varepsilon_V^{r\text{-mechanics}} = \varepsilon_{xx}^{r\text{-mechanics}} + \varepsilon_{yy}^{r\text{-mechanics}} + \varepsilon_{zz}^{r\text{-mechanics}}$, λ_r and μ_r are the Lame constants of the rubbery phase element.

Similarly, the 3D form model of the glassy phase element is expressed as

$$\sigma_{xx}^{g} = \lambda_g \varepsilon_V^{g\text{-mechanics}} + 2\mu_g \varepsilon_{xx}^{g\text{-mechanics}}, \quad \text{etc.} \tag{18}$$

$$\sigma_{xy}^{g} = 2\mu_g \varepsilon_{xy}^{g\text{-mechanics}}, \quad \text{etc.} \tag{19}$$

where $\varepsilon_V^{g\text{-mechanics}} = \varepsilon_{xx}^{g\text{-mechanics}} + \varepsilon_{yy}^{g\text{-mechanics}} + \varepsilon_{zz}^{g\text{-mechanics}}$, λ_g and μ_g are the Lame constants of the glassy phase element.

The 3D form of the thermal strain in Eq. (13) is thus

$$\varepsilon_{ij}^{T} = \delta_{ij} \int_{T_0}^{T} \alpha \, dT, \quad i, j = x, y, z \tag{20}$$

In view of Eq. (16) and Eq. (18), Eq. (15) becomes

$$\lambda_r \varepsilon_V^{r\text{-mechanics}} + 2\mu_r \varepsilon_{xx}^{r\text{-mechanics}} = \lambda_g \varepsilon_V^{g\text{-mechanics}} + 2\mu_g \varepsilon_{xx}^{g\text{-mechanics}}, \quad \text{etc.} \tag{21}$$

Eq. (14) provides the basis for the expressions of various principal components of the total strain and volume deformation $\varepsilon_V^{\text{total}} = \varepsilon_{xx}^{\text{total}} + \varepsilon_{yy}^{\text{total}} + \varepsilon_{zz}^{\text{total}}$ as given in Eq. (22) and Eq. (23).

$$\varepsilon_{xx}^{\text{total}} = (1-\gamma)\varepsilon_{xx}^{r\text{-mechanics}} + \gamma\varepsilon_{xx}^{g\text{-mechanics}} + \varepsilon_{xx}^{f} + \varepsilon_{xx}^{T}, \quad \text{etc.} \tag{22}$$

$$\varepsilon_V^{\text{total}} = (1-\gamma)\varepsilon_V^{r\text{-mechanics}} + \gamma\varepsilon_V^{g\text{-mechanics}} + \varepsilon_V^{f} + \varepsilon_V^{T}. \tag{23}$$

Inserting Eq. (22) and Eq. (23) into Eq. (21), we have

$$\varepsilon_{xx}^{g\text{-mechanics}} = \frac{\lambda_r(\varepsilon_V^{\text{total}} - \varepsilon_V^{f} - \varepsilon_V^{T}) + 2\mu_r(\varepsilon_{xx}^{\text{total}} - \varepsilon_{xx}^{f} - \varepsilon_{xx}^{T}) - (\gamma\lambda_r + (1-\gamma)\lambda_g)\varepsilon_V^{g\text{-mechanics}}}{2(\gamma\mu_r + (1-\gamma)\mu_g)}, \quad \text{etc.}, \tag{24}$$

$$\varepsilon_V^{g\text{-mechanics}} = \frac{(3\lambda_r + 2\mu_r)(\varepsilon_V^{\text{total}} - \varepsilon_V^{f} - \varepsilon_V^{T})}{3(\gamma\lambda_r + (1-\gamma)\lambda_g) + 2(\gamma\mu_r + (1-\gamma)\mu_g)}. \tag{25}$$

The shear components of total strain $\varepsilon^{g\text{-mechanics}}$ can be derived from Eq. (14) to give

$$\varepsilon_{xy}^{g\text{-mechanics}} = \frac{\left(\varepsilon_{xy}^{\text{total}} - \varepsilon_{xy}^{f} - \varepsilon_{xy}^{T}\right)\mu_r}{(1-\gamma)\mu_g + \gamma\mu_r}, \quad \text{etc.} \tag{26}$$

Substituting Eq. (24) and Eq. (26) into Eq. (18) and Eq. (19) yields the following 3D form of governing equations for the constitutive model.

$$\sigma_{xx}^{\text{total}} = \left(\varepsilon_V^{\text{total}} - \varepsilon_V^{f} - \varepsilon_V^{T}\right)\lambda(T) + 2\mu(T)\left(\varepsilon_{xx}^{\text{total}} - \varepsilon_{xx}^{f} - \varepsilon_{xx}^{T}\right), \quad \text{etc.,} \tag{27}$$

$$\sigma_{xy}^{\text{total}} = 2\mu(T)\left(\varepsilon_{xy}^{\text{total}} - \varepsilon_{xy}^{f} - \varepsilon_{xy}^{T}\right), \quad \text{etc.} \tag{28}$$

where

$$\lambda(T) = \frac{\mu_g\lambda_r}{\gamma\mu_r + (1-\gamma)\mu_g} + \frac{\gamma\mu_r\lambda_g - \gamma\mu_g\lambda_r}{\gamma\mu_r + (1-\gamma)\mu_g} * \frac{(3\lambda_r + 2\mu_r)}{3(\gamma\lambda_r + (1-\gamma)\lambda_g) + 2(\gamma\mu_r + (1-\gamma)\mu_g)},$$

$$\mu(T) = \frac{\mu_g\mu_r}{\gamma\mu_r + (1-\gamma)\mu_g}.$$

The constitutive relations in Eq. (27) and Eq. (28) can be collectively expressed as

$$\sigma_{ij} = \lambda(T)\delta_{ij}\varepsilon_{kk}^{el} + 2\mu(T)\varepsilon_{ij}^{el} \tag{29}$$

where $\varepsilon_{ij}^{el} = \varepsilon_{ij}^{\text{total}} - \varepsilon_{ij}^{f} - \varepsilon_{ij}^{T}$. Eq. (29) can be written in a Jaumann rate form as

$$\dot{\sigma}_{ij}^{J} = \lambda(T)\delta_{ij}\dot{\varepsilon}_{kk}^{el} + 2\mu(T)\dot{\varepsilon}_{ij}^{el} + \dot{\lambda}(T)\delta_{ij}\varepsilon_{kk}^{el} + 2\dot{\mu}(T)\varepsilon_{ij}^{el} \tag{30}$$

The Jaumann rate equation of Eq. (30) is integrated in a co-rotational framework to render

$$\Delta\sigma_{ij}^{J} = \lambda(T)\delta_{ij}\Delta\varepsilon_{kk}^{el} + 2\mu(T)\Delta\varepsilon_{ij}^{el} + \Delta\lambda(T)\delta_{ij}\varepsilon_{kk}^{el} + 2\Delta\mu(T)\varepsilon_{ij}^{el} \tag{31}$$

Once the frozen strain ε_{ij}^{f} is established, Eq. (31) provides us the basis for a 3D implementation of finite element model via UMAT subroutine in ABAQUS.

3.2. ***3D form of frozen strain.*** To calculate the frozen strain in Eq. (14), we have to recast the constitutive equation of shape memory effect (Eq. 12) into a three-dimensional form as shown in Eq. (32).

$$\begin{cases} \sigma_{ij}^{\text{total}} = C_{ij}\left(\varepsilon_{ij}^{\text{total}} - \varepsilon_{ij}^{f} - \varepsilon_{ij}^{T}\right) \\ \dfrac{d\varepsilon_{ij}^{f}}{dT} = \dfrac{d\gamma}{dT}[1 - f(T)]\left(C_r^{-1}\right)_{ij} C_{ij}\left(\varepsilon_{ij}^{\text{total}} - \varepsilon_{ij}^{f} - \varepsilon_{ij}^{T}\right) \end{cases} \tag{32}$$

where C_{ij} is the component of SMPs stiffness matrix C and $\left(C_r^{-1}\right)_{ij}$ represents the component of inverse stiffness matrix for any rubbery phase element. In view of Eq. (16), Eq. (17) and Eq. (29), the stiffness matrix of the rubbery phase elements (which is labeled by r) and consequently that of shape memory

material are expressed respectively as

$$\boldsymbol{C}_r = \begin{bmatrix} \lambda_r+2\mu_r & \lambda_r & \lambda_r & 0 & 0 & 0 \\ \lambda_r & \lambda_r+2\mu_r & \lambda_r & 0 & 0 & 0 \\ \lambda_r & \lambda_r & \lambda_r+2\mu_r & 0 & 0 & 0 \\ 0 & 0 & 0 & \mu_r & 0 & 0 \\ 0 & 0 & 0 & 0 & \mu_r & 0 \\ 0 & 0 & 0 & 0 & 0 & \mu_r \end{bmatrix} \tag{33}$$

$$\boldsymbol{C} = \begin{bmatrix} \lambda+2\mu & \lambda & \lambda & 0 & 0 & 0 \\ \lambda & \lambda+2\mu & \lambda & 0 & 0 & 0 \\ \lambda & \lambda & \lambda+2\mu & 0 & 0 & 0 \\ 0 & 0 & 0 & \mu & 0 & 0 \\ 0 & 0 & 0 & 0 & \mu & 0 \\ 0 & 0 & 0 & 0 & 0 & \mu \end{bmatrix} \tag{34}$$

The incremental form of the frozen strain in Eq. (32) is thus

$$\begin{cases} \Delta\varepsilon_{f\text{-}ij} = (\gamma_{ij} - \gamma_{ij}) * (1-f) * (\varepsilon_{\text{pre-}ij} - \varepsilon_{f\text{-}ij} - \varepsilon_{T\text{-}ij}) * CRC_{ij} \\ \varepsilon_{f\text{-}ij} = \varepsilon_{f\text{-}ij} + \Delta\varepsilon_{f\text{-}ij} \end{cases} \tag{35}$$

where $CRC_{ij} = (C_r^{-1})_{in}C_{nj}$. Eq. (35) provides the iterative relations for the determination of the frozen strain suitable for finite element implementation.

4. Verification of proposed numerical model

We have developed a numerical model describing the complex thermomechanical characteristics of SMPs by implementing the above 3D constitutive relations as a UMAT subroutine in the finite element package ABAQUS. The proposed model is verified through the comparisons of the numerical solutions acquired in the present study with those obtained experimentally and via the analytical approach reported earlier in [Liu et al. 2006; 2017b]. The material parameters adopted in the exercises as stipulated in Table 1

T_g	310 K
T_h	338 K
T_l	298 K
γ	$1 - \frac{1}{1+0.000036(T_h-T)^4}$
E_g	8538.93 MPa
N	719.28 mol/m^3
E_r	$3NkT$ MPa
α	$-2.066 \times 10^{-4} + 1.52 \times 10^{-6}T)$ K^{-1}
f	$\begin{cases} 0 & (T \le T_g) \\ (T-T_g)/T_g & (T > T_g) \end{cases}$

Table 1. Material parameters adopted from [Li et al. 2017b].

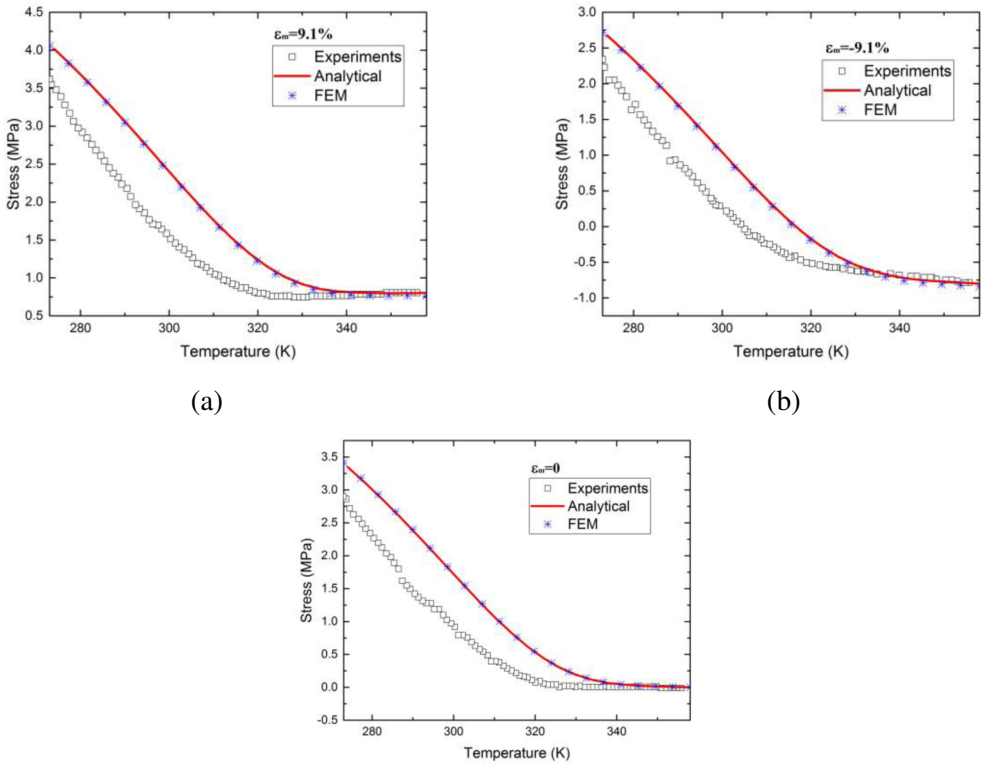

Figure 2. Comparison of FE solutions with theoretical computational results (using "analytical" symbol in figures) and experimental results [Liu et al. 2006] of stress in cooling process under various loading patterns: (a) $\varepsilon_m = 9.1\%$ (tension); (b) $\varepsilon_m = -9.1\%$ (compression); (c) $\varepsilon_m = 0$ (zero-strain).

are the same as those employed in Table 2 of [Li et al. 2017b]. The shape memory effects of this SMP material under various types of loading patterns namely those in (i) tension, (ii) compression and (iii) zero-strain condition are considered in the study.

Typically, the shape memory cycle comprises four processes. They are: (1) loading at a high temperature, (2) cooling under fixed strain constraint, (3) unloading at a low temperature and (4) reheating. The stress-temperature response in the cooling process and strain-temperature response in the reheating process are the key characteristics of the shape memory effect. Thus, we reproduce the thermomechanical behavior of SMPs during both the cooling period in Figure 2 and the reheating process in Figure 3. To demonstrate the stability of the proposed finite element approach, the numerical solutions are compared with both theoretical computational results (directly from theoretical formulas) and available experimental data. Figure 2 and Figure 3 show that the acquired numerical solutions match well with the computational results and provide similar trends with those obtained experimentally as reported by in [Liu et al. 2006].

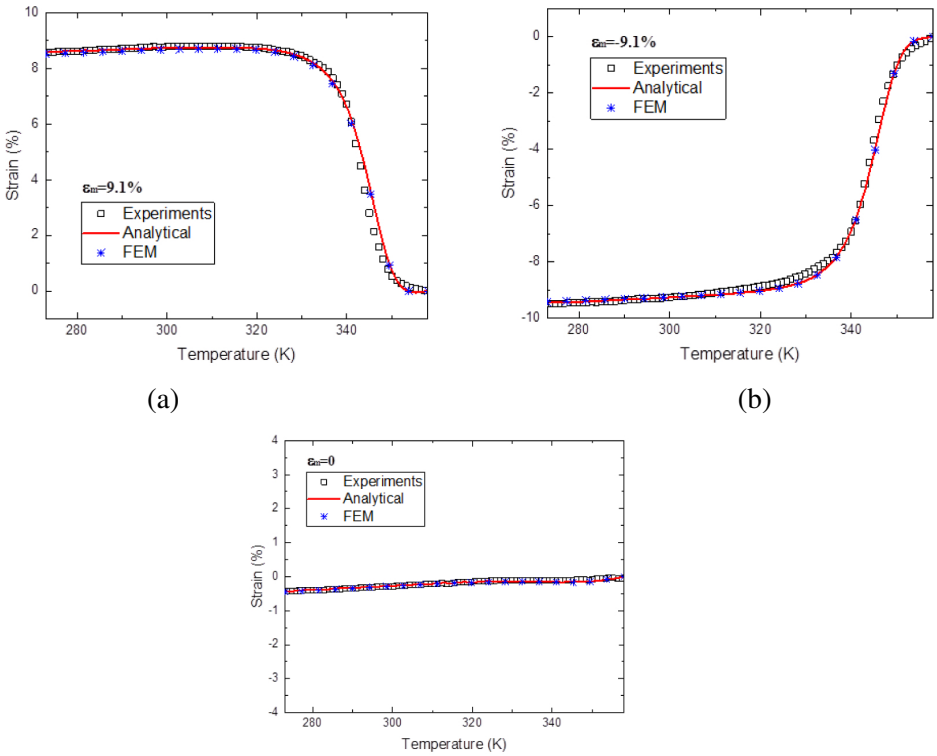

Figure 3. Comparison of FE solutions with theoretical computational results (using "analytical" symbol in figures) and experimental results [Liu et al. 2006] of strain in the reheating process under various loading patterns: (a) $\varepsilon_m = 9.1\%$ (tension); (b) $\varepsilon_m = -9.1\%$ (compression); (c) $\varepsilon_m = 0$ (zero-strain).

5. Deformation of complex structures

To further demonstrate the robustness of the present constitutive theory and its finite element implementation, the proposed numerical model is adopted to simulate the response of 2 complex SMP structures. They are: (i) a deployable structure to be presented in Section 5.1 and (ii) a self-folding structure from a 2D plate to a 3D structure to be elaborated in Section 5.2.

5.1. ***Deployable SMP structure.*** Intelligent deployable structure is a kind of mechanical components that demonstrate significant expansion in area and/or volume influenced by a control signal. It has a great potential for critical applications in various fields. A few examples include those employed as deployable antennas in the area of space exploration and intravascular stents in biomedical applications. With a unique combination of favorable properties (*e.g.,* low density and low cost), SMPs are considered as an ideal material for intelligent deployable structures. Rossiter et al. [2012] designed a SMP hexachiral deployable structure which can be kept at a compact size without any restraint and later be expanded to form a significantly larger structure after its shape recovery.

We adopt the proposed finite element model to simulate the hexachiral deployable structure depicted in Figure 4. The geometry of the structure is the same as the experimental sample used by Rossiter et al. [2012]. Figure 4(a) illustrates the SMP hexachiral structure as a full-sized deployment structure in its initial state. The SMP hexachiral structure is heated to a high temperature above T_g and then compressed to a compact configuration as depicted in Figure 4(b). It is then cooled down to retain the deformed compact shape. After removing the load constraint, an insignificant amount of elastic recovery is observed as shown in Figure 4(c). Finally, the hexachiral structure is expanded to its original full-size

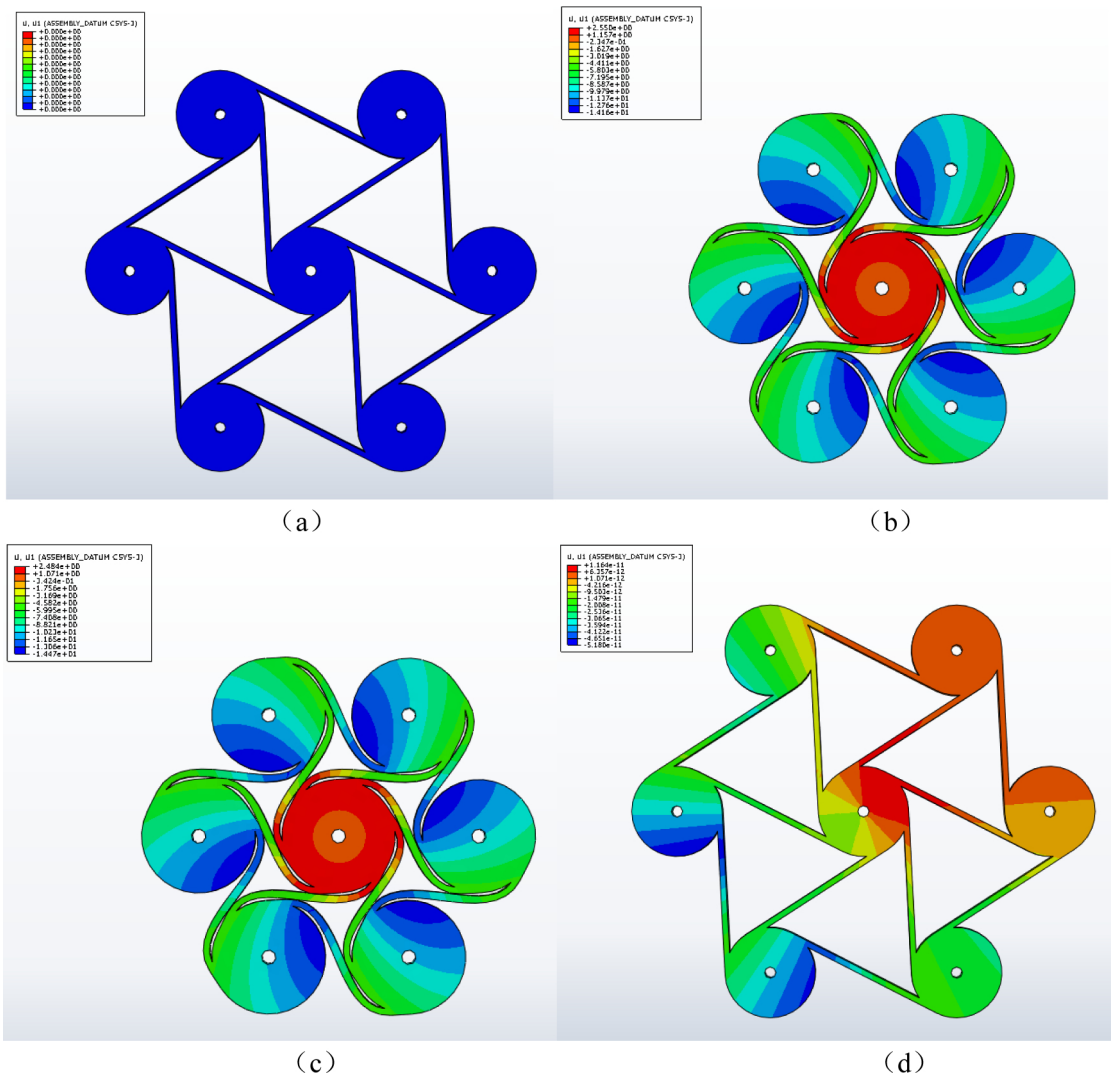

Figure 4. Finite element simulation of hexachiral deployable structure: (a) initial state; (b) compressed state at high temperature; (c) unloaded state after cooling; (d) deployed structure after shape recovery. Colors indicate radial displacements in a cylindrical coordinate system.

structure for deployment by reheating it to a high temperature as displayed in Figure 4(d). The present simulated results as illustrated in Figure 4 are consistent with the experimental outcomes observed by Rossiter et al. [2012]. This demonstrates the feasibility and stability of the proposed constitutive model to simulate various processes of development of the SMP deployable structure.

5.2. ***Self-folding structure.*** Complex three-dimensional (3D) manufacturing processes are often required in the industry. They are normally costly and time-consuming. Self-folding process provides a fast and effective technique for manufacturing three-dimensional structures. Self-folding is a common structural manufacturing method that can be observed in nature, e.g., those in organic molecules, insect wings, human brain and leaves of plants. This has great application prospects in various fields, including space exploration, logistics transportation and flexible electronic devices [Tolley et al. 2014]. The application of SMPs in self-folding structures has recently attracted wide attention. In this section, we design a self-folding structure using SMP materials and simulate the deformation processes of the self-folding structure from its two-dimensional plate strip to a three-dimensional structure.

The initial configuration of the self-folding structure is a two-dimensional rectangular plate strip shown in Figure 5. The plate thickness comprises two layers of the same shape memory polymer material. The bottom layer in dark blue covers the whole board while the upper SMPs layer is divided into several regions of blue portions connected intermittently by smaller yellow parts of self-folding hinge regions which can later be heated locally.

Figure 6 illustrates the deformation processes transforming a two-dimensional pattern to a three-dimensional configuration. First, we heat the original plate structure to a high temperature and apply a compressive deformation along the length of the plate. While retaining the deformed shape, the temperature of the whole structure is reduced to ensure that the deformation is frozen to keep the structure in the deformed configuration even after unloading. Finally, while keeping the temperature of the blue and dark blue regions constant, the yellow self-folding hinge regions are heated locally to extend the latter regions to their original shapes. As the deformation of the bottom plate restricts the expansion of the yellow

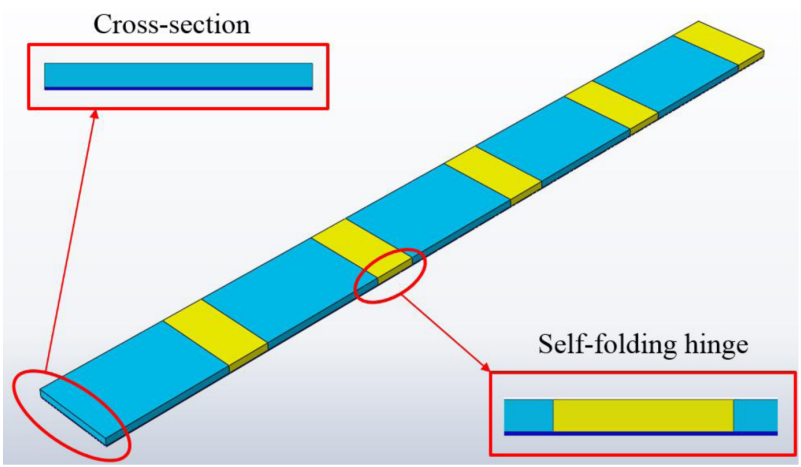

Figure 5. SMP self-folding structure: Plate thickness comprising two layers of blue and dark blue of same SMP material while yellow region as self-folding part.

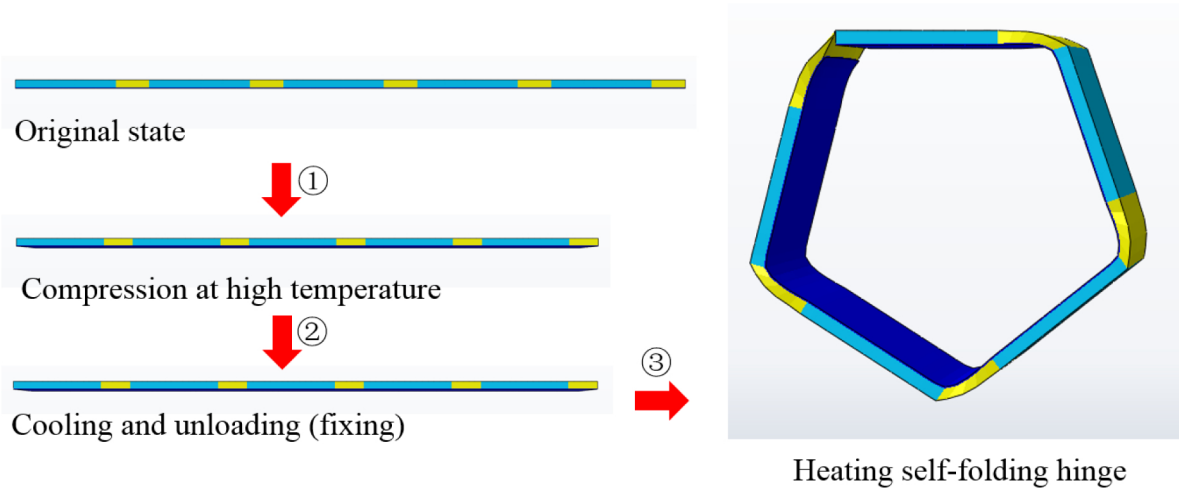

Figure 6. Deformation processes of self-folding structure from 2D to 3D shapes. Arrow 1: plate compressed at high temperature, Arrow 2: plate cooled down and unloaded. Arrow 3: yellow hinge region reheated to form 3D structure.

portions, the two-dimensional plate will fold into a three-dimensional pentagon as illustrated in Figure 6. This simple example demonstrates the potential of SMPs for self-folding applications. Many complex structures can be formed or constructed through the rational design and facilitated via the proposed numerical simulation processes.

6. Concluding remarks

In this paper, we have developed a 3D phase-evolution-based thermomechanical constitutive model for SMPs by extending our previous 1D formulation to enable the analysis of the deformation mechanism at the structural level. The 3D model has been implemented into a finite element package ABAQUS via subroutine UMAT. The proposed theoretical formulation and numerical implementation are validated by the prediction of the shape memory behavior of SMPs under a variety of loading patterns in: (i) tension, (ii) zero-strain and (iii) compression. By comparing results obtained from theoretical calculations, FEM simulations and experiments under the 3 loading conditions, we are confident that the proposed 3D model incorporating FE implementation be able to describe the deformation mechanism of SMP materials reasonably well. FE model as UMAT in ABAQUS is shown to be effective and stable for the study on the shape memory behavior of SMPs. The robustness of the proposed approach is demonstrated through the analyses of 2 complex SMP structures presented in section 5. The tests of the designed hexachiral SMP deployable structure at various stages of deformation mechanism are precisely captured by the numerical solutions conducted in the present study. We also design a self-folding structure comprising a plate with programmed loading and heating regions. The proposed FE solutions show that the designed plate will be morphed into a 3D structure after completing the appropriate programmed processes. The proposed approach accompanied by the finite element implementation will enable researchers to design other functional structures as well as to study the intricate deformation behaviors of various sophisticated SMP structures.

Acknowledgement

The authors are grateful for the support from the National Natural Science Foundation of China through grant numbers 11820101001 and 11572236.

References

[Baghani et al. 2012] M. Baghani, R. Naghdabadi, J. Arghavani, and S. Sohrabpour, "A thermodynamically-consistent 3D constitutive model for shape memory polymers", *Int. J. Plasticity* **35** (2012), 13–30.

[Baghani et al. 2014] M. Baghani, J. Arghavani, and R. Naghdabadi, "A finite deformation constitutive model for shape memory polymers based on Hencky strain", *Mech. Mater.* **73** (2014), 1–10.

[Behl et al. 2010] M. Behl, M. Y. Razzaq, and A. Lendlein, "Multifunctional shape-memory polymers", *Adv. Mater.* **22**:31 (2010), 3388–3410.

[Castano and Flatau 2014] L. M. Castano and A. B. Flatau, "Smart fabric sensors and e-textile technologies: a review", *Smart. Mater. Struct.* **23**:5 (2014), art. id. 053001.

[Chen and Lagoudas 2008a] Y. C. Chen and D. C. Lagoudas, "A constitutive theory for shape memory polymers, I", *J. Mech. Phys. Solids* **56**:5 (2008a), 1752–1765.

[Chen and Lagoudas 2008b] Y. C. Chen and D. C. Lagoudas, "A constitutive theory for shape memory polymers, II", *J. Mech. Phys. Solids* **56**:5 (2008b), 1766–1778.

[Conti et al. 2007] S. Conti, M. Lenz, and M. Rumpf, "Modeling and simulation of magnetic-shape-memory polymer composites", *J. Mech. Phys. Solids* **55** (2007), 1462–1486.

[Diani et al. 2006] J. Diani, Y. Liu, and K. Gall, "Finite strain 3D thermoviscoelastic constitutive model for shape memory polymers", *Poly. Eng. Sci.* **46**:4 (2006), 486–492.

[Diani et al. 2012] J. Diani, P. Gilormini, C. Frédy, and I. Rousseau, "Predicting thermal shape memory of crosslinked polymer networks from linear viscoelasticity", *Int. J. Solids Struct.* **49**:5 (2012), 793–799.

[Eskandari et al. 2018] A. H. Eskandari, M. Baghani, and S. Sohrabpour, "A time-dependent finite element formulation for thick shape memory polymer beams considering shear effects", *Int. J. Appl. Mech.* **10**:4 (2018), art. id. 1850043.

[Fang et al. 2018] C. Q. Fang, J. S. Leng, H. Y. Sun, and J. P. Gu, "A multi-branch thermoviscoelastic model based on fractional derivatives for free recovery behaviors of shape memory polymers", *Mech. Mater.* **120** (2018), 34–42.

[Gilormini and Diani 2012] P. Gilormini and J. Diani, "On modeling shape memory polymers as thermoelastic two-phase composite materials", *C. R. Mécanique* **340**:4-5 (2012), 338–348.

[Gu et al. 2015] J. Gu, H. Sun, and C. Fang, "A phenomenological constitutive model for shape memory polyurethanes", *J. Intel. Mat. Syst. Str.* **26**:5 (2015), 517–526.

[Hager et al. 2015] M. D. Hager, S. Bode, C. Weber, and U. S. Schubert, "Shape memory polymers: past, present and future developments", *Prog. Polym. Sci.* **49** (2015), 3–33.

[He et al. 2015] Y. He, S. Guo, Z. Liu, and K. M. Liew, "Pattern transformation of thermo-responsive shape memory polymer periodic cellular structures", *Int. J. Solids Struct.* **71** (2015), 194–205.

[Hu and Chen 2010] J. L. Hu and S. J. Chen, "A review of actively moving polymers in textile applications", *J. Mater. Chem.* **20**:17 (2010), 3346–3355.

[Hu et al. 2012] J. L. Hu, Y. Zhu, H. H. Huang, and J. Lu, "Recent advances in shape-memory polymers: structure, mechanism, functionality, modeling and applications", *Prog. Polym. Sci.* **37**:12 (2012), 1720–1763.

[Huang et al. 2005] W. Huang, B. Yang, L. An, C. Li, and Y. Chan, "Water-driven programmable polyurethane shape memory polymer: demonstration and mechanism", *Appl. Phys. Lett.* **86** (2005), art. id. 114105.

[Huang et al. 2020] R. Huang, S. J. Zheng, Z. S. Liu, and T. Y. Ng, "Recent advances of the constitutive models of smart materials- hydrogels and shape memory polymers", *Int. J. Appl. Mech.* **12**:2 (2020), art. id. 2050014.

[Lendlein et al. 2005] A. Lendlein, H. Jiang, O. Jünger, and R. Langer, "Light-induced shape-memory polymers", *Nature* **434**:7035 (2005), 879–882.

[Lendlein et al. 2010] A. Lendlein, M. Behl, B. Hiebl, and C. Wischke, "Shape-memory polymers as a technology platform for biomedical applications", *Expert. Rev. Med. Devices* **7**:3 (2010), 0357–379.

[Leng et al. 2009] J. S. Leng, H. B. Lu, Y. J. Liu, W. M. Huang, and S. Y. Du, "Shape-Memory polymers: a class of novel smart materials", *Mrs. Bull.* **34**:11 (2009), 848–855.

[Li and Liu 2018] Y. X. Li and Z. S. Liu, "A novel constitutive model of shape memory polymers combining phase transition and viscoelasticity", *Polymer* **143** (2018), 298–308.

[Li et al. 2015] Y. X. Li, S. S. Guo, Y. H. He, and Z. S. Liu, "A simplified constitutive model for predicting shape memory polymers deformation behavior", *Int. J. Comput. Mater. Sci. Eng.* **4**:1 (2015), art. id. 1550001.

[Li et al. 2017a] Y. X. Li, Y. H. He, and Z. S. Liu, "A viscoelastic constitutive model for shape memory polymers based on multiplicative decompositions of the deformation gradient", *Int. J. Plasticity* **91** (2017a), 300–317.

[Li et al. 2017b] Y. X. Li, J. Y. Hu, and Z. S. Liu, "A constitutive model of shape memory polymers based on glass transition and the concept of frozen strain release rate", *Int. J. Solids Struct.* **124** (2017b), 252–263.

[Li et al. 2018] Y. X. Li, R. X. Liu, and Z. S. Liu, "Study on dynamic behaviors of a shape memory polymer membrane", *Acta. Mech. Solid. Sin.* **31**:5 (2018), 635–651.

[Lin and Chen 1999] J. Lin and L. Chen, "Shape-memorized crosslinked ester-type polyurethane and its mechanical viscoelastic model", *J. Appl. Polym. Sci.* **73**:7 (1999), 1305–1319.

[Liu et al. 2006] Y. Liu, K. Gall, M. L. Dunn, A. R. Greenberg, and J. Diani, "Thermomechanics of shape memory polymers: uniaxial experiments and constitutive modeling", *Int. J. Plasticity* **22**:2 (2006), 279–313.

[Liu et al. 2015] Z. S. Liu, T. William, and T. Y. Ng, "Advances in mechanics of soft materials: a review of large deformation behavior of hydrogels", *Int. J. Appl. Mech.* **7**:5 (2015), art. id. 1530001.

[Liu et al. 2019a] R. X. Liu, Y. X. Li, and Z. S. Liu, "Experimental study on thermo-mechanical behavior of a thermosetting shape memory polymer", *Mech. Time-Depend. Mat.* **23**:3 (2019), 249–266.

[Liu et al. 2019b] R. X. Liu, S. Mcginty, F. S. Cui, X. Y. Luo, and Z. S. Liu, "Modelling and simulation of the expansion of a shape memory polymer stent", *Eng. Comput.* **36**:8 (2019), 2726–2746.

[Lucchesi et al. 2019] M. Lucchesi, B. Pintucchi, and N. Zani, "Orthotropic plane bodies with bounded tensile and compressive strength", *J. Mech. Mater. Struct.* **13**:5 (2019), 691–701.

[Luo and Mather 2013] X. Luo and P. T. Mather, "Shape memory assisted self-healing coating", *ACS Macro. Lett.* **2**:2 (2013), 152–156.

[Moon et al. 2015] S. Moon, F. Cui, and I. J. Rao, "Constitutive modeling of the mechanics associated with triple shape memory polymers", *Int. J. Eng. Sci.* **96** (2015), 86–110.

[Nguyen et al. 2008] T. D. Nguyen, H. J. Qi, F. Castro, and K. N. Long, "A thermoviscoelastic model for amorphous shape memory polymers: incorporating structural and stress relaxation", *J. Mech. Phys. Solids* **56**:9 (2008), 2792–2814.

[Pan and Liu 2018] Z. Z. Pan and Z. S. Liu, "A novel fractional viscoelastic constitutive model for shape memory polymers", *J. Polym. Sci. Pol. Phys.* **56**:16 (2018), 1125–1134.

[Pan et al. 2018] Z. Z. Pan, Y. Zhou, N. Zhang, and Z. S. Liu, "A modified phase-based constitutive model for shape memory polymers", *Polym. Int.* **67**:12 (2018), 1677–1683.

[Pan et al. 2019] Z. Z. Pan, R. Huang, and Z. S. Liu, "Prediction of the thermomechanical behavior of particle reinforced shape memory polymers", *Poly. Comp.* **40**:1 (2019), 353–363.

[Pieczyska et al. 2017] E. A. Pieczyska, M. Staszczak, K. Kowalczyk-Gajewska, M. Maj, K. Golasiński, S. Golba, H. Tobushi, and S. Hayashi, "Experimental and numerical investigation of yielding phenomena in a shape memory polymer subjected to cyclic tension at various strain rate", *Polym. Test.* **60** (2017), 333–342.

[Qi and Dunn 2010] H. J. Qi and M. L. Dunn, "Thermomechanical behavior and modeling approaches", pp. 75–100 in *Shape-memory. polymers and multifunctional composites*, edited by J. Leng and S. Du, CRC Press, 2010.

[Qi et al. 2008] H. J. Qi, T. D. Nguyen, F. Castro, C. M. Yakacki, and R. Shandas, "Finite deformation thermo-mechanical behavior of thermally induced shape memory polymers", *J. Mech. Phys. Solids* **56**:5 (2008), 1730–1751.

[Reese et al. 2010] S. Reese, M. Böl, and D. Christ, "Finite element-based multi-phase modelling of shape memory polymer stents", *Comput. Method. Appl. M* **199**:21-22 (2010), 1276–1286.

[Rossiter et al. 2012] J. Rossiter, F. Scarpa, K. Takashima, and P. Walters, "Design of a deployable structure with shape memory polymers", in *Behavior and mechanics of multifunctional materials and composites* (San Diego, 2012), SPIE **8342**, 2012.

[Shojaei and Li 2014] A. Shojaei and G. Li, "Thermomechanical constitutive modelling of shape memory polymer including continuum functional and mechanical damage effects", *Proc. Roy. Soc. A Math. Phys.* **470**:2170 (2014), art. id. 20140199.

[Shojaei et al. 2013] A. Shojaei, G. Li, and G. Z. Voyiadjis, "Cyclic viscoplastic-viscodamage analysis of shape memory polymers fibers with application to self-healing smart materials", *J. Appl. Mech.* **80**:1 (2013), 819–833.

[Srivastava et al. 2010] V. Srivastava, S. A. Chester, and L. Anand, "Thermally actuated shape-memory polymers: experiments, theory, and numerical simulations", *J. Mech. Phys. Solids* **58**:8 (2010), 1100–1124.

[Tian and Venkatesh 2013] M. Tian and T. A. Venkatesh, "Indentation of shape memory polymers: characterization of thermo-mechanical and shape recovery properties", *Polymer* **54**:4 (2013), 1405–1414.

[Tobushi et al. 1997] H. Tobushi, T. Hashimoto, S. Hayashi, and E. Yamada, "Thermomechanical constitutive modeling in shape memory polymer of polyurethane series", *J. Intel. Mat. Syst. Str.* **8**:8 (1997), 711–718.

[Tolley et al. 2014] M. T. Tolley, S. M. Felton, S. Miyashita, D. Aukes, D. Rus, and R. J. Wood, "Self-folding origami: shape memory composites activated by uniform heating", *Smart. Mat. Struct.* **23**:9 (2014), 094006.

[Valizadeh et al. 2018] I. Valizadeh, P. Steinmann, and A. Javili, "Growth-induced instabilities of an elastic film on a viscoelastic substrate: analytical solution and computational approach via eigenvalue analysis", *J. Mech. Mater. Struct.* **13**:4 (2018), 571–585.

[Volk et al. 2010] B. L. Volk, D. C. Lagoudas, and Y. C. Chen, "Analysis of the finite deformation response of shape memory polymers, II: 1D calibration and numerical implementation of a finite deformation, thermoelastic model", *Smart. Mater. Struct.* **19**:7 (2010), art. id. 075006.

[Yakacki and Gall 2009] C. M. Yakacki and K. Gall, "Shape-memory polymers for biomedical applications", pp. 147–175 in *Shape-Memory polymers*, edited by A. Lendlein, Adv. Polym. Sci. **226**, Springer, 2009.

[Yang and Li 2015] Q. Yang and G. Li, "Temperature and rate dependent thermomechanical modeling of shape memory polymers with physics based phase evolution law", *Int. J. Plasticity* **80** (2015), 168–186.

[Yu et al. 2014] K. Yu, A. J. W. Mcclung, G. P. Tandon, J. W. Baur, and H. J. Qi, "A thermomechanical constitutive model for an epoxy based shape memory polymer and its parameter identifications", *Mech. Time-Depend. Mat.* **18**:2 (2014), 453–474.

[Zheng et al. 2018] S. J. Zheng, Z. Q. Li, and Z. S. Liu, "The fast homogeneous diffusion of hydrogel under different stimuli", *Int. J. Mech. Sci.* **137** (2018), 263–270.

Received 31 Dec 2019. Revised 21 Apr 2020. Accepted 14 May 2020.

YUNXIN LI: liyunxinrrr@stu.xjtu.edu.cn
International Center for Applied Mechanics, State Key Laboratory for Strength and Vibration of Mechanical Structures, Xi'an Jiaotong University, Xi'an, 710049, China

and

Institute of Chemical Materials, CAEP, Mianyang 621999, China

RUOXUAN LIU: liuruoxuan@stu.xjtu.edu.cn
International Center for Applied Mechanics, State Key Laboratory for Strength and Vibration of Mechanical Structures, Xi'an Jiaotong University, Xi'an, 710049, China

ZISHUN LIU: zishunliu@mail.xjtu.edu.cn
International Center for Applied Mechanics, State Key Laboratory for Strength and Vibration of Mechanical Structures, Xi'an Jiaotong University, Xi'an, 710049, China

SOMSAK SWADDIWUDHIPONG: ceesomsa@nus.edu.sg
Department of Civil and Environmental Engineering, National University of Singapore, Singapore 117576, Singapore

JOURNAL OF MECHANICS OF MATERIALS AND STRUCTURES
Vol. 15, No. 3, 2020
https://doi.org/10.2140/jomms.2020.15.307

SLIP DAMPING OF A PRESS-FIT JOINT UNDER NONUNIFORM PRESSURE DISTRIBUTION ALONG THE INTERFACE

HUIFANG XIAO, YUNYUN SUN AND JINWU XU

The energy dissipation and the damping capacity of a press-fit joint under a vertical load are investigated using the continuum elastic beam model. The clamping pressure is considered to be of power law with distance along the contact interface and the corresponding relative displacements under vertical load are derived. Expression of the minimum critical vertical load inducing relative slip along the contact interface is determined. The hysteresis curves of the vertical forces as a function of the relative displacement at the contact interface are obtained for different pressure distribution laws and the associated energy dissipations are presented. The damping ratio of the assembled structure is further evaluated. It is shown that peak values of damping ratio exist for different pressure distribution laws and the normal load at which the peak damping ratio occurs is a function of the pressure distribution law. Three-dimensional finite element analysis validation is performed, which shows good agreement with model predictions.

1. Introduction

Bolted joints are indispensable in build-up machine and mechanical devices with different structure members assembled together, which provide coupling forces and moments between structures. The local relative slip occurring along the frictional joint interface contribute significantly to the damping mechanism of the structure and therefore plays an important role in the dynamic performance and fatigue life of the system [Berger 2002; Ahmadian and Jalali 2007; Yokoyama et al. 2012; Hammami et al. 2016; Choi et al. 2018].

Due to its significance, great effort has been expended on the relative microslip motion at the jointed contact interface as well as the associated energy dissipation and damping capability. As for the modeling of joint behavior, two kinds of models as discrete model and continuum model are developed to represent the microslip motion along the frictional interface in the mechanical joints. The basic discrete model of the frictional interface was developed in [Iwan 1966]. In the Iwan models, the microslip motions are characterized using reduced-order distributed-parameter models. Based on the Iwan model, different discrete models [Song et al. 2004; Segalman 2005; Miller and Quinn 2009; Li et al. 2017] were developed to capture different contact behaviors at the joint interface. As for the continuum models of the microslip motion in joints, the frictional interface is generally described using one-dimensional elastic beam with or without a shear layer between the beam and the frictional ground [Menq et al. 1986; Csaba 1998; Cigeroglu et al. 2006; Asadi et al. 2012].

The effects that related to the contact properties of the interacting surfaces will exhibit influence on the relative motion as well as the energy dissipation and damping capacity of the jointed assembly. These effects have also been studied widely by experiment methods or finite element (FE) simulations. Nanda

Keywords: press-fit joint, nonuniform pressure distribution, energy dissipation, damping ratio.

[2006] experimentally studied the effect of interfacial pressure intensity, diameter of the connecting bolts, number of layers, kinematic coefficient of friction as well as frequency and amplitude of excitation on the damping capacity of layered and jointed structure. The results show that the interfacial pressure intensity and number of layers play a major role on the damping capacity of the jointed structure. Daouk et al. [2017] investigated the effect of shear loading level on the energy dissipation of bolted joint through the model testing of a designed dynamic test rig based on a bolted structure. Stocchi et al. [2013] established a single lap composite bolted joint with countersunk fasteners under static shear tensile load and studied the influence of bolt clamping force, coefficient of friction and bolt-hole clearance on the joint behavior. Chen and Deng [2005] studied the frictional damping at joint interfaces under uniform pressure distribution using the finite element method. Thai and Uy [2015] developed a three-dimensional finite element model to study the effects of column sections and different types of blind bolts on the five motion stages of no slip, slip, full contact, damage and final failure of blind bolted endplate composite joints. Abad et al. [2014] performed both experimental tests and finite element simulations on a bolted lap joint to obtain the force-displacement relationship and to assess the effects of preload on the stick-slip regime between the bolted plates. The parameters of the Valanis model, describing the frictional behavior at the interface are also obtained using the calculated hysteresis cycles.

These previous studies were mostly restricted to the assumption of uniform pressure distribution at the interface, which can be only achieved in condition that the space between consecutive connecting bolts is about two times the diameter of the connecting bolts [Gould and Mikic 1972; Marshall et al. 2006]. The effect of nonuniform pressure distribution at the interface on the contact behavior has also received attention. Cigeroglu et al. [2006] presented a one-dimensional beam model to analyze the stick-slip transitions along the interface under convex and concave nonuniform pressure distributions. Xiao et al. [2014] investigated the energy dissipation in a shear lap joint by considering the effect of interface tangential contact stiffness and nonuniform pressure distribution at the interface. However, the models and results are limited to shear lap joints subjected to tangential load along the interface, which is different from the press-fit joints subjected to a vertical load.

The present work is the extension of the pervious study from shear lap joint to press-fit joint subjected to nonuniform pressure distribution along the interface and a vertical load at the free end. The variation of clamping pressure is assumed to be of exponent law with distance along the contact interface and the corresponding relative displacements under vertical load are derived using the continuum elastic beam model. The hysteresis curves of the vertical forces as a function of the relative displacement at the contact interface are obtained for different pressure distribution laws and the associated energy dissipations are presented. The damping ratio is further evaluated and compared with the finite element modeling results.

2. Description of the studied model

The schematic diagram of a press-fit joint under a vertical force at the free end is shown in Figure 1, left. Two rectangular beams with identical dimensions and material properties are bolt jointed under the clamping force F_n. The dimensions of the beams are length $2L$, height h, width b and the diameter of the bolt is $2R$. The resulted pressure distribution along the interface is parabolic and the influence zone is a circle with 3.5 times the diameter of the connecting bolt [Gould and Mikic 1972; Marshall et al. 2006], i.e., $L = 3.5R$, as shown in Figure 1, right.

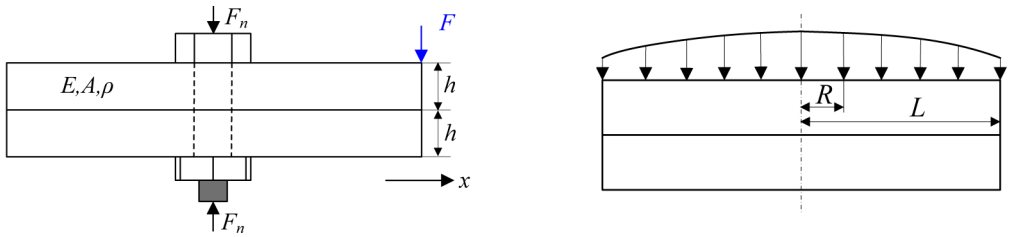

Figure 1. Left: schematic diagram of a press-fit joint under a vertical force at the free end. Right: pressure distribution along the interface.

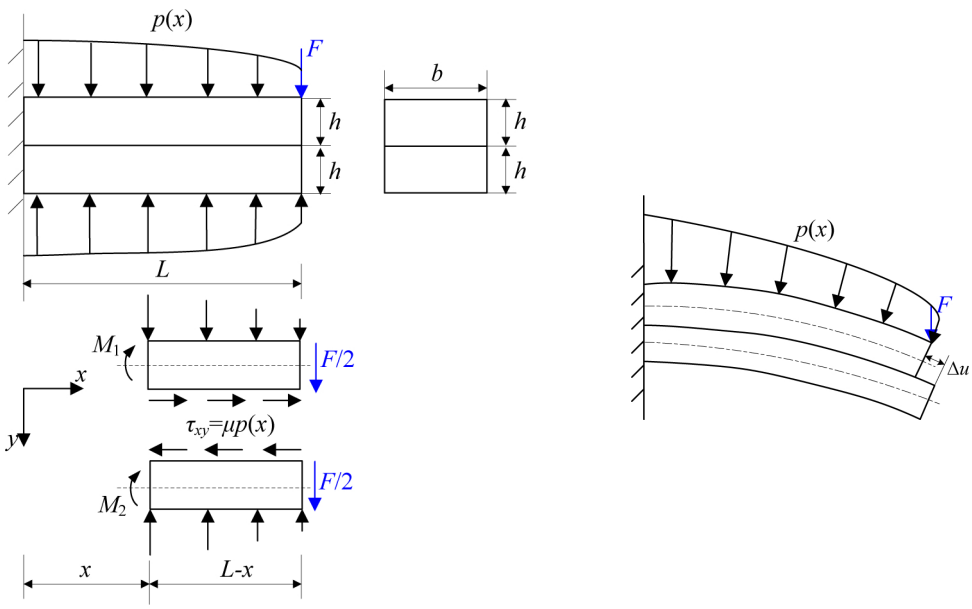

Figure 2. Left: model for examining the relative slip motion at the joint interface and the free-body diagram of the beams. Right: relative motion at the frictional interface under the vertical load, with u the relative displacement at the joint interface.

Figure 2, left, shows the model for examining the relative slip motion at the interface. The left end of the layered jointed beams is fixed. A vertical force F is applied at the right end of the beams. The friction law at the joint interface is represented using the Coulomb model with a constant friction coefficient μ. The relative slip motion at the frictional interface is induced by the vertical force F and is also influenced by the pressure distribution characteristics, as shown in Figure 2, right.

It is assumed that the interfacial pressure along the interface is of exponent law function and can be expressed as follows [Xiao et al. 2014]:

$$p(x) = p_0\left(1 - \frac{1}{2}\left(\frac{x}{L}\right)^{\alpha}\right), \tag{1}$$

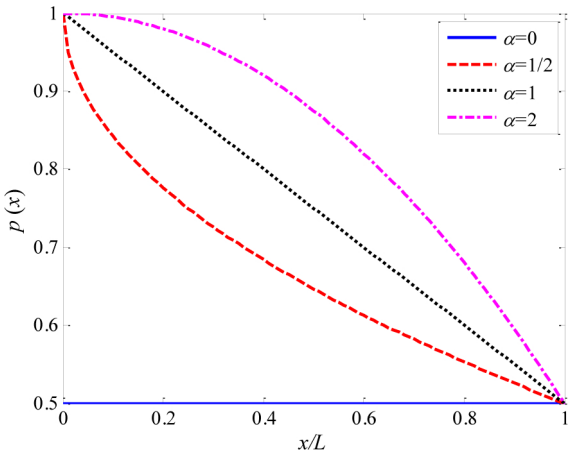

Figure 3. Pressure distributions along the interface for different laws with $p_0 = 1$.

where p_0 is the amplitude of pressure, α is the coefficient denoting different pressure laws, i.e., $\alpha \geq 0$. Figure 3, shows the profiles of pressure distributions for different laws.

3. Relative slip responses

According to the free-body diagram in Figure 2, left, the governing equation for the layered beams in bending can be expressed as

$$EI\frac{d^2w}{dx^2} - \frac{F}{2}(L-x) + \mu p(x)(L-x)b\frac{h}{2} = 0 \tag{2}$$

and the boundary conditions can be found as

$$(dw/dx)_{x=0} = 0, \quad w(0) = 0, \tag{3}$$

where $w(x)$ is the vertical deflection at point x, E is the Young's modulus, I is the moment of inertia of the beam. The solution for vertical deflection can be obtained as

$$w(x) = \frac{(F-\mu p_0 bh)L^3}{Ebh^3}\left[3\left(\frac{x}{L}\right)^2 - \left(\frac{x}{L}\right)^3\right] + \frac{3\mu p_0 L^3}{Eh^2(\alpha+2)}\left[\frac{1}{\alpha+1}\left(\frac{x}{L}\right)^{\alpha+2} - \frac{1}{\alpha+3}\left(\frac{x}{L}\right)^{\alpha+3}\right]. \tag{4}$$

We introduce nondimensional parameters for position, normal load and vertical deflection:

$$\bar{x} = \frac{x}{L}, \quad \bar{F} = \frac{F}{\mu p_0 bh}, \quad \bar{w} = \frac{w}{\mu p_0 L^3/Eh^2}.$$

The nondimensional vertical deflection can be written as

$$\bar{w}(\bar{x}) = (\bar{F}-1)(3\bar{x}^2 - \bar{x}^3) + \frac{3}{\alpha+2}\left[\frac{1}{\alpha+1}\bar{x}^{\alpha+2} - \frac{1}{\alpha+3}\bar{x}^{\alpha+3}\right]. \tag{5}$$

Figure 4 shows the nondimensional vertical deflection along the beam length for different pressure distribution laws with $\alpha = 0, \frac{1}{2}, 1, 2$. The nondimensional normal load used in calculation is $\bar{F} = 3$. It can be seen that the vertical deflection increases along the beam length from $\bar{w} = 0$ at the fixed end to the

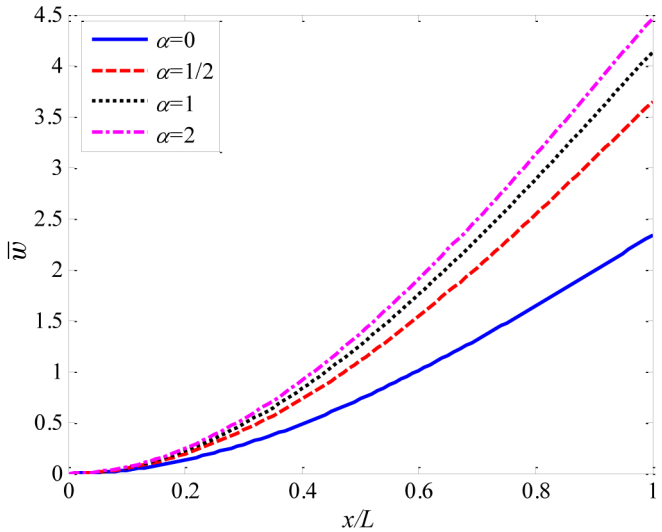

Figure 4. Nondimensional vertical deflection along the beam length for different pressure distribution laws. The nondimensional normal load used in calculation is $\bar{F} = 3$.

maximum at free end where the load is applied. The pressure distribution laws show significant effect on the vertical deflection. The vertical deflection under a uniform pressure distribution with $\alpha = 0$, is smaller than that of the nonuniform pressure distributions at the same position. The nonuniform pressure distribution $\alpha = 2$ has the maximum value of deflection.

3.1. ***Relative slip displacement.*** The relative dynamic slip at the contact interface is given by [Masuko et al. 1973]

$$u(x) = u_2(x) - u_1(x), \tag{6}$$

where $u_1(x)$ and $u_2(x)$ are the displacements at position x on opposite sides of the interface. The displacements are related to the in-plane bending stress and moment about the centroid of each half of the beam as

$$\begin{aligned} u_1(x) &= \frac{1}{E}\int_0^x \frac{\mu p(x)(L-x)}{h}dx - \frac{h}{2}\frac{dw_1}{dx}, \\ u_2(x) &= \frac{1}{E}\int_0^x -\frac{\mu p(x)(L-x)}{h}dx + \frac{h}{2}\frac{dw_2}{dx}. \end{aligned} \tag{7}$$

Assuming the vertical deflection is continuous across the section, i.e., $w_1(x) = w_2(x) = w(x)$, and combining (1), (4), (6) and (7), the relative slip can be expressed as

$$u(x) = \frac{(3F - 5\mu p_0 bh)L^2}{Ebh^2}\left[2\left(\frac{x}{L}\right) - \left(\frac{x}{L}\right)^2\right] - \frac{5\mu p_0 L^2}{Eh}\left[\frac{1}{(\alpha+2)}\left(\frac{x}{L}\right)^{\alpha+2} - \frac{1}{(\alpha+1)}\left(\frac{x}{L}\right)^{\alpha+1}\right]. \tag{8}$$

Introducing the nondimensional parameter $\bar{u} = u/[\mu p_0 L^2/(Eh)]$, the nondimensional relative slip can be written as

$$u'(\bar{x}) = (3\bar{F} - 5)(2\bar{x} - \bar{x}^2) - 5\left[\frac{1}{\alpha+2}\bar{x}^{\alpha+2} - \frac{1}{\alpha+1}\bar{x}^{\alpha+1}\right]. \tag{9}$$

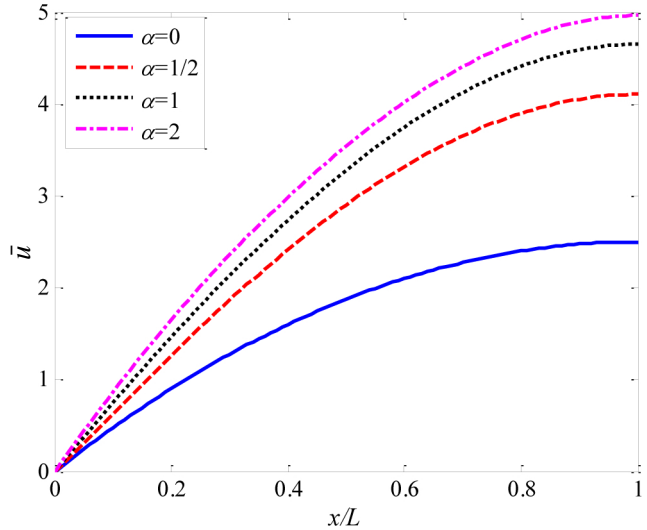

Figure 5. Nondimensional relative slip along the beam length for different pressure distribution laws. The nondimensional normal load $\overline{F} = 3$.

Figure 5 shows the nondimensional relative slip along the beam length for different pressure distribution laws with $\alpha = 0, \frac{1}{2}, 1, 2$. It can be seen that the relative slip also increases along the beam length from $\overline{w} = 0$ at the fixed end to the maximum at free end, similar as that for the vertical deflection. Effect of pressure distribution laws on the relative slip is obvious. The relative slip under a uniform pressure distribution with $\alpha = 0$, is smaller than that of the nonuniform pressure distributions at the same position. The relative slip increases with increasing pressure law value α.

3.2. ***Energy dissipation.*** The energy dissipation per cycle at the frictional interface is expressed as [Xiao et al. 2014]

$$E_d = 4b \int_0^L \mu p(x) u(x)\, dx. \tag{10}$$

Substituting the pressure distribution law (1) and the relative slip displacement expression (8) into (10), the energy dissipation can be obtained as

$$E_d = \frac{4\mu p_0 (3F - 5\mu p_0 bh) L^2}{Eh^2} C_1 - \frac{20(\mu p_0 L)^2 b}{Eh} C_2, \tag{11}$$

where

$$C_1 = \frac{2}{3} - \frac{1}{\alpha+2} + \frac{1}{2(\alpha+3)}, \quad C_2 = \frac{1}{(\alpha+2)(\alpha+3)} - \frac{1}{(\alpha+1)(\alpha+2)} - \frac{1}{2(\alpha+2)(2\alpha+3)} + \frac{1}{4(\alpha+1)^2}.$$

Introducing the nondimensional parameter $E_f = \dfrac{E_d}{(\mu p_0 L)^2 b/(Eh)}$, we can express the nondimensional energy dissipation per cycle as

$$E_f = (12\overline{F} - 20)C_1 - 20C_2. \tag{12}$$

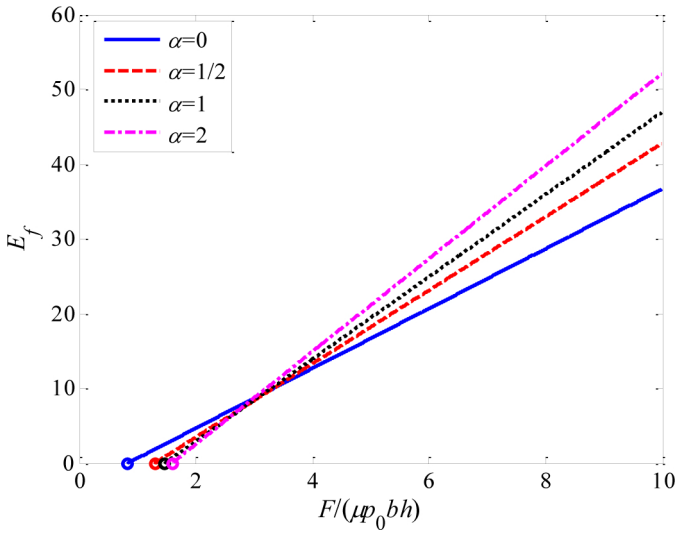

Figure 6. Nondimensional energy dissipation as a function of nondimensional normal load for different pressure distribution laws. The symbols ◯ is for the minimum force values inducing relative slip.

It is noted that the energy dissipation has $E_f > 0$ when relative slip occurs. Accordingly, the minimum force to induce the relative slip at the contact interface is determined as

$$\overline{F}_{\min} = \frac{5}{3}\left(1 + \frac{C_2}{C_1}\right). \tag{13}$$

It can be seen that the minimum force to induce the relative slip is only a function of the pressure distribution law.

Figure 6 shows the normalized energy dissipation per cycle, E_f, versus the normal load $F/(\mu p_0 bh)$ for the four different pressure distribution laws. As can be seen, effect of pressure distribution law on the energy dissipation is obvious and depends on the applied normal load. For small normal load, i.e., $F/(\mu p_0 bh) < 3$, the largest energy dissipation occurs at the uniform pressure distribution for the same normal load; whilst the nonuniform pressure distribution $\alpha = 2$ has the minimum value. However, as the normal load increases, i.e., $F/(\mu p_0 bh) > 3$, the largest energy dissipation occurs with $\alpha = 2$; whilst the uniform pressure distribution has the minimum energy dissipation The increasing rate of energy dissipation with normal load increases with pressure law value α, i.e., the slop of the curve increases for the same normal load with increasing α value.

Figure 7 shows the variation of the minimum normal load inducing relative slip motion at the contact interface with pressure distribution law. The minimum normal load exhibits a quick increase with pressure distribution law for small value of α, i.e., $\alpha < 2$. As the law value becomes larger, the minimum normal load almost keeps the same value of $F_{min} = 1.65$ and not varying with pressure distribution law values.

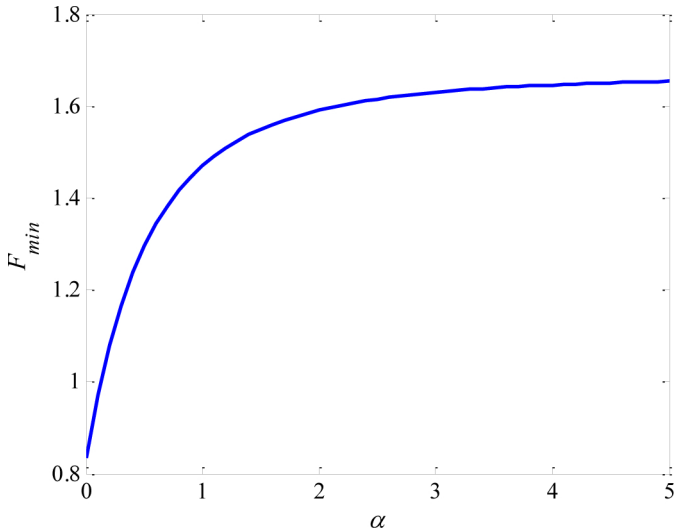

Figure 7. Variation of the minimum nondimensional normal load for relative slipping occurring as a function of pressure distribution law.

3.3. ***Hysteresis curves.*** The vertical deflection at the right end of the beam where the load is applied, $W = \overline{w}(1)$, can be obtained from (5) by setting $\bar{x} = 1$ as

$$W = \overline{w}(1) = 2(\overline{F} - 1) + \frac{3}{(\alpha+2)}\left(\frac{1}{\alpha+1} - \frac{1}{\alpha+3}\right). \tag{14}$$

Equation (14) is the monotonic loading force-deflection relationship at the free end for the layered beams, which illustrates a linear relationship between force and deflection with a constant stiffness value of $\frac{1}{2}$. To determine the whole hysteresis loop under the cyclic vertical load, it is necessary to compute the force-deflection relationship for the unloading and reloading process. It is noted that relative slip can be only initiated when the applied load reaches the minimum load F_{min} in (13). For load smaller than F_{min}, no relative slip occurs at the interface and the beams are in elastic deflection regime with the elastic stiffness has the expression of

$$k_1 = \frac{\overline{F}_{\min}}{W_{\min}} = \frac{\overline{F}_{\min}}{2(\overline{F}_{\min} - 1) + \frac{3}{(\alpha+2)}\left(\frac{1}{\alpha+1} - \frac{1}{\alpha+3}\right)}. \tag{15}$$

Equation (15) shows that the stiffness, i.e., slope of the force-deflection relationship in elastic deflection regime is dependent on the pressure distribution law. The unloading process follows the same elastic deflection regime with stiffness k_1. Accordingly, the force-deflection relationship in the unloading and reloading process can be determined as

$$F_u = k_1(W_u - W^*) - F^*, \tag{16}$$

$$F_r = k_2(W_r + W^*) - F^*, \tag{17}$$

where F_u and F_r are the unloading and reloading force respectively, F^* and W^* are the force and displacement values at which the loading process reversed, k_2 is the slope of the loading force-deflection

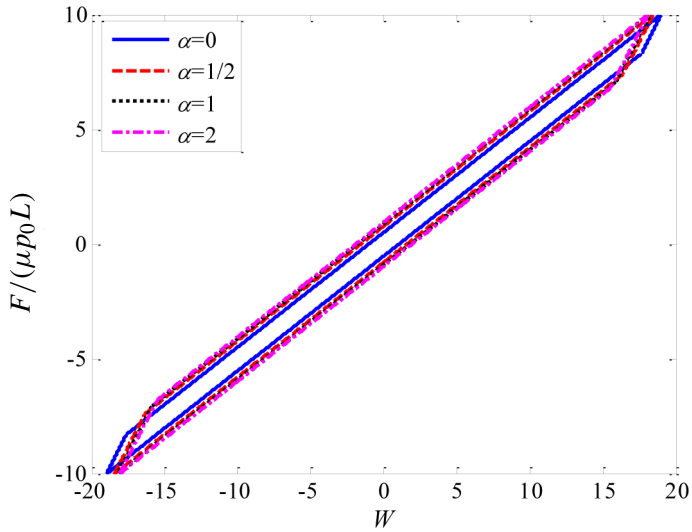

Figure 8. Effect of pressure distribution laws on the hysteresis loop.

relationship, i.e., $k_2 = \frac{1}{2}$, W_u and W_r are the unloading and reloading displacement, respectively. The reloading displacement, W_r, is the negative of the unloading displacement with a negative argument

$$W_r = -W_u. \tag{18}$$

It is clear from (15), (16) and (17) that the properties of the hysteresis loop are embedded in the first loading curve and the minimum load initiating the relative slip

Figure 8 shows the hysteresis curves for different pressure distribution laws. In order to illustrate the effect of pressure distribution laws, the load reversals are chosen to be identical as $F^* = 10$. It can be seen that the pressure distribution law significantly affects the area of the hysteresis cycle and the corresponding value of energy dissipated. The slopes of the force-deflection relationship in the loading and reloading process are constant with $k_2 = \frac{1}{2}$ and are identical for different pressure distribution laws. Although the slope of the force-deflection relationship in the unloading process, i.e., k_1 depends on the pressure distribution law α, the variation of k_1 with α is very slight, as shown in Figure 9. The slope k_1 can be also regarded as constant value. Consequently, the force-deflection curves in the unloading process for different pressure distribution laws are also parallel with almost identical stiffness values.

3.4. ***Damping ratio.*** The damping capacity of the layered beam structure can be characterized using the damping ratio

$$\zeta = \frac{\delta}{\sqrt{(2\pi)^2 + \delta^2}} \approx \frac{\delta}{2\pi}, \tag{19}$$

where δ is the logarithmic damping coefficient and is related to the energy dissipation from two consecutive cycles as follows:

$$\delta = \frac{1}{2} \ln\left(1 + \frac{E_d}{E_{ne}}\right), \tag{20}$$

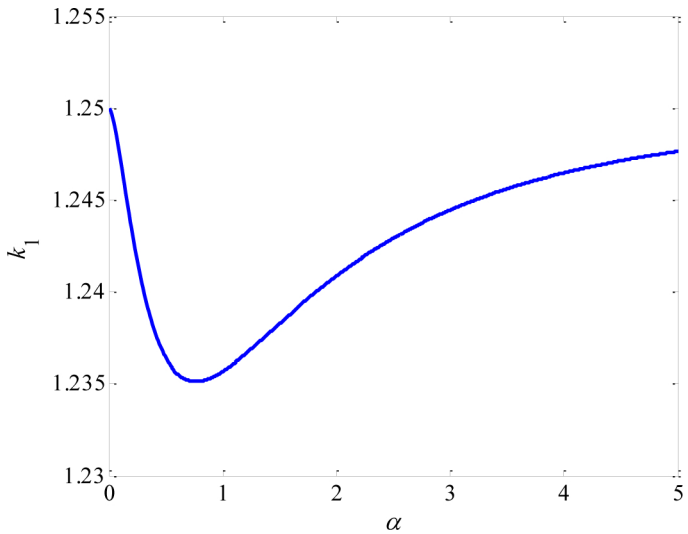

Figure 9. Variation of the slope for force-deflection relationship in the unloading process.

where E_d is the energy loss per cycle, E_{ne} is the maximum

$$E_{ne} = \frac{3}{2}\frac{EI}{L^4}w^2(L), \tag{21}$$

where $I = 2bh^3/3$ is the moment of inertia of the clamped layered beam, $w(L)$ is the vertical deflection at the free end where the load is applied and can be obtained using (4). Accordingly, the strain energy can be determined as

$$E_{ne} = \frac{4bL^2}{Eh}\left[\frac{F-\mu p_0 bh}{bh} + \frac{3\mu p_0}{(\alpha+1)(\alpha+2)(\alpha+3)}\right]^2. \tag{22}$$

Combining (19), (20), (11) and (22), the damping ratio of the layered beams can be determined.

Figure 10 shows the relationship between damping ratio and nondimensional normal load $F/(\mu p_0 bh)$ for different pressure distribution laws with $\alpha = 0, \frac{1}{2}, 1, 2$. Effect of pressure distribution law on the energy dissipation is obvious and this effect is also depends on the applied normal load. For small normal load, the value of damping ratio increases with applied normal load and the largest damping ratio occurs for the uniform pressure distribution with $\alpha = 0$, and the minimum damping ratio is obtained for the pressure distribution with pressure distribution law $\alpha = 2$. As the normal load increases, the value of damping ratio decreases and the largest damping ratio occurs for the pressure distribution with pressure distribution law $\alpha = 2$, and the minimum damping ratio is obtained for uniform pressure distribution. The peak values of damping ratio exist for different pressure distribution laws.

The normal load at which the peak damping ratio occurs can be determined by

$$\frac{d\zeta}{d\bar{F}} = 0. \tag{23}$$

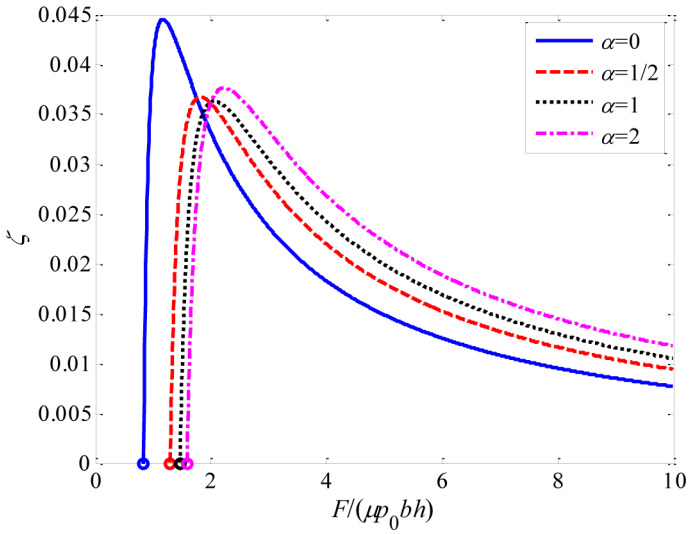

Figure 10. Plots of the relationship between damping ratio and nondimensional normal load for different pressure distribution laws. The symbol ◯ denotes the minimum force values inducing relative slip.

The corresponding normal load is determined as

$$F_0 = \frac{10C_2}{3C_1} + \frac{10}{3} + C_3 - 1, \tag{24}$$

where

$$C_3 = \frac{3}{(\alpha+1)(\alpha+2)(\alpha+3)}.$$

Figure 11 shows the dependence of the normal load at which the peak damping ratio occurring, F_0, on the pressure distribution law. It can be seen that the variation of normal load F_0 with law α shows similar behavior as that for the minimum normal load inducing relative slip motion, as shown in Figure 6. The value of F_0 exhibits a quick increase with pressure distribution law for small value of α, i.e., $\alpha < 2$. As the law value becomes larger, the peak damping ratio normal load almost keeps the same value of $F_0 = 2.25$ and not varying with pressure distribution laws.

4. Comparison with finite element modeling

In order to validate the developed model for slip damping calculation, the layered cantilever beam model as shown in Figure 2, left, is further studied using 3D dynamic finite element analysis (FEA) to determine the damping ratio at the interface. The calculated values of damping ratio using FEA are compared with that using the developed model of (19)–(22) for four different pressure distribution laws of uniform pressure distribution with $\alpha = 0$ and nonuniform pressure distribution with $\alpha = \frac{1}{2}$, 1, 2.

The half-power bandwidth method [Ewins 2000] is employed to determine the damping ratio of the layered cantilever beam model for FEA results. In this method, the frequency response function (FRF) of the system is obtained firstly. Figure 12 shows the schematic diagram of the frequency response function.

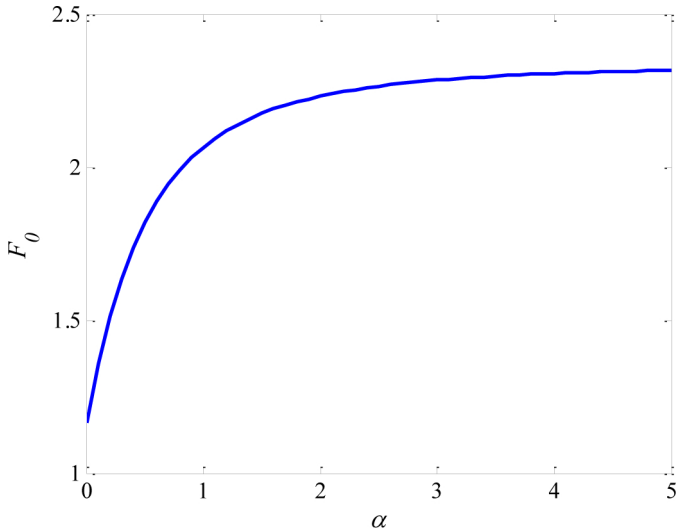

Figure 11. Plot of the variation of the normal load at which the peak damping ratio occurring with the pressure distribution law.

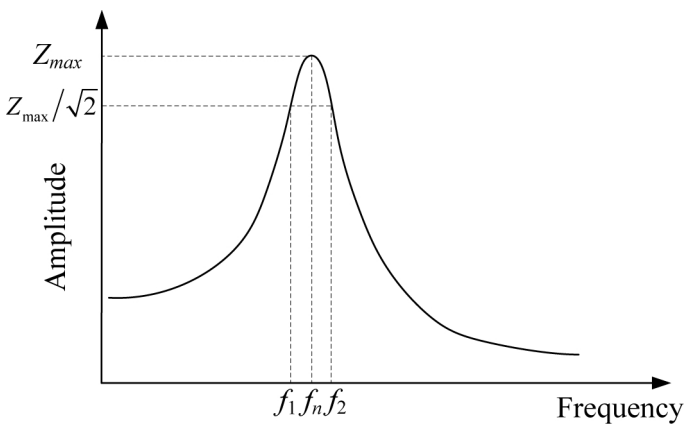

Figure 12. Half-power bandwidth method for estimation of the damping ratio.

The maximum displacement at resonance is $Z_{\max}$ and the corresponding resonant frequency is f_n. The half-power points are determined at which the amplitudes are $Z_{\max}/\sqrt{2}$ and the corresponding frequencies are f_1 and f_2, located on either side of the resonant frequency. The damping ratio is evaluated as

$$\zeta = \frac{f_2 - f_1}{2f_n}, \tag{25}$$

where f_n is the resonant frequency, f_1 and f_2 are the half-power points at which the amplitude is $Z_{\max}/\sqrt{2}$, $Z_{\max}$ is the amplitude at resonance.

In order to obtain the frequency response function (FRF) of the system, the layered cantilever beams are excited at the free end with an impulse excitation. The impulse has the rectangular shape shown in

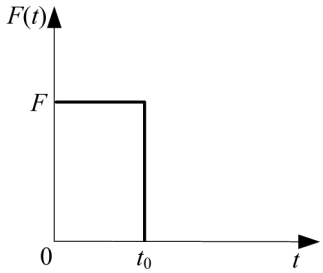

Figure 13. Rectangular impulse force applied at the free end of the beams.

Figure 13 and is modeled as

$$F(t) = F, \quad 0 \le t \le t_0, \tag{26}$$
$$F(t) = 0, \qquad t > t_0, \tag{27}$$

(28)

where F and t_0 are the amplitude and duration of the impulse excitation.

The output vibration signals on the other side at the free end of the beam are collected. The frequency response function (FRF) of the system can be calculated by dividing the acceleration responses of the beam with respect to the impulse excitation in frequency domain. The damping ratio can be then evaluated from the frequency spectrum.

Figure 14 shows the finite element mesh for the layered cantilever beam model. The dimensions of the beams are 300 mm×50 mm×8 mm. The beams are discretized using element SOLID185. The contact interaction at the frictional interface is modeled using surface-to-surface contact and calculated using the penalty method [Zhong 1993]. The mesh convergence is obtained by iteratively increasing the mesh density until the responses differed by less than 1% between iterations [Xiao et al. 2012]. The nodes at the left hand side of the beams were constrained from moving in all directions. A rectangle pulse with time duration of $t_0 = 1 \times 10^{-5}$s is applied on the upper surface of the assembly at the free end. The responses at the bottom surface of the assembly at the free end are collected. Four different pressure distributions with amplitude p_0=1 MPa and law $\alpha = 0$, $\frac{1}{2}$, 1 and 2 are applied on the upper surface of the beam, respectively. The time step employed in the calculations is 1×10^{-5} s.

In order to examine the accuracy of the finite element model, the static analysis of the layered cantilever beam model with a static vertical force at the free end is performed firstly. The amplitude of the vertical force is F=160N. The vertical deflection and relative slip along the beam length for different pressure

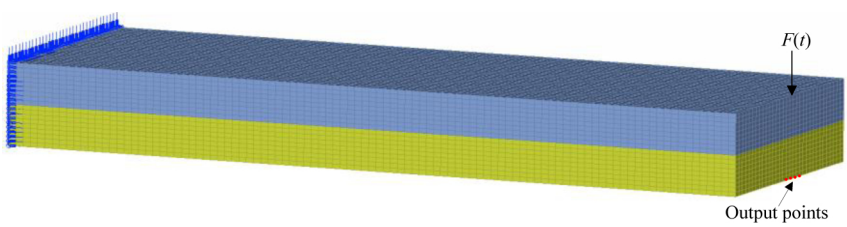

Figure 14. Finite element mesh for the layered cantilever beam model.

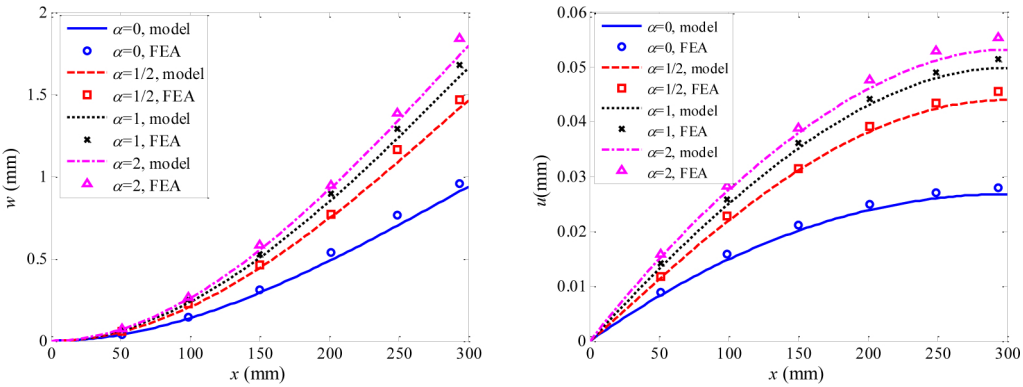

Figure 15. Comparison of vertical deflection and relative slip along the beam length for different pressure distribution laws between theoretical predictions and FEA under normal load F=160N.

distribution laws are calculated using the established FE model. The obtained FEA results are compared with the theoretical model predictions, as shown in Figure 15. It can be seen that the FEA results agree well with the theoretical predictions.

Figure 16 shows examples of the obtained frequency response function (FRF) for the first bending mode of the system under different amplitudes of impulse excitation and different pressure distribution laws. It can be seen that the natural frequency of the system at this mode is f_n=373 Hz. The values of damping ratio are calculated using (25) as $\zeta = 0.033, 0.026, 0.032, 0.024$, respectively.

Figure 17 shows the comparison of damping ratio versus applied normal load between model predictions and FEA results for different pressure distribution laws. It can be seen that that the model predictions agree well with the FEA results, which validates the developed model and the obtained results.

5. Conclusions

In this work, the energy dissipation and the damping capacity of clamped and layered beams under vertical load has been studied using continuum elastic beam model by considering the effect of nonuniform pressure distribution of exponent law. The relative dynamic slip along the contact interface and the associated frictional energy dissipation has been presented. It has been shown that minimum critical vertical loads exist to induce the relative slip along the contact interface. The hysteresis curves at the contact interface have been presented and the damping ratio of the assembled structure has been evaluated. It is shown that peak values of damping ratio exist for different pressure distribution laws and the normal load at which the peak damping ratio occurs is a function of the pressure distribution law. Good agreement between model predictions and three-dimensional finite element analysis validates the developed model and the obtained results. The present study can help to estimate the damping capacity of the layered and jointed structures in order to maximize it as the requirement in real applications. However, the present work is limited to the clamped and layered structures with single interface. Actually, the multilayered composite bolted joints are receiving widespread applications due to their excellent performance high stiffness and strength. Further research is necessary to be conducted on the interfacial slip damping in multilayered bolted structures.

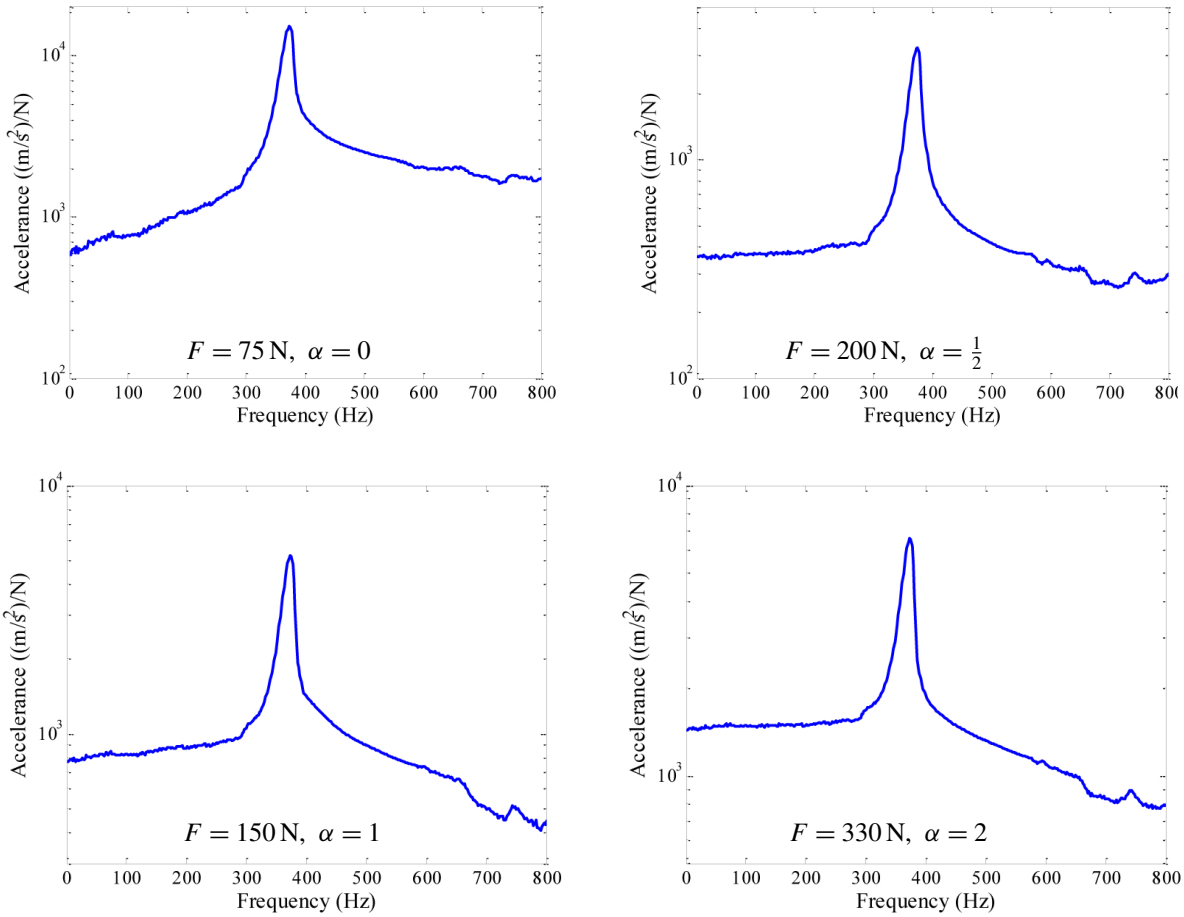

Figure 16. Frequency response function of the system for different amplitudes of impulse excitation and different pressure distribution laws.

Acknowledgement

This work was supported by the National Natural Science Foundation of China, grant number 51775037.

References

[Abad et al. 2014] J. Abad, F. J. Medel, and J. M. Franco, "Determination of Valanis model parameters in a bolted lap joint: Experimental and numerical analyses of frictional dissipation", *Int. J. Mech. Sci.* **89** (2014), 289–298.

[Ahmadian and Jalali 2007] H. Ahmadian and H. Jalali, "Identification of bolted lap joints parameters in assembled structures", *Mech. Syst. Signal Process.* **21** (2007), 1041–1050.

[Asadi et al. 2012] K. Asadi, H. Ahmadian, and H. Jalali, "Micro/macro-slip damping in beams with frictional contact interface", *J. Sound Vib.* **331** (2012), 4704–4712.

[Berger 2002] E. J. Berger, "Friction modelling for dynamic system simulation", *Appl. Mech. Rev.* (*ASME*) **55(6)** (2002), 535–577.

[Chen and Deng 2005] W. Chen and X. Deng, "Structural damping caused by micro-slip along frictional interfaces", *Int. J. Mech. Sci.* **47** (2005), 1191–1211.

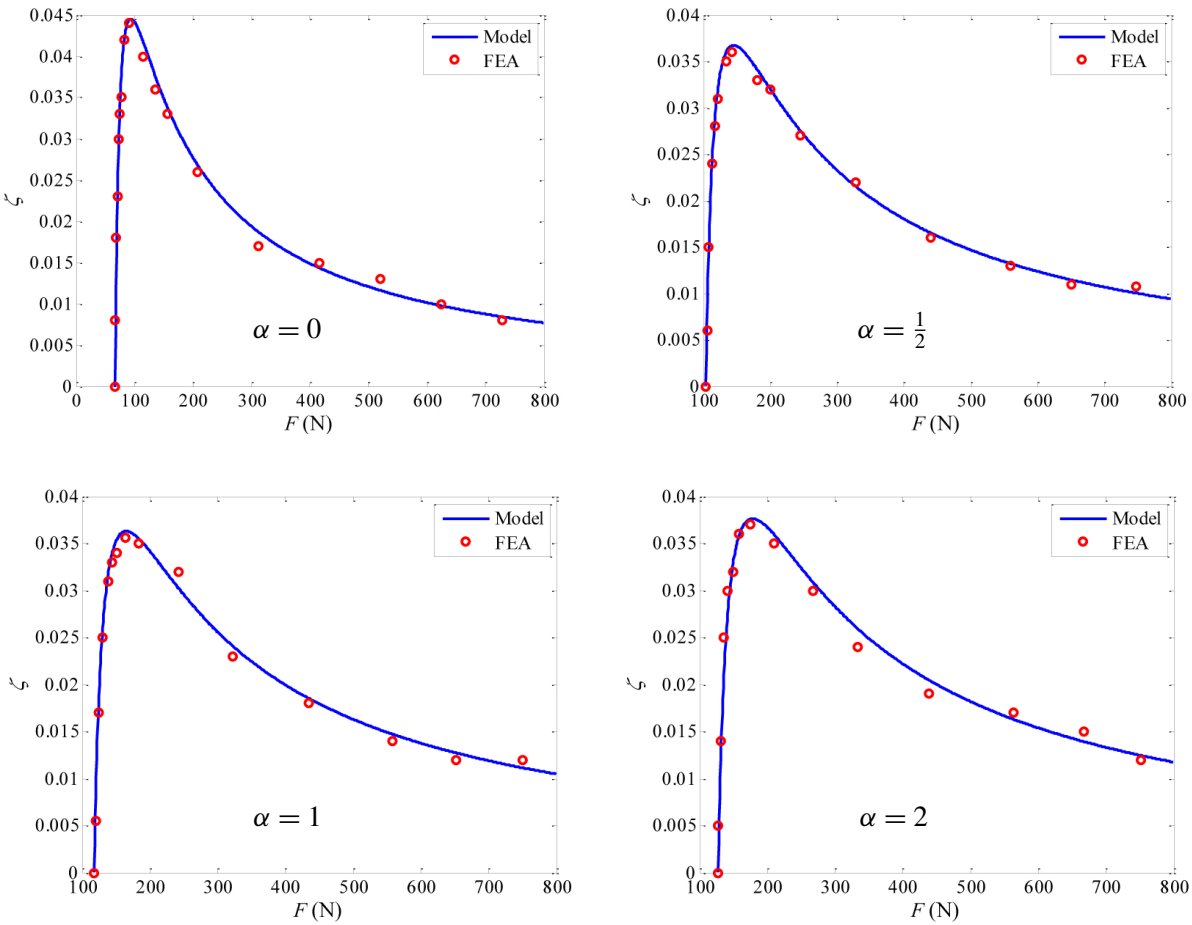

Figure 17. Comparison of damping ratio versus normal load between model predictions and FEA results for different pressure distribution laws.

[Choi et al. 2018] J.-I. Choi, S. M. Hasheminia, H.-J. Chun, J.-C. Park, and H. S. Chang, "Failure load prediction of composite bolted joint with clamping force", *Compos. Struct.* **189** (2018), 247–255.

[Cigeroglu et al. 2006] E. Cigeroglu, W. M. Lu, and C.-H. Menq, "One-dimensional dynamic microslip friction model", *J. Sound Vib.* **292** (2006), 881–898.

[Csaba 1998] G. Csaba, "Forced response analysis in time and frequency domains of a tuned bladed disk with friction dampers", *J. Sound Vib.* **214** (1998), 395–412.

[Daouk et al. 2017] S. Daouk, F. Louf, C. Cluzel, O. Dorival, L. Champaney, and S. Audebert, "Study of the dynamic behavior of a bolted joint under heavy loadings", *J. Sound Vib.* **392** (2017), 307–324.

[Ewins 2000] D. Ewins, *Modal testing: theory*, Practice and Application Research Studies Press Ltd, 2000.

[Gould and Mikic 1972] H. H. Gould and B. B. Mikic, "Areas of contact and pressure distribution in bolted joints", *J. Eng. Industry* (*ASME*) **94**:3 (1972), 864–870.

[Hammami et al. 2016] C. Hammami, E. Balmes, and M. Guskov, "Numerical design and test on an assembled structure of a bolted joint with viscoelastic damping", *Mech. Syst. Signal Process.* **70–71** (2016), 714–724.

[Iwan 1966] W. D. Iwan, "A distributed-element model for hysteresis and its steady-state dynamic response", *J. Appl. Mech.* (*ASME*) **33** (1966), 893–900.

[Li et al. 2017] Y. K. Li, Z. M. Hao, J. Q. Feng, and D. G. Zhang, "Investigation into discretization methods of the six-parameter Iwan model", *Mech. Syst. Signal Process.* **85** (2017), 98–110.

[Marshall et al. 2006] M. B. Marshall, R. Lewis, and R. S. Dwyer-Joyce, "Characterisation of contact pressure distribution in bolted joints", *Strain* **42** (2006), 31–43.

[Masuko et al. 1973] M. Masuko, Y. Ito, and K. Yoshida, "Theoretical analysis for a damping ratio of jointed cantibeam", *Bull. Jpn. Soc. Mech. Eng.* **16** (1973), 1421–1432.

[Menq et al. 1986] C.-H. Menq, J. Bielak, and J. H. Griffin, "The influence of microslip on vibratory response, part I: a new microslip model", *J. Sound Vib.* **107(2)** (1986), 279–293.

[Miller and Quinn 2009] J. D. Miller and D. D. Quinn, "A two-sided interface model for dissipation in structural systems with frictional joints", *J. Sound Vib.* **321** (2009), 201–219.

[Nanda 2006] B. K. Nanda, "Study of the effect of bolt diameter and washer on damping in layered and jointed structures", *J. Sound Vib.* **290** (2006), 1290–1314.

[Segalman 2005] D. J. Segalman, "A four-parameter Iwan model for lap-type joints", *J. Appl. Mech.* (*ASME*) **72** (2005), 752–760.

[Song et al. 2004] Y. Song, C. J. Hartwigsen, D. M. McFarland, A. F. Vakakis, and L. A. Bergman, "Simulation of dynamics of beam structures with bolted joints using adjusted Iwan beam elements", *J. Sound Vib.* **273** (2004), 249–276.

[Stocchi et al. 2013] C. Stocchi, P. Robinson, and S. T. Pinho, "A detailed finite element investigation of composite bolted joints with countersunk fasteners", *Composites A* **52** (2013), 143–150.

[Thai and Uy 2015] H.-T. Thai and B. Uy, "Finite element modeling of blind bolted composite joints", *J. Constr. Steel Res.* **112** (2015), 339–353.

[Xiao et al. 2012] H. F. Xiao, Y. M. Shao, and C. K. Mechefske, "Transmission of vibration and energy through layered and jointed plates subjected to shock excitation", *J. Mech. Eng. Sci.* **226(7)** (2012), 1765–1777.

[Xiao et al. 2014] H. F. Xiao, Y. M. Shao, and J. W. Xu, "Investigation into the energy dissipation of a lap joint using the one-dimensional microslip friction model", *Eur. J. Mech. A Solids* **43** (2014), 1–8.

[Yokoyama et al. 2012] T. Yokoyama, M. Olsson, S. Izumi, and S. Sakai, "Investigation into the self-loosening behavior of bolted joint subjected to rotational loading", *Eng. Failure Anal.* **23** (2012), 35–43.

[Zhong 1993] Z. H. Zhong, *Finite element procedures for contact-impact problems*, Oxford University Press, 1993.

Received 10 Sep 2018. Revised 26 Mar 2019. Accepted 26 Feb 2020.

HUIFANG XIAO: huifangxiao@ustb.edu.cn
, *University of Science and Technology Beijing, Beijing, 100083, China*

YUNYUN SUN: yunyunsunustb@163.com
, *University of Science and Technology Beijing, Beijing, China, China*

JINWU XU: jwxuustb@163.com
, *University of Science and Technology Beijing, Beijing, 100083, China*

JOURNAL OF MECHANICS OF MATERIALS AND STRUCTURES
Vol. 15, No. 3, 2020
https://doi.org/10.2140/jomms.2020.15.325

BENDING OF NONCONFORMING THIN PLATES BASED ON THE FIRST-ORDER MANIFOLD METHOD

XIN QU, FANGFANG DIAO, XINGQIAN XU AND WEI LI

As the convergence, good numerical accuracy and high computing efficiency of nonconforming elements cannot be achieved simultaneously using the finite element method (FEM) or the current numerical manifold method (NMM), the first-order NMM was developed to analyze the bending of thin plates. The first-order Taylor expansion was selected to construct the local displacement function, which endowed the generalized degrees of freedom with physical meanings and decreased the rank deficiency. Additionally, the new relations between the global and local rotation functions in the first-order approximation were derived by adopting two sets of rotation functions, $\{\theta_{xi}, \theta_{yi}\}$ and $\{\theta_x{}^i, \theta_y{}^i\}$. Regular meshes were selected to improve the convergence performance. With the penalized formulation fitted to the NMM for Kirchhoff's thin plate problems, a unified scheme was proposed to deal with irregular and regular boundaries of the domain. The typical examples indicated that the numerical solutions achieved using the first-order NMM rapidly converged to the analytical solutions, and the accuracy of such numerical solutions was vastly superior to that achieved using the FEM and the zero-order NMM.

1. Introduction

A thin plate is one of the most widely used essential structural components, and the numerical analysis of such thin plate with the finite element method (FEM) has provided important guidance for applications in structural engineering [Deng and Murakawa 2008; Kersemans et al. 2014; Miyazaki et al. 2016; Xing and Liu 2009]. The bending of thin plates is associated with fourth-order differential equations, and the classical thin plate theory based on the assumptions formalized by Kirchhoff demands both the transverse displacement and normal rotation to be continuous, i.e., C^1 continuous [Ciarlet 1978; Timoshenko and Woinowsky-Krieger 1959]. This requirement makes it difficult to construct conforming elements. The solution obtained with conforming elements will give bounds to the energy of the correct solution, but, will yield inferior accuracy to that achieved with nonconforming elements on many occasions [Liu and Trung 2010; Zienkiewicz and Taylor 2005]. Thus, such nonconforming elements are often recommended for practical usage. Unfortunately, the convergence of these nonconforming elements significantly depends on the mesh regularity [Ciarlet 1978; Lascaux and Lesaint 1975; Shi 1984]. Furthermore, regular meshes cannot be available for FEM in some cases, particularly in a domain with irregular physical boundaries. Although the mesh-dependence phenomenon of nonconforming elements can be overcome using transformed elements [Shi 1990; Tang et al. 1981; Zhao 1988], the traditional method of constructing displacement functions is not fitted to these transformed elements and good numerical performance cannot be achieved with one element in any situation through numerical experience [Zheng et al. 2013]. Since two completely independent cover systems are used in the numerical manifold method (NMM),

Keywords: nonconforming element, convergence, numerical manifold method, first-order Taylor expansion.

regular meshes can always be selected to improve the convergence performance [Shi 1991], which can solve the abovementioned problems.

At present, some achievements have been made in the analysis of thin plate bending using the NMM. For instance, Zhou and Deng [2008], Zheng et al. [2013] and Qu et al. [2016] solved the convergence problem of nonconforming elements using variational principles, which demonstrated that the NMM provided an alternative way to rescue nonconforming elements. Zhang et al. [2010], Luo et al. [2010] and Wen and Luo [2012] proposed different methods to construct weighted functions, which successfully increased the computational accuracy and convergence rate. These achievements obtained using the NMM further developed the theory of thin plate bending problems. However, these studies still had some issues to be resolved. For the first three studies, the accuracy was not satisfactory when dealing with complex boundary conditions. For the other studies, considerable effort was required to construct shape functions and the applicability was not widespread, reducing the efficiency. Thus, it is necessary to establish a new method that takes into account the accuracy, efficiency, and convergence.

In this study, the first-order Taylor expansion was employed to construct the local displacement function, which endowed the generalized degrees of freedom with physical meanings [Qu and Zheng 2014] and decreased the rank deficiency [Xu et al. 2014]. Obviously, the first-order approximation is the most economical way to upgrade the order of the local deflection function. Additionally, the new relations between the global and local rotation functions in the first-order approximation were derived by adopting two sets of rotation functions, $\{\theta_{xi}, \theta_{yi}\}$ and $\{\theta_x{}^i, \theta_y{}^i\}$. Regular meshes were selected to improve the convergence performance since two completely independent cover systems were used in the NMM. In this way, the best interpolation accuracy, good convergence performance and high computational efficiency can be achieved in the analysis of thin plate bending using the first-order NMM. Then, with the penalized formulation fitted to the NMM for Kirchhoff's thin plate problems, a unified scheme was proposed to deal with irregular and regular boundaries of the domain, and the corresponding computational procedure is introduced in this paper. Finally, three numerical examples were presented to verify the first-order NMM by comparing with the results achieved using the FEM and the zero-order NMM.

2. First-order NMM

In general, the integration over the entire problem is divided into a summation of integrations over all the elements, and the solution is constructed by an interpolation polynomial. However, the continuity of the normal rotation on element surfaces in a nonconforming thin plate cannot be achieved. Thus, the continuous requirements for the variation of the interpolation function cannot be satisfied in this case, which leads to a linear δ-type singular distribution of some derivatives. Importantly, the legality of using the Green theorem cannot be guaranteed, and the final numerical solutions may not always converge to the analytical solutions. The "patch test" proposed in [Bazeley et al. 1965], is considered to be a standard approach for testing the convergence of nonconforming elements. If an element can pass the "patch test", its convergence can be achieved [Bazeley et al. 1965]. The existing literature [Wang 2003; Xie 2009; Zienkiewicz and Taylor 2005] and numerical experience have shown that the elements formed by regular meshes, as proposed by the NMM, are able to pass the "patch test". Therefore, in this paper, rectangular meshes were selected to analyze thin plate bending problems.

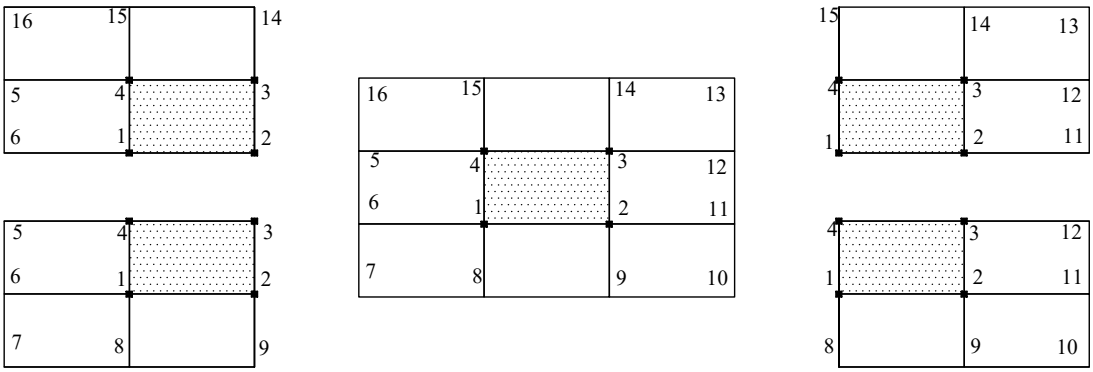

Figure 1. A manifold element and its "physical stars".

A series of the identical rectangular meshes called the finite element meshes were employed as mathematical meshes to cover the neutral surface of a thin plate. In the mathematical covers, one mathematical patch corresponding to one node was the domain composed of rectangular elements connected to it (customarily called a "mathematical star"). Taking Figure 1 as an example, mathematical star 1 is the large rectangle 7-8-9-2-3-4-5-6 that contains four small rectangles 7-8-1-6, 8-9-2-1, 1-2-3-4 and 6-1-4-5; mathematical star 2 is the large rectangle 8-9-10-11-12-3-4-1 that contains four small rectangles 8-9-2-1, 9-10-11-2, 2-11-12-3 and 1-2-3-4; mathematical star 3 is the large rectangle 1-2-11-12-13-14-15-4 that contains four small rectangles 1-2-3-4, 2-11-12-3, 3-12-13-14 and 4-3-14-15; mathematical star 4 is the large rectangle 6-1-2-3-14-15-16-5 that contains four small rectangles 6-1-4-5, 1-2-3-4 , 4-3-14-15 and 5-4-15-16.

By intersecting the neutral surface of the thin plate with all the mathematical stars, "physical stars" can be achieved. All the physical stars constitute physical covers or physical meshes. The overlapping domain of four physical stars forms a manifold element. In Figure 1, the mathematical meshes match the problem domain, and thus, the mathematical stars are the physical stars. The overlapping domain of the physical stars 1, 2, 3 and 4 is the rectangle 1-2-3-4, which is a manifold element.

By cohering four physical stars with their corresponding weighted (shape) functions, the global deflection function of a manifold element can be obtained as

$$w = \sum_{i=1}^{4} \boldsymbol{N}_i \boldsymbol{\delta}_i, \quad (i = 1, 2, 3, 4), \tag{1}$$

where $\boldsymbol{N}_i$ is the weighted (shape) function of physical star i, and $\boldsymbol{\delta}_i$ is the local displacement function of physical star i.

2.1. ***First-order local displacement function.*** In general, there are two ways to upgrade the order of the global displacement function, i.e., constructing a high-order shape function and adopting a high-order local displacement function. However, equation (9) is difficult to satisfy, and thus, constructing the high-order shape function is difficult in the bending of the nonconforming thin plate. Thus, constructing the high-order local displacement function becomes the only reasonable way to upgrade the order of the global displacement function. Lagrange and Hermite piecewise interpolation polynomials are often

used to construct the local displacement functions. Since the derivatives of the deflection function at nodes must be retained in the thin plate bending analysis, Hermite piecewise interpolation functions were adopted in this study.

Once the high-order local displacement function is adopted, more generalized degrees of freedom will be generated. However, the constraint equations do not increase correspondingly. Therefore, the constraint strength of an element is decreased, which may make the element convergence worse. Fortunately, this risk can be reduced to a minimum in the NMM, because the two completely independent cover systems allow the best meshes to be selected as the mathematical meshes for interpolation to improve the convergence performance, such as the rectangular meshes selected in the previous analysis.

In principle, it is available for each physical star to be assigned independently a local deflection function, $w_i(x, y)$, and a local rotation function about the x axis, $\theta_{xi}(x, y)$, and a local rotation function about the y axis, $\theta_{yi}(x, y)$. The undetermined constants in these three functions are uniformly characterized as the generalized degrees of freedom. When constants are chosen as the deflection and rotation functions, it renders the so-called zero-order approximation. For the zero-order approximation, if mathematical meshes match physical meshes, the results are almost the same as those achieved using the FEM. When a linear polynomial is selected as the local deflection function and constants are employed as the local rotation functions about the x and y axes, it is called the first-order approximation. Obviously, the first-order approximation is the most economical way to upgrade the order of the local deflection function. Thus, the first-order approximation was selected to construct a high-order local displacement function.

To endow the generalized degrees of freedom with physical meanings, the local deflection function was constructed following a previously reported method [Qu and Zheng 2014; Xu et al. 2014]. The local deflection function $w_i(x, y)$ was regarded as the first-order Taylor expansion of the global deflection function $w(x, y)$ at (x_i, y_i), which can be written as

$$w_i(x, y) = w^i + w_x^i(x - x_i) + w_y^i(y - y_i), \tag{2}$$

$$w^i = w(x_i, y_i), \quad w_x^i = \left.\frac{\partial w(x, y)}{\partial x}\right|_{(x_i, y_i)}, \quad w_y^i = \left.\frac{\partial w(x, y)}{\partial y}\right|_{(x_i, y_i)}. \tag{3}$$

The physical relations between the global deflection and rotation functions can be expressed as

$$-\theta_y = \frac{\partial w(x, y)}{\partial x}, \quad \theta_x = \frac{\partial w(x, y)}{\partial y}, \tag{4}$$

where θ_x and θ_y denote the global rotation functions about the x and y axes, respectively.

Then, (2) can be also written as

$$w_i(x, y) = w^i - \theta_y^i(x - x_i) + \theta_x^i(y - y_i), \tag{5}$$

where θ_x^i and θ_y^i, induced by the local deflection function $w_i(x, y)$ at (x_i, y_i), are called the additional rotation functions.

Therefore, the local displacement function can be written as

$$\begin{Bmatrix} w_i(x,y) \\ \theta_{xi} \\ \theta_{yi} \end{Bmatrix} = \begin{pmatrix} 1 & 0 & 0 & -(x-x_i) & y-y_i \\ 0 & 1 & 0 & 0 & 0 \\ 0 & 0 & 1 & 0 & 0 \end{pmatrix} \begin{pmatrix} w^i \\ \theta_{xi} \\ \theta_{yi} \\ \theta_y^i \\ \theta_x^i \end{pmatrix}, \tag{6}$$

where θ_{xi} and θ_{yi} denote the local rotation functions about the x and y axes, respectively.

From (6), the generalized degrees of freedom array of physical star i in the first-order approximation can be written as

$$\{\boldsymbol{\delta}_i\} = \begin{Bmatrix} \{w_i\} \\ \theta_{xi} \\ \theta_{yi} \end{Bmatrix} = \begin{Bmatrix} w^i \\ \theta_{xi} \\ \theta_{yi} \\ \theta_y^i \\ \theta_x^i \end{Bmatrix}. \tag{7}$$

Since every manifold element is formed by four overlapping physical stars, there are 20 degrees of freedom in a manifold element. Substituting (7) into (1), the global deflection function of an element can be given as

$$w = \sum_{i=1}^{4} \boldsymbol{N}_i \boldsymbol{\delta}_i = \sum_{i=1}^{4} N_i w^i + N_{xi}\theta_{xi} + N_{yi}\theta_{yi} + N_i \theta_x^i (y-y_i) - N_i \theta_y^i (x-x_i), \tag{8}$$

where $\boldsymbol{N}_i = [N_i, N_{xi}, N_{yi}]$ must meet (9):

$$\begin{aligned} &N_i(r_j) = \delta_{ij}, \quad \frac{\partial N_i(r_j)}{\partial x} = 0, \quad \frac{\partial N_i(r_j)}{\partial y} = 0, \\ &N_{xi}(r_j) = 0, \quad \frac{\partial N_{xi}(r_j)}{\partial x} = 0, \quad \frac{\partial N_{xi}(r_j)}{\partial y} = \delta_{ij}, \\ &N_{yi}(r_j) = 0, \quad \frac{\partial N_{yi}(r_j)}{\partial x} = -\delta_{ij}, \quad \frac{\partial N_{yi}(r_j)}{\partial y} = 0. \end{aligned} \tag{9}$$

Combining (4), (8) and (9), the partial derivatives of deflection function can be obtained:

$$(\theta_x)_i = \left.\frac{\partial w}{\partial y}\right|_i = \frac{\partial N_i}{\partial y} w_i + \frac{\partial N_{xi}}{\partial y}\theta_{xi} + \frac{\partial N_{yi}}{\partial y}\theta_{yi} + N_i \theta_x^i = \theta_{xi} + \theta_x^i, \tag{10}$$

$$(\theta_y)_i = -\left.\frac{\partial w}{\partial x}\right|_i = -\frac{\partial N_i}{\partial x} w_i - \frac{\partial N_{xi}}{\partial x}\theta_{xi} - \frac{\partial N_{yi}}{\partial x}\theta_{yi} + N_i \theta_y^i = \theta_{yi} + \theta_y^i. \tag{11}$$

According to (10) and (11), the global rotations $(\theta_x)_i$ and $(\theta_y)_i$ contained not only the local rotations θ_{xi} and θ_{yi}, but also the additional rotations θ_x^i and θ_y^i. The reason for this was that the partial derivatives of the first-order local deflection function were not equal to zero, and thus, additional terms appeared after differentiating the global deflection function, which corresponded to the additional rotations θ_x^i and θ_y^i. In

such a case, the relations between the global and local rotation functions in the zero-order approximation, shown in (12), did not hold anymore:

$$(\theta_x)_i = \theta_{xi}, \quad (\theta_y)_i = \theta_{yi}. \tag{12}$$

2.2. ***Shape function.*** In this study, the center of a rectangle served as the origin in the local coordinate system, and the ξ and η axes were parallel to the x and y axes, respectively, as shown in Figure 2. The transformation relations of these two coordinate systems can be expressed as

$$x = x_0 + a\xi, \quad y = y_0 + b\eta, \tag{13}$$

$$\begin{aligned} x_0 &= \tfrac{1}{2}(x_1 + x_3) = \tfrac{1}{2}(x_2 + x_4), \quad y_0 = \tfrac{1}{2}(y_1 + y_3) = \tfrac{1}{2}(y_2 + y_4), \\ a &= \tfrac{1}{2}(x_3 - x_1) = \tfrac{1}{2}(x_4 - x_2), \quad b = \tfrac{1}{2}(y_3 - y_1) = \tfrac{1}{2}(y_4 - y_2), \end{aligned} \tag{14}$$

where (x_i, y_i) $(i = 1, 2, 3, 4)$ is the global coordinate of node i.

In the local coordinate system, the coordinate of node i is (ξ_i, η_i) $(i = 1, 2, 3, 4)$, and its value is ± 1. In this paper, the commonly used shape functions in the local coordinate $\xi_0\eta$ were adopted as

$$\begin{aligned} N_i &= \frac{(1+\xi_0)(1+\eta_0)(2+\xi_0+\eta_0-\xi^2-\eta^2)}{8}, \\ N_{xi} &= \frac{-b\eta_i(1+\xi_0)(1+\eta_0)(1-\eta^2)}{8}, \quad (i = 1, 2, 3, 4), \\ N_{yi} &= \frac{a\xi_i(1+\xi_0)(1+\eta_0)(1-\xi^2)}{8}, \end{aligned} \tag{15}$$

where $\xi_0 = \xi\xi_i$ and $\eta_0 = \eta\eta_i$. An element with the abovementioned shape functions can be easily proven to be a nonconforming element [Lascaux and Lesaint 1975; Reddy 2006].

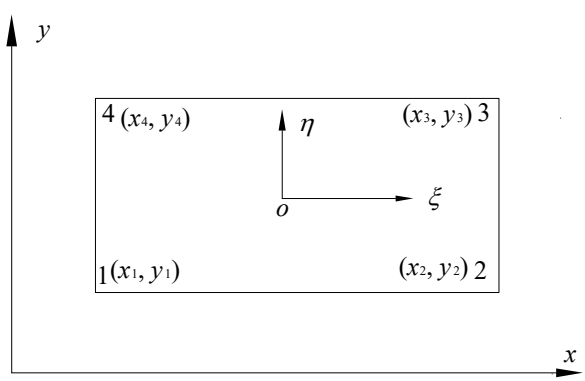

Figure 2. Global and local coordinate systems.

3. Element analyses

The total potential energy based on Kirchhoff's thin plate theory [Timoshenko and Woinowsky-Krieger 1959] can be expressed as

$$\Pi_p = \frac{1}{2}\iint_{\boldsymbol{\Omega}} (\boldsymbol{\kappa}^T \boldsymbol{D}\boldsymbol{\kappa} - \bar{p}w)\, dx\, dy - \int_{\boldsymbol{S}_3} \bar{q}w\, dS + \int_{\boldsymbol{S}_M} \overline{M}_{\boldsymbol{n}} \frac{\partial w}{\partial \boldsymbol{n}} dS, \tag{16}$$

where $\boldsymbol{\Omega}$ indicates the solution domain, $\boldsymbol{\kappa}$ is the generalized strain, $\bar{p}$ is a distributed load, $\bar{q}$ is a linearly transverse load, $\overline{M}_n$ is a bending moment, and $\boldsymbol{n}$ is the exterior unit normal vector. A quantity under the bar "–" indicates that it is known, and $\boldsymbol{S}_M = \boldsymbol{S}_2 \cup \boldsymbol{S}_3$.

In general, the boundary of $\boldsymbol{\Omega}$ can be divided into three disconnected parts, that is, $\partial\boldsymbol{\Omega} = \boldsymbol{S}_1 \cup \boldsymbol{S}_2 \cup \boldsymbol{S}_3$ [Timoshenko and Woinowsky-Krieger 1959]. $\boldsymbol{S}_1$ is clamped, if

$$\text{on } \boldsymbol{S}_1\text{:} \quad w = \bar{w}, \quad \frac{\partial w}{\partial \boldsymbol{n}} = \bar{\varphi}_n, \tag{17}$$

where $\bar{w}$ is the deflection and $\bar{\varphi}_n$ is the normal angle. $\boldsymbol{S}_2$ is simply supported, if

$$\text{on } \boldsymbol{S}_2\text{:} \quad w = \bar{w}, \quad M_n = \overline{M}_n, \tag{18}$$

where $\overline{M}_n$ is the bending moment. $\boldsymbol{S}_3$ is free, if

$$\text{on } \boldsymbol{S}_3\text{:} \quad M_n = \overline{M}_n, \quad \frac{\partial M_{ns}}{\partial \boldsymbol{s}} + Q_n = \bar{q}, \tag{19}$$

where M_{ns} is the twisting moment, and Q_n is the lateral shear force.

The local frame on the boundary is constituted by $\boldsymbol{n}$ and $\boldsymbol{s}$ and displayed in Figure 3. The exterior unit normal vector $\boldsymbol{n}$ and the unit tangential vector $\boldsymbol{s}$ are defined as

$$\boldsymbol{n} = (n_x, n_y)^{\mathrm{T}}, \quad \boldsymbol{s} = -(n_y, n_x)^{\mathrm{T}}. \tag{20}$$

The transformations of the first-order derivatives can be written as

$$\frac{\partial}{\partial \boldsymbol{n}} = n_x \frac{\partial}{\partial x} + n_y \frac{\partial}{\partial y}, \quad \frac{\partial}{\partial \boldsymbol{s}} = -n_y \frac{\partial}{\partial x} + n_x \frac{\partial}{\partial y}. \tag{21}$$

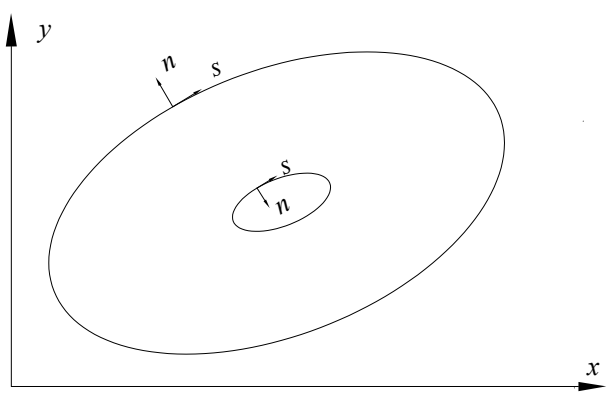

Figure 3. Definition of local frame.

The generalized strain $\boldsymbol{\kappa}$ can be expressed as

$$\{\boldsymbol{\kappa}\} = \begin{Bmatrix} -\partial^2 w/\partial x^2 \\ -\partial^2 w/\partial y^2 \\ -2(\partial^2 w/\partial x\, \partial y) \end{Bmatrix}, \tag{22}$$

$$\boldsymbol{D} = D \begin{bmatrix} 1 & \mu & 0 \\ \mu & 1 & 0 \\ 0 & 0 & 1-\mu \end{bmatrix}, \tag{23}$$

$$D = \frac{Eh^3}{12(1-\mu^2)}, \tag{24}$$

where D is the flexural rigidity of the plate, h is the thickness of a thin plate, E is the modulus of elasticity, and μ is the Poisson's ratio.

The FEM requires all of the nodes to be on the domain boundaries to impose the essential boundary conditions. This creates difficulties when dealing with complex boundaries, because considerable effort is required to solve the mismatch between the meshes and domain boundaries. Fortunately, by using the Lagrange multiplier method and penalty method, the essential boundary conditions can be weakly imposed in the NMM. In this paper, the essential boundary conditions were imposed by using the penalty method. The penalized formulation fitted to the total potential energy can be expressed as

$$\Pi_p^* = \Pi_p + \int_{\boldsymbol{S}_w} \frac{1}{2} k_w (w - \overline{w})^2 \, dS + \int_{\boldsymbol{S}_1} \frac{1}{2} k_M \left(\frac{\partial w}{\partial \boldsymbol{n}} - \bar{\varphi}_n \right)^2 dS, \tag{25}$$

where $\boldsymbol{S}_w = \boldsymbol{S}_1 \cup \boldsymbol{S}_2$ is the essential boundary; k_w and k_M are the penalty parameters, and the suggested values are $10^3 E$–$10^5 E$.

4. Discretization scheme

According to the principle of minimum potential energy, letting $\delta \Pi_p^*(w) = 0$, the true deflection was obtained. The discretized algebraic equations can be written as

$$\boldsymbol{K}\boldsymbol{\delta} = \boldsymbol{f}, \tag{26}$$

where $\boldsymbol{K}$ is the global stiffness matrix, and $\boldsymbol{f}$ is the equivalent nodal force vector. Matrix $\boldsymbol{K}$ is obtained by assembling the stiffness matrix $\boldsymbol{K}^e$ from all of the elements and displacement boundary segments. Vector $\boldsymbol{f}$ is obtained by assembling the vector $\boldsymbol{f}^e$.

The nodal moment $\boldsymbol{M}$ can be derived as

$$\boldsymbol{M} = \boldsymbol{D}\boldsymbol{\kappa}, \tag{27}$$

where the generalized strain $\boldsymbol{\kappa}$ can be written as

$$\begin{aligned} \boldsymbol{\kappa} &= \boldsymbol{B}\boldsymbol{\delta}^e = \begin{bmatrix}\boldsymbol{B}_1 & \boldsymbol{B}_2 & \boldsymbol{B}_3 & \boldsymbol{B}_4\end{bmatrix}\begin{bmatrix}\boldsymbol{\delta}_1^{\mathrm{T}} & \boldsymbol{\delta}_2^{\mathrm{T}} & \boldsymbol{\delta}_3^{\mathrm{T}} & \boldsymbol{\delta}_4^{\mathrm{T}}\end{bmatrix}^{\mathrm{T}}, \\ \boldsymbol{B} &= \begin{bmatrix}\boldsymbol{B}_1 & \boldsymbol{B}_2 & \boldsymbol{B}_3 & \boldsymbol{B}_4\end{bmatrix}, \quad \boldsymbol{\delta}^e = \begin{bmatrix}\boldsymbol{\delta}_1^{\mathrm{T}} & \boldsymbol{\delta}_2^{\mathrm{T}} & \boldsymbol{\delta}_3^{\mathrm{T}} & \boldsymbol{\delta}_4^{\mathrm{T}}\end{bmatrix}^{\mathrm{T}}, \end{aligned} \tag{28}$$

$$B_i = -\begin{bmatrix} \partial^2 \boldsymbol{N}_i/\partial x^2 \\ \partial^2 \boldsymbol{N}_i/\partial y^2 \\ 2(\partial^2 \boldsymbol{N}_i/\partial x\,\partial y)\end{bmatrix} = -\begin{bmatrix} \frac{1}{a^2}(\partial^2 \boldsymbol{N}_i/\partial \xi^2) \\ \frac{1}{b^2}(\partial^2 \boldsymbol{N}_i/\partial \eta^2) \\ \frac{2}{ab}(\partial^2 \boldsymbol{N}_i/\partial \xi\,\partial \eta)\end{bmatrix} = -\frac{1}{ab}\begin{bmatrix} \frac{b}{a}(\partial^2 \boldsymbol{N}_i/\partial \xi^2) \\ \frac{a}{b}(\partial^2 \boldsymbol{N}_i/\partial \eta^2) \\ 2(\partial^2 \boldsymbol{N}_i/\partial \xi\,\partial \eta)\end{bmatrix}. \tag{29}$$

From (16), (25) and (26), the element stiffness matrix $\boldsymbol{K}^e$ is composed of the system stiffness matrix $\boldsymbol{k}$, the matrices due to constrained deflection $\boldsymbol{k_w}$, and normal rotation $\boldsymbol{k_\theta}$, as

$$\boldsymbol{K}^e = \boldsymbol{k} + \boldsymbol{k_w} + \boldsymbol{k_\theta}, \tag{30}$$

where the system stiffness matrix $\boldsymbol{k}$ can be divided into submatrices as

$$\boldsymbol{k} = \begin{bmatrix} \boldsymbol{k}_{11} & \boldsymbol{k}_{12} & \boldsymbol{k}_{13} & \boldsymbol{k}_{14} \\ \boldsymbol{k}_{21} & \boldsymbol{k}_{22} & \boldsymbol{k}_{23} & \boldsymbol{k}_{24} \\ \boldsymbol{k}_{31} & \boldsymbol{k}_{32} & \boldsymbol{k}_{33} & \boldsymbol{k}_{34} \\ \boldsymbol{k}_{41} & \boldsymbol{k}_{42} & \boldsymbol{k}_{43} & \boldsymbol{k}_{44} \end{bmatrix}, \tag{31}$$

$$\boldsymbol{k}_{ij} = \int_{\Omega_e} \boldsymbol{B}_i^{\mathrm{T}} \boldsymbol{D} \boldsymbol{B}_j \, dx\, dy. \tag{32}$$

$\boldsymbol{k_w}$ and $\boldsymbol{k_\theta}$ can be expressed as

$$\boldsymbol{k_w} = \int_{\boldsymbol{S}_w} k_w \boldsymbol{N}^{\mathrm{T}} \boldsymbol{N}\, dS, \quad \boldsymbol{k_\theta} = \int_{\boldsymbol{S}_1} k_M \frac{\partial \boldsymbol{N}^{\mathrm{T}}}{\partial \boldsymbol{n}} \frac{\partial \boldsymbol{N}}{\partial \boldsymbol{n}} dS. \tag{33}$$

The equivalent load vector can be expressed as

$$\boldsymbol{f}^e = \boldsymbol{Q}^e + \int_{\boldsymbol{S}_w} \bar{w}\, k_w \boldsymbol{N}^{\mathrm{T}} dS + \int_{\boldsymbol{S}_w} \bar{\varphi}_n\, k_M \frac{\partial \boldsymbol{N}^{\mathrm{T}}}{\partial \boldsymbol{n}} dS, \tag{34}$$

$$\boldsymbol{Q}^e = \begin{bmatrix}\boldsymbol{Q}_1^{\mathrm{T}} & \boldsymbol{Q}_2^{\mathrm{T}} & \boldsymbol{Q}_3^{\mathrm{T}} & \boldsymbol{Q}_4^{\mathrm{T}}\end{bmatrix}^{\mathrm{T}}. \tag{35}$$

Suppose that a thin plate is subjected to a bending moment $\overline{M}$, transverse line load $\bar{q}$, and uniformly distributed load of intensity $\bar{p}$, and thus, the equivalent nodal forces can be written as

$$\boldsymbol{Q}_i = \begin{Bmatrix} F_{zi} \\ M_{\theta_{xi}} \\ M_{\theta_{yi}} \end{Bmatrix} = \iint_{\Omega_e} \boldsymbol{N}_i^{\mathrm{T}} \bar{p}\, dx\, dy + \int_{S_3} \boldsymbol{N}_i^{\mathrm{T}} \bar{q}\, ds - \int_{\boldsymbol{S}_M} \frac{\partial \boldsymbol{N}_i^{\mathrm{T}}}{\partial n} \overline{M}\, ds, \quad (i = 1, 2, 3, 4). \tag{36}$$

5. Numerical examples

5.1. ***Rectangular plate with four edges simply supported subjected to distributed and concentrated loads.*** A rectangular plate with four edges simply supported is shown in Figure 4. A distributed load of intensity q and a concentrated load p were exerted on the plate.

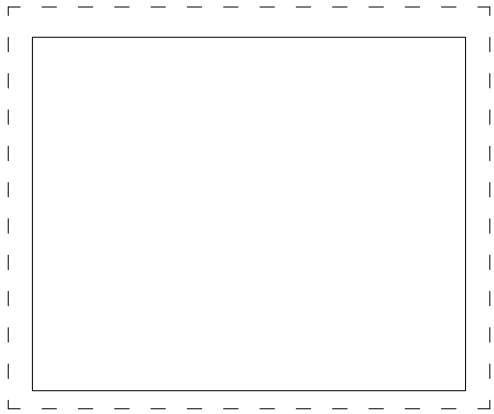

Figure 4. A rectangular plate with four edges simply supported.

The analytical solutions of the deflection in a simply supported plate subjected to a distributed load of intensity q [Reddy 2006] can be expressed as

$$w = \frac{16q}{\pi^6 D} \sum_{m=1,3,5,\ldots}^{\infty} \sum_{n=1,3,5,\ldots}^{\infty} \frac{\sin\frac{m\pi(x+a/2)}{a} \sin\frac{n\pi(y+b/2)}{a}}{mn(m^2/a^2 + n^2/b^2)^2}, \tag{37}$$

where $a = 1$ is the plate width, $b = 1$ is the plate length, $q = 1$, and $D = 1$.

The analytical solutions of the deflection in a simply supported plate subjected to a concentrated load p [Reddy 2006] can be expressed as

$$w = \frac{4p}{\pi^4 abD} \sum_{m=1,3,5,\ldots}^{\infty} \sum_{n=1,3,5,\ldots}^{\infty} (-1)^{(m+n)/2-1} \frac{\sin\frac{m\pi(x+a/2)}{a} \sin\frac{n\pi(y+b/2)}{a}}{(m^2/a^2 + n^2/b^2)^2}, \tag{38}$$

where $p = 1$.

The deflection error is defined as

$$w_{\text{err}} = \frac{|\bar{w} - w|}{w} \times 100\%, \tag{39}$$

where w and $\bar{w}$ are the analytical and numerical solutions of the deflection, respectively. The meshes with 4×4, 8×8, 16×16, 32×32, 64×64 elements are displayed in Figure 5.

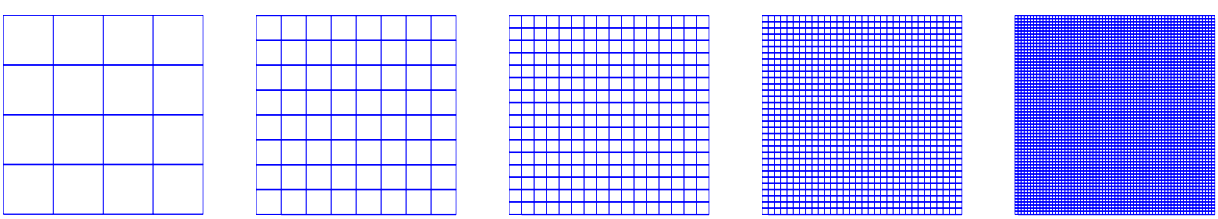

Figure 5. Calculational meshes with different elements of a simply supported rectangular plate; from left to right: 4×4, 8×8, 16×16, 32×32, 64×64.

Figures 6 and 7 show the deflection errors of a simply supported rectangular plate subjected to the distributed load and the concentrated load with the mesh with 64×64 elements achieved with the first-order NMM, respectively. The maximum deflection error of a simply supported rectangular plate subjected to the distributed load with the mesh with 64×64 elements, occurred at the four corners of the rectangular plate, was 0.046762%. The maximum deflection error subjected to the concentrated load, occurred at the center of the rectangular plate, was 0.050923%.

Figures 8 and 9 show the central deflections of a simply supported rectangular plate subjected to the distributed load and the concentrated load achieved with the FEM, the first-order NMM and the analytical method, respectively, and these results are listed in Table 1.

The results achieved with the first-order NMM compared well with the analytical solutions and were slightly better than those achieved with the FEM.

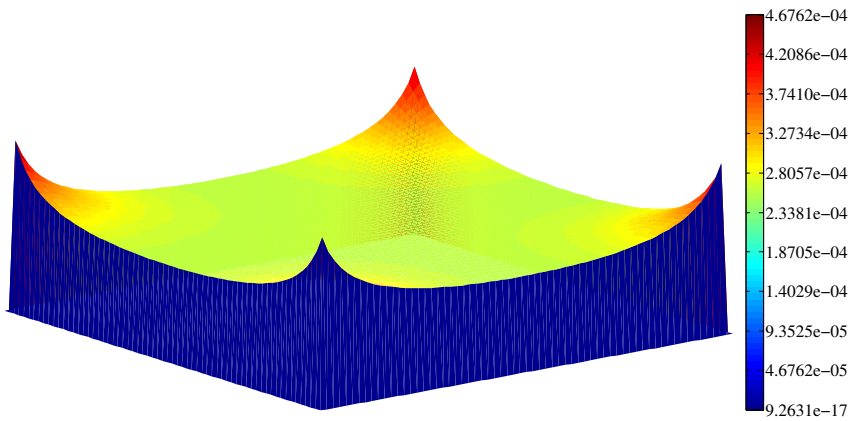

Figure 6. Deflection errors of a simply supported rectangular plate under distribute load using the first-order NMM with the mesh with 64×64 elements.

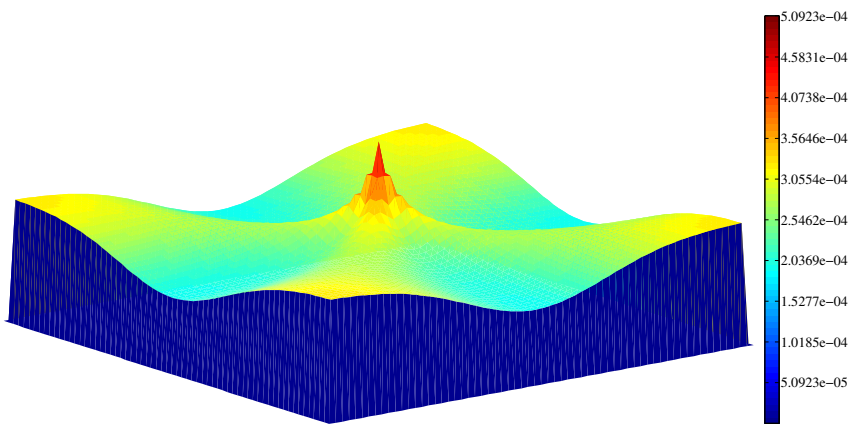

Figure 7. Deflection errors of a simply supported rectangular plate under concentrated load using the first-order NMM with the mesh with 64×64 elements.

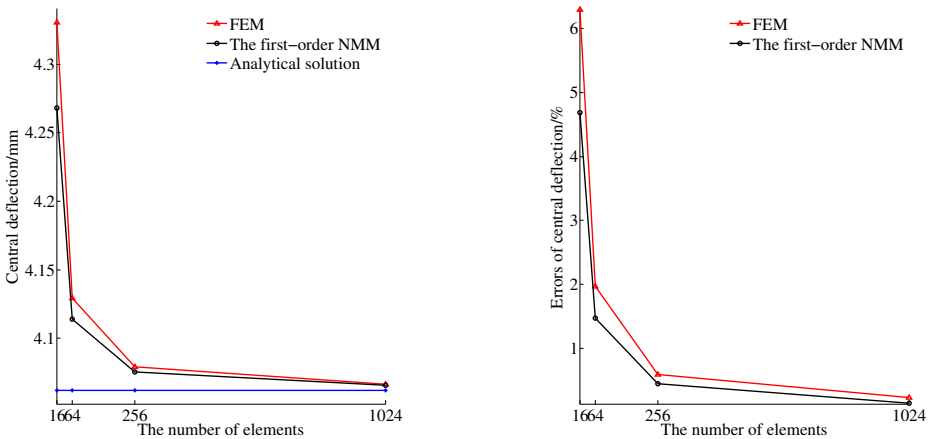

Figure 8. Central deflection comparisons of a simply supported rectangular plate under distributed load using the FEM, the first-order NMM and the analytical method.

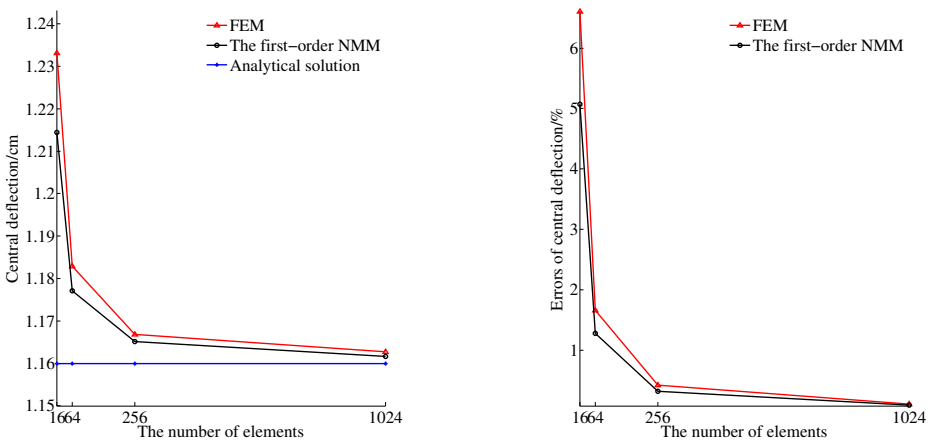

Figure 9. Central deflection comparisons of a simply supported rectangular plate under concentrated load using the FEM, the first-order NMM and the analytical method.

	distributed load (10^{-3} m)		concentrated load (10^{-2} m)	
mesh size	FEM	first-order NMM	FEM	first-order NMM
4×4	4.3304(6.61%)	4.2681(5.07%)	1.2331(6.30%)	1.2144(4.69%)
8×8	4.1293(1.66%)	4.1138(1.28%)	1.1829(1.97%)	1.1771(1.47%)
16×16	4.0791(0.42%)	4.0752(0.32%)	1.1669(0.59%)	1.1652(0.45%)
32×32	4.0665(0.11%)	4.0656(0.09%)	1.1627(0.23%)	1.1616(0.14%)
64×64	4.0634(0.03%)	4.0632(0.03%)	1.1607(0.06%)	1.1605(0.04%)
analytical solution	4.0620		1.1600	

Table 1. Central deflections of a simply supported rectangular plate under distributed and concentrated loads using the FEM, the first-order NMM and the analytical method.

5.2. ***Clamped and simply supported circular plates subjected to distributed load.*** Clamped and simply supported circular plates subjected to a distributed load of intensity q are shown in Figure 10.

The analytical solution of the deflection in a clamped circular plate subjected to a distributed load of intensity q [Reddy 2006] can be expressed as

$$w = \frac{q(x^2 + y^2 - r^2)}{64D}, \tag{40}$$

where $D = 1$, $q = 1$, and $r = 1$.

The analytical solution of the deflection in a simply supported circular plate subjected to a distributed load of intensity q [Reddy 2006] can be expressed as

$$w = \frac{q}{64D}\left[(x^2 + y^2 - r^2)^2 + \frac{4r^2(x^2 + y^2 - r^2)}{1 + \mu}\right], \tag{41}$$

where $\mu = 0.3$. The meshes used for the zero-order NMM and the first-order NMM are shown in Figure 11, and the meshes used for various FEM are shown in Figure 12.

To illustrate the efficiency of the first-order NMM developed in this study, the shell63-type element in ANSYS 10.0 developed by ANSYS Inc. (Pittsburgh, PA, USA), was selected to analyze this plate. The shell63-type element is a plate element with six parameters, the displacements in the directions of the x, y and z axes and the rotations about these three axes. Because the distributed load was perpendicular to the neutral surface, the displacements in the directions of the x and y axes and the rotation about the z axis were considered to be equal to zero. Thus, the shell63-type element can simulate the bending problems of thin plates.

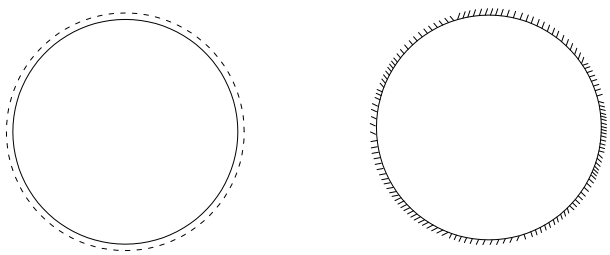

Figure 10. Circular plates: simply supported boundary (left) and clamped boundary (right).

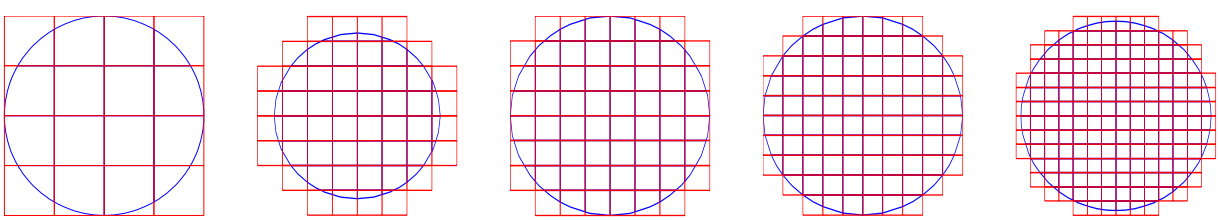

Figure 11. Calculational meshes with different element sizes of circular plates divided for the zero-order NMM and the first-order NMM; from left to right: 0.5×0.5, 0.3×0.3, 0.25×0.25, 0.2×0.2, 0.15×0.15.

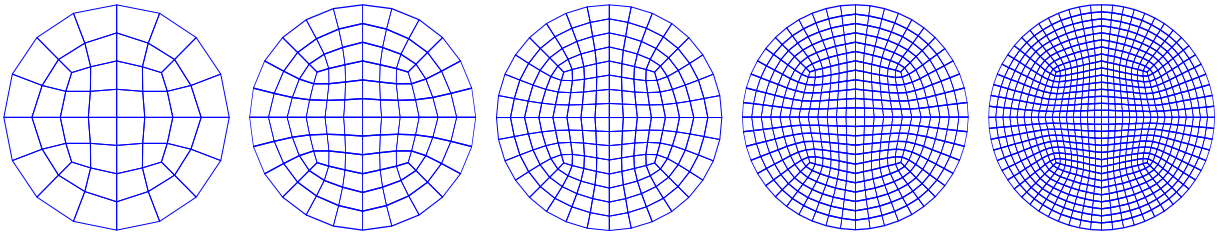

Figure 12. Calculational meshes with different elements of circular plates divided for various FEM; from left to right: 48, 108, 192, 432, 768.

Figures 13 and 14 show the deflections of clamped and simply supported circular plates subjected to a distributed load of intensity q achieved with the first-order NMM and the analytical method. The central deflections achieved with the zero-order NMM, the first-order NMM and the analytical method are listed in Table 2. The central deflections achieved with the shell63-type element in ANSYS 10.0, RPAQ [Cen et al. 2006; Long et al. 2005], TACQ [Cen and Long 1999] and the analytical method are listed in Table 3. In the first column of tables 2 and 3, the length represents the largest element diagonal. Figures 15 and 16 show the central deflections and their errors calculated with different methods.

The results achieved with the first-order NMM compared well with the analytical solutions and were much better than those calculated with the shell63-type element in ANSYS 10.0, RPAQ, TACQ and the zero-order NMM. The convergence processes of the central deflections of a clamped circular plate and a simply supported plate subjected to distributed load calculated with the zero-order NMM and the first-order NMM were oscillatory, and the trends of the deflection errors achieved with the two methods were similar.

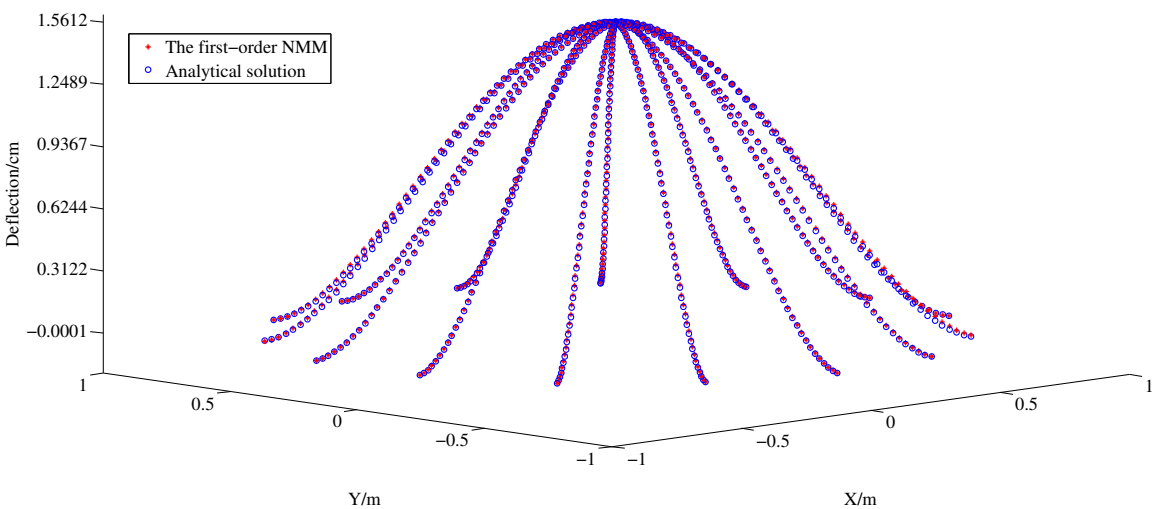

Figure 13. Deflection comparisons of a clamped circular plate under distributed load using the first-order NMM with 0.15×0.15 mesh and the analytical method.

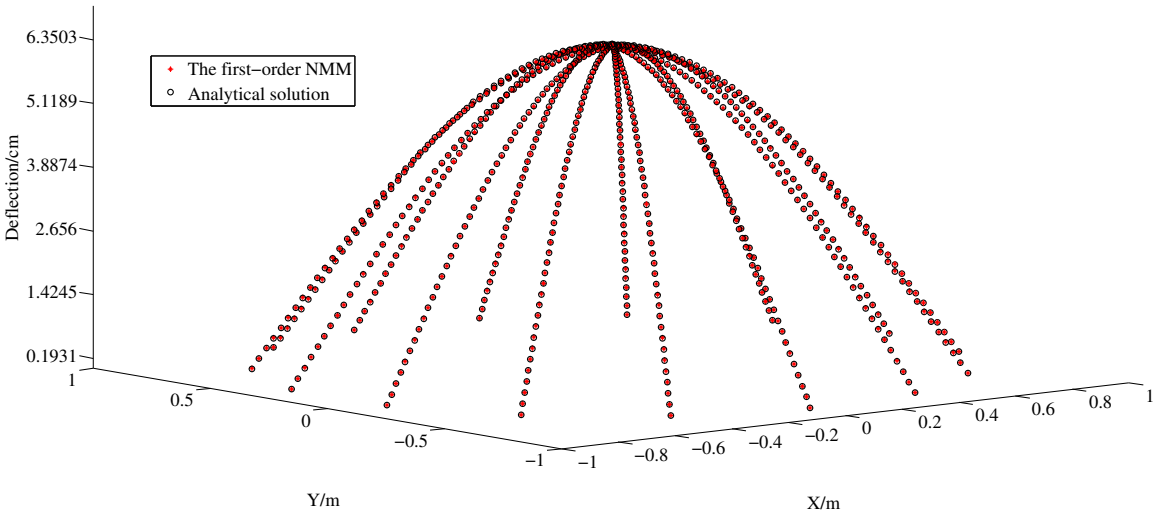

Figure 14. Deflection comparisons of a simply supported circular plate under distributed load using the first-order NMM with 0.15×0.15 mesh and the analytical method.

length (10^{-1} m)/ (element number)	simply supported boundary (10^{-2} m) zero-order NMM	first-order NMM	clamped boundary (10^{-2} m) zero-order NMM	first-order NMM
7.0711/(16)	6.5251(2.43%)	6.5034(2.09%)	1.6466(5.38%)	1.5997(2.38%)
4.2426/(52)	6.3512(0.3%)	6.3561(0.22%)	1.5717(0.59%)	1.5463(1.04%)
3.5355/(60)	6.3569(0.21%)	6.3813(0.17%)	1.5629(0.03%)	1.5586(0.25%)
2.8284/(88)	6.3813(0.17%)	6.3747(0.07%)	1.5553(0.46%)	1.5629(0.03%)
2.1213/(164)	6.3535(0.26%)	6.3741(0.06%)	1.5628(0.02%)	1.5622(0.02%)
analytical solution	6.3702		1.5625	

Table 2. Central deflections of simply supported and clamped circular plates under distributed load using the zero-order NMM, the first-order NMM and the analytical method.

length (10^{-1} m)/ (element number)	simply supported boundary (10^{-2} m) FEM	RPAQ	TACQ	clamped boundary (10^{-2} m) FEM	RPAQ	TACQ
7.368/(48)	6.2753(1.49%)	6.541(2.68%)	–	1.5819(1.24%)	1.264(19.1%)	–
4.3051/(108)	6.3285(0.65%)	6.414(0.69%)	6.4088(0.61%)	1.5715(0.58%)	1.484(5.02%)	1.4790(5.34%)
2.3301/(192)	6.3469(0.37%)	6.381(0.17%)	6.3807(0.16%)	1.5672(0.3%)	1.543(1.25%)	1.5422(1.30%)
1.5696/(432)	6.3599(0.16%)	–	–	1.5644(0.12%)	–	–
1.1814/(768)	6.3644(0.09%)	–	–	1.5635(0.06%)	–	–
analytical solution	6.3702			1.5625		

Table 3. Central deflections of simply supported and clamped circular plates under distributed load using the FEM, RPAQ [Cen et al. 2006], TACQ [Cen and Long 1999] and the analytical method.

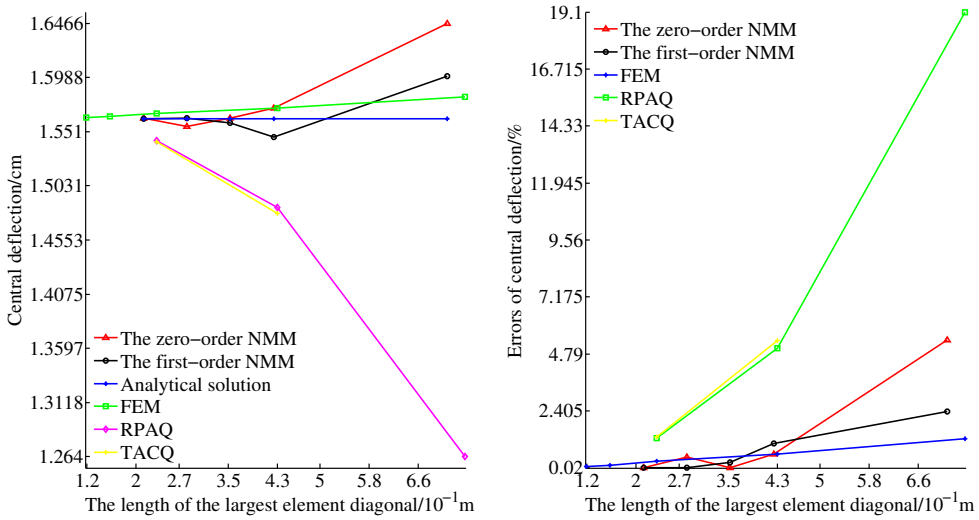

Figure 15. Central deflections and error comparisons of a clamped circular plate under distributed load using the different methods.

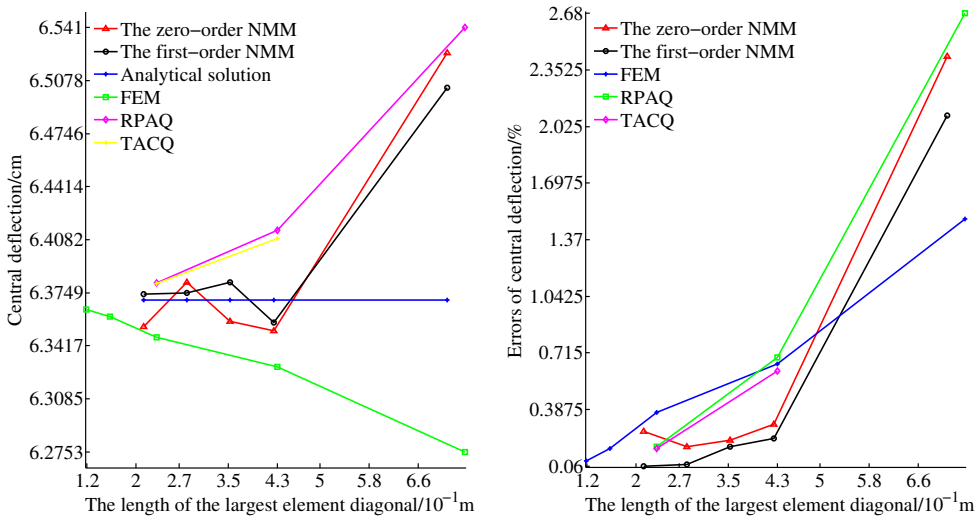

Figure 16. Central deflections and error comparisons of a simply supported circular plate under distributed load using different methods.

5.3. ***Simply supported annular plate subjected to transverse line load.*** An annular plate depicted in Figure 17 (left) with the inner edge subjected to a transverse line load p was studied here, with its outer edge simply supported and its inner edge free. The analytical solution of the deflection for this numerical example [Reddy 2006] can be expressed as

$$w=\frac{pba^2}{8D}\left[\left(1-\frac{x^2+y^2}{a^2}\right)\left(\frac{3+\mu}{1+\mu}-2\kappa\right)+\frac{2(x^2+y^2)}{a^2}\ln\sqrt{\frac{x^2+y^2}{a^2}}+4\kappa\left(\frac{1+\mu}{1-\mu}\right)\ln\sqrt{\frac{x^2+y^2}{a^2}}\right], \quad (42)$$

where $\kappa = \beta^2/(1-\beta^2)\ln\beta$, $\beta = b/a$, $p = 0.01$, $\mu = 0.3$, with $a = 5$ and $b = 1$ as the outer and inner radii of the annular plate, respectively. The mesh used for the zero-order NMM and the first-order NMM is shown in Figure 17 (middle), and the mesh with 3200 elements used for the FEM is shown in Figure 17 (right).

Figure 18 displays the deflections and deflection errors of a simply supported annular plate with the inner edge subjected to transverse line load achieved with the first-order NMM. The maximum deflection error that occurred at the inner edge was 3.8637%. Figure 19 shows the numerical solutions of the deflection on the line $y = 0$ and the corresponding analytical solutions achieved with the first-order NMM, the zero-order NMM, the FEM and the analytical method. The deflections achieved with the first-order NMM compared well with the analytical solutions and were much better than those achieved with the zero-order NMM and the FEM.

Compared with the above methods discussed in the examples, the results calculated with the first-order NMM introduced in this study were more accurate than those achieved with the other methods, since the first-order NMM incorporated both the regular meshes and the first-order displacement function in the bending analysis of nonconforming thin plates. Additionally, the validity of the first-order NMM was verified by comparing the results of the above three examples.

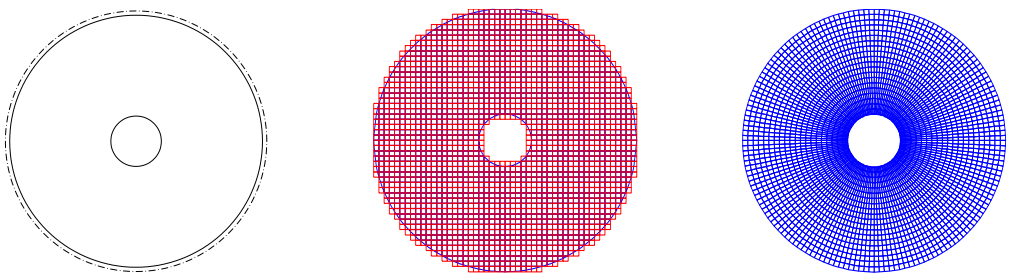

Figure 17. An annular plate: simply supported boundary (left); 0.2×0.2 mesh divided for the first-order NMM and the zero-order NMM (middle); the mesh with 3200 elements divided for the FEM (right).

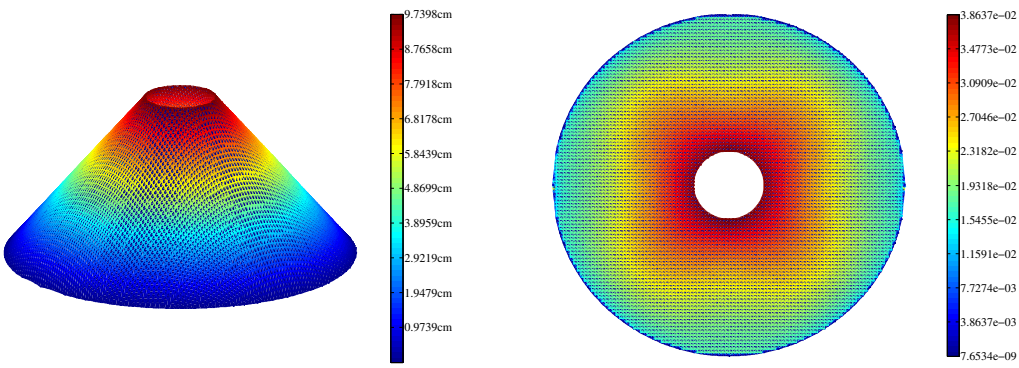

Figure 18. Results of a simply supported annular plate subjected to transverse line load using the first-order NMM with 0.2×0.2 mesh: deflections (left) and deflection errors (right).

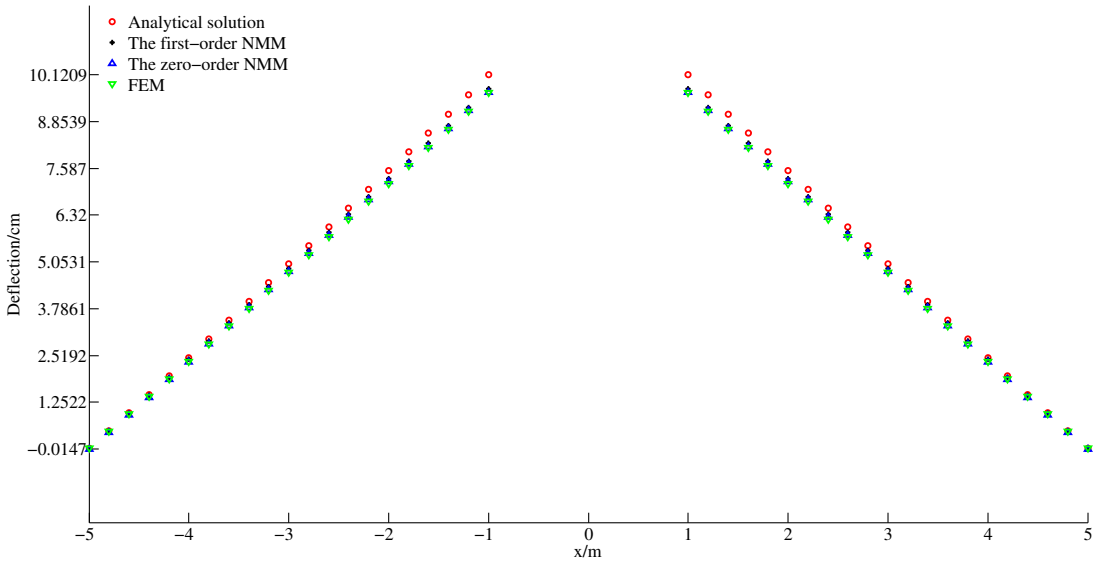

Figure 19. Deflection comparisons of a simply supported annular plate subjected to transverse line load using the different methods.

6. Conclusions

The major advantage of the NMM over the FEM is that it adopts two completely independent covers, which allows the best meshes to be selected as the mathematical cover for interpolation to improve the convergence performance. Another feature is the flexibility in constructing the local displacement function. Using these properties, the first-order NMM was developed to solve the convergence issues of nonconforming elements and improve the accuracy and efficiency. Compared with other methods of upgrading the order of the approximation function, the first-order Taylor expansion endows the generalized degrees of freedom with physical meanings and decreases the rank deficiency. Additionally, the first-order approximation is the most economical way to upgrade the order of the local deflection function. Importantly, the new relations between the global and local rotation functions in the first-order approximation were derived by adopting two sets of rotation functions, $\{\theta_{xi}, \theta_{yi}\}$ and $\{\theta_x{}^i, \theta_y{}^i\}$. The discussed examples showed that the numerical solutions achieved with the first-order NMM rapidly converged to the analytical solutions and their accuracy was vastly superior to that achieved with the FEM and the zero-order NMM, which verified the first-order NMM.

Acknowledgements

This study has been supported by the Doctoral Scientific Research Foundation of Anyang Institute of Technology (No. BSJ2018009), the National Basic Research program of China (No. 2013CB733201), the National Natural Science Foundation of China (No. 41867040) and the Youth Program of National Natural Science Foundation of China (No. 11902134).

We thank LetPub (www.letpub.com) for its linguistic assistance during the preparation of this manuscript. Special thanks to Professor Lijun Su for his significant suggestions.

References

[Bazeley et al. 1965] G. P. Bazeley, Y. K. Cheung, B. M. Irons, and O. C. Zienkiewicz, "Triangular elements in plate bending — conforming and non-conforming solutions", pp. 547–576 in *Proceedings of the 1st Conference on Matrix Methods in Structural Mechanics* (Dayton), 1965.

[Cen and Long 1999] S. Cen and Y. Q. Long, "A quadrilateral thin-thick plate bending element by using area coordinate method", *Eng. Mech.* **16**:2 (1999), 1–15.

[Cen et al. 2006] S. Cen, Y. Q. Long, Z. H. Yao, and S. P. Chiew, "Application of the quadrilateral area co-ordinate method: a new element for Mindlin–Reissner plate", *Int. J. Numer. Methods Eng.* **66**:1 (2006), 1–45.

[Ciarlet 1978] P. G. Ciarlet, *The finite element method for elliptic problems*, North-Holland, Amsterdam, 1978.

[Deng and Murakawa 2008] D. Deng and H. Murakawa, "Prediction of welding distortion and residual stress in a thin plate butt-welded joint", *Comput. Mater. Sci.* **43**:2 (2008), 353–365.

[Kersemans et al. 2014] M. Kersemans, A. Martens, N. Lammens, K. Van Den Abeele, J. Degrieck, F. Zastavnik, L. Pyl, H. Sol, and W. Van Paepegem, "Identification of the elastic properties of isotropic and orthotropic thin-plate materials with the pulsed ultrasonic polar scan", *Exp. Mech.* **54**:6 (2014), 1121–1132.

[Lascaux and Lesaint 1975] P. Lascaux and P. Lesaint, "Some nonconforming finite elements for the plate bending problem", *R.A.I.R.O. Analyse Numérique* **9**:R1 (1975), 9–53.

[Liu and Trung 2010] G. R. Liu and N. T. Trung, *Smoothed finite element methods*, CRC Press, Boca Raton, 2010.

[Long et al. 2005] Y. Q. Long, X. M. Chen, and S. Cen, "A locking-free and robust quadrilateral reissner plate element", *Chin. J. Comput. Mech.* **22**:4 (2005), 385–391.

[Luo et al. 2010] S. M. Luo, W. B. Wen, S. Y. Chen, and Z. R. Zhang, "A new triangular element of numerical manifold method", *J. Plast. Eng.* **17**:6 (2010), 131–135.

[Miyazaki et al. 2016] H. Miyazaki, Y. Yoshizawa, K. Hirao, T. Ohji, and H. Hyuga, "Round-robin test on the fracture toughness of ceramic thin plates through modified single edge-precracked plate method", *J. Eur. Ceram. Soc.* **36**:13 (2016), 3245–3248.

[Qu and Zheng 2014] X. Qu and H. Zheng, "Mixed-order manifold method based on Taylor expansion", *J. Yangtze Riv. Scienti. Res. Ins.* **31**:8 (2014), 87–92.

[Qu et al. 2016] X. Qu, H. Zheng, L. J. Su, and C. G. Li, "Incompatible manifold method for thin plate problems based on the best quality mesh", *Chin. J. Comput. Mech.* **33**:6 (2016), 819–825.

[Reddy 2006] J. N. Reddy, *Theory and analysis of elastic plates and shells*, CRC Press, Boca Raton, 2006.

[Shi 1984] Z. C. Shi, "The generalized patch test for zienkiewicz's triangles", *J. Comput. Math.* **2**:3 (1984), 279–286.

[Shi 1990] Z. C. Shi, "On the accuracy of the quasi-conforming and generalized conforming finite elements", *Chin. Ann. Math. Ser. B* **11**:2 (1990), 148–155.

[Shi 1991] G. H. Shi, "Manifold method of material analysis", pp. 57–76 in *Transactions of the Ninth Army conference on applied mathematics and computing* (Minneapolis), 1991.

[Tang et al. 1981] L. M. Tang, W. J. Chen, and Y. X. Liu, "The quasi-conforming elements for thin plate bending analysis", *J. Build. Struct.* **2** (1981), 10–22.

[Timoshenko and Woinowsky-Krieger 1959] S. Timoshenko and S. Woinowsky-Krieger, *Theory of plates and shells*, 2nd ed., McGraw-Hill Book Company, 1959.

[Wang 2003] X. C. Wang, *The finite element methods*, Tsinghua University Press, Beijing, 2003.

[Wen and Luo 2012] W. B. Wen and S. M. Luo, "Polygonal manifold element for thin plate bending analysis", *Eng. Mech.* **29**:10 (2012), 249–256.

[Xie 2009] P. L. Xie, *Nonconforming finite element methods for the fourth order elliptic problems*, Fudan University, Shanghai, 2009.

[Xing and Liu 2009] Y. F. Xing and B. Liu, "High-accuracy differential quadrature finite element method and its application to free vibrations of thin plate with curvilinear domain", *Int. J. Numer. Methods Eng.* **80**:13 (2009), 1718–1742.

[Xu et al. 2014] D. D. Xu, H. Zheng, and Y. T. Yang, "Linearly independent higher-order numerical manifold method", *Chin. J. Geotech. Eng.* **36**:3 (2014), 482–488.

[Zhang et al. 2010] Z. R. Zhang, X. W. Zhang, and W. G. Lü, "numerical method based on compatible manifold element for thin plate bending", *Chin. J. Mech. Eng.* **23**:1 (2010), 100–109.

[Zhao 1988] J. Q. Zhao, "Discussion on constructing principle and convergence problem of the generalized conforming element", *J. Civil Eng.* **21**:4 (1988), 35–37.

[Zheng et al. 2013] H. Zheng, Z. J. Liu, and X. R. Ge, "Numerical manifold space of Hermitian form and application to Kirchhoff's thin plate problems", *Int. J. Numer. Methods Eng.* **95**:9 (2013), 721–739.

[Zhou and Deng 2008] X. Y. Zhou and A. F. Deng, "Numerical manifold method of analysis for beam and plate based ongeneralized variational principle", *Chin. J. Solid Mech.* **29**:3 (2008), 313–318.

[Zienkiewicz and Taylor 2005] O. C. Zienkiewicz and R. L. Taylor, *The finite element method for solid and structural mechanics*, 6th ed., Butterworth-Heinemann, 2005.

Received 18 Nov 2018. Revised 8 Oct 2019. Accepted 6 Mar 2020.

XIN QU: xqu1987@163.com
School of Civil and Architecture Engineering, Anyang Institute of Technology, Anyang 455000, China

FANGFANG DIAO: diaoff1986@163.com
School of Foreign Languages, Anyang Institute of Technology, Anyang 455000, China

XINGQIAN XU: xuxingqian_123@163.com
College of Water Conservancy, Yunnan Agricultural University, Kunming 650201, China

WEI LI: liw9012@163.com
Institute of Civil Engineering and Architecture, Linyi University, Linyi 276005, China

JOURNAL OF MECHANICS OF MATERIALS AND STRUCTURES
Vol. 15, No. 3, 2020
https://doi.org/10.2140/jomms.2020.15.345

DEFORMATION OF HETEROGENEOUS MICROSTRETCH ELASTIC BARS

DORIN IEŞAN

The material points of microstretch continua undergo a uniform microdilatation and a rigid microrotation. This paper is concerned with the deformation of a bar composed by two different microstretch elastic materials. The intended applications of the solution are to bone implants and various compound cylinders. The bar is reinforced by a longitudinal rod and is subjected to extension, bending, torsion and flexure. First, the problem of bending and extension is investigated. The solution involves the solving of three plane strain problems. Then, we study the problem of torsion and flexure. The results are used to investigate the extension of a right circular cylinder reinforced by a circular rod.

1. Introduction

A microstretch continuum is a material with microstructure in which the microelements can stretch and contract independently of their translations and rotations. The theory of microstretch continua was introduced in [Eringen 1999] as a generalization of the Cosserat theory. When the microdilatation is zero, the microstretch continuum reduces to the Cosserat model. The applications of the theory of microstretch continua are to composite materials, porous solids, bones and various materials with inner structure. The Cosserat elastic solid was used as model for carbon nanotubes and composite materials [Lakes 2001; Chandraseker et al. 2009; Ha et al. 2016] and for bones [Lakes 1982; Fatemi et al. 2002]. Lakes [1982] presented some experimental observations on the mechanical behavior of bones and remarked that "Human bone, a natural fibrous composite, displays size effects in torsion and bending which are consistent with Cosserat elasticity rather than classical elasticity". The cancellous bone is considered as a porous body [Kohles and Roberts 2002] so the linear theory of microstretch elastic solids is adequate to describe the mechanical behavior of bones. Various papers have been devoted to the study of bone implants and anisotropic cylinders [Hanumantharaju and Shivanand 2009; Thielen et al. 2009; Taliercio and Veber 2016]. The bone and the implant form a body which can be modeled as a continuum composed of different materials.

We study the deformation of a heterogeneous bar which is made of two materials, welded together along the surface of separation. The deformation of homogeneous microstretch elastic cylinders has been investigated in [Ieşan and Nappa 1995; Ieşan 2008; 2019a; 2019b]. We assume that the bar is composed of two homogenous and isotropic microstretch elastic materials and is subjected to extension, bending, torsion and flexure.

The paper is structured as follows. First, we present the basic equations of isotropic microstretch elastic solids and formulate the problem of a reinforced rod. Then, we define the plane strain problem associated to a heterogeneous body. In the following section we present the solution of the problem of extension and bending. It is shown that this problem reduces to the study of some two-dimensional

Keywords: microstretch elastic materials, heterogeneous bars, flexure of reinforced cylinders.

problems in which the external data depend only on the constitutive coefficients. Then, we study the problem of torsion and flexure. The flexure of the cylinder produces a torsion of the bar about its axis. Finally, we use the method to investigate the extension of a circular cylinder reinforced by a circular rod.

2. Preliminaries

We present the basic equations of the microstretch elastic solids and the formulation of the problem. We consider a continuum which in undeformed state occupies the regular domain B of Euclidean three-dimensional space and is bounded by the surface ∂B. Throughout this paper a fixed system of rectangular cartesian axes Ox_k, $(k = 1, 2, 3)$, is used. We shall employ standard indicial notations: Greek subscripts take on the values 1 and 2 whereas Latin subscripts (unless otherwise specified) are understood to range over $(1, 2, 3)$, and summation over repeated subscripts is implied. We denote by n_j the components of the outward unit normal of ∂B and introduce the notation $f_{,k} = \partial f/\partial x_k$. We study the deformation of isotropic solids in the linear theory of microstretch elastic continua. Let u_k be the displacement vector, let φ_k be the microrotation vector, and let ψ be the microstretch function. We denote by ε_{ijk} the alternating symbol. The strain measures are defined by

$$e_{ij} = u_{j,i} + \varepsilon_{jik}\,\varphi_k, \quad \kappa_{ij} = \varphi_{j,i}, \quad \gamma_i = \psi_{,i}. \tag{2-1}$$

Let t_{ij} be the stress tensor, m_{ij} be the couple stress tensor, σ_i be the microstretch stress vector, and ζ be the microstress function. The constitutive equations are

$$\begin{aligned} &t_{ij} = \lambda e_{rr}\,\delta_{ij} + (\mu + \kappa)\,e_{ij} + \mu e_{ji} + \lambda_0 \psi \delta_{ij}, \quad m_{ij} = \alpha \kappa_{rr}\,\delta_{ij} + \beta \kappa_{ji} + \gamma \kappa_{ij} + b_0\,\varepsilon_{kji}\gamma_k, \\ &\sigma_i = a_0\,\gamma_i + b_0\,\varepsilon_{irs}\,\kappa_{sr}, \qquad\qquad \zeta = \lambda_0\,e_{rr} + \lambda_1 \psi, \end{aligned} \tag{2-2}$$

where λ, μ, κ, λ_0, λ_1, α, β, γ, b_0 and a_0 are constitutive coefficients. In the linear elasticity the Cosserat model is characterized by the coefficients λ, μ, κ, α, β, γ. The tractions acting at a regular point of ∂B are defined by

$$t_i = t_{ji}\,n_j, \quad m_i = m_{ji}\,n_j, \quad \sigma = \sigma_i n_i. \tag{2-3}$$

In the absence of body loads, the equilibrium equations are

$$t_{ji,j} = 0, \quad m_{ji,j} + \varepsilon_{irs}\,t_{rs} = 0, \quad \sigma_{j,j} - \zeta = 0. \tag{2-4}$$

In what follows we assume that the domain B is a right cylinder of length h with the cross-section Σ and the lateral boundary Π. The rectangular coordinate frame is chosen such that the x_3-axis is parallel to the generator of B. We denote by Σ_1 and Σ_2 the terminal cross-sections and assume that these are located at $x_3 = 0$ and $x_3 = h$, respectively. Let L be the boundary of Σ_1. We assume that the cylinder is free of lateral loading. We have

$$t_{\alpha i}\,n_\alpha = 0, \quad m_{\alpha i} n_\alpha = 0, \quad \sigma_\alpha\,n_\alpha = 0 \quad \text{on } \Pi. \tag{2-5}$$

We assume that the load of the cylinder is distributed over its ends in a way which fulfills the equilibrium conditions of the body. We use Saint-Venant's formulation in which the pointwise assignment of the terminal tractions is replaced by prescribing the corresponding resultant force and resultant moment. Let the loading applied on Σ_1 be equivalent to the resultant force $\boldsymbol{R} = (R_1, R_2, R_3)$ and the resultant

moment $\boldsymbol{M} = (M_1, M_2, M_3)$. The cross-section Σ_2 is subjected to tractions that satisfy the conditions of the equilibrium of the cylinder. The conditions on the end Σ_1 can be expressed as

$$\int_{\Sigma_1} t_{3i}\, da = -R_i, \qquad \int_{\Sigma_1} (x_\alpha t_{33} - \varepsilon_{3\alpha\beta} m_{3\beta})\, da = \varepsilon_{\alpha\beta 3} M_\beta, \qquad \int_{\Sigma_1} (\varepsilon_{3\alpha\beta} x_\alpha t_{3\beta} + m_{33})\, da = -M_3. \tag{2-6}$$

The formulation of Saint-Venant leads to the four basic problems of extension ($R_\alpha = 0,\ M_j = 0$), bending ($R_j = 0,\ M_3 = 0$), torsion ($R_j = 0,\ M_\alpha = 0$) and flexure ($R_3 = 0,\ M_j = 0$).

Let Γ be a closed curve contained in Σ_1, which is the boundary of a regular domain Ω_2 contained in Σ_1. We suppose that Γ and L have no common points and denote by Ω_1 the domain bounded by Γ and L. Let B_ρ be the cylinder:

$$B_\rho = \{(x_1, x_2, x_3) : (x_1, x_2) \in \Omega_\rho, \quad 0 < x_3 < h\}, \quad \rho = 1, 2.$$

We suppose that B_ρ is occupied by an elastic material with the constitutive coefficients $\lambda^{(\rho)}$, $\mu^{(\rho)}$, $\kappa^{(\rho)}$, $\lambda_0^{(\rho)}$, $\lambda_1^{(\rho)}$, $\alpha^{(\rho)}$, $\beta^{(\rho)}$, $\gamma^{(\rho)}$, $b_0^{(\rho)}$ and $a_0^{(\rho)}$. We assume that the elastic potential corresponding to the material that occupies the cylinder B_ρ is a positive definite quadratic form in the independent constitutive variables.

Let S be the surface of separation of the two materials. We assume that the cylinder B is composed of two different materials which are welded together along S (Figure 1) and that there is no separation of material along S in the course of deformation. The functions u_j, φ_j, ψ, t_j, m_j and σ must be continuous in passing from one medium to another, so that we have

$$\begin{gathered} [u_j]_1 = [u_j]_2, \qquad [\varphi_j]_1 = [\varphi_j]_2, \qquad [\psi]_1 = [\psi]_2, \\ [t_{\alpha j}]_1 n_\alpha^0 = [t_{\alpha j}]_2 n_\alpha^0, \quad [m_{\alpha j}]_1 n_\alpha^0 = [m_{\alpha j}]_2 n_\alpha^0, \quad [\sigma_\alpha]_1 n_\alpha^0 = [\sigma_\alpha]_2 n_\alpha^0 \quad \text{on } S, \end{gathered} \tag{2-7}$$

where $(n_1^0, n_2^0, 0)$ are the components of the unit normal to S, and the expressions in brackets are calculated for the domains B_1 and B_2, respectively.

Saint-Venant's problem consists in the determination of the functions u_j, φ_j and ψ which satisfy the equations (2-1), (2-2) and (2-4) on B_1 and B_2, the conditions (2-5) on the lateral surface, the conditions (2-6) on Σ_1 and the conditions (2-7) on S. The constants R_j and M_j, and the constitutive coefficients are prescribed. In what follows we use the method established in [Ieşan 1976a; 1976b; 1976c] to study the deformation of inhomogeneous cylinders. This method has been extended to study generalized models in [Lyons et al. 2002; Ieşan and Scalia 2009; Ieşan 2008; Bîrsan and Altenbach 2011; Bîrsan et al. 2012].

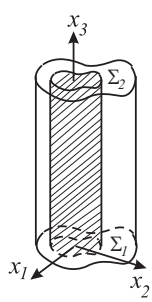

Figure 1. A heterogeneous rod.

3. Plane strain

We introduce the plane strain problem associated to a cylinder composed by two materials. We assume now that the cylinder is subjected to a body force $f_j^{(\rho)}$, a body couple $g_j^{(\rho)}$, and to the microstretch body force $l^{(\rho)}$, on B_ρ, $(\rho = 1, 2)$. Moreover, we suppose that the lateral surface of the cylinder is subjected to surface tractions $\tilde{t}_j$, to surface moments $\tilde{m}_j$ and to microstretch traction $\tilde{\sigma}$. We assume that all external data are independent of the axial coordinate and that $f_3^{(\rho)} = 0$, $g_\alpha^{(\rho)} = 0$, $\tilde{t}_3 = 0$, $\tilde{m}_\alpha = 0$.

We say that the cylinder B is in a state of plane strain, parallel to the x_1Ox_2-plane if the functions u_j, φ_j and ψ have the properties

$$u_\alpha = u_\alpha(x_1, x_2), \quad u_3 = 0, \quad \varphi_\alpha = 0, \quad \varphi_3 = \varphi_3(x_1, x_2), \quad \psi = \psi(x_1, x_2) \quad \text{on } B. \tag{3-1}$$

It follows from (2-1), (2-2) and (3-1) that e_{ij}, κ_{ij}, γ_i, t_{ij}, m_{ij}, σ_i and ζ are all independent of the axial coordinate. The nonzero strain measures are

$$e_{\alpha\beta} = u_{\beta,\alpha} + \varepsilon_{\beta\alpha3}\,\varphi_3, \quad \kappa_{\alpha3} = \varphi_{3,\alpha}, \quad \gamma_\alpha = \psi_{,\alpha}. \tag{3-2}$$

The constitutive equations (2-2) imply that, in the case of plane strain, the nonzero components of the stress tensor, couple stress tensor and microstretch stress vector are $t_{j\beta}$, $m_{\alpha3}$, $m_{3\alpha}$ and σ_α. Further,

$$\begin{gathered} t_{a\beta} = \lambda^{(\rho)} e_{\nu\nu}\,\delta_{\alpha\beta} + (\mu^{(\rho)} + \kappa^{(\rho)})\,e_{\alpha\beta} + \mu^{(\rho)} e_{\beta\alpha} + \lambda_0^{(\rho)}\psi\,\delta_{\alpha\beta}, \\ m_{\alpha3} = \gamma^{(\rho)}\kappa_{\alpha3} + b_0^{(\rho)}\varepsilon_{3\alpha\beta}\,\psi_{,\beta}, \quad \sigma_\alpha = a_0^{(\rho)}\gamma_\alpha + b_0^{(\rho)}\varepsilon_{3\beta\alpha}\,\kappa_{\beta3}, \quad \zeta = \lambda_0^{(\rho)} e_{\nu\nu} + \lambda_1^{(\rho)}\psi. \end{gathered} \tag{3-3}$$

The equations of equilibrium in the case of plane strain can be expressed as

$$t_{\beta\alpha,\beta} + f_\alpha^{(\rho)} = 0, \quad m_{\alpha3,\alpha} + \varepsilon_{3\alpha\beta}\,t_{\alpha\beta} + g_3^{(\rho)} = 0, \quad \sigma_{\alpha,\alpha} - \zeta + l^{(\rho)} = 0 \quad \text{on } \Omega_\rho. \tag{3-4}$$

The conditions (2-7) reduce to

$$\begin{gathered} [u_\alpha]_1 = [u_\alpha]_2, \qquad [\varphi_3]_1 = [\varphi_3]_2, \qquad [\psi]_1 = [\psi]_2, \\ [t_{\beta\alpha}]_1 n_\beta^0 = [t_{\beta\alpha}]_2 n_\beta^0, \quad [m_{\alpha3}]_1 n_\alpha^0 = [m_{\alpha3}]_2 n_\alpha^0, \quad [\sigma_\alpha]_1 n_\alpha^0 = [\sigma_\alpha]_2 n_\alpha^0 \quad \text{on } \Gamma. \end{gathered} \tag{3-5}$$

The conditions on the boundary Π become

$$[t_{\beta\alpha}]_1 n_\beta = \tilde{t}_\alpha, \quad [m_{\alpha3}]_1 n_\alpha = \tilde{m}_3, \quad [\sigma_\alpha]_1 n_\alpha = \tilde{\sigma} \quad \text{on } L. \tag{3-6}$$

The plane strain problem consists in finding the functions u_α, φ_3 and ψ which satisfy the equations (3-2)–(3-4) on Ω_ρ, the conditions (3-5) on Γ and the conditions (3-6) on L. The functions $f_\alpha^{(\rho)}$, $g_3^{(\rho)}$, $l^{(\rho)}$, $\tilde{t}_\alpha$, $\tilde{m}_3$ and $\tilde{\sigma}$ are given C^∞-fields. The necessary and sufficient conditons for the existence of a solution to the plane strain problem are [Fichera 1973]

$$\int_L \tilde{t}_\alpha\,ds + \sum_{\rho=1}^{2}\int_{\Omega_\rho} f_i^{(\rho)}\,da = 0, \quad \int_L (\varepsilon_{3\alpha\beta}\,x_\alpha\,\tilde{t}_\beta + \tilde{m}_3)\,ds + \sum_{\rho=1}^{2}\int_{\Omega_\rho} (\varepsilon_{3\alpha\beta}\,x_\alpha\,f_\beta^{(\rho)} + g_3^{(\rho)})\,da = 0. \tag{3-7}$$

If the conditions (3-5) are replaced by

$$\begin{gathered} [u_\alpha]_1 = [u_\alpha]_2, \qquad [\varphi_3]_1 = [\varphi_3]_2, \qquad [\psi]_1 = [\psi]_2, \\ [t_{\beta\alpha}]_1 n_\beta^0 = [t_{\beta\alpha}]_2 n_\beta^0 + p_\alpha, \quad [m_{\alpha3}]_1 n_\alpha^0 = [m_{\alpha3}]_2 n_\alpha^0 + q, \quad [\sigma_\alpha]_1 n_\alpha^0 = [\sigma_\alpha]_2 n_\alpha^0 + s, \end{gathered} \tag{3-8}$$

where p_α, q and s are prescribed functions, then the necessary and sufficient conditions for the existence of the solution are

$$\begin{gathered}\int_L \tilde{t}_\alpha\, ds + \sum_{\rho=1}^{2} \int_{\Omega_\rho} f_\alpha^{(\rho)}\, ds + \int_\Gamma p_\alpha\, ds = 0,\\ \int_L (\varepsilon_{3\alpha\beta}\, x_\alpha\, \tilde{t}_\beta + \widetilde{m}_3)\, ds + \sum_{\rho=1}^{2} \int_{\Omega_\rho} (\varepsilon_{3\alpha\beta}\, x_\alpha\, f_\beta^{(\rho)} + g_3^{(\rho)})\, da + \int_\Gamma (\varepsilon_{3\alpha\beta}\, x_\alpha\, p_\beta + q)\, ds = 0.\end{gathered} \tag{3-9}$$

If $\widetilde{m}_3 = 0$ and $g_3^{(\rho)} = 0$, then the conditions (3-9) reduce to those used in classical elasticity to study the deformation of heterogeneous cylinders [Muskhelishvili 1953]. By using (3-2) and (3-3) we can express the equilibrium equations (3-4) in terms of functions u_α, φ_3 and ψ. We obtain the equations of equilibrium:

$$\begin{aligned}&(\mu^{(\rho)} + \kappa^{(\rho)})\, \Delta u_\alpha + (\lambda^{(\rho)} + \mu^{(\rho)})\, u_{\nu,\nu\alpha} + \kappa^{(\rho)} \varepsilon_{3\alpha\beta}\, \varphi_{3,\beta} + \lambda_0^{(\rho)} \psi_{,\alpha} + f_\alpha^{(\rho)} = 0,\\ &\gamma^{(\rho)} \Delta\varphi_3 + \kappa^{(\rho)} \varepsilon_{3\alpha\beta}\, u_{\beta,\alpha} - 2\kappa^{(\rho)} \varphi_3 + g_3^{(\rho)} = 0, \quad a_0^{(\rho)} \Delta\psi - \lambda_0^{(\rho)} u_{\nu,\nu} - \lambda_1^{(\rho)} \psi + l^{(\rho)} = 0\end{aligned} \tag{3-10}$$

on Ω_ρ, $(\rho = 1, 2)$, where Δ is the Laplacian.

4. Extension and bending of heterogeneous cylinders

We assume that the loading applied on the end located at $x_3 = 0$ is statically equivalent to the force $(0, 0, R_3)$ and the moment $(M_1, M_2, 0)$. The conditions on Σ_1 become

$$\int_{\Sigma_1} t_{3\alpha}\, da = 0, \tag{4-1}$$

$$\int_{\Sigma_1} t_{33}\, da = -R_3, \tag{4-2}$$

$$\int_{\Sigma_1} (x_\alpha\, t_{33} - \varepsilon_{3\alpha\beta}\, m_{3\beta})\, da = \varepsilon_{\alpha\beta 3}\, M_\beta, \tag{4-3}$$

$$\int_{\Sigma_1} (\varepsilon_{3\alpha\beta}\, x_\alpha\, t_{3\beta} + m_{33})\, da = 0. \tag{4-4}$$

The problem of extension and bending consists in finding the functions u_j, φ_j and ψ which satisfy the equations (2-1), (2-2) and (2-4) on B_ρ, the conditions (2-5) on Π, the conditions (2-7) on S, and the conditions (4-1)–(4-4) for $x_3 = 0$. Following [Ieşan 2019b] we try to solve this problem assuming that

$$\begin{gathered}u_\alpha = -\frac{1}{2} c_\alpha x_3^2 + \sum_{k=1}^{3} c_k\, u_\alpha^{(k)}, \quad u_3 = (c_1 x_1 + c_2 x_2 + c_3)\, x_3,\\ \varphi_\alpha = \varepsilon_{3\alpha\beta}\, c_\beta\, x_3, \quad \varphi_3 = \sum_{k=1}^{3} c_k\, \varphi_3^{(k)}, \quad \psi = \sum_{k=1}^{3} c_k \psi^{(k)},\end{gathered} \tag{4-5}$$

where $u_\alpha^{(k)}$, $\varphi_3^{(k)}$ and $\psi^{(k)}$ are unknown functions which are independent of x_3, and c_k are unknown constants. In what follows we shall prove that the functions $u_\alpha^{(k)}$, $\varphi_3^{(k)}$ and $\psi^{(k)}$ satisfy a plane strain problem $P^{(k)}$, $(k = 1, 2, 3)$, associated to the composed cylinder B.

Let us denote by $e_{\alpha\beta}^{(k)}$, $\kappa_{\alpha 3}^{(k)}$ and $\gamma^{(k)}$ the strain measures (3-2) associated to the functions $u_\alpha^{(k)}$, $\varphi_3^{(k)}$ and $\psi^{(k)}$, $(k = 1, 2, 3)$. Thus, we have

$$e_{\alpha\beta}^{(k)} = u_{\beta,\alpha}^{(k)} + \varepsilon_{\beta\alpha 3}\,\varphi_3^{(k)}, \quad \kappa_{\alpha 3}^{(k)} = \varphi_{3,\alpha}^{(k)}, \quad \gamma_\alpha^{(k)} = \psi_{,\alpha}^{(k)}. \tag{4-6}$$

We introduce the notations

$$\begin{gathered} t_{a\beta}^{(k)} = \lambda^{(\rho)} e_{\nu\nu}^{(k)} \delta_{\alpha\beta} + (\mu^{(\rho)} + \kappa^{(\rho)})\, e_{\alpha\beta}^{(k)} + \mu^{(\rho)} e_{\beta\alpha}^{(k)} + \lambda_0^{(\rho)} \psi\, \delta_{\alpha\beta}, \\ m_{\alpha 3}^{(k)} = \gamma^{(\rho)} \kappa_{\alpha 3}^{(k)} + b_0^{(\rho)} \varepsilon_{3\alpha\beta}\, \gamma_\beta^{(k)}, \quad \sigma_\alpha^{(k)} = a_0^{(\rho)} \gamma_\alpha^{(k)} + b_0^{(\rho)} \varepsilon_{3\beta\alpha}\, \kappa_{\beta 3}, \quad \zeta^{(k)} = \lambda_0^{(\rho)} e_{\nu\nu}^{(k)} + \lambda_1^{(\rho)} \psi^{(k)}, \\ t_{33}^{(k)} = \lambda^{(\rho)} e_{\nu\nu}^{(k)} + \lambda_0^{(\rho)} \psi^{(k)}, \quad m_{3\alpha}^{(k)} = \beta^{(\rho)} \kappa_{\alpha 3}^{(k)} + b_0^{(\rho)} \varepsilon_{3\alpha\nu}\, \gamma_\nu^{(k)} \quad \text{on } \Omega_\rho. \end{gathered} \tag{4-7}$$

In view of (2-1), (4-5)–(4-7), the constitutive equations (2-2) imply

$$\begin{gathered} t_{\alpha\beta} = \lambda^{(k)}(c_1 x_1 + c_2 x_2 + c_3)\, \delta_{\alpha\beta} + \sum_{k=1}^{3} c_k\, t_{\alpha\beta}^{(k)}, \quad t_{\alpha 3} = t_{3\alpha} = 0, \\ t_{33} = (\lambda^{(\rho)} + 2\mu^{(\rho)} + \kappa^{(\rho)})(c_1 x_1 + c_2 x_2 + c_3) + \sum_{k=1}^{3} c_k\, t_{33}^{(k)}, \\ m_{\alpha 3} = m_{33} = 0, \quad m_{\alpha 3} = \beta^{(\rho)} \varepsilon_{3\alpha\beta}\, c_\beta + \sum_{k=1}^{3} c_k\, m_{\alpha 3}^{(k)}, \quad m_{3\alpha} = \gamma^{(\rho)} \varepsilon_{3\alpha\nu}\, c_\nu + \sum_{k=1}^{3} c_k\, m_{3\alpha}^{(k)}, \\ \sigma_\alpha = -b_0^{(\rho)} c_\alpha + \sum_{k=1}^{3} c_k\, \sigma_\alpha^{(k)}, \quad \sigma_3 = 0, \quad \zeta = \lambda_0^{(\rho)}(c_1 x_1 + c_2 x_2 + c_3) + \sum_{k=1}^{3} c_k\, \zeta^{(k)} \quad \text{on } B_\rho. \end{gathered} \tag{4-8}$$

Let us substitute (4-8) into the equations of equilibrium (2-4). We require that the resulting equations be satisfied for any constant c_k. Thus, we find that the functions $t_{\alpha\beta}^{(k)}$, $m_{\alpha 3}^{(k)}$, $\sigma_\alpha^{(k)}$ and $\zeta^{(k)}$, $(k = 1, 2, 3)$, satisfy

$$\begin{gathered} t_{\beta\alpha,\beta}^{(\nu)} + \lambda^{(\rho)} \delta_{\alpha\nu} = 0, \quad t_{\beta\alpha,\beta}^{(3)} = 0, \quad m_{\beta\alpha,\beta}^{(k)} + \varepsilon_{3\rho\nu}\, t_{\rho\nu}^{(k)} = 0, \\ \sigma_{\alpha,\alpha}^{(\nu)} - \zeta^{(\nu)} - \lambda_0^{(\rho)} x_\nu = 0, \quad \sigma_{\alpha,\alpha}^{(3)} - \zeta^{(3)} - \lambda_0^{(\rho)} = 0, \quad \nu = 1, 2 \quad \text{on } \Omega_\rho. \end{gathered} \tag{4-9}$$

The equilibrium equations are satisfied if (4-9) holds. It follows from (2-5) and (4-8) that the conditions on the lateral surface are satisfied for any constants c_1, c_2 and c_3 if we have

$$[t_{\beta\alpha}^{(k)}]_1\, n_\beta = \tilde{t}_\alpha^{(k)}, \quad [m_{\alpha 3}^{(k)}]_1\, n_\alpha = \widetilde{m}_3^{(k)}, \quad [\sigma_\alpha^{(k)}]_1\, n_\alpha = \tilde{\sigma}^{(k)} \quad \text{on } L, \tag{4-10}$$

where we have used the notations

$$\tilde{t}_\beta^{(\alpha)} = -\lambda^{(1)} x_\alpha\, n_\beta, \quad \tilde{t}_\beta^{(3)} = -\lambda^{(1)} n_\beta, \quad \widetilde{m}_3^{(\alpha)} = \beta^{(1)} \varepsilon_{3\alpha\nu}\, n_\nu, \quad \widetilde{m}_3^{(3)} = 0, \quad \tilde{\sigma}^{(\alpha)} = b_0^{(1)} n_\alpha, \quad \tilde{\sigma}^{(3)} = 0. \tag{4-11}$$

Similarly, we conclude the conditions (2-7) on the surface S are satisfied if the unknown functions satisfy

$$\begin{gathered}[u_\alpha^{(k)}]_1=[u_\alpha^{(k)}]_2,\quad [\varphi_3^{(k)}]_1=[\varphi_3^{(k)}]_2,\quad [\psi^{(k)}]_1=[\psi^{(k)}]_2,\quad [t_{\beta\alpha}^{(k)}]_1\,n_\beta^0=[t_{\beta\alpha}^{(k)}]_2\,n_p+p_\alpha^{(k)},\\ [m_{\alpha 3}^{(k)}]\,n_\alpha^0=[m_{\alpha 3}^{(k)}]_2\,n_\alpha^0+q^{(k)},\quad [\sigma_\alpha^{(k)}]_1\,n_\alpha^0=[\sigma_\alpha^{(k)}]_2\,n_\alpha^0+s^{(k)}\quad \text{on } \Gamma.\end{gathered}\tag{4-12}$$

Here, $p_\alpha^{(k)}$, $q^{(k)}$ and $s^{(k)}$ are defined by

$$\begin{aligned}&p_\alpha^{(\beta)}=(\lambda^{(2)}-\lambda^{(1)})\,x_\beta\,n_\alpha^0, && p_\alpha^{(3)}=(\lambda^{(2)}-\lambda^{(1)})\,n_\alpha^0,\\ &q^{(\eta)}=(\beta^{(1)}-\beta^{(2)})\,\varepsilon_{3\eta\alpha}\,n_\alpha^0,\quad q^{(3)}=0, && s^{(\beta)}=(b_0^{(1)}-b_0^{(2)})\,n_\beta^0,\quad s^{(3)}=0.\end{aligned}\tag{4-13}$$

Thus, the functions $u_\alpha^{(k)}$, $\varphi_3^{(k)}$ and $\psi^{(k)}$ are the solutions of the plane strain problems $P^{(k)}$ which are characterized by the geometrical equations (4-6), the constitutive equations (4-7) and the equilibrium equations (4-9) on Ω_ρ, and the boundary conditions (4-10) and (4-11). The functions $t_{33}^{(k)}$ and $m_{3\alpha}^{(k)}$ can be found after the determination of $u_\alpha^{(k)}$, $\varphi_3^{(k)}$ and $\psi^{(k)}$ from the problems $P^{(k)}$, $(k=1,2,3)$. It is easy to see that the necessary and sufficient conditions (3-9) for the existence of the solution are satisfied for each problem $P^{(k)}$, $(k=1,2,3)$. We note that the external loading in the problems $P^{(k)}$ depend only the constitutive coefficients and the cross-section of the cylinder.

Let us prove that the constants c_1, c_2 and c_3 can be determined from the conditions on the ends. First, we note that the conditions (4-1) and (4-4) are satisfied on the basis of equations (4-8).

The conditions (4-2) and (4-3) reduce to the following system for the constants c_1, c_2 and c_3:

$$A_{\alpha j}\,c_j=\varepsilon_{3\alpha\beta}\,M_\beta,\quad A_{3j}\,c_j=-R_3.\tag{4-14}$$

Here, we have used the notations

$$\begin{aligned}A_{\alpha\beta}&=\sum_{\rho=1}^{2}\int_{\Omega_\rho}\{(\lambda^{(\rho)}+2\mu^{(\rho)}+\kappa^{(\rho)})\,x_\alpha x_\beta+x_\alpha\,t_{33}^{(\beta)}+\varepsilon_{3\nu\alpha}\,m_{3\nu}^{(\beta)}+\gamma^{(\rho)}\delta_{\alpha\beta}\}\,da,\\ A_{\alpha 3}&=\sum_{\rho=1}^{2}\int_{\Omega_\rho}\{(\lambda^{(\rho)}+2\mu^{(\rho)}+\kappa^{(\rho)})\,x_\alpha+x_\alpha\,t_{33}^{(3)}+\varepsilon_{3\nu\alpha}\,m_{3\nu}^{(3)}\}\,da,\\ A_{3\alpha}&=\sum_{\rho=1}^{2}\int_{\Omega_\rho}[(\lambda^{(\rho)}+2\mu^{(\rho)}+\kappa^{(\rho)})\,x_\alpha+t_{33}^{(\alpha)}]\,da,\\ A_{33}&=\sum_{\rho=1}^{2}\int_{\Omega_\rho}(\lambda^{(\rho)}+2\mu^{(\rho)}+\kappa^{(\rho)}+t_{33}^{(3)})\,da.\end{aligned}\tag{4-15}$$

The constants A_{ij} can be found if we know the functions $u_\alpha^{(k)}$, $\varphi_3^{(k)}$ and $\psi^{(k)}$, $(k=1,2,3)$. By using the methods of the classical elasticity [Muskhelishvili 1953; Ieşan 2008] we can prove that the positive definiteness of the elastic potential and the reciprocal theorem imply

$$\det(A_{ij})>0,\quad A_{ij}=A_{ji}.\tag{4-16}$$

The constants c_j are determined by the system (4-14). Thus, the solution of the problem is given by (4-5).

5. Torsion and flexure

The problem of torsion and flexure consists in finding the displacement vector, the microrotation vector and the microstretch function, which satisfy the equations (2-1), (2-2) and (2-4), the conditions (2-5) on the lateral surface, the conditions (2-7) on the surface separation, and the conditions (2-6) on Σ_1, when $R_3 = 0$ and $M_\alpha = 0$. We seek the solution of the problem in the form

$$\begin{gathered} u_\alpha = -\frac{1}{6}a_\alpha x_3^3 + x_3\sum_{k=1}^{3} a_k\, u_\alpha^{(k)} + d x_3\, \varepsilon_{\beta\alpha 3}\, x_\beta, \quad u_3 = \frac{1}{2}(a_1 x_1 + a_2 x_2 + a_3)\, x_3^2 + F_3, \\ \varphi_\alpha = \frac{1}{2}x_3^2\, \varepsilon_{3\alpha\beta}\, a_\beta + F_\beta, \quad \varphi_3 = d x_3 + x_3\sum_{k=1}^{3} a_k\, \varphi_3^{(k)}, \quad \psi = x_3\sum_{k=1}^{3} a_k\, \psi^{(k)}, \end{gathered} \tag{5-1}$$

where a_k and d are unknown constants, $u_\alpha^{(k)}$, $\varphi_3^{(k)}$ and $\psi^{(k)}$ are the solution to the problem $P^{(k)}$, and F_j are unknown functions of x_1 and x_2. We denote by $\omega = (F_1, F_2, F_3)$ the ordered triplet of functions F_1, F_2 and F_3, and introduce the notations

$$\begin{aligned} &T_{\alpha 3}^{(\rho)}\omega = (\mu^{(\rho)} + \kappa^{(\rho)})\, F_{3,\alpha} + \kappa^{(\rho)}\varepsilon_{\alpha\beta 3}\, F_\beta, && T_{3\alpha}^{(\rho)}\omega = \mu^{(\rho)} F_{3,\alpha} + \kappa^{(\rho)}\varepsilon_{3\beta\alpha}\, F_\beta, \\ &M_{\alpha\beta}^{(\rho)}\omega = \alpha^{(\rho)} F_{\eta,\eta}\, \delta_{\alpha\beta} + \beta^{(\rho)} F_{\alpha,\beta} + \gamma^{(\rho)} F_{\beta,\alpha}, && N_\alpha^{(\rho)}\omega = n_\beta\, M_{\beta\alpha}^{(\rho)}\omega, \quad N_3^{(\rho)}\omega = n_\alpha\, T_{\alpha 3}^{(\rho)}\omega. \end{aligned} \tag{5-2}$$

and

$$\begin{aligned} &L_\nu^{(\rho)}\omega = \alpha^{(\rho)} F_{\eta,\eta\nu} + \beta^{(\rho)} F_{\lambda,\nu\lambda} + \gamma^{(\rho)} F_{\nu,\lambda\lambda} + \varepsilon_{\nu\eta 3}\, \kappa^{(\rho)} F_{3,\eta} - 2\kappa^{(\rho)} F_\nu, \\ &L_3^{(\rho)}\omega = (\mu^{(\rho)} + \kappa^{(\rho)})\, F_{3,\alpha\alpha} + \varepsilon_{\alpha\beta 3}\, \kappa^{(\rho)} F_{\beta,\alpha} \quad \text{on } \Omega_\rho. \end{aligned} \tag{5-3}$$

From (2-1), (5-1) and the constitutive equations we obtain

$$\begin{aligned} t_{\alpha\beta} &= \lambda^{(\rho)}(a_1 x_1 + a_2 x_2 + a_3)\, x_3\, \delta_{\alpha\beta} + x_3\sum_{k=1}^{3} a_k\, t_{\alpha\beta}^{(k)}, \\ t_{33} &= (\lambda^{(\rho)} + 2\mu^{(\rho)} + \kappa^{(\rho)})(a_1 x_1 + a_2 x_2 + a_3)\, x_3 + x_3\sum_{k=1}^{3} a_k(\lambda^{(\rho)} e_{\nu\nu}^{(\rho)} + \lambda_0^{(\rho)}\psi^{(k)}), \\ t_{\alpha 3} &= T_{\alpha 3}^{(\rho)}\omega + d\mu^{(\rho)}\varepsilon_{3\beta\alpha}\, x_\beta + \mu^{(\rho)}\sum_{k=1}^{3} a_k\, u_\alpha^{(k)}, \\ t_{3\alpha} &= T_{3\alpha}^{(\rho)}\omega + d\varepsilon_{3\beta\alpha}(\mu^{(\rho)} + \kappa^{(\rho)})\, x_\beta + (\mu^{(\rho)} + \kappa^{(\rho)})\sum_{k=1}^{3} a_k\, u_\alpha^{(k)}, \\ m_{\nu\eta} &= M_{\nu\eta}^{(\rho)}\omega + \alpha^{(\rho)} d\delta_{\nu\eta} + \sum_{k=1}^{3} a_k(\alpha^{(\rho)}\delta_{\nu\eta}\, \varphi_3^{(k)} + \varepsilon_{3\eta\nu}\, b_0^{(\rho)}\, \psi^{(k)}), \\ m_{33} &= (\alpha^{(\rho)} + \beta^{(\rho)} + \gamma^{(\rho)})\left(d + \sum_{k=1}^{3} a_k \varphi_3^{(k)}\right) + \alpha^{(\rho)} F_{\eta,\eta}, \\ m_{\alpha 3} &= \left(\beta^{(\rho)}\varepsilon_{\alpha\nu 3}\, a_\nu + \sum_{k=1}^{3} a_k\, m_{\alpha 3}^{(k)}\right) x_3, \quad m_{3\alpha} = \left(\gamma^{(\rho)}\varepsilon_{\alpha\beta 3}\, a_\beta + \sum_{k=1}^{3} a_k\, m_{3\alpha}^{(k)}\right) x_3, \end{aligned} \tag{5-4a}$$

$$\sigma_\alpha = \left(\sum_{k=1}^{3} a_k \sigma_\alpha^{(\rho)} - b_0^{(\rho)} a_\alpha\right) x_3, \quad \sigma_3 = b_0^{(\rho)} \varepsilon_{3\alpha\beta} F_{\alpha,\beta} + a_0^{(\rho)} \sum_{k=1}^{3} a_k \psi^{(k)},$$
$$\zeta = \left(\lambda_0^{(\rho)}(a_1 x_1 + a_2 x_2 + a_3) + \sum_{k=1}^{3} a_k \zeta^{(k)}\right) x_3 \quad \text{on } B_\rho. \tag{5-4b}$$

By using (4-9), (5-3), (5-4a) and (5-4b) we see that the equilibrium equations (2-4) reduce to

$$L_j^{(\rho)} \omega = S_j^{(\rho)} \quad \text{on } \Omega_\rho, \tag{5-5}$$

where

$$S_\nu^{(\rho)} = d\kappa^{(\rho)} x_\nu + \gamma^{(\rho)} \varepsilon_{3\beta\nu} a_\beta - \sum_{k=1}^{3} a_k [m_{3\nu}^{(k)} + \alpha^{(\rho)} \varphi_{3,\nu}^{(k)} - \varepsilon_{\nu\beta 3} \kappa^{(\rho)} u_\beta^{(k)}],$$
$$S_3^{(\rho)} = -(\lambda^{(\rho)} + 2\mu^{(\rho)} + \kappa^{(\rho)})(a_1 x_1 + a_2 x_2 + a_3) - \sum_{k=1}^{3} a_k [(\lambda^{(\rho)} + \mu^{(\rho)}) e_{\alpha\alpha}^{(k)} + \lambda_0^{(\rho)} \psi^{(k)}]. \tag{5-6}$$

In view of (4-10), (4-11), (5-2), (5-4a) and (5-4b), the boundary conditions (2-5) can be written as

$$N_j^{(1)} \omega = h_j \quad \text{on } L, \tag{5-7}$$

where

$$h_\alpha = -\alpha^{(1)} d n_\alpha - n_\nu \sum_{k=1}^{3} a_k (\alpha^{(1)} \delta_{\nu\alpha} \varphi_3^{(k)} + \varepsilon_{3\alpha\nu} b_0^{(1)} \psi^{(k)}),$$
$$h_3 = d\mu^{(1)} \varepsilon_{3\alpha\beta} x_\beta n_\alpha - n_\alpha \mu^{(1)} \sum_{k=1}^{3} a_k u_\alpha^{(k)}. \tag{5-8}$$

The conditions on the surface of separation S reduce to

$$[F_j]_1 = [F_j]_2, \quad (N_j^{(1)} \omega)(n^0) = (N_j^{(2)} \omega)(n^0) + \varepsilon_j \ \text{ on } \Gamma. \tag{5-9}$$

Here, $(N_j^{(\rho)} \omega)(n^0)$ denotes the operator $N_j^{(\rho)} \omega$ for $n_\alpha = n_\alpha^0$ and ε_j are defined by

$$\varepsilon_\nu = (\alpha^{(2)} - \alpha^{(1)}) n_\nu^0, \quad \varepsilon_3 = (\mu^{(1)} - \mu^{(2)}) \left(d\varepsilon_{3\alpha\beta} x_\beta - \sum_{k=1}^{3} a_k u_\alpha^{(k)}\right) n_\alpha^0. \tag{5-10}$$

It is known [Fichera 1973] that the necessary and sufficient condition for the existence of a solution to the problem (5-5), (5-7) and (5-9) is

$$\int_L h_3 \, ds + \int_\Gamma \varepsilon_3 \, ds = \sum_{\rho=1}^{2} \int_{\Omega_\rho} S_3^{(\rho)} \, da. \tag{5-11}$$

In view of (5-6), (5-8) and (5-10), the condition (5-11) reduces to

$$A_{3j} a_j = 0, \tag{5-12}$$

where A_{3j} are defined in (4-15). By using the equations of equilibrium (2-4) we get

$$t_{3\alpha} = t_{\alpha 3} + \varepsilon_{3\beta\alpha}\, m_{j\beta,j} = t_{\alpha 3} + x_\alpha\, t_{k3,k} + \varepsilon_{3\beta\alpha}\, m_{j\beta,j} = (x_\alpha\, t_{\nu 3} + \varepsilon_{3\beta\alpha}\, m_{\nu\beta})_{,\nu} + x_\alpha\, t_{33,3} + \varepsilon_{3\beta\alpha}\, m_{3\beta,3}.$$

Thus, in view of (2-5) and (2-7), we obtain

$$\int_{\Sigma_1} t_{3\alpha}\, da = \int_{\Sigma_1} (x_\alpha\, t_{33,3} + \varepsilon_{3\beta\alpha}\, m_{3\beta,3})\, da. \tag{5-13}$$

With the help of (5-4a), (5-13) and (4-15), the first two conditions from (2-6) become

$$A_{\alpha j}\, a_j = -R_\alpha. \tag{5-14}$$

On the basis of (4-16), the equations (5-12) and (5-14) determine the constants a_k. Let us determine now the constant d. We introduce the notation $V = (G_1, G_2, G_3)$, where G_j satisfy the following boundary value problem

$$\begin{gathered} L_\alpha^{(\rho)} V = \kappa^{(\rho)} x_\alpha, \quad L_3^{(\rho)} V = 0 \quad \text{on } \Omega_\rho, \qquad [V_j]_1 = [V_j]_2, \quad (N_\alpha^{(1)} V)(n^0) = (N_\alpha^{(2)} V)(n^0), \\ (N_3^{(1)} V)(n^0) = (N_3^{(2)} V)(n^0) + (\mu^{(1)} - \mu^{(2)})\, \varepsilon_{3\alpha\beta}\, x_\beta\, n_\alpha^0, \quad \text{on } \Gamma, \\ N_\nu^{(1)} V = -\alpha^{(1)} n_\nu, \quad N_3^{(1)} V = \mu^{(1)} \varepsilon_{3\alpha\beta}\, x_\beta\, n_\alpha \quad \text{on } L. \end{gathered} \tag{5-15}$$

If we define the functions F_j^0 by

$$F_j^0 = F_j - dG_j, \tag{5-16}$$

and denote $\omega^0 = (F_1^0, F_2^0, F_3^0)$, then ω^0 satisfies

$$L_j^{(\rho)} \omega^0 = \gamma^{(\rho)}\, \varepsilon_{3\beta\nu}\, a_\beta - \sum_{k=1}^{3} a_k [m_{3\nu}^{(k)} + \alpha^{(\rho)} \varphi_{3,\nu}^{(k)} - \varepsilon_{\nu\beta 3}\, \kappa^{(\rho)} u_\beta^{(k)}], \quad L_3^{(\rho)} \omega^0 = S_3^{(\rho)} \quad \text{on } \Omega_\rho, \tag{5-17}$$

and the conditions

$$\begin{gathered} [F_j^0]_1 = [F_j^0]_2, \quad (N_\nu^{(1)} \omega^0)(n^0) = (N_\nu^{(2)} \omega^0)(n^0) + \varepsilon_\nu, \\ (N_3^{(1)} \omega^0)(n^0) = (N_3^{(2)} \omega^0)(n^0) - (\mu^{(1)} - \mu^{(2)})\, n_\alpha^0 \sum_{k=1}^{3} a_k\, u_\alpha^{(k)} \quad \text{on } \Gamma, \\ N_\alpha^{(1)} \omega^0 = -n_\nu \sum_{k=1}^{3} a_k (\alpha^{(1)} \delta_{\nu\alpha}\, \varphi_3^{(k)} + \varepsilon_{3\alpha\nu}\, b_0^{(1)} \psi^{(k)}), \quad N_3^{(1)} \omega^0 = -\mu^{(1)} n_\alpha \sum_{k=1}^{3} a_k\, u_\alpha^{(k)} \quad \text{on } L. \end{gathered} \tag{5-18}$$

Clearly, the conditions for the existence of the functions G_j and F_j^0 are satisfied. The functions $t_{3\alpha}$ and m_{33} can be expressed as

$$\begin{gathered} t_{3\alpha} = T_{3\alpha}^{(\rho)} \omega^0 + d\,[T_{3\alpha}^{(\rho)} V + \varepsilon_{3\beta\alpha} (\mu^{(\rho)} + \kappa^{(\rho)})\, x_\beta] + (\mu^{(\rho)} + \kappa^{(\rho)}) \sum_{k=1}^{3} a_k\, u_\alpha^{(k)}, \\ m_{33} = (\alpha^{(\rho)} + \beta^{(\rho)} + \gamma^{(\rho)}) \sum_{k=1}^{3} a_k \varphi_3^{(k)} + \alpha^{(\rho)} F_{\eta,\eta}^0 + d(\alpha^{(\rho)} + \beta^{(\rho)} + \gamma^{(\rho)} + \alpha^{(\rho)} G_{\eta,\eta}). \end{gathered} \tag{5-19}$$

In view of (5-19), the last condition from (2-6) determines the constant d,

$$d = -D^{-1}(M_3 + M_3^*), \tag{5-20}$$

where

$$\begin{aligned} D &= \sum_{\rho=1}^{2} \int_{\Omega_\rho} [\varepsilon_{3\alpha\beta}\, x_\alpha T_{3\beta}^{(\rho)} V + (\mu^{(\rho)} + \kappa^{(\rho)}) x_\nu x_\nu + a^{(\rho)} + \beta^{(\rho)} + \gamma^{(\rho)} + \alpha^{(\rho)} G_{\nu,\nu}]\, da, \\ M_3^* &= \sum_{\rho=1}^{2} \int_{\Omega_\rho} \{\varepsilon_{3\alpha\beta}\, x_\alpha\, T_{3\beta}^{(\rho)} + \alpha^{(\rho)} F_{\nu,\nu}^0 + \sum_{k=1}^{3} a_k [(\alpha^{(\rho)} + \beta^{(\rho)} + \gamma^{(\rho)})\, v_3^{(k)}] \\ &\qquad + \varepsilon_{3\alpha\beta}\, x_\alpha (\mu^{(\rho)} + \kappa^{(\rho)})\, u_\beta^{(k)}\}\, da. \end{aligned} \tag{5-21}$$

As in classical elasticity we can show that the torsional rigidity D is different from zero. The other conditions from (2-6) are satisfied on the basis of relations (5-4a). Thus, the solution of the problem is given by (5-1).

In the case of flexure we have $M_3 = 0$, but the constant d could be different from zero. In general, the flexure of the bar is accompanied by torsion. The torsion problem is characterized by $R_j = 0$ and $M_\alpha = 0$. In this case, from (5-12) and (5-14) we find that the constants a_k are equal to zero. It follows that the torsion does not produce a microdilatation. The solution of the flexure problem shows that the microrotation vector and the microstretch function are, in general, different from zero.

6. Extension of a cylinder reinforced by a longitudinal rod

This section is concerned with the problem of extension of a circular cylinder composed by two different microstretch elastic materials. In this case in the conditions (2-6) we have $R_\alpha = 0$ and $M_j = 0$. We assume that the domains Ω_1 and Ω_2 are defined by $\Omega_1 = \{(x_1, x_2, x_3) : r_2^2 < x_1^2 + x_2^2 < r_1^2, x_3 = 0\}$ and $\Omega_2 = \{(x_1, x_2, x_3) : 0 \le x_1^2 + x_2^2 < r_2^2, x_3 = 0\}$, where r_1 and r_2 are the radiuses of the concentric circles L and Γ, respectively. To investigate this problem we use the solution (4-5). First, we have to study the plane strain problems $P^{(k)}$, and then to calculate the constants c_j. We seek the solution of the problem $P^{(3)}$ in the form

$$u_\alpha^{(3)} = U_{,\alpha}, \quad \varphi^{(3)} = 0, \quad \psi^{(3)} = \Phi, \tag{6-1}$$

where U and Φ are unknown functions which depend only on the variable $r = (x_1^2 + x_2^2)^{1/2}$. Clearly,

$$u_{\alpha,\alpha}^{(3)} = \Delta U = \tfrac{1}{r}(rU')', \quad e_{\alpha\beta}^{(3)} = U_{,\alpha\beta} = \delta_{\alpha\beta} r^{-1} U' - x_\alpha x_\beta r^{-3} U' + x_\alpha x_\beta r^{-2} U'', \tag{6-2}$$

where $U' = dU/dr$. From (4-7) and (6-1) we find that

$$\begin{aligned} t_{\alpha\beta}^{(3)} &= \lambda^{(\rho)} \delta_{\alpha\beta}\, \Delta U + (2\mu^{(\rho)} + \kappa^{(\rho)})\, U_{,\alpha\beta} + \lambda_0^{(\rho)} \Phi\, \delta_{\alpha\beta}, \\ m_{\alpha 3}^{(3)} &= 0, \quad \sigma_\alpha^{(3)} = a_0^{(\rho)} \Phi_{,\alpha}, \quad \zeta^{(3)} = \lambda_0^{(\rho)} \Delta U + \lambda_1^{(\rho)} \Phi \quad \text{on } \Omega_\rho. \end{aligned} \tag{6-3}$$

In view of (3-10), the equilibrium equations (4-9) reduce to

$$\Delta U + e_{(\rho)} \Phi = A_1^{(\rho)}, \quad \Delta \Phi - \tau_{(\rho)}^2 \Phi = \frac{\lambda_0^{(\rho)}}{a_0^{(\rho)}} (1 + A_1^{(\rho)}) \quad \text{on } \Omega_\rho, \tag{6-4}$$

where $A_1^{(1)}$ and $A_1^{(2)}$ are arbitrary constants and

$$e_{(\rho)} = \lambda_0^{(\rho)}/(\lambda^{(\rho)} + 2\mu^{(\rho)} + \kappa^{(\rho)}), \quad \tau_{(\rho)}^2 = \frac{\lambda_1^{(\rho)}}{a_0^{(\rho)}} - \frac{\lambda_0^{(\rho)}}{a_0^{(\rho)}} e_{(\rho)}. \tag{6-5}$$

The positive definiteness of elastic potential imply that $\tau_{(\rho)}^2 > 0$. From the equations (6-4) we find

$$\begin{aligned} U' &= -\eta_{(\rho)}\Phi_0' + \chi_{(\rho)} r + \xi_{(\rho)} A_1^{(\rho)} r + A_2^{(\rho)} r^{-1}, \\ \Phi &= \Phi_0 - 2d_{(\rho)}(1 + A_1^{(\rho)}), \\ \Phi_0 &= C_1^{(\rho)} I_0(\tau_{(\rho)} r) + C_2^{(\rho)} K_0(\tau_{(\rho)} r) \quad \text{on } \Omega_\rho, \end{aligned} \tag{6-6}$$

where $A_2^{(\rho)}$, $C_1^{(\rho)}$ and $C_2^{(\rho)}$ are arbitrary constants, I_n and K_n are modified Bessel functions of order n, and we have used the notations

$$\eta_{(\rho)} = e_{(\rho)}/\tau_{(\rho)}^2, \quad \chi_{(\rho)} = e_{(\rho)} d_{(\rho)}, \quad d_{(\rho)} = \lambda_0^{(\rho)}(2\tau_{(\rho)}^2 a_0^{(\rho)})^{-1}, \quad \xi_{(\rho)} = \lambda_1^{(\rho)}(d_{(\rho)}/\lambda_0^{(\rho)}). \tag{6-7}$$

Since U' and Φ must be bounded for $r = 0$, we conclude that

$$A_2^{(2)} = 0, \quad C_2^{(2)} = 0. \tag{6-8}$$

With the help of (6-1) and (6-6) we obtain

$$\begin{aligned} u_\alpha^{(3)} &= x_\alpha(-\eta_{(\rho)}\Phi_0' r^{-1} + \chi_{(\rho)} + \xi_{(\rho)} A_1^{(\rho)} + A_2^{(\rho)} r^{-2}) \quad \text{on } \Omega_\rho, \\ t_{\alpha\beta}^{(3)} n_\alpha &= n_\beta\{(2\mu^{(1)} + \kappa^{(1)})\eta_{(\rho)}\Phi_0' r^{-1} - (2\mu^{(1)} + \kappa^{(1)})\chi_{(\rho)} + k_{(\rho)} A_1^{(1)} - (2\mu^{(1)} + \kappa^{(1)}) r^{-2} A_2^{(1)}\}, \\ \sigma_\alpha^{(3)} n_\alpha &= a_0^{(1)}\Phi_0' \quad \text{on } L, \end{aligned} \tag{6-9}$$

where

$$k_{(\rho)} = d_{(\rho)}[\lambda_1^{(\rho)}(2\lambda^{(\rho)} + 2\mu^{(\rho)} + \kappa^{(\rho)}) - 2(\lambda_0^{(\rho)})^2]/\lambda_0^{(\rho)}. \tag{6-10}$$

If we impose the conditions (4-10) and (4-12) corresponding to the problem $P^{(3)}$, then we obtain a linear system of equations for the constants $A_1^{(\rho)}$, $C_1^{(\rho)}$, $(\rho = 1, 2)$, $A_2^{(1)}$ and $C_2^{(1)}$. Thus, the condition $\sigma_\alpha^{(3)} n_\alpha = 0$ on L reduces to

$$C_2^{(1)} = \nu_1 C_1^{(2)}, \tag{6-11}$$

where

$$\nu_1 = I_1(\tau_{(1)} r_1)/K_1(\tau_{(1)} r_1). \tag{6-12}$$

From (6-6) and (6-11) we get

$$\begin{aligned} &\Phi_0 = C_1^{(1)} Q(r), \qquad \Phi_0' = C_1^{(1)} \tau_{(1)} \Lambda(r) \quad \text{on } \Omega_1, \\ &\Phi_0 = C_1^{(2)} I_0(\tau_{(2)} r), \quad \Phi_0' = C_1^{(2)} \tau_{(2)} I_1(\tau_{(2)} r) \quad \text{on } \Omega_2, \end{aligned} \tag{6-13}$$

where

$$Q(r) = I_0(\tau_{(1)} r) + \nu_1 K_0(\tau_{(1)} r), \quad \Lambda(r) = I_1(\tau_{(1)} r) - \nu_1 K_1(\tau_{(1)} r). \tag{6-14}$$

The condition imposed to the function $\sigma^{(3)}$ on Γ leads to

$$C_1^{(2)} = \nu_2 C_1^{(1)}, \tag{6-15}$$

where

$$\nu_2 = a_0^{(1)}\tau_{(1)}\,\Lambda(r_2)[a_0^{(2)}\tau_{(2)}\,I_1(\tau_{(2)}\,r_2)]^{-1}. \tag{6-16}$$

Let us introduce the notations

$$A_1^{(1)} = X_1, \quad A_2^{(1)} = X_2, \quad A_1^{(2)} = X_3, \quad C_1^{(1)} = X_4. \tag{6-17}$$

The remaining conditions from (4-10) and (4-12) reduce to the following system for the constants $A_\alpha^{(1)}$, $A_1^{(2)}$ and $C_1^{(1)}$,

$$\sum_{s=1}^{4} a_{rs}\,X_s = b_r, \quad r = 1, 2, 3, 4, \tag{6-18}$$

where

$$\begin{aligned}
&a_{11} = -2d_{(1)}, \quad a_{12} = 0, \quad a_{13} = 2d_{(2)}, \quad a_{14} = Q(r_2) - \nu_2\,I_0(\tau_{(2)}\,r_2),\\
&a_{21} = \xi_{(1)}, \quad a_{22} = r_2^{-1}, \quad a_{23} = -\xi_{(2)},\\
&a_{24} = \eta_{(2)}\,\tau_{(2)}\,\nu_2\,r_2^{-1}\,I_1(\tau_{(2)}\,r_2) - \eta_{(1)}\,\tau_{(1)}\,r_2^{-1}\,\Lambda(r_2),\\
&a_{31} = k_{(1)}, \quad a_{32} = -(2\mu^{(1)} + \kappa^{(1)})\,r_2^{-2}, \quad a_{33} = -k_{(2)},\\
&a_{34} = (2\mu^{(1)} + \kappa^{(1)})\,\eta_{(1)}\,\tau_{(1)}\,r_2^{-1}\,\Lambda(r_2) - (2\mu^{(2)} + \kappa^{(2)})\,\eta_{(2)}\,\nu_2\,r_2^{-1}\tau_{(2)}\,I_1(\tau_{(2)}\,r_2),\\
&a_{41} = k_{(1)}, \quad a_{42} = -(2\mu^{(1)} + \kappa^{(1)})\,r_1^{-2}, \quad a_{43} = 0,\\
&a_{44} = (2\mu^{(1)} + \kappa^{(1)})\,\eta_{(2)}\,\tau_{(1)}\,r_1^{-1}\,\Lambda(r_1),\\
&b_1 = 2(d_{(1)} - d_{(2)}), \quad b_2 = \chi_{(2)} - \chi_{(1)},\\
&b_3 = (2\mu^{(1)} + \kappa^{(1)})\,\chi_{(1)} - (2\mu^{(2)} + \kappa^{(2)})\,\chi_{(2)} + \lambda^{(2)} - \lambda^{(1)},\\
&b_4 = (2\mu^{(1)} + \kappa^{(1)})\,\chi_{(1)} - \lambda^{(1)}.
\end{aligned} \tag{6-19}$$

We assume that the constitutive coefficients are independent. From (6-18) we can determine the constants $A_\alpha^{(1)}$, $A_1^{(2)}$ and $C_1^{(1)}$. The constants $C_2^{(1)}$ and $C_1^{(2)}$ can be calculated by (6-11) and (6-15). Thus, from (6-1), (6-6), (6-9) and (6-13) we find that the solution of the problem $P^{(3)}$ is given by

$$\begin{aligned}
u_\alpha^{(3)} &= x_\alpha\{-\eta_{(1)}\,C_1^{(1)}\,\tau_{(1)}\,r^{-1}\,\Lambda(r) + \chi_{(1)} + \xi_{(1)}A_1^{(1)} + A_2^{(1)}r^{-2}\} \quad \text{on } \Omega_1,\\
u_\alpha^{(3)} &= x_\alpha\{-\eta_{(2)}\,\tau_{(2)}\,C_1^{(2)}\,r^{-1}\,I_1(\tau_{(2)}\,r) + \chi_{(2)} + \xi_{(2)}A_1^{(2)}\} \quad \text{on } \Omega_2,\\
\psi^{(3)} &= \{C_1^{(1)}\,Q(r) - 2d_{(1)}(1 + A_1^{(1)})\} \quad \text{on } \Omega_1,\\
\psi^{(3)} &= \{C_1^{(2)}\,I_0(\tau_{(2)}\,r) - 2d_{(2)}(1 + A_1^{(2)})\} \quad \text{on } \Omega_2, \quad \varphi^{(3)} = 0.
\end{aligned} \tag{6-20}$$

From (4-7) and (6-2) we find

$$t_{33}^{(3)} = \lambda^{(\rho)}\,r^{-1}(r'U')' + \lambda_0^{(\rho)}[\Phi_0 - 2d_{(\rho)}(1 + A_1^{(\rho)})] \quad \text{on } \Omega_\rho. \tag{6-21}$$

In view of (6-6), (6-13), (6-21) and (4-15), we obtain

$$A_{\alpha 3} = 0, \quad A_{33} = H, \tag{6-22}$$

where

$$
\begin{aligned}
H &= \pi(\lambda^{(2)}+2\mu^{(2)}+\kappa^{(2)})\,r_2^2+\pi(\lambda^{(2)}+2\mu^{(1)}+\kappa^{(1)})(r_1^2-r_2^2)\\
&\quad +2\pi(h_{11}A_1^{(1)}+h_{12}A_1^{(2)}+h_{13}C_1^{(1)}+h_{14}C_1^{(2)}+h_0),\\
h_{11} &= (r_1^2-r_2^2)(\lambda^{(1)}-d_{(1)}\lambda_0^{(1)}), \qquad h_{12} = r_2^2(\lambda^{(2)}-d_{(2)}\lambda_0^{(2)}),\\
h_{13} &= G(r_1)-G(r_2), \qquad\qquad\qquad h_{14} = r_2(\lambda_0^{(2)}\tau_{(2)}^{-1}-\lambda^{(2)}e_{(2)})\,I_1(\tau_{(2)}r_2),\\
h_0 &= (r_1^2-r_2^2)(\lambda^{(1)}\chi_{(1)}-d_{(1)}\lambda_0^{(1)})-d_{(2)}\lambda_0^{(2)}r_2^2+\lambda^{(2)}r_2^2\,\chi_{(2)},\\
G(r) &= r\{\lambda_0^{(1)}\tau_{(1)}^{-1}[I_1(\tau_{(1)}r)-\nu_1K_1(\tau_{(1)}r)]-\lambda^{(2)}e_{(1)}\Lambda(r)\}.
\end{aligned}
\tag{6-23}
$$

With the help of (4-16) and (6-22) we obtain $A_{3\alpha}=0$. In the case of extension we have $M_j=0$, so that the system (4-14) has the solution

$$c_1=0, \quad c_2=0, \quad c_3=-R_3/H. \tag{6-24}$$

Thus, the solution of the extension problem can be expressed as

$$u_\alpha = c_3\,u_\alpha^{(3)}, \quad u_3=c_3\,x_3, \quad \varphi_j=0, \quad \psi=c_3\,\psi^{(3)},$$

where $u_\alpha^{(3)}$ and $\psi^{(3)}$ are given by (6-20).

7. Conclusions

The paper is concerned with the deformation of a bar composed by two different microstretch elastic materials welded together along the surface of separation. The results established in this paper can be summarized as follows:

(a) We study the deformation of a heterogeneous bar which is subjected to extension, bending, torsion and flexure.

(b) We show that the solution of the problem of extension and bending can be reduced to the study of some two-dimensional problems.

(c) We establish the solution of the problem of torsion and flexure by a transversal force.

(d) We use the method to investigate the extension of a circular cylinder reinforced by a longitudinal rod.

Acknowledgement

The author thanks the referees for their helpful suggestions.

References

[Bîrsan and Altenbach 2011] M. Bîrsan and H. Altenbach, "On the theory of porous elastic rods", *Int. J. Solids Struct.* **48**:6 (2011), 910–924.

[Bîrsan et al. 2012] M. Bîrsan, H. Altenbach, T. Sadowski, V. A. Eremeyev, and D. Pietras, "Deformation analysis of functionally graded beams by the direct approach", *Compos. B Eng.* **43**:3 (2012), 1315–1328.

[Chandraseker et al. 2009] K. Chandraseker, S. Mukherjee, J. T. Paci, and G. C. Schatz, "An atomistic-continuum Cosserat rod model of carbon nanotubes", *J. Mech. Phys. Solids* **57**:6 (2009), 932–958.

[Eringen 1999] A. C. Eringen, *Microcontinuum field theories: I — foundations and solids*, Springer, New York, 1999.

[Fatemi et al. 2002] J. Fatemi, F. Van Keulen, and P. R. Onck, "Generalized continuum theories: application to stress analysis in bone", *Meccanica* (*Milano*) **37**:4 (2002), 385–396.

[Fichera 1973] G. Fichera, "Existence theorems in elasticity", pp. 347–389 in *Linear theories of elasticity and thermoelasticity*, edited by C. Truesdell, Springer, Berlin, Heidelberg, 1973.

[Ha et al. 2016] C. S. Ha, M. E. Plesha, and R. S. Lakes, "Chiral three-dimensional lattices with tunable Poisson's ratio", *Smart Mater. Struct.* **25**:5 (2016), 054005.

[Hanumantharaju and Shivanand 2009] H. G. Hanumantharaju and H. K. Shivanand, "Static analysis of bi-polar femur bone implant using FEA", *Int. J. Recent Eng.* **1**:5 (2009), 118–121.

[Ieşan 1976a] D. Ieşan, "Saint-Venant's problem for inhomogeneous bodies", *Int. J. Eng. Sci.* **14**:4 (1976), 353–360.

[Ieşan 1976b] D. Ieşan, "Saint-Venant's problem for heterogeneous anisotropic elastic solids", *Ann. Mat. Pura Appl.* **108**:1 (1976), 149–159.

[Ieşan 1976c] D. Ieşan, "Saint-Venant's problem for inhomogeneous and anisotropic elastic bodies", *J. Elasticity* **6**:3 (1976), 277–294.

[Ieşan 2008] D. Ieşan, *Classical and generalized models of elastic rods*, Chapman and Hall, New York, 2008.

[Ieşan 2019a] D. Ieşan, "Deformation of microstretch elastic beams loaded on the lateral surface", *Math. Mech. Solids* **24**:7 (2019), 2274–2294.

[Ieşan 2019b] D. Ieşan, "Torsion of chiral porous elastic beams", *J. Elasticity* **134**:1 (2019), 103–118.

[Ieşan and Nappa 1995] D. Ieşan and L. Nappa, "Extension and bending of microstretch elastic circular cylinders", *Int. J. Eng. Sci.* **33**:8 (1995), 1139–1151.

[Ieşan and Scalia 2009] D. Ieşan and A. Scalia, "Porous elastic beams reinforced by longitudinal rods", *Z. Angew. Math. Phys.* **60**:6 (2009), 1156–1177.

[Kohles and Roberts 2002] S. S. Kohles and J. B. Roberts, "Linear poroelastic cancellous bone anisotropy: trabecular solid elastic and fluid transport properties", *J. Biomech. Eng.* (*ASME*) **124**:5 (2002), 521–526.

[Lakes 1982] R. Lakes, "Dynamical study of couple stress effects in human compact bone", *J. Biomech. Eng.* (*ASME*) **104**:1 (1982), 6–11.

[Lakes 2001] R. Lakes, "Elastic and viscoelastic behavior of chiral materials", *Int. J. Mech. Sci.* **43**:7 (2001), 1579–1589.

[Lyons et al. 2002] C. K. Lyons, R. B. Guenther, and M. R. Pyles, "Considering heterogeneity in a cylindrical section of a tree", *Int. J. Solids Struct.* **39**:18 (2002), 4665–4675.

[Muskhelishvili 1953] N. I. Muskhelishvili, *Some basic problems of the mathematical theory of elasticity: fundamental equations, plane theory of elasticity, torsion and bending*, Noordhoff, Groningen, 1953.

[Taliercio and Veber 2016] A. Taliercio and D. Veber, "Torsion of elastic anisotropic micropolar cylindrical bars", *Eur. J. Mech. A Solids* **55** (2016), 45–56.

[Thielen et al. 2009] T. Thielen, S. Maas, A. Zuerbes, D. Waldmann, K. Anagnostakos, and J. Kelm, "Mechanical behaviour of standardized, endoskeleton-including hip spacers implanted into composite femurs", *Int. J. Med. Sci.* **6**:5 (2009), 280–286.

Received 4 Nov 2019. Revised 5 Mar 2020. Accepted 24 Apr 2020.

DORIN IEŞAN: iesan@uaic.ro
Octav Mayer Institute of Mathematics, Romanian Academy, Bd. Carol I, nr. 8, 700508 Iaşi, Romania

JOURNAL OF MECHANICS OF MATERIALS AND STRUCTURES
Vol. 15, No. 3, 2020
https://doi.org/10.2140/jomms.2020.15.361

COMPARISON OF SERIES AND FINITE DIFFERENCE SOLUTIONS TO REMOTE TENSILE LOADINGS OF A PLATE HAVING A LINEAR SLOT WITH ROUNDED ENDS

DAVID J. UNGER

Plane stress linear elastic solutions are obtained for a straight slot with rounded ends subject to remotely applied tensile tractions. The series solutions are obtained using a Kolosov–Muskhhelishvili complex variable approach together with an expansion technique developed extensively by G. N. Savin. The finite difference solutions employ an orthogonal curvilinear coordinate system and simulate loads applied at infinity using finite boundaries that are large in comparison to the slot length. The slot shape is similar to the geometry found in the D. Riabouchinsky free streamline problem for fluid flow around two flat plates. Both uniaxial loadings normal to the slot and uniform biaxial loadings are examined.

1. Introduction

The problems addressed in this paper are similar to mode I crack problems [Unger 2011] found in linear elastic fracture mechanics. Unlike crack problems, the conformal mapping of a slot onto a unit circle to facilitate solution involves the use of a transcendental function. However, the most powerful analytical solution technique known for solving plane linear elastic problems limits the mapping function to be at most a rational function of the mapping variable in order to guarantee solution [Muskhelishvili 1977]. The traditional way to avoid this problem is to use a power series expansion of an algebraic or transcendental function in terms of the transformation variable of the mapping function [Savin 1961]. This is the technique employed here.

Once a proper conformal mapping function is identified, a numerical finite difference scheme can also be formulated using the orthogonal curvilinear coordinates defined by the conformal mapping or one that is closely related to it. However, use of a series expansion as a solution technique often generates oscillatory behavior in the solution even after many terms of the expansion are retained including those utilizing modern optimization techniques of the genetic-algorithm variety [Vigdergauz 2006]. This can make the determination of the largest principal stress problematic and consequently the stress concentration factor. The use of a finite difference solution scheme for comparison helps verify the maximum value of the principal stress as numerical solutions of this type are not prone to oscillations.

A summary of classical stress concentration factors for holes of various types in plates for linear elastic behavior may be found in the most currently revised edition of Peterson's handbook [Pilkey et al. 2020]. A large compilation of stress concentration factor literature for analyses conducted after 1974 appears in [Hardy and Malik 1992]. Another relatively recent reference on stress concentration factors is [Savruk and Kazberuk 2017].

Keywords: stress concentration factor, Riabouchinsky free streamline problem.

One motivation for this analysis is that fracture mechanics specimens require a straight slot of finite width be cut into a plate before a fatigue crack can be generated at the tip of the slot. The knowledge of the stress concentration factor due to the slot itself helps quantify the overall state of stress into which the crack propagates [Collins 1993; Rice 1988].

Typically, linear elastic solutions of slots of finite widths are often approximated by use of elongated elliptical hole or parabolic notch analyses [Tada et al. 2000; Creager and Paris 1967]. Nevertheless, there can be large discrepancies between the predictions of linear elastic solutions for elongated ellipses and notches and those of finite-width slots. This can be readily discerned for a mode III slot problem of this shape [Unger 2012a; 2012b], which has a closed-form solution, and those of an ellipse [Neuber 2001] with a similar aspect ratio of semimajor to semiminor axes.

2. Series solution of the slot problem

The mapping function of a plane exterior to a slot geometry of the type shown in Figure 1 onto the interior of a unit circle is [Unger 2016; 2018]

$$z=\omega(\zeta)=\frac{a}{2}\left\{-(1-k_1)\frac{1+\zeta^2}{2\zeta}+\operatorname{sgn}(\operatorname{Re}\zeta)[k_1K(m)-E(m)]\right.$$
$$\left.+i(1+k_1)\left[E\left(\sin^{-1}\frac{i}{k_2}\frac{1-\zeta^2}{2\zeta},k_2^2\right)-\frac{(1-k_1)^2}{(1+k_1)^2}F\left(\sin^{-1}\frac{i}{k_2}\frac{1-\zeta^2}{2\zeta},k_2^2\right)\right]\right\}, \tag{1}$$

where the various parameters of the elliptic integrals [Abramowitz and Stegun 1964] of (1) are defined by

$$m=1-m_1,\quad k_1=\sqrt{m_1},\quad k_2=\frac{2\sqrt{k_1}}{1+k_1},\quad 0\le m_1\le 1 \tag{2}$$

and a is a scaling parameter with units of length.

The aspect ratio A_R of total slot length to the total slot width is [Unger 2016]

$$A_R=\frac{1-\sqrt{m_1}(K(m)+1)+E(m)}{2[E(m_1)-(1-\sqrt{m_1})K(m_1)]}. \tag{3}$$

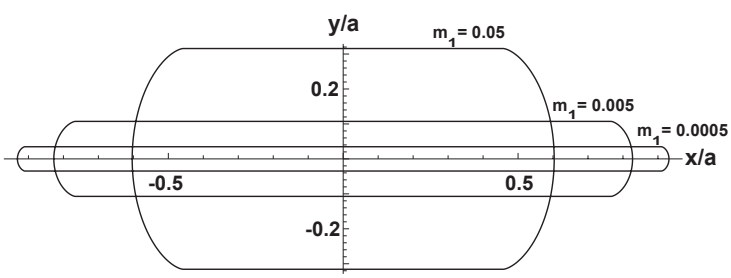

Figure 1. Variation of slot aspect ratio and shape with elliptic integral parameter.

The curved tip at the right-hand side of the slot has the following parametric relationship [Unger 2019] with θ in Cartesian coordinates $z = x + iy$:

$$x_{\text{tip}} = \frac{a}{2}[(1-k_1)\cos\theta - k_1 K(m) + E(m)], \quad -\frac{\pi}{2} \le \theta \le \frac{\pi}{2},$$
$$y_{\text{tip}} = \frac{a}{2}(1+k_1)\left[E\left(\sin^{-1}\left(\frac{\sin\theta}{k_2}\right), k_2^2\right) - \frac{(1-k_1)^2}{(1+k_1)^2}F\left(\sin^{-1}\left(\frac{\sin\theta}{k_2}\right), k_2^2\right)\right], \quad \text{for } -\frac{\pi}{2} \le \theta \le \frac{\pi}{2}, \tag{4}$$

where θ is the angle of the polar representation of the transform variable ζ

$$\zeta = \rho\exp(i\theta), \quad 0 \le \rho \le 1, \quad -\pi \le \theta \le \pi, \tag{5}$$

and where ρ is the radius.

This shape was first obtained in connection with the solution of the free streamlines of an ideal fluid flowing past two side-by-side flat plates [Riabouchinsky 1921]. An analogy with the antiplane slot problem was investigated in detail in [Unger 2018; 2019]. Note that the slot tip will actually change shape slightly with m_1 in Figure 1, but it does so almost imperceptibly for small changes in this parameter. As $m_1 \to 0$, the slot tip shape approaches asymptotically that of a cycloid [Unger 2018]. This particular shape was chosen for the slot as it provides a single analytical expression for a smooth transition from its flat surfaces to its rounded ends. This is an important attribute when solving the problem analytically. In contrast, the ovaloid, which is a slot shape composed of flat surfaces connected by semicircular ends, requires two different meshes composed individually of Cartesian and polar coordinates for solution [Bowie and Freese 1978].

Let us perform a series expansion of $z(\zeta)$ of (1) about the point ζ equals zero retaining only the first three terms of the series

$$z(\zeta) = -\frac{a}{2\zeta} + \frac{a(3m_1^{1/2}-1)\zeta}{2(m_1^{1/2}+1)} + \frac{2am_1^{1/2}(m_1^{1/2}-1)^2\zeta^3}{3(m_1^{1/2}+1)^3} + \cdots. \tag{6}$$

Note that if one wishes to expand this series beyond the three terms shown, using the symbolic software Mathematica, it may be easier to first differentiate $z(\zeta)$ of (1) with respect to ζ and then expand the derivative. This would be followed by integrating the resulting series of the derivative with respect to ζ to obtain the series expansion of $z(\zeta)$.

The symbol σ is traditionally used to represent ζ on the surface of the unit circle where ρ of (5) equals one:

$$\sigma = \exp(i\theta). \tag{7}$$

Similarly, $z(\zeta)$ on the unit circle γ is traditionally represented by the symbol $\omega(\sigma)$ such that (6) becomes

$$\omega(\sigma) = -\frac{a}{2\sigma} + \frac{a(3m_1^{1/2}-1)\sigma}{2(m_1^{1/2}+1)} + \frac{2am_1^{1/2}(m_1^{1/2}-1)^2\sigma^3}{3(m_1^{1/2}+1)^3} + \cdots. \tag{8}$$

Now one of the complex functions that is used in a Muskhelishvili solution scheme is a function designated as $\varphi(\zeta)$. Following the series expansion technique developed in [Savin 1961], one decomposes the

function $\varphi(\zeta)$ for a remote tensile traction T_∞ applied along a single axis by

$$\varphi(\zeta) = T_\infty\, z(\zeta)/4 + \varphi_0(\zeta), \tag{9}$$

where the following integral equation must be solved:

$$\varphi_0(\zeta) + \frac{1}{2\pi i}\int_\gamma \frac{\omega(\sigma)}{\overline{\omega'(\sigma)}}\overline{\varphi_0'(\sigma)}\frac{d\sigma}{\sigma-\zeta} = \frac{1}{2\pi i}\int_\gamma (f_1^0 + i f_2^0)\frac{d\sigma}{\sigma-\zeta}. \tag{10}$$

The bar above a variable in (10) represents the complex conjugate of a related function without the bar. Part of the integrand on the right-hand side of (10) is given by

$$f_1^0 + i f_2^0 = -\frac{T_\infty}{2}[\omega(\sigma) - \exp(2i\alpha)\,\overline{\omega(\sigma)}], \tag{11}$$

where α represents an angle in the direction of the applied traction at infinity T_∞. Now the complex conjugate of $z(\zeta)$ is given by

$$\bar{z}(\bar{\zeta}) = -\frac{a}{2\bar{\zeta}} + \frac{a(3m_1^{1/2}-1)\bar{\zeta}}{2(m_1^{1/2}+1)} + \frac{2am_1^{1/2}(m_1^{1/2}-1)^2\bar{\zeta}^3}{3(m_1^{1/2}+1)^3} + \cdots, \tag{12}$$

where

$$\bar{\zeta} = \rho\exp(-i\theta), \quad 0 \le \rho \le 1, \quad -\pi \le \theta \le \pi. \tag{13}$$

Consequently, from (12) one infers on the slot boundary

$$\overline{\omega(\sigma)} = -\frac{a}{2}\sigma + \frac{a(3m_1^{1/2}-1)}{2(m_1^{1/2}+1)\sigma} + \frac{2am_1^{1/2}(m_1^{1/2}-1)^2}{3(m_1^{1/2}+1)^3\sigma^3} + \cdots \tag{14}$$

as $\bar{\sigma} = 1/\sigma$. Taking the first derivative of (12) with respect to $\bar{\zeta}$ produces

$$\bar{z}'(\bar{\zeta}) = \frac{a}{2\bar{\zeta}^2} + \frac{a(3m_1^{1/2}-1)}{2(m_1^{1/2}+1)} + \frac{2am_1^{1/2}(m_1^{1/2}-1)^2\bar{\zeta}^2}{(m_1^{1/2}+1)^3} + \cdots. \tag{15}$$

Because $\bar{\sigma} = 1/\sigma$, $\bar{z}'(\bar{\zeta})$ may be rewritten on the unit circle γ as

$$\overline{\omega'(\sigma)} = \frac{a}{2}\sigma^2 + \frac{a(3m_1^{1/2}-1)}{2(1+m_1^{1/2})} + \frac{2am_1^{1/2}(m_1^{1/2}-1)^2}{(1+m_1^{1/2})^3\sigma^2} + \cdots. \tag{16}$$

Let us now expand the function φ_0 of (9) in a power series in ζ of the form

$$\varphi_0(\zeta) = (b_1 + ic_1)\zeta + (b_3 + ic_3)\zeta^3 + \cdots, \tag{17}$$

where the various coefficients of the ζ expansion (b_1, c_1, b_3, c_3) are assumed to be real variables. On the unit circle γ, $\varphi_0(\zeta)$ becomes

$$\varphi_0(\sigma) = (b_1 + ic_1)\sigma + (b_3 + ic_3)\sigma^3 + \cdots. \tag{18}$$

Similarly, the complex conjugate of (17) is

$$\bar{\varphi}_0(\bar{\zeta}) = (b_1 - ic_1)\bar{\zeta} + (b_3 - ic_3)\bar{\zeta}^3 + \cdots, \tag{19}$$

with its first derivative being

$$\bar{\varphi}_0'(\bar{\zeta}) = (b_1 - ic_1) + 3(b_3 - ic_3)\bar{\zeta}^2 + \cdots . \tag{20}$$

On the unit circle boundary γ, $\bar{\varphi}_0'(\bar{\zeta})$ becomes

$$\overline{\varphi_0'(\sigma)} = (b_1 - ic_1) + \frac{3(b_3 - ic_3)}{\sigma^2} + \cdots . \tag{21}$$

The integrals of (10) can be evaluated using residue theory as all of the singularities that appear in the integrand are either simple or multiple poles.

The evaluation [Churchill 1960; Spiegel 1964] of an arbitrary integral in the complex plane having a single singularity at $z = z_0$ is

$$\int_\gamma f(z)\, dz = 2\pi i a_{-1}, \tag{22}$$

where a_{-1} is the residue at $z = z_0$. If multiple singularities arise within the unit circle γ, then the residue a_{-1} in (22) is simply replaced by the sum of the residues. It is assumed that the integral in (22) has no branch points. The residue a_{-1} can be determined for a simple pole by the following limit

$$a_{-1} = \lim_{z \to z_0} (z - z_0)\, f(z). \tag{23}$$

If a higher order pole exists at $z = z_0$, then the following alternative to (23) can be used

$$a_{-1} = \lim_{z \to z_0} \frac{1}{(n-1)!} \frac{d^{n-1}}{dz^{n-1}} [(z - z_0)^n f(z)], \quad n \geq 2, \tag{24}$$

where n is the order of the pole.

The residues of the integral on the left-hand side of (10) are evaluated at $\sigma = 0$ and $\sigma = \zeta$, as singularities exist there. In addition, residues are determined at the four roots of the following quartic equation in σ:

$$\sigma^4 + \frac{-1 + 3m_1^{1/2}}{1 + m_1^{1/2}} \sigma^2 + \frac{4m_1^{1/2}(-1 + m_1^{1/2})^2}{(1 + m_1^{1/2})^3} = 0, \tag{25}$$

which are explicitly

$$\sigma \longrightarrow \pm \frac{1}{\sqrt{2}} \sqrt{-3 + \frac{4}{1 + m_1^{1/2}} \pm \frac{\sqrt{1 - 7m_1^{1/2}(3 - 5m_1^{1/2} + m_1)}}{(1 + m_1^{1/2})^{3/2}}}. \tag{26}$$

The algebraic equation (25) is used to locate the roots of $\overline{\omega'(\sigma)} = 0$, which introduce singularities in the integrand, and consequently require evaluation using residue theory. All four of the roots (26) fall within the complex unit circle γ for $0 \leq m_1 \leq 1$, which is a necessary condition from residue theory for their inclusion in the evaluation.

The result of the evaluation of this integral by residue theory is

$$\frac{1}{2\pi i} \int_\gamma \frac{\omega(\sigma)}{\overline{\omega'(\sigma)}} \overline{\varphi_0'(\sigma)} \frac{d\sigma}{\sigma - \zeta} = \frac{4(b_1 - ic_1) m_1^{1/2} (-1 + m_1^{1/2})^2 \zeta}{3(1 + m_1^{1/2})^3}. \tag{27}$$

The subroutine for symbolic residue evaluation in Mathematica was used for determining the integral (27) in this example. Note that when numerical iteration is used for determining roots instead of an analytical expression, relationships (23) and (24) may have to be employed to determine the residues.

Similarly, the integral on the right-hand side of (10) requires residue evaluation at $\sigma = 0$ and $\sigma = \zeta$ producing the result

$$\frac{1}{2\pi i}\int_\gamma (f_1^0 + i f_2^0)\frac{d\sigma}{\sigma - \zeta} = -\frac{T_\infty a\zeta[-3 + 3e^{2ia}(1+m_1^{1/2})^3 + m_1^{1/2}[3 + 15m_1^{1/2} + 9m_1 + 4(-1+m_1^{1/2})^2\zeta^2]]}{12(1+m_1^{1/2})^3}. \quad (28)$$

By substituting (17), (27), and (28) into (10), one finds a relationship for determining the coefficients of the expansion of $\varphi_0(\zeta)$

$$aT_\infty\zeta\big[-3 + 3e^{2i\alpha}(1+m_1^{1/2})^3 + m_1^{1/2}[3 + 15m_1^{1/2} + 9m_1 + 4(m_1^{1/2}-1)^2\zeta^2]\big] + 12(1+m_1^{1/2})^3[(b_1 + ic_1)\zeta + (b_3 + ic_3)\zeta^3] + 16(b_1 - ic_1)m_1^{1/2}(m_1^{1/2}-1)^2\zeta = 0. \quad (29)$$

By setting the real and imaginary parts of the coefficients on ζ and ζ^3 individually equal to zero in (29), one determines the coefficients of the series as

$$b_1 = 3aT_\infty(1+m_1^{1/2})^2\left[\frac{1 - 3m_1^{1/2} - (1+m_1^{1/2})\cos 2\alpha}{4(3 + 13m_1^{1/2} + m_1 + 7m_1^{3/2})}\right], \quad (30)$$

$$c_1 = \frac{3aT_\infty(1+m_1^{1/2})^3 \sin 2\alpha}{4(-3 - 5m_1^{1/2} - 17m_1 + m_1^{3/2})}, \quad (31)$$

$$b_3 = -\frac{aT_\infty(-1+m_1^{1/2})^2 m_1^{1/2}}{3(1+m_1^{1/2})^3}, \quad c_3 = 0. \quad (32)$$

Now, a relationship established in [Muskhelishvili 1977] is

$$\sigma_\rho + \sigma_\theta = 4\,\mathrm{Re}\left[\frac{\varphi'(\zeta)}{z'(\zeta)}\right], \quad (33)$$

where σ_ρ and σ_θ are normal stresses in the ρ and θ directions. On the slot boundary, which is traction free, σ_ρ is zero so that (33) becomes [Savin 1961]

$$\sigma_\theta(\sigma) = 4\,\mathrm{Re}\left[\frac{\varphi'(\sigma)}{\omega'(\sigma)}\right]. \quad (34)$$

From (34) the stress concentration factor may be determined as the maximum principal stress will always be located on the surface of the slot.

This analysis is provided here only to demonstrate the basic technique used to generate the curves shown in Figures 2 and 3, whose analyses contain many more terms of ζ than the series (6). The series (6) was truncated after only three terms, as even a single additional term in the form of a fifth power of ζ would greatly increase the length of the solution presented for an arbitrary value of m_1.

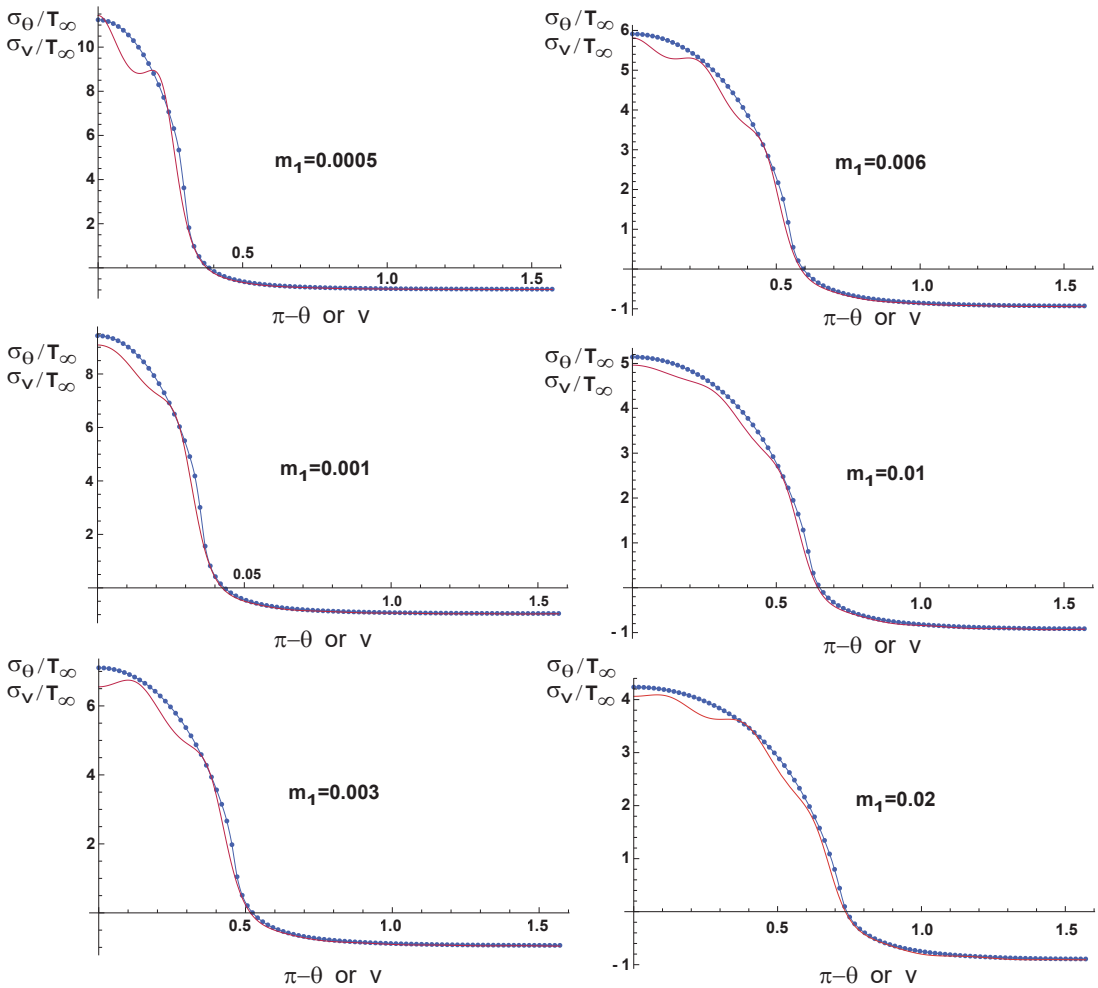

Figure 2. Stress distribution along slot surface under uniaxial loading for various slot aspect ratios (3).

All of the curves shown in Figures 2 and 3 were generated with expansions containing odd powers of ζ up to the twenty-third power using specific values of m_1. Two exceptions are also shown for the case $m_1 = 0.02$, where ζ was expanded only up to the twenty-first power.

The extreme length of these solutions preclude their being published in their entirety. Also note that finding roots of σ where singularities occur in the integrands often require numerical iteration for specific rather than arbitrary values of m_1. This was avoidable in the simple case of (25) because an analytical solution for the roots is possible (26) for arbitrary m_1. One must find all of the roots within the integrand of the integrals in (10) provided that the roots fall within the unit circle γ. This is necessary in order to evaluate the integrals in (10) using residue theory.

It is the curves showing oscillatory behavior in Figures 2 and 3 that were generated with this series expansion technique. The curves of Figure 2 were produced by taking $\alpha = \pi/2$, in (11), which corresponds to the direction of the remote tensile load T_∞ in the y-direction. The curves in Figure 3 were produced

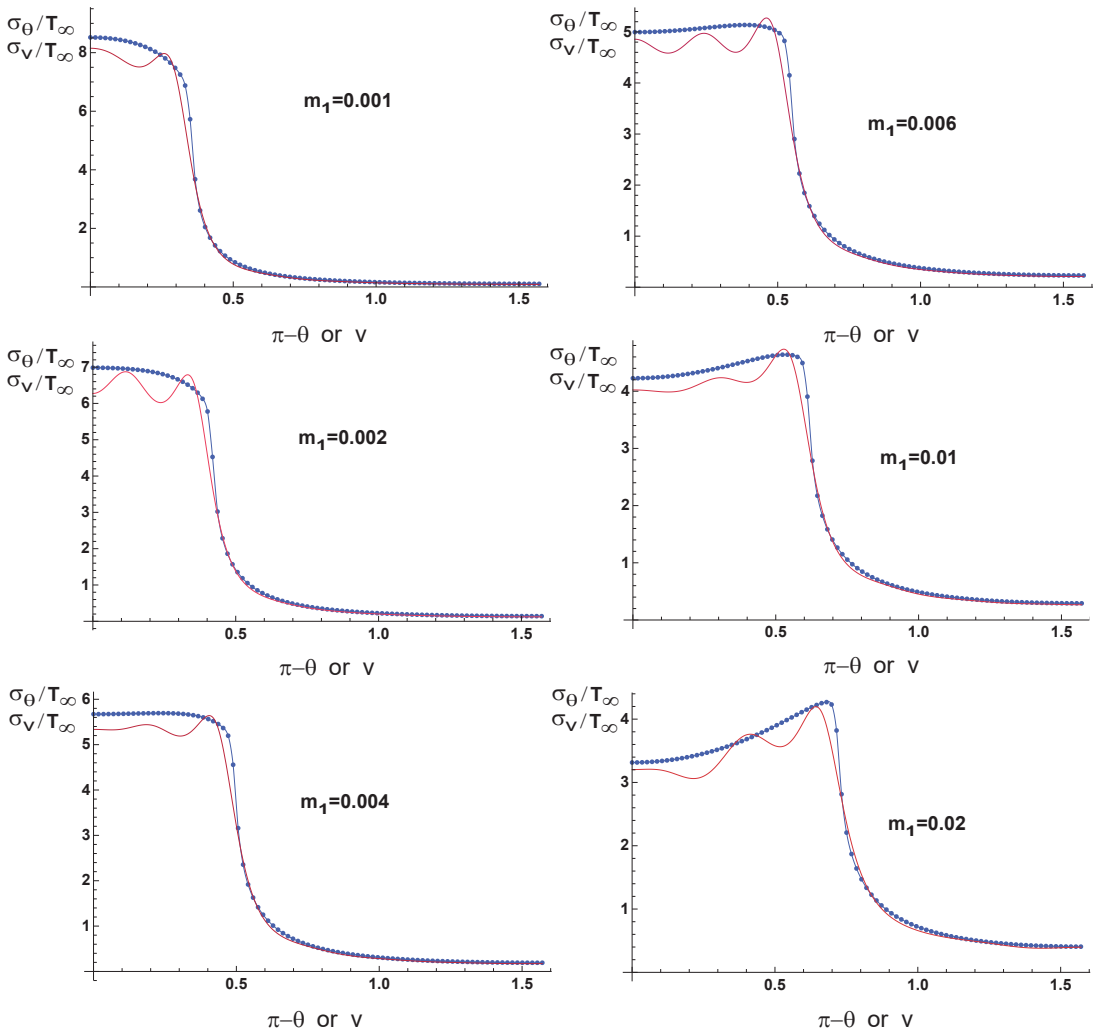

Figure 3. Stress distribution along slot surface under biaxial loading for various slot aspect ratios (3).

by superposing a solution with $\alpha = \pi/2$ to one with $\alpha = 0$ to simulate a uniform biaxial loading T_∞ of the plate at infinity.

The remaining curves of Figures 2 and 3 showing numerical data points joined by continuous curves were obtained from finite differences solutions, whose details are discussed in the following section.

3. Finite difference solutions of the slot problem

The isotropic plane stress linear elastic slot solution is determined in this section by finding an appropriate Airy stress function numerically. An Airy function $\phi = \phi(x, y)$ must solve the following fourth order

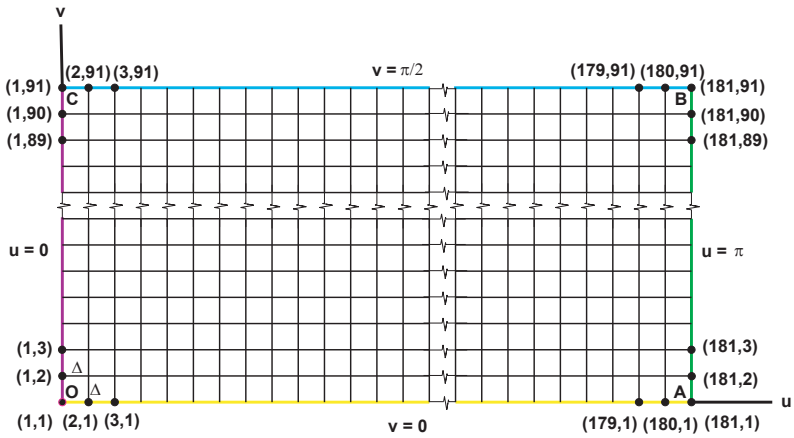

Figure 4. Square finite difference grid map of the curvilinear orthogonal coordinate system.

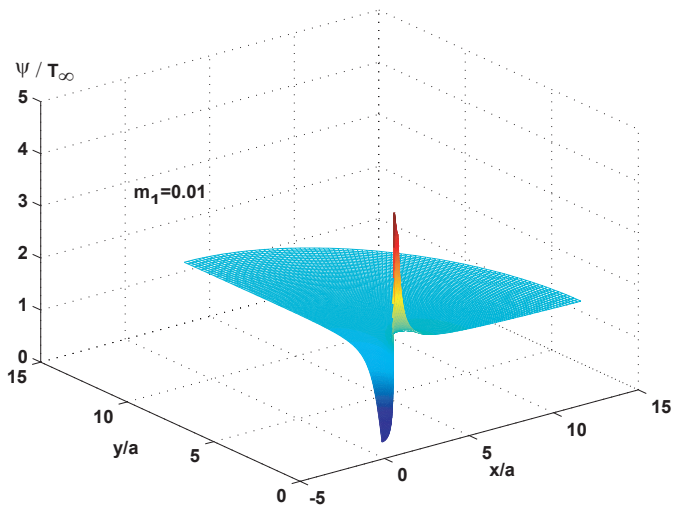

Figure 5. Sum of in-plane normal stresses ψ for biaxial loading.

partial differential equation, which is referred to as the biharmonic equation [Malvern 1969]

$$\nabla^4\phi = \nabla^4\phi(x, y) = \frac{\partial^4\phi(x, y)}{\partial x^4} + 2\frac{\partial^4\phi(x, y)}{\partial x^2\,\partial y^2} + \frac{\partial^4\phi(x, y)}{\partial y^4} = 0. \tag{35}$$

Equation (35) is valid provided that no body forces are present. The properties of the operator ∇^4 in (35) allow the biharmonic equation to be decomposed as

$$\nabla^4\phi = 0 \Longrightarrow \nabla^2(\nabla^2\phi) = 0 \Longrightarrow \nabla^2\psi = 0 \quad \text{for } \psi = \nabla^2\phi, \tag{36}$$

where the Laplacian operator ∇^2 is defined in Cartesian coordinates (x, y) by

$$\nabla^2(\,) = \frac{\partial^2(\,)}{\partial x^2} + \frac{\partial^2(\,)}{\partial y^2}. \tag{37}$$

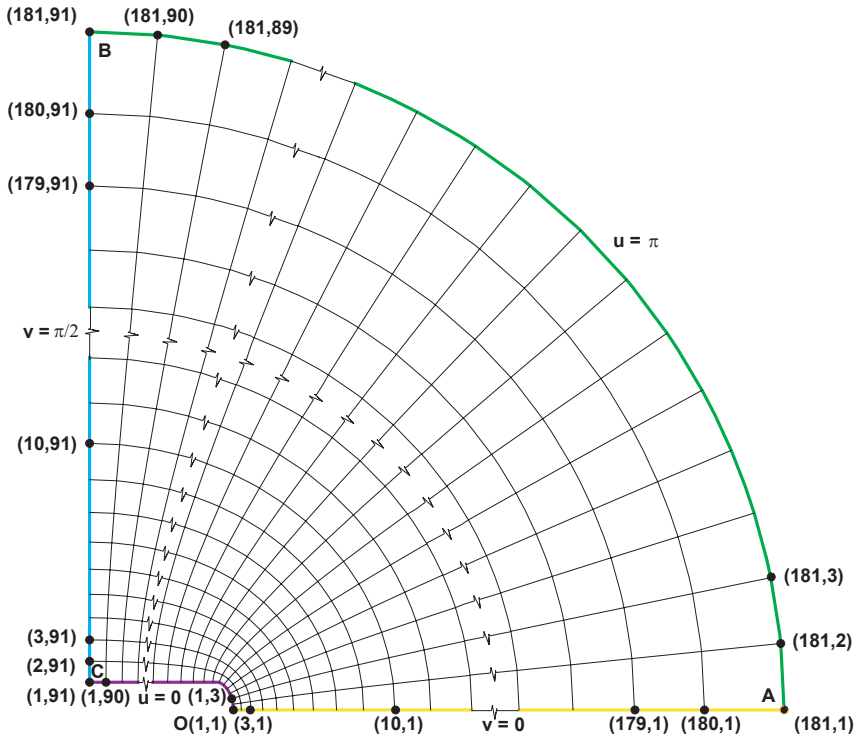

Figure 6. Curvilinear orthogonal coordinate system (u, v) of the slot problem.

The function ψ in (36) is referred to as a harmonic function indicating that it solves Laplace's equation

$$\nabla^2 \psi = 0. \tag{38}$$

By (36) the Airy function may also be thought of as solving Poisson's equation

$$\nabla^2 \phi = \psi. \tag{39}$$

Hence, a solution of the biharmonic equation may be decomposed into solving two second order partial differential equations simultaneously, (38) and (39), as noted previously in [Greenspan 1974].

The use of an orthogonal curvilinear system that naturally accommodates the slot geometry will greatly simplify the application of boundary conditions to the governing equation. A coordinate system closely related to (1) will be used here. Let us introduce the following substitution for ζ in (1):

$$\zeta = -\exp(-w), \quad \text{where } w = u + iv, \quad 0 \le u \le \infty, \quad -\pi \le v \le \pi. \tag{40}$$

A schematic drawing of this coordinate system (u, v) is shown in Figure 6 for the first quadrant of the xy plane. As $m_1 \to 0$, the coordinates u and v of (40) approach standard elliptical coordinates, where u is a family of confocal ellipses and v is a family of orthogonal hyperbolas. For a general value of m_1, the slot boundary is located at $u = 0$. On the slot boundary, the coordinate $\rho = 1$ so that $v = \pi - \theta$, as can be inferred from (5) and (40).

In the coordinate system defined by w, Poisson's equation (39) may be written as

$$\frac{\partial^2\phi}{\partial u^2}+\frac{\partial^2\phi}{\partial v^2}=h^2(u,v)\,\psi(u,v), \tag{41}$$

where the metric coefficient $h(u,v)$ in (41) can be determined using one of the following relationships:

$$h(u,v)=\sqrt{\frac{dz}{dw}\frac{d\bar{z}}{d\bar{w}}}=\sqrt{\mathrm{Re}^2(dz/dw)+\mathrm{Im}^2(dz/dw)}=\left|\frac{dz}{dw}\right|. \tag{42}$$

Laplace's equation (38) becomes in the new curvilinear system

$$\frac{\partial^2\psi}{\partial u^2}+\frac{\partial^2\psi}{\partial v^2}=0. \tag{43}$$

A nine-point finite difference scheme for Poisson's equation in [Rosser 1975], which also agrees with one in [Collatz 1960], is chosen for solution of (41) for interior nodes (i,j):

$$\begin{aligned}\phi_{i,j}=&\tfrac{1}{20}(\phi_{i-1,j+1}+\phi_{i+1,j+1}+\phi_{i-1,j-1}+\phi_{i+1,j-1})+\tfrac{1}{5}(\phi_{i,j+1}+\phi_{i-1,j}+\phi_{i+1,j}+\phi_{i,j-1})\\&-\frac{\Delta^2}{300}(82h^2_{i,j}\psi_{i,j}+h^2_{i-1,j+1}\psi_{i-1,j+1}+h^2_{i,j+1}\psi_{i,j+1}+h^2_{i+1,j+1}\psi_{i+1,j+1}+h^2_{i-1,j}\psi_{i-1,j}\\&+h^2_{i+1,j}\psi_{i+1,j}+h^2_{i-1,j-1}\psi_{i-1,j-1}+h^2_{i,j-1}\psi_{i,j-1}+h^2_{i+1,j-1}\psi_{i+1,j-1}),\end{aligned} \tag{44}$$

where Δ is the incremental change between adjacent nodes in the square mesh shown in Figure 4. The indices of the mesh range from $i=1$ to 181 and $j=1$ to 91.

Similarly, an equivalent formulation for the discretization of Laplace's equation (43) for interior nodes:

$$\psi_{i,j}=\tfrac{1}{5}(\psi_{i,j+1}+\psi_{i-1,j}+\psi_{i+1,j}+\psi_{i,j-1})+\tfrac{1}{20}(\psi_{i-1,j+1}+\psi_{i+1,j+1}+\psi_{i-1,j-1}+\psi_{i+1,j-1}). \tag{45}$$

Now the boundary condition for ψ along slot OC of Figure 6 must be derived. As the slot is traction free, the following relationships may be imposed [Malvern 1969] to satisfy this boundary condition:

$$\phi(0,v)=\left.\frac{\partial\phi}{\partial u}\right|_{u=0}=0. \tag{46}$$

As ϕ is constant along the slot by (46), the following relationships for partial derivatives of ϕ with respect to v and a reduction of Poisson's equation to an ordinary differential equation along the slot are deduced:

$$\left.\frac{\partial\phi}{\partial v}\right|_{u=0}=0\longrightarrow\left.\frac{\partial^2\phi}{\partial v^2}\right|_{u=0}=0\longrightarrow\frac{d^2\phi(0,v)}{du^2}=h^2(0,v)\,\psi(0,v). \tag{47}$$

Sixth order, forward, finite difference representations [Miller 1975] of partial derivatives of ϕ along the slot boundary $(i=1)$ follow

$$\begin{aligned}\left.\frac{\partial\phi}{\partial u}\right|_{1,j}&=0=\frac{1}{60\Delta}(-147\phi_{1,j}+360\phi_{2,j}-450\phi_{3,j}+400\phi_{4,j}-225\phi_{5,j}+72\phi_{6,j}-10\phi_{7,j}),\\\left.\frac{\partial^2\phi}{\partial u^2}\right|_{1,j}&=\frac{1}{180\Delta^2}(812\phi_{1,j}-3132\phi_{2,j}+5265\phi_{3,j}-5080\phi_{4,j}+2970\phi_{5,j}-972\phi_{6,j}+137\phi_{7,j}).\end{aligned} \tag{48}$$

In addition, from (46), one infers along the slot that

$$\phi(0, v) = \phi_{1,j} = 0 \quad \text{for } j = 1 \text{ to } 91. \tag{49}$$

From the ordinary differential equation in (47), combined with relationships (48) and (49), the discretized value of ψ along the slot boundary is

$$\psi_{1,j} = \frac{10\phi_{2,j} - 5\phi_{3,j} + 2.2222\phi_{4,j} - 0.625\phi_{5,j} + 0.08\phi_{6,j}}{h_{i,j}^2 \Delta^2}, \quad j \neq 1 \text{ or } 91. \tag{50}$$

Note that $\phi_{7,j}$ was chosen for elimination between equations (48) in the derivation of (50).

Equations (49) and (50) constitute the boundary conditions on ϕ and ψ respectively along slot OC of Figure 6 with the exception of the endpoints for ψ.

Other boundary conditions that must be satisfied along sides OA and BC of Figure 6 are due to symmetry

$$\text{OA and BC:} \quad \frac{\partial \phi}{\partial v} = 0, \quad \frac{\partial \psi}{\partial v} = 0. \tag{51}$$

The condition on ϕ defined by (51) was satisfied by employing simple forward and backward second order finite difference equations

$$\begin{aligned} &\text{OA:} \quad \phi_{i,1} = (4\phi_{i,2} - \phi_{i,3})/3, \qquad i \neq 1 \text{ or } 181, \\ &\text{BC:} \quad \phi_{i,91} = (4\phi_{i,90} - \phi_{i,89})/3, \quad i \neq 1 \text{ or } 181. \end{aligned} \tag{52}$$

The second boundary condition of (51) on ψ was combined with second order finite difference representations for Laplace's equation (43) in order to obtain the following relationships that are appropriate for homogeneous Neumann boundary conditions [Li and Lam 1964]

$$\begin{aligned} &\text{OA:} \quad \psi_{i,1} = (\psi_{i-1,1} + \psi_{i+1,1} + 2\psi_{i,2})/4, \qquad i \neq 1 \text{ or } 181, \\ &\text{BC:} \quad \psi_{i,91} = (\psi_{i-1,91} + \psi_{i+1,91} + 2\psi_{i,90})/4, \quad i \neq 1 \text{ or } 181. \end{aligned} \tag{53}$$

Along the exterior boundary AB, which represents infinity, two different types of loadings were considered. The first was for a uniaxial loading T_∞ in the direction of the y-axis (Figure 1). The second was for a uniform biaxial loading in the x and y directions. In the specific cases, the following relationships were used:

$$\begin{aligned} &\text{uniaxial loading on AB:} \quad \begin{cases} \phi_{181,j} = (T_\infty/2)\, x_{181,j}^2 \\ \psi_{181,j} = T_\infty, \end{cases} \qquad j = 1 \text{ to } 91, \\ &\text{biaxial loading on AB:} \quad \begin{cases} \phi_{181,j} = (T_\infty/2)(x_{181,j}^2 + y_{181,j}^2) \\ \psi_{181,j} = 2T_\infty, \end{cases} \qquad j = 1 \text{ to } 91. \end{aligned} \tag{54}$$

At the ends of the slot, points O and C respectively, second order finite difference representations of Laplace's equation were combined with second order finite difference equations of the second boundary condition of (51) to obtain

$$\psi_{1,1} = \psi_{3,1} + 2\psi_{1,2} - 2\psi_{2,1}, \quad \psi_{1,91} = \psi_{3,91} + 2\psi_{1,90} - 2\psi_{2,91}. \tag{55}$$

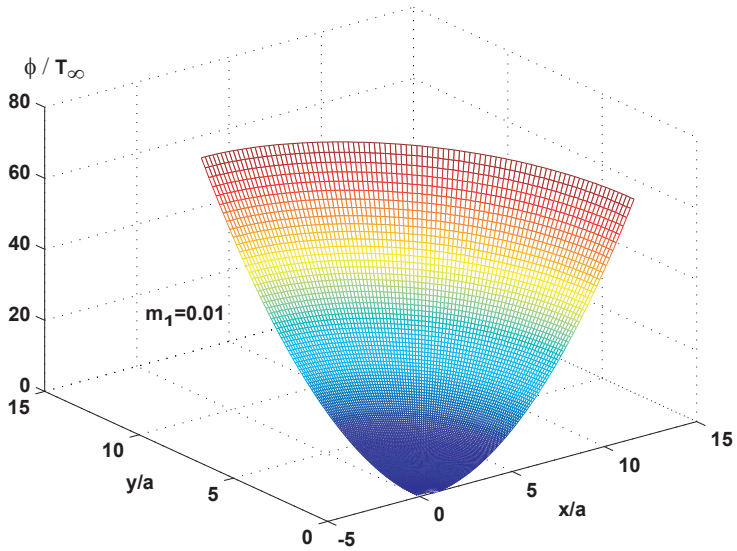

Figure 7. Airy stress function ϕ for biaxial loading.

A Jacobi iteration scheme [Akai 1994] was chosen to solve the governing equations for ϕ and ψ, (41) and (43) respectively, subject to boundary conditions (49), (50), (52)–(55). The value of the grid increment Δ used in the finite difference analysis was $\pi/180$. The value of u varied from 0 to π in the analysis, while the coordinate v varied from 0 to $\pi/2$. For $u = \pi$, there is approximately a one degree variation in the angle v between adjacent nodes in the physical plane. Representative plots of the solutions for ψ and ϕ for the biaxial loading case with $m_1 = 0.01$ are shown in Figures 5 and 7, respectively.

Note that

$$\psi = \sigma_x + \sigma_y = \sigma_u + \sigma_v, \tag{56}$$

where σ_x, σ_y, σ_u, and σ_v are normal stresses in their respective directions, which are designated by subscripts. On the slot boundary, σ_u is zero so that $\sigma_v = \psi$ by (56).

The MATLAB software was used for the numerical analysis. Subroutines for the evaluations of elliptic integrals for complex arguments were written by Igor Moiseev and downloaded from the MATHWORKS file exchange.

The convergence of the numerical scheme for the stress concentration factor for the uniaxial case of loading for a value of $m_1 = 0.01$, representing an infinite boundary, is shown in Figure 8 as the outer radius of the boundary R is increased. The value of R was calculated at the coordinate $v = 0$. It was determined numerically that little variance occurred in K_t beyond the value $u = \pi$ as indicated in the figure. This value of R is also small enough to maintain numerical stability of the iterative process as ϕ grows concurrently large. The mesh size itself was chosen to be fine enough to provide accurate numerical results while at the same time minimizing computation time for convergence of the iterative solution.

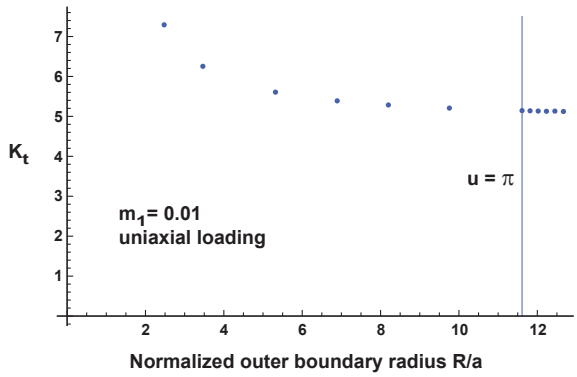

Figure 8. Convergence of numerical solution for stress concentration factor as a function of outer boundary radius.

4. Comparison of solutions

The numerical data points for various values of m_1 are shown in Figure 2 for a uniaxial tensile loading of the slot and in Figure 3 for a biaxial tensile loading of the slot. When the maximum principal stresses are plotted for the numerical data, fairly smooth curves connecting the data points are observed (Figure 9). In contrast, a plot of the maximum principal stresses for the series solutions would exhibit significant amounts of scatter in the data due to the oscillatory behavior of the solutions. On the other hand, there is still a discernable qualitative agreement between the series and the finite difference solutions plotted in Figures 2 and 3 along the slot surfaces. This fact lends additional support to the assumption that the boundaries representing infinity in the finite difference solutions are sufficiently distant from the origin that any additional length added to the existing boundary will have a negligible effect on the maximum principal stress.

An exact stress concentration factor K_t exists for the antiplane or mode III slot problem of this shape [Unger 2012a; 2012b; 2016; 2018; 2019]:

$$\text{antiplane shear loading:} \quad K_t = \tau_{\max}/\tau_\infty = 1/m_1^{1/4}, \tag{57}$$

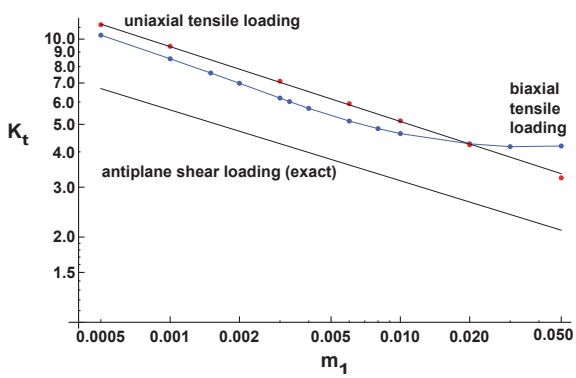

Figure 9. Stress concentration factor versus elliptic integral parameter.

where $\tau_{\max}$ is the largest equivalent shear stress and τ_∞ is the applied shear traction at infinity. Being a power law relationship, it appears as a straight line when plotted on the log-log scale of Figure 9. (Other authors who have found asymptotic solutions to semiinfinite slot problems with a cycloidal tip for a mode III loading are cited and discussed in [Unger 2012a; 2012b; 2018]).

A numerical fit to the data points for the uniaxial tensile loading case plotted in Figure 9 using the Mathematica software has the power law relationship

$$\text{uniaxial tensile loading:} \quad K_t = \sigma_v^{\max}/T_\infty = 1.52/m_1^{0.264}, \tag{58}$$

where $\sigma_v^{\max}$ is the maximum value of the normal stress σ_v in the v-direction. This value also corresponds to the maximum principal value of stress. The relationship (58) is plotted as a straight line through the uniaxial tensile data points in Figure 9. Combining (58) with (3) will allow a relationship between aspect ratio and the stress concentration factor to be generated. This simple power law relationship breaks down for values of m_1 greater than about 0.05. A plot of stress concentration factor versus slot aspect ratio is provided in Figure 10, which contains points having corresponding values of m_1 larger than 0.05. The value of slot aspect ratio corresponding to $m_1 = 0.05$ is approximately 1.88.

For the biaxial tensile loading, a transition occurs around $m_1 = 0.00316$ for the location of the maximum principal stress on the curved portion of the slot. For $m_1 \le 0.00316$, the largest principal stress occurs at the slot tip. For $m_1 > 0.00316$, the largest principal stress lies somewhere between the slot tip and the point where the flat surfaces begin. Figure 3 illustrates this behavior. The location of the coordinate v on the slot ($u = 0$) where the flat surfaces meet the rounded portions is

$$v = \cos^{-1}\frac{1 - m_1^{1/2}}{1 + m_1^{1/2}}. \tag{59}$$

A comparison is now made between the results obtained here for the case of the uniaxial tensile loaded slot of the type shown in Figure 1 to the work in [Bowie and Freese 1978] for a uniaxial tensile loaded ovaloid. Recall that the ovaloid is linear slot cut into a plate having semicircular ends. Thus the geometry of the ovaloid is very similar to the slot geometry addressed in this paper. It should also provide a qualitative check on the accuracy of the analysis presented here.

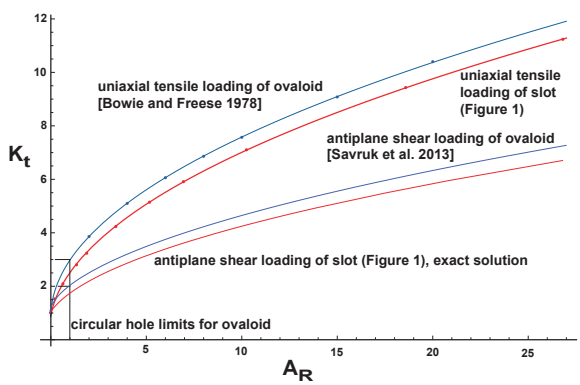

Figure 10. Comparison of stress concentration factor versus aspect ratio for two elongated holes.

The present author [Unger 2016] generated a continuous and smooth curve fit to the data points generated in [Bowie and Freese 1978] of the form

$$K_t = 0.850 + 2.13\sqrt{A_R}. \tag{60}$$

Note that this expression becomes invalid for values of stress concentration factor lower than a value of three as the ovaloid degenerates to a circular hole at that particular value.

A similar fit to the data points shown in Figure 9 for the uniaxial tensile loading of the slot together with a few additional data points covering the low aspect ratio region is

$$K_t = 0.324 + 2.11\sqrt{0.0783 + A_R}. \tag{61}$$

Unlike the ovaloid expression (60), the relationship (61) is valid down to an aspect ratio of zero where the shape of the slot degenerates to a vertical line that is parallel to the direction of load.

By comparing the two curves representing (60) and (61) in Figure 10, one can infer that the slot shape of Figure 1 produces lower stress concentration factors K_t than the ovaloid for identical aspect ratios of the slot. This might be attributed to the fact that the ovaloid has a smaller radius of curvature at the slot tip than does those of Figure 1 for the same aspect ratio [Unger 2016]. The radius of curvature ρ_t for the slot tip corresponding to relationship (4) is given by

$$\rho_t = 2a\frac{m_1^{1/2}}{1 - m_1^{1/2}}. \tag{62}$$

The radius of curvature at the tip of the ovaloid is naturally determined as half the width of the slot because its ends are semicircular in shape.

Similarly, a curve fit to numerical data points generated for the antiplane shear loading of the ovaloid was provided in [Savruk et al. 2013; Savruk and Kazberuk 2017] as

$$K_t = 1.3442\sqrt{A_R} + \frac{1}{1 + 0.5249\sqrt{A_R}}. \tag{63}$$

In Figure 10, this relationship is compared to the exact solution for the slot of Figure 1. The exact formula is obtained by combining (3) with (57).

One notes from Figure 10 that for both uniaxial tensile loading and antiplane shear loading of the slot of Figure 1 have lower stress concentration factors than those of the ovaloid for identical aspect ratios.

5. Conclusions

The finite difference solutions for the slot problem addressed in this article produce more reliable values of stress concentration factor than do the series solutions.

While the slot shape addressed in this paper produces lower stress concentration factors than does the ovaloid for identical hole aspect ratios, the close proximity of the two curves for each individual case in Figure 10 suggests that the additional complication of milling the slot tip of the specified shape (4) is unjustified in most cases. For the antiplane slot problem, relationship (57) remains the only exact solution of its kind for comparison.

In closing, the material contained within this article may help experimentalists in the field of fracture mechanics to better determine the state of stress into which a crack propagates in a specimen.

References

[Abramowitz and Stegun 1964] M. Abramowitz and I. A. Stegun, *Handbook of mathematical functions with formulas, graphs, and mathematical tables*, National Bureau of Standards Applied Mathematics Series **55**, U.S. Government Printing Office, Washington, D.C., 1964.

[Akai 1994] T. J. Akai, *Applied numerical methods for engineers*, Wiley, New York, 1994.

[Bowie and Freese 1978] O. L. Bowie and C. E. Freese, "Analysis of notches using conformal mapping", pp. 69–134 in *Stress analysis of notch problems: stress solutions to a variety of notch geometries used in engineering design*, edited by G. C. Sih, Mechanics of fracture **5**, Sijthoff & Noordhoff, Alphen aan den Rijn, 1978.

[Churchill 1960] R. V. Churchill, *Complex variables and applications*, McGraw-Hill, New York, 1960.

[Collatz 1960] L. Collatz, *The numerical treatment of differential equations*, 3rd ed., Springer, Berlin, 1960.

[Collins 1993] J. Collins, *Failure of materials in mechanical design: analysis, prediction, prevention*, 2nd ed., Wiley, New York, 1993.

[Creager and Paris 1967] M. Creager and P. C. Paris, "Elastic field equations for blunt cracks with reference to stress corrosion cracking", *Int. J. Fract. Mech.* **3**:4 (1967), 247–252.

[Greenspan 1974] D. Greenspan, *Discrete numerical methods in physics and engineering*, Mathematics in Science and Engineering **107**, Academic Press, New York, 1974.

[Hardy and Malik 1992] S. J. Hardy and N. H. Malik, "A survey of post-peterson stress concentration factor data", *Int. J. Fatigue* **14**:3 (1992), 147–153.

[Li and Lam 1964] W.-H. Li and S.-H. Lam, *Principles of fluid mechanics*, Addison-Wesley, Reading, 1964.

[Malvern 1969] L. E. Malvern, *Introduction to the mechanics of a continuous medium*, Prentice-Hall, Englewood Cliffs, 1969.

[Miller 1975] R. E. Miller, "Boundary value problems for mechanics", Class notes, TAM 493, University of Illinois at Urbana-Champaign, 1975.

[Muskhelishvili 1977] N. I. Muskhelishvili, *Some basic problems of the mathematical theory of elasticity*, 2nd ed., Noordhoff International Publishing, Leiden, 1977.

[Neuber 2001] H. Neuber, *Kerbspannungslehre*, 4th ed., Springer, Berlin, 2001.

[Pilkey et al. 2020] W. D. Pilkey, D. F. Pilkey, and Z. Bi, *Peterson's stress concentration factors*, 4th ed., Wiley, Hoboken, 2020.

[Riabouchinsky 1921] D. Riabouchinsky, "On steady fluid motions with free surfaces", *Proc. London Math. Soc.* **s-19**:1 (1921), 206–215.

[Rice 1988] R. C. Rice, *Fatigue design handbook*, Society of Automotive Engineers, Warrendale, 1988.

[Rosser 1975] J. B. Rosser, "Nine-point difference solutions for Poisson's equation", *Comput. Math. Appl.* **1**:3-4 (1975), 351–360.

[Savin 1961] G. N. Savin, *Stress concentration around holes*, Pergamon Press, Oxford, 1961.

[Savruk and Kazberuk 2017] M. P. Savruk and A. Kazberuk, *Stress concentration at notches*, Springer, 2017.

[Savruk et al. 2013] M. P. Savruk, A. Kazberuk, and G. Tarasyuk, "Stress concentration near holes in the elastic plane subjected to antiplane deformation", *Mater. Sci.* (*Russia*) **48**:4 (2013), 415–426.

[Spiegel 1964] M. R. Spiegel, *Complex variables with an introduction to conformal mapping and its applications including 640 solved problems*, McGraw-Hill, New York, 1964.

[Tada et al. 2000] H. Tada, P. C. Paris, and G. R. Irwin, *The stress analysis of cracks handbook*, 3rd ed., ASME Press, New York, 2000.

[Unger 2011] D. J. Unger, *Analytical fracture mechanics*, Dover, Mineola, 2011.

[Unger 2012a] D. J. Unger, "Linear elastic solutions for slotted plates", *J. Elasticity* **108**:1 (2012), 67–82.

[Unger 2012b] D. J. Unger, "Erratum to: linear elastic solutions for slotted plates", *J. Elasticity* **108**:1 (2012), 83.

[Unger 2016] D. J. Unger, "Linear elastic solutions for slotted plates revisited", pp. 2042–2043 in *Proc. of XXIV International Congress of Theoretical and Applied Mechanics*, 2016.

[Unger 2018] D. J. Unger, "Free streamline hydrodynamic analogy for a linear elastic antiplane slot problem with perfectly plastic ligaments at its ends", *J. Elasticity* **132**:2 (2018), 261–270.

[Unger 2019] D. J. Unger, "Visualizing the crack driving force through fluid analogy", *J. Mech. Behav. Mater.* **28**:1 (2019), 89–94.

[Vigdergauz 2006] S. Vigdergauz, "The stress-minimizing hole in an elastic plate under remote shear", *J. Mech. Mater. Struct.* **1**:2 (2006), 387–406.

Received 27 Dec 2019. Revised 30 Mar 2020. Accepted 18 Apr 2020.

DAVID J. UNGER: du2@evansville.edu
Department of Mechanical and Civil Engineering, University of Evansville, 1800 Lincoln Avenue, Evansville, IN 47722, United States

JOURNAL OF MECHANICS OF MATERIALS AND STRUCTURES
Vol. 15, No. 3, 2020
https://doi.org/10.2140/jomms.2020.15.379

FACTORS THAT INFLUENCE THE LATERAL CONTACT FORCES IN BUCKLING-RESTRAINED BRACES: ANALYTICAL ESTIMATES

FRANCESCO GENNA

Dedicated to the memory of Laura Da Lisca

An analytical technique for the calculation of the lateral contact forces in buckling-restrained braces (BRBs), proposed by Dehghani and Tremblay (2017), is critically revised and improved. The resulting algorithm is implemented and adopted with the only aim of highlighting what factors are important in the calculation of the lateral thrust in BRBs. Many of these factors seem to have a marginal importance in comparison with the buckled shape of the core, the core steel constitutive law, and the stiffness of the retention profiles. Possible conclusions deriving from this analysis are (i) only the calculation of analytical upper and lower limits for the lateral thrust in BRBs may have a sense, but these limits are always much distant from each other, and (ii) it is worthless trying to adopt over-detailed calculation techniques for this important quantity.

1. Introduction

Buckling-restrained braces (BRBs), designed to dissipate energy also in compression through the limitation of the elastic-plastic buckling amplitude of a steel core, are increasingly adopted in engineering practice. Their design is based on commonly accepted procedures, aimed at preventing their global buckling, failures due to plastic collapse/fatigue, and failures of the end connection (or other) details. There is not space here for a review of this topic and of the abundant literature concerning it. Useful information could be obtained, for example, from [Takeuchi and Wada 2017].

In spite of this situation, a main engineering quantity, in BRBs, still seems to remain very difficult to be accurately calculated. This quantity is the lateral contact force, or thrust, generated by the buckled core when reaching contact against the external retention profiles. These forces, at each contact point, have both a normal and a tangential component. The retention profiles should be designed on the basis of the values of these contact forces. If the normal contact forces become too high, there is the risk, for example in the case of bolted all-steel BRBs, of an explosive failure of the bolts.

Yet the determination of the lateral contact forces in any BRB is very problematic, which makes problematic also the correct design of the retention profiles. Strangely, there seems to be very little published work on the experimental side of this specific aspect. Almost the totality of the attention has been devoted to the BRB hysteretic (axial) behavior only. Besides the references quoted in the sequel of this work, to this author's knowledge only [Dehghani and Tremblay 2018] provides some information of the experimental type about the lateral thrust in BRBs; [Dehghani and Tremblay 2017; Jiang et al. 2015] also devote some attention to this aspect, but through numerical analyses only.

Keywords: buckling-restrained braces, contact forces, analytical methods.

In this work the term "total lateral thrust", denoted by the symbol Q_{TOT}, indicates the sum of all the contact normal forces at one side of the BRB core. The value of Q_{TOT} depends on many factors, some of which are difficult to properly take into account. The main one is the shape and the number of the core buckled waves. It was shown in [Genna and Bregoli 2014] that, given a value of the axial shortening of the BRB core beyond its first buckling limit, both the number of buckled waves and the wave shape are not uniquely defined, but that several buckled configurations exist, all equally possible. Finite element (FEM) analyses [Genna 2019] have shown that the computed value of the total lateral thrust is extremely sensitive to any modeling detail. Different FEM models may produce, for the same BRB problem, values of Q_{TOT} differing from each other by a factor of almost 3. In [Genna 2020], it was shown experimentally that the measured values of Q_{TOT}, in 11 nominally identical BRB samples, varied in a range one order of magnitude wider than the range of the experimentally measured axial forces. The minimum value measured of Q_{TOT} was one half of the maximum one.

Even having full control over all the other important factors — which is not the case anyway — the multiplicity of possible buckled configurations alone makes it impossible to predict with an acceptable engineering accuracy the value of the total lateral thrust in BRBs. The configuration "chosen" by a buckled BRB core, especially after a sequence of tensile-compressive loading cycles, depends essentially on the existing imperfections. No engineer has enough control over the imperfections to enable a sensible choice between multiple solutions associated with quite different values of structural forces.

This complication appears to be inherent in any BRB design type. In fact, every BRB, by its very nature, comprises a yielding segment which undergoes a multiwave plastic buckling under shortening. This phenomenon is the essence of any BRB properly functioning; there is no way to avoid it, or stay clear from it, as happens for example when dealing with ordinary compressed structural elements. In these, it is normal practice to stay well below the theoretical buckling limit so as to reduce to a minimum the sensitivity of the response to the imperfections. But in an element designed to work exploiting buckling this sensitivity always exists, and dominates the response, at least in some of its aspects. The axial force in BRBs, for example, is not sensitive to the imperfections, precisely because the buckled amplitude is limited; but the lateral thrust Q_{TOT} definitely is, as clearly shown in [Genna 2019; 2020].

Workarounds to this unfortunate situation seem to be of two types. A first one is to resort to extensive preliminary experimental verifications of each new BRB design, so as to have significant statistics, covering a large enough variety of imperfections, providing an engineering sufficient guarantee of the structural safety. This obviously is a very expensive procedure, and not ordinary engineering practice.

Another possibility could be to compute a theoretical range of values for the total lateral thrust, and selecting some value high enough to allow a safe design procedure. To this purpose, analytical tools could be adopted.

Several attempts have been made to produce analytical techniques for the calculation of the lateral thrust in BRBs. Many of these techniques, however, appear to be based on wrong assumptions, among which the main one is of adopting Euler's relationship between the compressive axial load and the buckled wavelength. It was proved first in [Genna and Gelfi 2012], and later in [Genna and Bregoli 2014], that, owing to the existence of contact, this is not the case, by a large amount.

One of the most refined analytical techniques is proposed in [Dehghani and Tremblay 2017], where many aspects of the problem are taken into account. This technique appears correct in its main essence, but seems to give even too much attention to details which may be of little or no importance with respect

to the tremendous uncertainty introduced by the selection of the shape and number of buckled waves. In the present work the technique of Dehghani and Tremblay [2017] is taken as a starting point. An attempt is made at improving some aspects and possibly rectifying some imprecisions. Several engineering and modeling factors are taken explicitly into account, and can be controlled.

This analytical tool is adopted here with the only aim of understanding which are the important factors for the calculation of the total lateral thrust, and which are inessential. No comparison with "real" results, either experimental or FEM, is made. If interested, the reader may find some experimental and/or numerical results, to be compared with the analytical ones of Section 4 later on, in [Bregoli et al. 2016; Genna 2019; Metelli et al. 2016; Dehghani and Tremblay 2018; 2017].

The results illustrated here may help in allowing one to eventually produce the simplest possible analytical tool yet able to provide an acceptable range of values (a single "exact" one does not exist, as explained here above) for the lateral thrust in a given BRB. It will remain a (difficult anyway) decision of engineers how to select, in the computed range, the most appropriate lateral thrust value, to be adopted for the correct design of the retention profiles.

2. Considered BRB model and general assumptions

Reference is made to the BRB model shown in Figure 1. The top image shows a dissipative core, of length L, with a rectangular cross-section of height t and width b, placed between two restraining profiles whose global elastic stiffness, including possible connection elements such as bolts, is denoted by K_{TOT} (dimension of force/displacement) at each side of the core. At the top and the bottom of the core a free gap exists of width equal to $g/2$. It is assumed, with no loss of generality, that the core is connected to the restraining profiles at the center point, where therefore no relative slip can occur. This point is indicated as *FP* (fixed point). The core is assumed to be made of an elastic-plastic hardening material, and the restraining profiles are assumed to behave elastically.

The image below shows a sketch of the BRB buckled configuration under an adequate axial shortening, associated to horizontal compressive forces H_{END} at the core ends. From here on, reference will be made to horizontal and vertical force components always assuming that the axis of the undeformed core is horizontal. At each contact point, between core and restraining profiles, both normal and tangential forces develop. The tangential forces, due to friction, cause a jump in the horizontal internal force at each contact point, thus causing several jumps of the horizontal forces in each half-wave. This, in turn, produces an increase in the normal contact forces moving away from the *FP*; this is the reason for the sketched increase of the retention profiles opening in the central image of Figure 1.

It has to be remarked that the reality might be different, in dependence on the local stiffness details of the restraining profiles (for example, connection bolts). These can cause smaller openings at the core ends rather than at its mid-zone. In the present work, however, no local stiffness detail of the restraining profiles will be taken into consideration.

In the configuration shown in Figure 1, the relative slip between core and retention profiles occurs from the ends of the core towards the *FP*; therefore, all the tangential contact forces are directed to the left in the left part of the core, and to the right in the right part.

The bottom images in Figure 1 depict a single buckled wave and illustrate the adopted mechanical scheme. In this, at each contact zone the local stiffness provided by the retention profiles is approximated

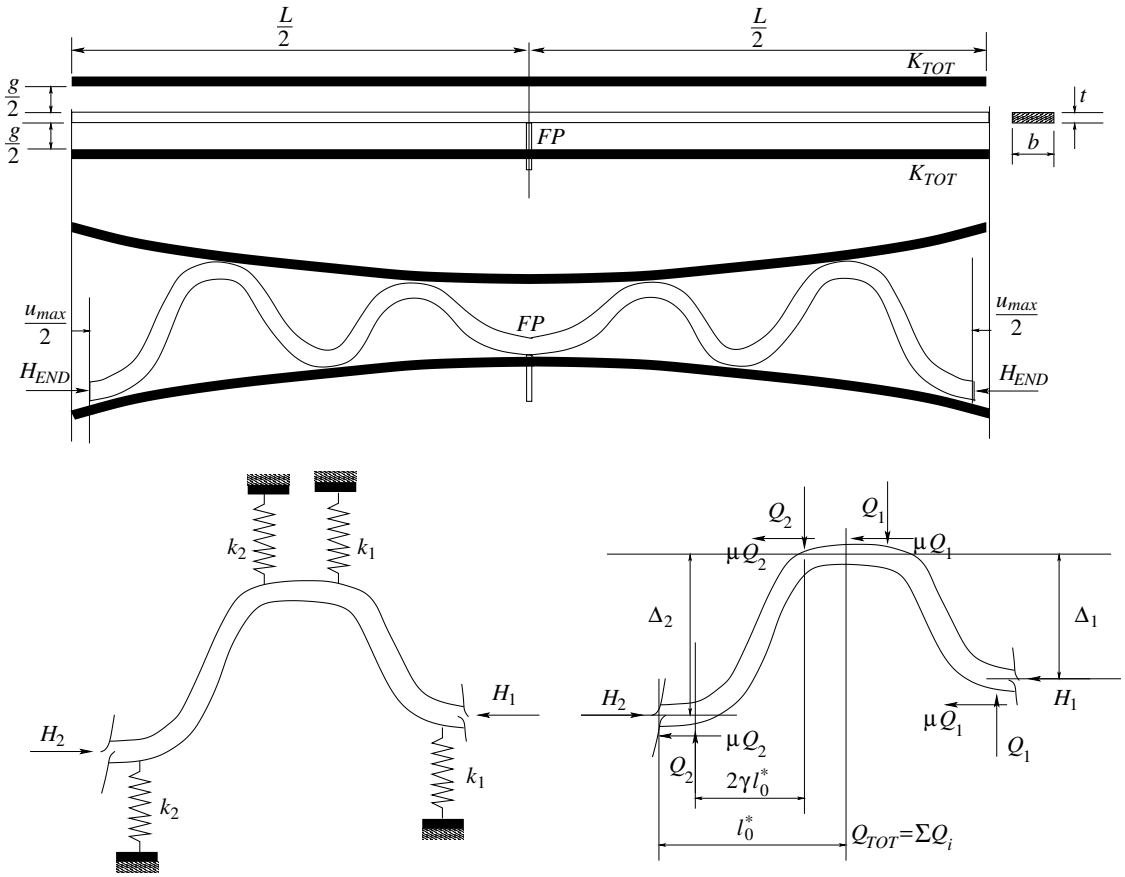

Figure 1. Top: BRB scheme. Center: BRB buckled shape under axial shortening. Bottom: detail of a core buckled wave, taken from the left side of the BRB, where the relative slip between core and restraining profiles occurs towards the left.

by two linear elastic springs. The core buckled half-wave length is denoted by l_0 with reference to the undeformed configuration, and by l_0^* on the deformed configuration (more details about this later on). The symbol γ, in the right bottom image, defines the central portion of a buckled half-wave which joins two contact points at the opposite sides of the core, so that the length of this portion, denoted by l_B, is equal to

$$l_B = 2\gamma l_0. \tag{1}$$

The other symbols adopted in the right bottom image refer to the horizontal internal forces H_i, existing in the various portions of the core, and to the contact forces. The normal contact forces at each contact point are denoted by Q_i. A Coulomb friction model is assumed, governed by a friction coefficient μ, which provides a maximum possible value, for the tangential forces, equal to μQ_i at each contact point. The total lateral thrust Q_{TOT} is the sum of all the normal contact forces Q_i at one side of the core:

$$Q_{TOT} = \sum_{i=1}^{C} Q_i \tag{2}$$

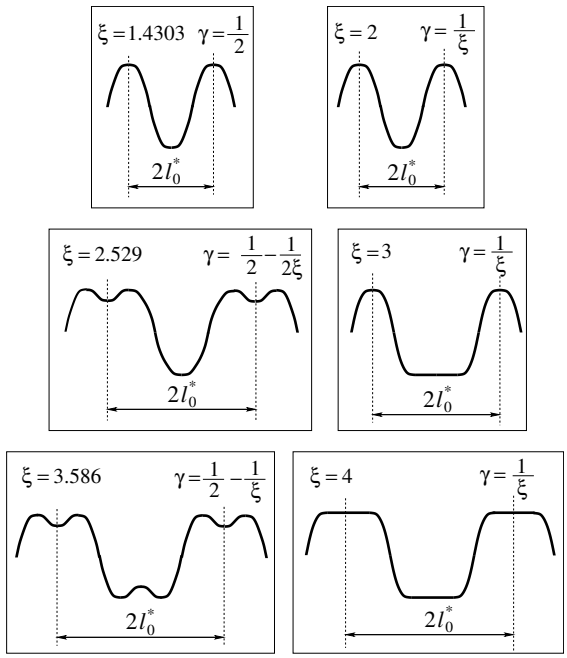

Figure 2. Possible buckled shapes of BRB cores, according to [Genna and Bregoli 2014]. The indicated values of parameters ξ and γ are valid only for sufficiently stiff restraining profiles.

where C denotes the total number of contact points at each side of the core. This is the main quantity of interest in the present work.

The main difficulty, in this problem, is the determination of the buckled half-wave length l_0 associated to a given value of the horizontal load in the core. This issue was first tackled in [Genna and Bregoli 2014], where a much simplified situation was studied, but it was nevertheless found that at least 6 possible buckled configurations can exist under the same horizontal load. For each of these configurations a specific corresponding value of the horizontal force could be obtained. A convenient way for expressing this relationship is the following one, for the moment ((11) will be adopted later on for the elastic-plastic case) associated to a purely elastic buckling of the BRB core:

$$l_0 = \xi \pi \sqrt{\frac{EI}{H}} \tag{3}$$

where E is the Young modulus of the material, I is the weak-axis moment of inertia of the core cross-section (here $I = bt^3/12$), H is the horizontal internal force associated to the buckled half-wavelength, and ξ is a parameter that depends on the shape of the buckled wave. Equation (3), for $\xi = 1$, provides the familiar Euler buckling load. Owing to the existence of the restraining profiles, for this problem the value of ξ can take values much higher than $\xi = 1$. To each possible value of ξ, a unique value of γ of (1) is associated.

Figure 2 illustrates the 6 possible buckled configurations, for one buckled wave, individuated in [Genna and Bregoli 2014], together with the corresponding values for the parameters ξ and γ. In this figure, for

simplicity, it is assumed that two adjacent half-waves have the same length l_0^* in the deformed configuration. This happens only if the contact between core and restraining profiles is frictionless. The indicated numerical values for the parameter ξ are rigorously valid only for the limiting case of rigid restraining profiles. Nevertheless, the normal stiffness of the restraining profiles is high enough to allow the formation of these buckled configuration for the indicated values of ξ. The difference between the top two cases is associated to their development under an increasing core shortening: for $\xi = 1.4303$ a point contact remains, and for $\xi = 2$ a flat line contact starts developing.

From the theoretical viewpoint no situation, among the 6 illustrated in Figure 2, is to be preferred. This leaves open the choice of a wide range of values for ξ (even wider if the restrainers have an insufficient stiffness). Notice that, given a value of l_0, for $\xi = 2$ the corresponding horizontal force is 4 times larger than Euler's one, according to (3), and for $\xi = 4$ it is 16 times larger than Euler's load. Therefore, the definition of parameter ξ is a crucial point in this calculation.

In setting up the equations for computing the Q_i values, and their resultant Q_{TOT}, the following main assumptions will be made.

(a) The studied BRB model is supposed, for simplicity, to be subjected to tensile and compressive cycles of the same amplitude, defined by the peak value of the average strain ε_0:

$$\varepsilon_0 = \frac{u_{max}}{L}, \tag{4}$$

u denoting the horizontal displacement of the core ends, and u_{max} its peak value. A generalization to unsymmetric cycles is easy to consider.

(b) The bending moment at the contact points is always considered equal to zero. This allows one to greatly simplify the problem, and is in fact a crucial assumption, taken also in [Dehghani and Tremblay 2017], to obtain a technique which solves the problem one half-wave at a time. In reality, if a line contact develops the bending moment is rigorously equal to zero in all the contact zones; but if a point contact develops this may not be the case.

(c) The fixed point *FP*, assumed to be at the mid-point of the core as in Figure 1, is supposed to be in contact with one restraining profile, and the buckled configuration is assumed to be symmetric with respect to the *FP*. This assumption is somewhat limiting, since it is known, from both experiments and numerical simulations, that the buckled configuration, even considering it made by identical half-waves, can be associated to a rigid rotation of the core, so that the contact points, at the two core ends, can be at the opposite sides of the core, with an odd total number of half-waves [Bregoli et al. 2016].

(d) The adopted stress-strain equation for the steel core is the uniaxial one of Ramberg and Osgood [1943]:

$$\sigma = \frac{E\varepsilon}{1 + \alpha(|\sigma|/\sigma_0)^{n-1}} \tag{5}$$

where σ_0 is the yield stress, and α and n are material parameters.

(e) The local tangential contact forces due to the friction, at each contact point, will usually be considered equal to their maximum value, i.e., μQ_i if Q_i is the value of the local normal contact force at that point. This assumption is correct if a continuous slip occurs between core and restraining profiles after contact

is reached. Nevertheless, preliminary experimental results shown in [Genna 2020] indicate that this may not always be the case. A part of the results shown in Section 4 will explore the importance of this aspect.

(f) In order to adapt (3) to the elastic-plastic case, an approach similar to the one taken in [Bregoli et al. 2016], accounting also for later observations [Dehghani and Tremblay 2017; Genna 2020], is followed.

In the first place, to account for the assumed cyclic loading type, the value of the horizontal load in (3) is redefined following what was proposed in [Bregoli et al. 2016] but accounting for a nonlinear stress-strain constitutive law:

$$H_{cic} = \sigma_{cic} A, \quad \sigma_{cic} = \sigma(\varepsilon_{cic}), \quad \varepsilon_{cic} = \left(2\varepsilon - \frac{\sigma_0}{E}\right) \tag{6}$$

where ε indicates the actual value of the average core strain in the considered configuration and in the considered point. This replaces (9) of [Dehghani and Tremblay 2017].

Next, in (3) the Young modulus E should be replaced by a different modulus, that takes into account the reduced stiffness existing in the plastic range. In [Genna and Gelfi 2012], use of Shanley's theory was made, replacing the value of E with the value of a tangent modulus E_t. Dehghani and Tremblay [2017] have adopted an "effective modulus", intermediate between the elastic and the tangent one (their (1)). They proposed an empirical nonlinear model both for the stress-strain equation and for their "effective modulus". In the present work a third approach is followed, based on recent results to be found in [Genna 2020], both experimental and numerical. According to these results, for this BRB problem the formation of a new buckled wave occurs with plastic loading in the compressed portion of the core cross-section, and elastic unloading in the portion elongated due to the bending. This suggests the adoption of the reduced modulus E_R of the von Kármán theory of elastic-plastic buckling (see for example [Bažant and Cedolin 1991]). Accordingly, in the present work the adopted material modulus for the expression of the buckled half-wave length will be

$$E_R = \left[\frac{1}{2}\left(\frac{1}{\sqrt{E}} + \frac{1}{\sqrt{E_t}}\right)\right]^{-2} \tag{7}$$

valid for a rectangular cross-section [Bažant and Cedolin 1991], and where E_t is the local tangent modulus provided by (5) at a strain equal to ε_{cic} of (6), i.e.,

$$E_t = E\left[\alpha n\left(\frac{\sigma_{cic}}{\sigma_0}\right)^{n-1} + 1\right]^{-1}. \tag{8}$$

Finally, it may be of importance to replace the standard value of the moment of inertia I of (3) with one corrected to take into account the effect of both the elastic Poisson effect and the plastic incompressibility (here we introduce another difference with respect to [Dehghani and Tremblay 2017]). For a given average compressive axial strain ε, at some point along the core axis, these effects produce a transversal strain ε_t, here associated to widening of both the core sides, equal to

$$|\varepsilon_t| = \tfrac{1}{2}\varepsilon + \frac{\sigma}{E}\left(\nu - \tfrac{1}{2}\right), \tag{9}$$

ν being the elastic Poisson coefficient. As a consequence, the modified cross-section moment of inertia is given by

$$I^* = \tfrac{1}{12} b t^3 (1 + c_\nu |\varepsilon_t|)^4. \tag{10}$$

The coefficient c_v, to be set equal to 0 or 1, is inserted to enable the evaluation of the importance of this effect.

In conclusion, the expression adopted to relate the value of the horizontal force to the buckled half-wave length is

$$l_0 = \xi\pi\sqrt{\frac{E_R I^*}{H_{cic}}}. \tag{11}$$

(g) A constant value for the parameter ξ in (11), chosen among the 6 possible of Figure 2, is considered along all the buckled core, implying that all the buckled half-waves have the same shape. In reality this is not guaranteed to happen: waves of different shapes, along one BRB core, are often observed in both experimental and numerical results. This phenomenon is a further big complication, due to the sensitivity to imperfections, and very difficult, if not impossible, to be properly taken into account in a theory.

Moreover, and unlike what was done previously for example in [Bregoli et al. 2016], the value for ξ has been considered as a datum, one of the 6 values of Figure 2. In [Bregoli et al. 2016], the periodicity of the buckled shape was assumed for simplicity, and also only an integer number of equal half-waves was always considered, assuming that both the extreme points of the core were at contact with the restraining profiles. To account for this situation, in [Bregoli et al. 2016], the final value of ξ had to be adjusted, starting anyway from one of those indicated in Figure 2, so as to produce a value of l_0 associated to an integer number of half-waves. If ξ is considered as unknown, however, the adopted solution technique to compute Q_{TOT} would become much more complicated, requiring the solution of the problem for the full BRB core instead of solving one half-wave at a time. Therefore, and considering also that the value of l_0 in reality changes at each half-wave because of friction, it was decided here to keep the chosen value of ξ fixed for all the half-waves except the last (core ends) one, as explained in the next section.

(h) No account is taken of a possible strong-axis buckling of the core or of other out-of-plane effects. Strong-axis buckling may happen in reality (limited anyway by the restraining profiles, and with just one wave), but it does not seem to influence the main weak-axis behavior [Genna 2019].

(i) No account is taken of the important dependence of the lateral thrust on the number of loading cycles, even when they are of the same amplitude. As shown experimentally [Metelli et al. 2016], at each new cycle of the same amplitude, at least for the first cycles, the lateral thrust increases significantly, up to 100%, owing to a progressive "flattening" of the core portions in contact with the restraining profiles. Accounting for this phenomenon analytically seems for the moment out of the question. It must be noted that this phenomenon can be found numerically using a standard hardening model with no dependence on the cycle number. Therefore, the adoption of a stress-strain equation including a dependence on the cycle number, as done in [Dehghani and Tremblay 2017], is not crucial to obtain this effect. This is a further reason to choose the simple Ramberg–Osgood constitutive model of (5), which requires the definition of just 3 plastic material parameters.

Further specific details on the modeling technique are given in the next section.

3. Solution technique

The main purpose of the model described in the previous section is the calculation of the lateral thrust Q_{TOT} associated to a given set of data, including a prescribed end displacement maximum amplitude u_{max}. The

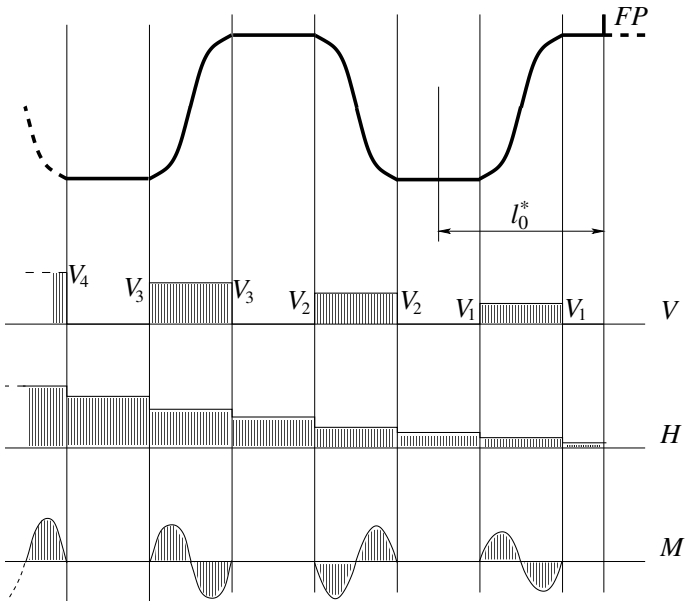

Figure 3. Considered buckled shape for the analytical developments (symmetric line contact). The diagram marked by a V shows the internal vertical force along the buckled core; the one marked by N shows the internal horizontal force along the core; the bottom one, marked by M, shows the bending moment along the core. In the frictionless case, the values of V remain constant, i.e., $V_1 = V_2 = V_3 =$, etc., and also the force H has no jumps along the core. Likewise, in the frictionless case the bending moment diagrams in the inclined portions of the core are the same for all the waves.

approach followed is based on the one described in [Dehghani and Tremblay 2017]. The calculation proceeds one half-wave at a time, accounting for the variation of both the internal forces and the associated half-wave lengths due to the friction. Beside what already illustrated in the previous section, however, other modifications have been introduced, as explained next.

3.1. ***Governing equations.*** Figure 3 sketches the considered geometry of the buckled core and the associated evolution of the internal forces. V is the vertical internal force, i.e., the shear force in the flat core portions. V is considered positive if it gives a positive contribution to the lateral thrust. H is the horizontal internal force, i.e., the axial force in the flat core portions, considered positive if compressive; and M is the bending moment. In the core portion of Figure 3, the motion occurs towards the right, and the contact tangential forces are all directed towards the left; this is the reason for the increase of the internal forces proceeding from the FP towards the left.

In Figure 3, as well as in all the analytical calculations, a symmetric line contact configuration has been assumed as the basic buckled configuration. This is convenient because it allows one to treat the local contact forces as split into two concentrated parts, located at the two extreme points of the flat contacting portions of the core. This is reflected in the assumed plot of the internal vertical forces V of the figure. In this way, unlike the case of single point contact configurations, the equilibrium equations for a single half-wave involve only quantities defined on that half-wave.

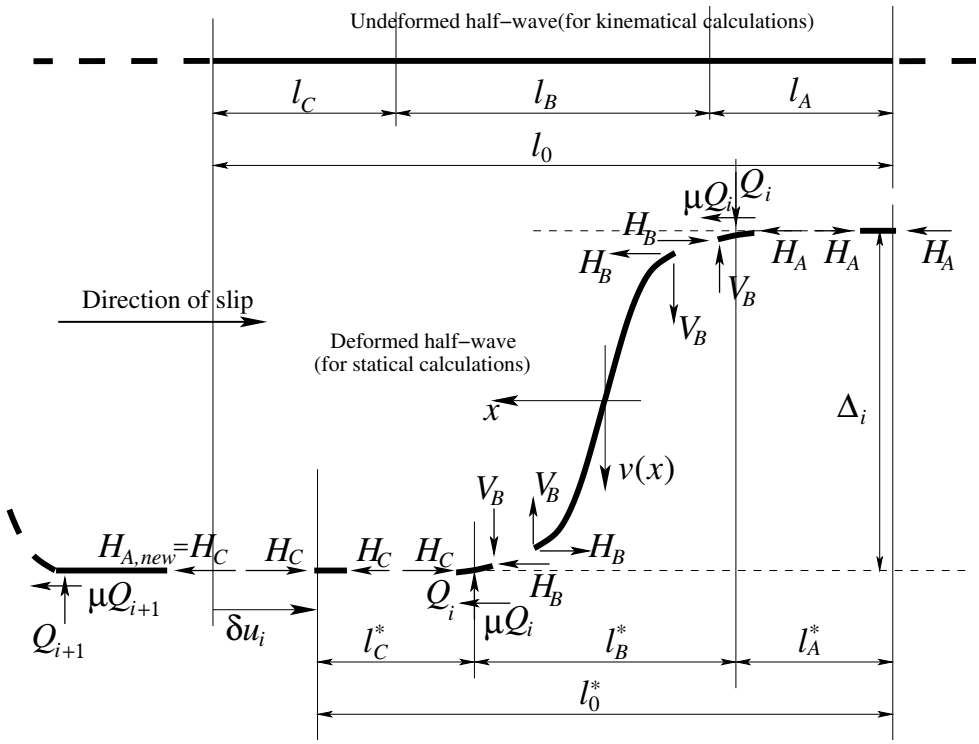

Figure 4. Undeformed (top) and deformed (bottom) shape of a generic half-wave of the buckled core. H denotes horizontal internal forces; V denotes internal vertical forces; Q denotes a local normal contact force. μ is the friction coefficient. All the other symbols are explained in the text.

Since the results of Section 4 will consider also values of ξ related to point contact configurations, for these cases it will be assumed that the single contact point configuration is the limiting case, with zero length, of a line contact configuration, so that the equilibrium equations, as described next, remain still valid.

Figure 4 shows all the forces — external and internal — considered on a single generic half-wave. The top image refers to the undeformed — horizontal — shape, where l_0, given by (11), is the half-wave length, and l_A, l_B, and l_C denote the three portions of the half-wave. l_B is the length of the central part, inclined in the deformed configuration, defined by the parameter γ as in (1).

The lengths of the 2 lateral flat portions are assumed, with no loss of accuracy even for the cases in which they are not, to be equal:

$$l_A = l_C = \tfrac{1}{2}(l_0 - l_B) = \frac{1-2\gamma}{2} l_0 \tag{12}$$

(see (1)). These quantities will be adopted for all the calculations involving the kinematics of this problem, which is treated in a second-order theory, i.e., as infinitesimal. Equilibrium is instead defined on the deformed configuration, shown in the bottom part of Figure 4.

The half-wave axis line has undergone a bending limited by the restraining springs. The vertical distance between the core axes at the top and the bottom points of the central part, denoted as Δ_i in Figure 4, can be expressed as

$$\Delta_i = g + c_{spr}\frac{2Q_i}{k_i} - c_\nu t \varepsilon_{tB}. \tag{13}$$

Here, g is the initial total gap between core and restraining profiles; the second addend derives from the elastic opening of the restraining profiles; the last term accounts for both the Poisson and the plastic incompressibility effects, as was done in (10). In this term, the lateral strain ε_{tB} is the one existing in the inclined portion of the core, given by (9). The local spring stiffness k_i is determined as

$$k_i = \frac{K_{TOT} l_0}{L} \tag{14}$$

(recall that two springs are introduced at each contact line, as in Figure 1, each of stiffness k_i). The coefficients c_{spr} and c_ν, in (13), enable the evaluation of the importance of the associated terms. If $c_{spr} = 0$ the restraining profiles are treated as rigid. If $c_\nu = 0$ the Poisson + plastic incompressibility effects are neglected.

The horizontal shortening δu_i of the considered half-wave is the sum of two terms, an axial one, associated to the average strains, and a bending one, denoted by u_B, as

$$\delta u_i = (\varepsilon_A l_A + \varepsilon_B l_B + \varepsilon_C l_C) + c_{ub} u_B, \tag{15}$$

in which a coefficient c_{ub} has been inserted to enable the evaluation of the importance of the bending contribution to the axial shortening.

In all the equations adopted in this work, compression and shortening are always considered positive.

The value for the contribution u_B, denoting by $v(x)$ the bending deflection function in the central portion of the half-wave (see Figure 4), can be evaluated, in a second-order theory, by the standard expression

$$u_B = \frac{1}{2}\int_{-\gamma l_0}^{\gamma l_0} v'^2(x)\, dx. \tag{16}$$

The function $v(x)$ can be approximated as

$$v(x) = \frac{\Delta_i}{2}\sin\frac{2\pi x}{4\gamma l_0}. \tag{17}$$

Inserting (17) into (16) one obtains

$$u_B = \frac{\pi^2 \Delta_i^2}{32\gamma l_0}, \tag{18}$$

different from (8) of [Dehghani and Tremblay 2017].

Equilibrium is governed by the following equations:

$$V_B = Q_i, \tag{19}$$

vertical translation of the top small portion of core subjected to the local contact forces;

$$H_B = H_A + \mu Q_i, \tag{20}$$

horizontal translation of the top small portion of core subjected to the local contact forces;

$$H_C = H_B + \mu Q_i = H_A + 2\mu Q_i, \tag{21}$$

horizontal translation of the bottom small portion of core subjected to the local contact forces; and

$$H_B \Delta_i = V_B l_B^* = Q_i l_B^*, \tag{22}$$

rotation of the inclined segment of core. In this equation use was made of the deformed length l_B^*, which can be obtained, on the basis of Figure 4, as

$$l_B^* = l_B - c_{l*}(l_B \varepsilon_B + u_B). \tag{23}$$

Once again, a coefficient c_{l*} was inserted to enable the evaluation of the importance of the difference between l_B and l_B^* in these calculations.

These equations are different from the simpler ones adopted in [Dehghani and Tremblay 2017]. There, in fact, the horizontal forces have been considered constant in the whole half-wave, ignoring the jumps due to the tangential frictional forces between the flat and the inclined portions of the half-wave.

Finally, the relationships between stresses and forces are

$$H_A = \sigma_A A_A^*, \quad H_B = \sigma_B A_B^*, \quad H_{B,cic} = \sigma_{B,cic} A_B^*, \quad H_C = \sigma_C A_C^*. \tag{24}$$

Here, the starred quantities, for the cross-section areas A_n, account for the core lateral expansion due to the combined Poisson and plastic incompressibility effects, and are computed as

$$A_n^* = A_n(1 + c_\nu |\varepsilon_{n,t}|)^2 \tag{25}$$

where the lateral strains $\varepsilon_{n,t}$ are defined as in (9), and where the coefficient c_ν has the same purpose as in (10) and (13).

In these equations, all the stresses are related to the corresponding strains via (5).

3.2. ***Solution procedure for the case with $\mu > 0$.*** The above equations are used to compute all the Q_i values, half-wave by half-wave, and to obtain the total lateral thrust Q_{TOT} through (2). As done in [Dehghani and Tremblay 2017], the local contact forces Q_i are computed one half-wave at a time, starting from the first one, at the fixed point *FP*. Owing to the assumed symmetry of the problem with respect to the *FP*, only one half of the core is considered, for example the left one, of length $L/2$. The results computed for this left half will be multiplied by 2 to obtain the lateral thrust Q_{TOT} for the full BRB.

The loading, for the problem, is the average global strain ε_0 of (4). A fixed value for the coefficient ξ, among those shown in Figure 2, must be selected.

First half-wave. For the first half-wave, the input term is the average strain ε_A in the top flat portion of Figure 4, uniquely related in a yet unknown way to ε_0. This is given a tentative value $\varepsilon_{1,A}$, and an external iterative loop will be employed to calculate its correct value. In the calculations presented here, this initial value has always been $\varepsilon_{1,A} = \varepsilon_0/2$.

Given a numerical value for $\varepsilon_{1,A}$, the equations presented above allow one to compute all the unknowns in terms of the stress σ_B only. The constitutive law (5) gives the stress σ_A. A tentative value for σ_B is then chosen, and a Newton–Raphson procedure will iterate on it, at each half-wave, to compute its correct value.

Given a tentative value for σ_B, the associated average strain ε_B is given by the inverse of (5). Next, (6) gives $\varepsilon_{B,cic}$, from which, using (6), (7), (10), and (11), one determines the value of $l_{0,1}$ for this half-wave. Equation (20) gives Q_i:

$$Q_i = \frac{\sigma_B A_B^* - \sigma_A A_A^*}{\mu} \tag{26}$$

which holds only if $\mu > 0$. The frictionless case, much easier, will be summarized in the next subsection.

Equation (21) allows one to compute numerically, via the Newton–Raphson technique, the values of both σ_C and ε_C. Next, the values of Δ_i (13), l_B^* (23), and u_B (18) can all be determined from the quantities already computed.

At this point, only the rotation equilibrium equation (22) remains to be satisfied, in the unknown value of σ_B. As said, a Newton–Raphson iterative procedure is adopted to compute the correct value of σ_B. In this procedure, the derivative of (22) with respect to σ_B has to be computed numerically.

Once convergence is reached for σ_B, the values of all the other quantities are also determined, and one can compute the shortening δu_1 of the first half-wave from (15). The length of the first half-wave is obviously $l_{0,1}$.

Generic half-wave. If $l_{0,1}$ is smaller than $L/2$ (otherwise the problem is ill-posed), the next half-wave is taken into account. The following calculations are repeated as many times as necessary, as explained later on.

The input is now the stress σ_A, equal, for equilibrium, to the stress σ_C of the previous half-wave. This is easy to understand, if one considers the next half-wave as the specular, horizontally to the left, of the previous one as shown in Figure 4 (and so on for the subsequent half-waves).

The governing equations are then exploited as before, adopting a new tentative value for σ_B and then iterating on it to satisfy (22), to obtain its correct value. At the end of the calculation, a test on the total length of the solved half-waves must be performed. Call this length L_{comp}, with

$$L_{comp} = \sum_k l_{0,k}, \tag{27}$$

k running from 1 to the number of the current half-wave. If $L_{comp} \le L/2$ then the current half-wave is a "normal" half-wave. Otherwise this half-wave can not be of the computed length l_0, but must be shorter: therefore this is the last half-wave, to be treated in a different way.

If the current half-wave is not the last one, at this point the accumulated horizontal displacement over all the solved half-waves is computed, by adding the contribution of the current half-wave. One moves then on to the next generic half-wave.

If $L_{comp} > L/2$, one ignores the calculations done for this half-wave and goes to the last half-wave.

Last half-wave. We now denote by $l_{0,theor}$ the last half-wave length computed in the previous step, a length which, added to all the previous ones, exceeds the total core length available. The actual length of the last half-wave, according to the check illustrated here above, can be anything from infinitesimal to infinitesimally smaller than $l_{0,theor}$. There is no clear rule to treat this case, and a somewhat arbitrary procedure was followed. We observe that nothing is said, about this point, in [Dehghani and Tremblay 2017].

In the first place, the length of the last half-wave is known from (27), and given by

$$l_{0,last} = L_{comp} - \frac{L}{2} \tag{28}$$

(recall that here $L_{comp} > L/2$). It is then assumed that two possible situations may exist.

If $l_{0,last}$ is smaller than the sum of l_A and l_B associated to $l_{0,theor}$, i.e.,

$$l_{0,last} < \left(\tfrac{1}{2} + \gamma\right) l_{0,theor}, \tag{29}$$

one considers the last wave as a "short" one, flat, with no further contribution to the total thrust Q_{TOT}. Only the total length is updated, and the total shortening, by adding a final value for δu_i which ignores the bending contribution.

If, on the contrary,

$$l_{0,last} \geq \left(\tfrac{1}{2} + \gamma\right) l_{0,theor}, \tag{30}$$

then this wave is treated as a "long" one, with contact points at both the upper and the lower sides of the core, and with known half-wave length (28). The new associated value of ξ is computed from (11) used in an inverse way. This half-wave gives therefore a full contribution to the total thrust, that can now be computed as for any other intermediate wave.

At the end of the solution of this last half-wave, by construction the total accumulated length is equal to $L/2$, and the total horizontal displacement δu is computed by adding the contribution of the last half-wave.

External loop over $\varepsilon_{1,A}$. Recall now that all this procedure starts from a tentative value for the strain $\varepsilon_{1,A}$ in the very first segment of the core, at the *FP*. In general, therefore, even though all the equilibrium equations are satisfied, the computed value of δu will be different from the given value $u_{max}/2$ (recall that the presented calculation holds for one half of the core), associated to the given average strain ε_0. An external iterative loop is therefore implemented which, after each set of calculations, updates the tentative value for $\varepsilon_{1,A}$ in the first half-wave by means of the equation

$$\varepsilon_{1,A}^{new} = \varepsilon_{1,A}^{old} \frac{u_{max}}{2\delta u}. \tag{31}$$

One then restarts from the first half-wave, and proceeds until convergence on ε_A of the first wave is reached, so as to have the correct shortening value at the ends of the core. Unfortunately, there is no guarantee to always obtain this convergence for all the possible choices of ξ. In some cases, especially for the smaller values ($\xi = 1.4303$ and $\xi = 2$), no solution to the problem could be found. It is not easy to tell if this happens because these values for ξ are physically meaningless, for the given set of data, or because the implemented method introduces unrealistic contributions for some values of ξ.

Attention should be paid, in the said calculations, to all the cases in which $\gamma = 0.5$, because these cases, as obvious from Figure 4, correspond to the absence of the flat segments A and C in all the buckled half-waves. The necessary changes in all the equations, however, are trivial.

3.3. ***Solution procedure for the case with*** $\boldsymbol{\mu = 0}$**.** In the frictionless case (26) is no longer valid, obviously. On the other hand, since the average stress and strain are constant all along the BRB core, the situation is much simpler, because now all the half-waves are equal, and have the same value of Q_i,

except the last one. Therefore, given a tentative value for $\varepsilon_{1,A}$ in the first core segment at the *FP*, the only unknown to be computed is the normal contact force Q_i, and (22) is adopted for this calculation. Once again, a Newton–Raphson loop is implemented for solving (22) given a tentative value for Q_i. Once a converged value of Q_i is computed, the corresponding value of l_0 allows one to determine the number of "standard" half-waves (with length l_0) associated to it. From this, one obtains the length of the last half-wave (shorter than l_0), the sum of the normal contact forces, and the accumulated shortening. The last half-wave is treated as in the case with friction, only computing, if necessary, the last contact force Q_i instead of σ_B from (22).

When all the half-waves have been solved, the same iterative procedure on $\varepsilon_{1,A}$ is adopted to obtain convergence also on the given shortening value u_{max}.

4. Total lateral thrust: computed results

The technique illustrated in the previous section was implemented in a Fortran code which requires a fraction of a second to run for a single BRB problem. Reference is first made to the following set of data parameters, which describe one of the reduced-scale, all-steel, bolted BRBs studied in [Metelli et al. 2016]:

- $L = 560\,\text{mm}$, $\varepsilon_0 = 0.02$, $u_{max} = 11.2\,\text{mm}$;
- $b = 50\,\text{mm}$, $t = 5\,\text{mm}$;
- $g = 1\,\text{mm}$;
- $K_{TOT} = 416372\,\text{N/mm}$;
- $E = 150000\,\text{MPa}$, $\nu = 0.33$, $\sigma_0 = 230\,\text{MPa}$, $n = 13$, $\alpha = 0.01$;
- $\mu = 0.15$.

This BRB is expected to furnish a severe test to the adopted algorithm, because of the high gap to section height ratio, close to the limit of its possible practical applicability. This high ratio is associated to a "large" buckled amplitude and to other possible difficulties, both theoretical and practical, as suggested, for example, in [Takeuchi and Wada 2017]. At the same time, however, this BRB is expected to provide a clearer evidence of the difficulties that accompany the calculation of the total lateral thrust Q_{TOT}.

Note that, in this work, no attention is given to the issue of producing engineering interesting results for any BRB type. The only aim is to highlight the really important factors which contribute to the determination of the total lateral thrust.

The first result, shown in Figure 5, is the dependence of Q_{TOT} on the choice of the wavelength parameter ξ, setting equal to 1 all the c_i coefficients of the previous sections. This dependence appears to be the most important among all the considered factors. If one changes the value of ξ, in fact, the computed value of Q_{TOT} can change by a factor of about 2, and the total number of buckled waves (for the full core) N is predicted in a range between $N = 6$ and $N = 10$.

Figure 6 summarizes the importance of the other factors on the computed value of Q_{TOT}. This figure, as well as all the following ones except when explicitly indicated, shows results all obtained with $\xi = 3$, as suggested in previous work [Bregoli et al. 2016].

In Figure 6, the vertical axis shows the value of Q_{TOT} normalized with respect to the "best" one, which considers all the contributions to the adopted equations (leftmost bar, marked by "All", and central bar

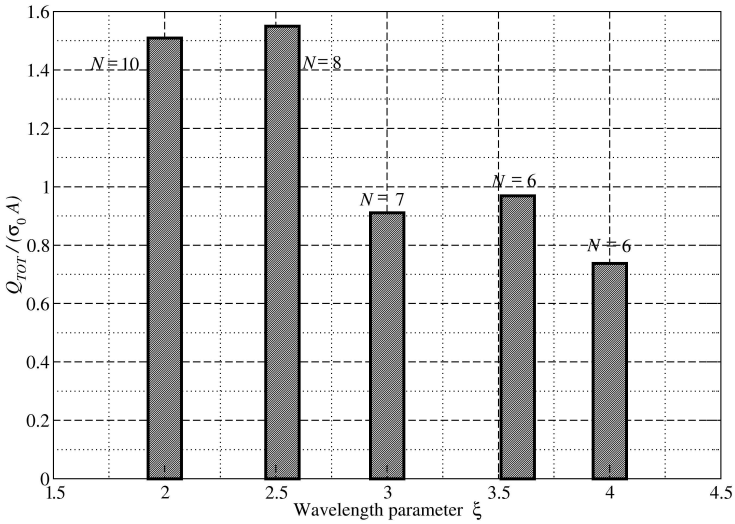

Figure 5. Reduced-scale BRB example. Variation of the total lateral thrust Q_{TOT} with the choice of parameter ξ of (11). N denotes the predicted total number of buckled waves in the BRB. The result for $\xi = 1.4303$ is missing because of lack of convergence.

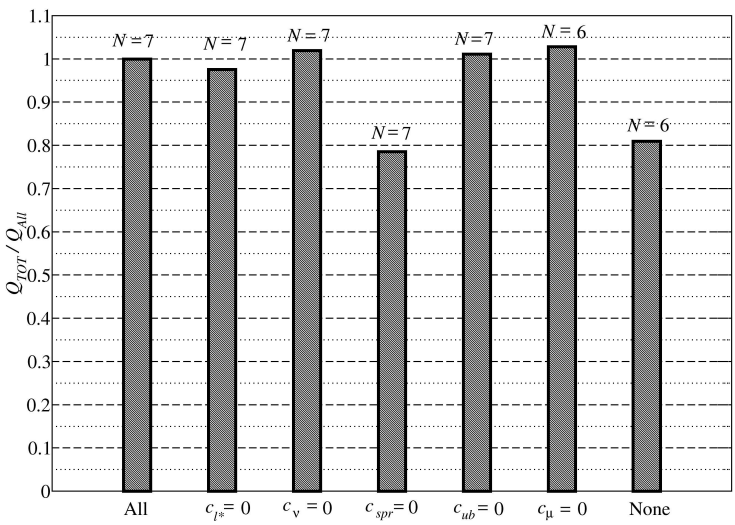

Figure 6. Reduced-scale BRB. Variation of Q_{TOT} associated to different adopted assumptions. Results computed adopting $\xi = 3$. Symbols as explained in the text.

in Figure 5). The second bar, with the $c_{l*} = 0$ label, refers to calculations done neglecting the effect of writing (22) on the deformed configuration for the horizontal length (see (23)). The third bar shows the result which ignores the Poisson and plastic incompressibility effects, i.e., sets $c_\nu = 0$ in (10), (13), and (25). The fourth bar refers to the case of a rigid containment, i.e., $c_{spr} = 0$ in (13). The fifth bar refers to the case in which the bending contribution to the horizontal shortening is neglected in the calculations, by setting $c_{ub} = 0$ in (15) and (23).

The last two bars refer to the frictionless case: the one marked by $c_\mu = 0$ ignores only the friction, keeping in all the other contributions; the last one, marked by "None", sets all the c_i parameters and μ equal to zero.

Now the differences among the computed values of Q_{TOT} appear less important than in the previous figure. Only the assumption of a rigid containment causes a drop of about 20% in the value of Q_{TOT} (fourth and last bar); otherwise the differences are minimal.

The next figures show in more detail the influence of several parameters on 6 output variables for this problem. The output variables are, from left to right and from top to bottom:

- the total thrust Q_{TOT} normalized with respect to the nominal first yield force $\sigma_0 A$;
- the horizontal force in the core at the *FP*, H_{FP}, also normalized with respect to the first yield force (this ratio depends essentially on the hardening properties of the material);
- the ratio between the horizontal force at the ends of the core, H_{END}, and the horizontal force at the *FP* (the higher this ratio the higher is the contribution of the frictional tangential contact forces);
- the ratio between the average strain at the *FP* and the given average strain ε_0 of (4);
- the ratio between the average strain at the ends of the core, ε_{END}, and the average strain at the *FP* (this is also related to the amount of frictional forces existing between core and restraining profiles);
- the ratio between the total bending contribution to the core shortening, $\sum u_B$, and the total shortening u_{max} itself.

Figure 7 shows the influence of the tangential frictional contact forces, which enter the calculations only in (20) and (21). Varying the value of the friction coefficient μ, as done in Figure 7, is the same as considering μ fixed at some value and examining the effect of introducing tangential contact forces smaller than their theoretical maximum, equal to μQ_i at each contact point. Tangential forces smaller than μQ_i may occur if no relative slip occurs between core and restraining profiles.

Figure 7 shows that, for this BRB, and for $\xi = 3$, the effect of increased frictional forces (top left image, solid line) is to reduce Q_{TOT}. In this case, the assumption of a maximum value for the tangential contact forces would be unsafe, even though the variation in Q_{TOT} is not very high. Nevertheless, this effect can be different. For example, selecting $\xi = 4$ in this calculation, an increasing curve for Q_{TOT} is produced (dashed line in the top left image). In this case, the assumption of the maximum value for the contact tangential forces would be to the safe side.

It is difficult to understand from the equations the general trend for this, since in (18) to (25) several terms contain the contact force Q_i, with conflicting effects. The global change in the value of Q_{TOT}, due to a change of the tangential frictional contact forces, however, is here at most of the order of 10%.

Note, however, that larger changes in the value of Q_{TOT} could be predicted if, upon a change of μ, a change would occur in the predicted number of buckled waves, N. With $\xi = 3$ or $\xi = 4$, the number N remains the same for all the considered values of μ ($N = 7$ for $\xi = 3$, and $N = 6$ for $\xi = 4$). But if one adopts $\xi = 2.529$, in this calculation, one obtains $N = 9$ for small values of μ, and $N = 8$ for large values of μ. The corresponding values of Q_{TOT}, much larger than with $\xi = 3$ or $\xi = 4$ because of the larger value of N, have then a maximum change, with μ, of about 35%. The bottom image of Figure 7, solid line, shown this case. Moreover, with $\xi = 2.529$, the trend for Q_{TOT} is first increasing and then decreasing, passing through a discontinuity (just suggested by the numerical results, which do not find

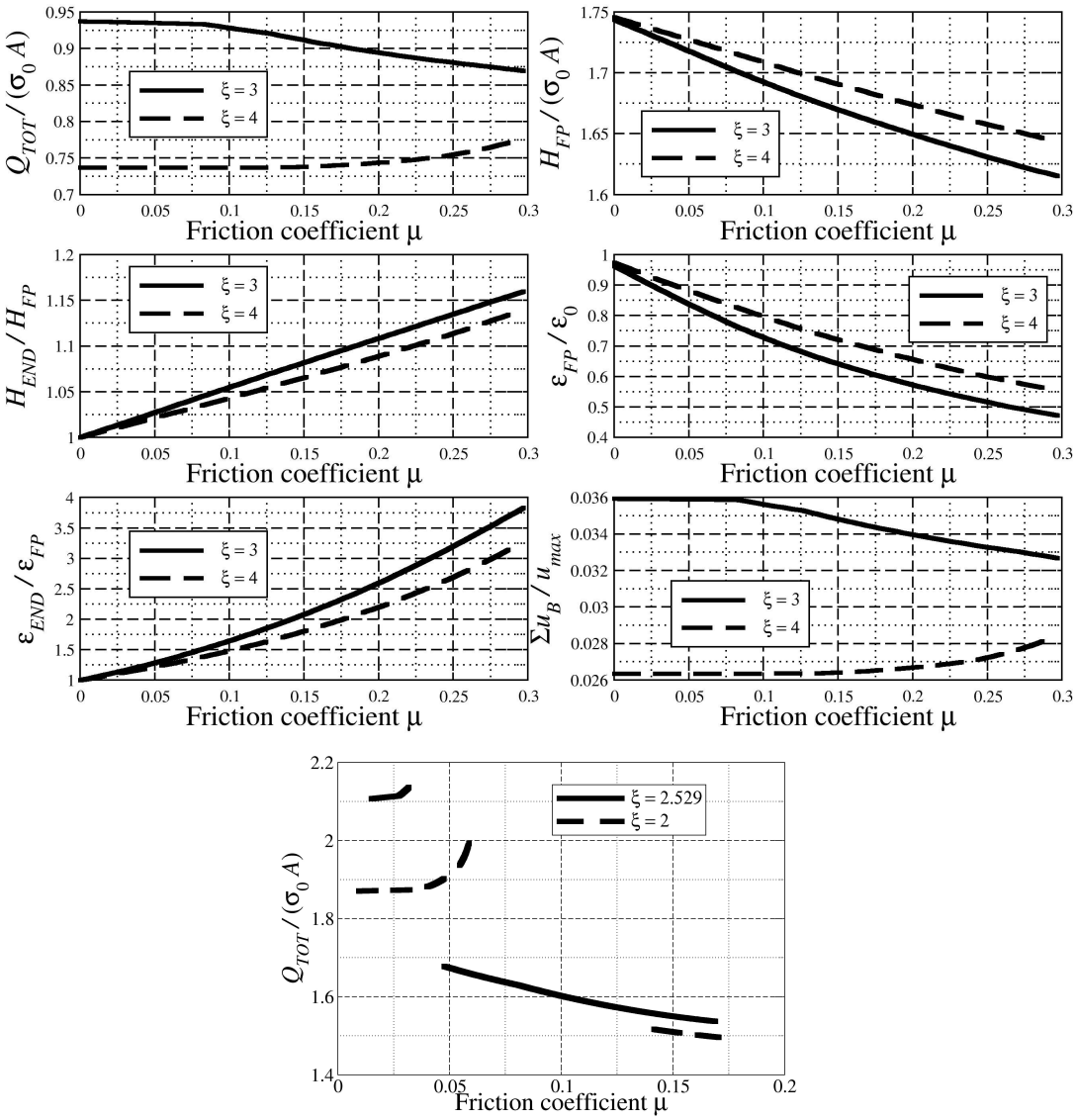

Figure 7. Reduced-scale BRB. Dependence of various mechanical quantities on the friction coefficient μ, with $\xi = 3$ (solid lines) and $\xi = 4$ (dashed lines). The bottom image plots Q_{TOT} computed adopting $\xi = 2.529$ (solid lines) and $\xi = 2$ (dashed lines). Other symbols are explained in the text.

convergence around the discontinuity zone) when N changes. The dashed line in the bottom image of Figure 7 refers to the case with $\xi = 2$, which, despite a large range of values of μ with no convergence, shows more clearly the tendency of Q_{TOT} to jump across some value of μ.

From this image already (but later images will show this more clearly), it appears that the value of Q_{TOT} has a discontinuous dependence on some parameters. This is important to keep in mind, because it is a clear symptom of the difficulty in accurately predicting, by any method, the value of Q_{TOT}.

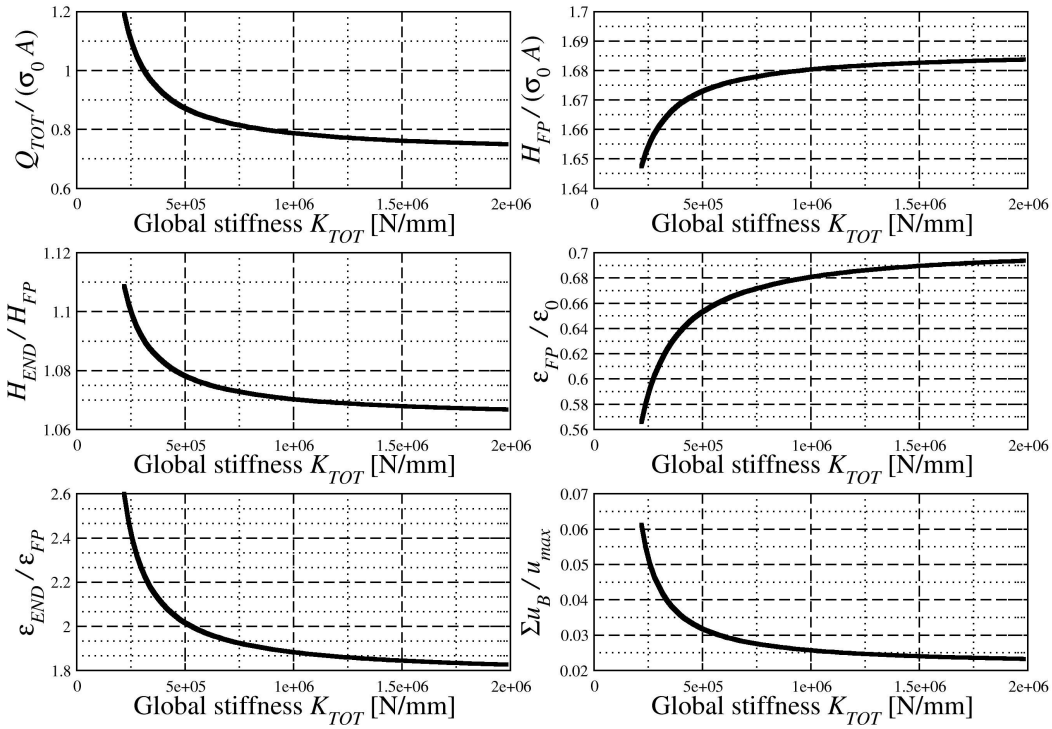

Figure 8. Reduced-scale BRB. Dependence of various mechanical quantities on the restrainer global elastic stiffness K_{TOT}. Results computed adopting $\xi = 3$. Other symbols as explained in the text.

The right bottom image in Figure 7 shows that the contribution obtained by accounting for the bending deflection u_B of (18) is negligible (order of few percents), although for $\xi = 3$ is larger than for $\xi = 4$, and with an opposite trend for increasing μ. This seems reasonable considering that $\xi = 4$ is associated to a shorter inclined portion of the buckled half-waves than $\xi = 3$.

The other images in Figure 7 indicate that some of the plotted variables are sensitive to the value of μ. Nevertheless, with the exception of H_{END}, whose value changes by about 15% in the considered range of values for μ, these variables have little engineering importance.

Figure 8 shows the effect of the global elastic stiffness K_{TOT} of the restraining profiles on the same output quantities. If K_{TOT} becomes small, all the plotted quantities tend to grow (positively or negatively) rapidly. In the frictionless, linear elastic case, Genna and Bregoli [2014] have shown analytically this jump of the total thrust, which can pass through vertical asymptotes (typical of linear elasticity only), for decreasing values of K_{TOT}. If K_{TOT} is too small, moreover, all the values for the ξ coefficients should be reconsidered, since they might be much higher than those adopted here, as shown in [Genna and Bregoli 2014].

Figure 9 refers to the value of the Young modulus E. This influences the reduced modulus E_R which governs the half-wave length through (11), and its effect, on Q_{TOT}, is not negligible at all, while all the other plots do not show anything new. Figure 10 illustrates the effect of varying the yield stress σ_0, a parameter of obvious importance. Once again, a change in σ_0 produces a significant change in Q_{TOT}.

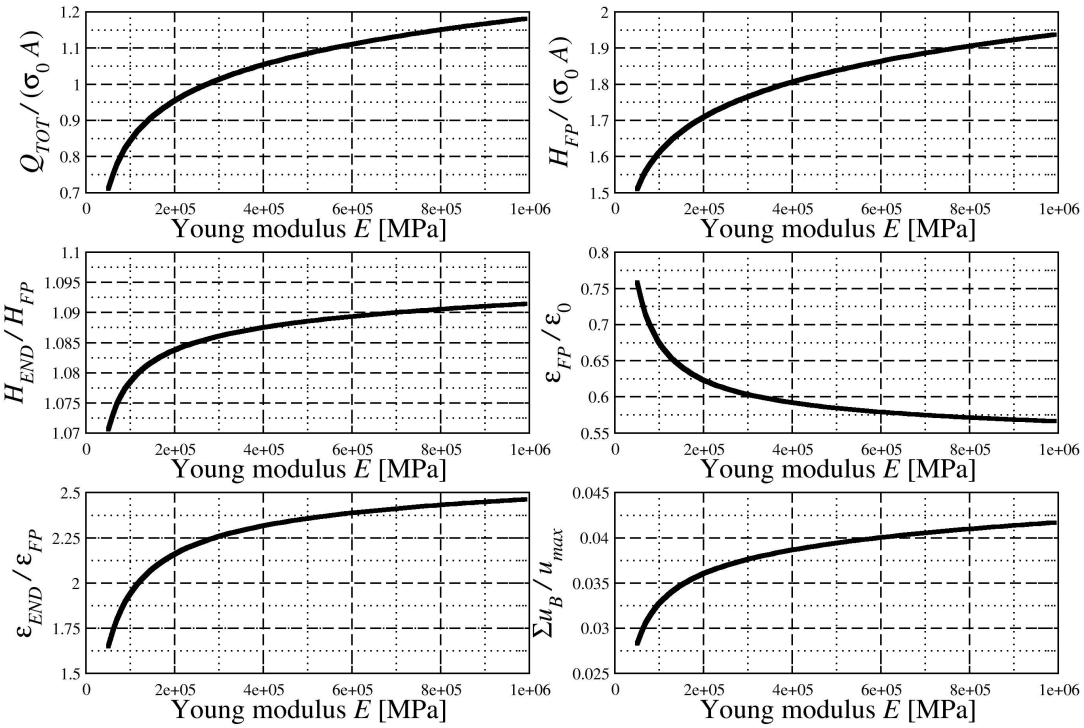

Figure 9. Reduced-scale BRB. Dependence of various mechanical quantities on the core Young modulus E. Results computed adopting $\xi = 3$. Other symbols as explained in the text.

Figure 11 refers to the exponent n of the Ramberg–Osgood equation adopted for the steel constitutive law (5). In this equation, $n = 1$ corresponds to a linear elastic material, and increasing values of n produce a nonlinear hardening that, for $n \to \infty$, tends to perfect plasticity at $\sigma = \sigma_0$. Changing the value of n produces a very large change in Q_{TOT}, with significant discontinuities. These are due to a change in the predicted number of buckled waves associated to the same final core shortening. In all the previous plots (Figures 7 to 10), for $\xi = 3$, the number N of buckled waves was always $N = 7$; here, N goes from $N = 4$ for small values of n to $N = 8$ for large values of n. Correspondingly, Q_{TOT} changes much.

An increase of the exponent n produces also very large values for ε_{END}, since the material stiffness tends then to vanish. Large values of n make the material approach perfect plasticity; this is confirmed also by $H_{FP} \to \sigma_0 A$ in the top right image. In any case, however, the $\sum u_B$ quantity remains negligible.

In general, it can be observed that the definition of the stress-strain law in its entirety plays a very important role in this calculation.

The next two figures are equivalent to Figures 5 and 6, but refer to a different BRB setup, taken from [Dehghani and Tremblay 2017]. Here the design parameters are the following:

- $L = 3000\,\text{mm}$, $\varepsilon_0 = 0.03$, $u_{max} = 90\,\text{mm}$;
- $b = 150\,\text{mm}$, $t = 19.05\,\text{mm}$;
- $g = 0.9\,\text{mm}$;

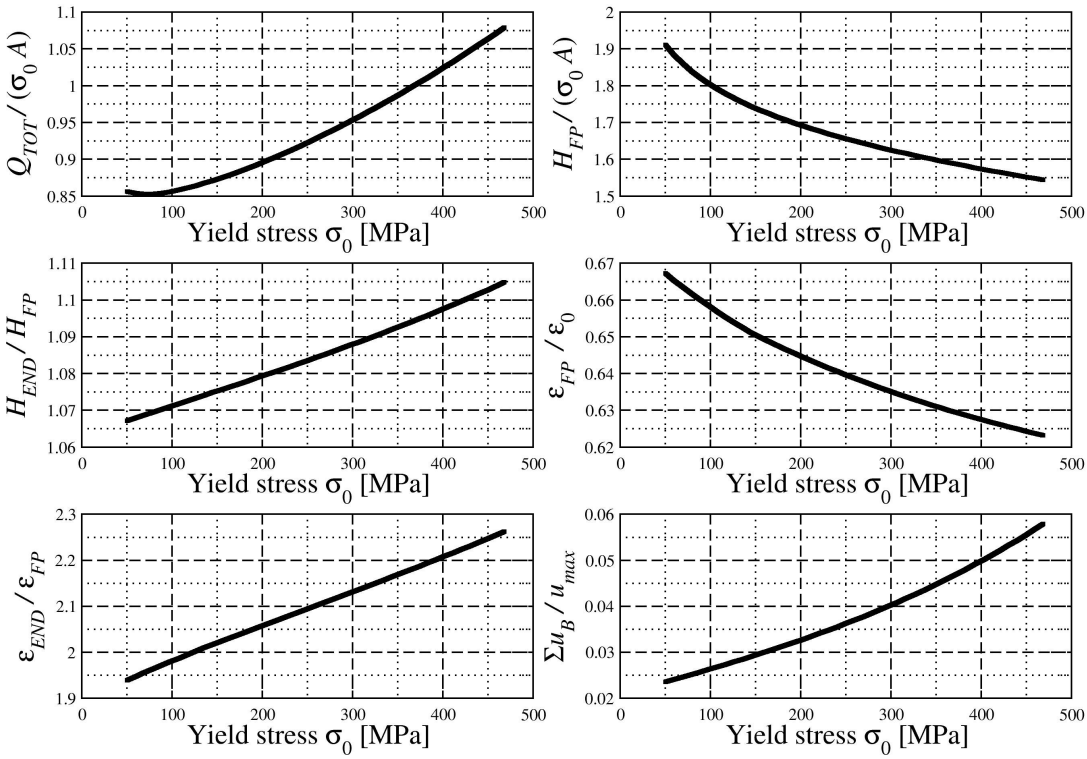

Figure 10. Reduced-scale BRB. Dependence of various mechanical quantities on the core first yield stress σ_0. Results computed adopting $\xi = 3$. Other symbols as explained in the text.

- $K_{TOT} = 2400000\,\mathrm{N/mm}$;
- $E = 150000\,\mathrm{MPa}$, $\nu = 0.33$, $\sigma_0 = 330\,\mathrm{MPa}$, $n = 13$, $\alpha = 0.01$;
- $\mu = 0.15$.

This is a full-scale, all-steel BRB, with a much longer dissipative core length L, a much bigger cross-section of the core, a much higher restrainer stiffness, but a smaller total gap g than the one considered in the first example. The smallness of this gap is expected to reduce much, in proportion, both the amplitude of the buckled bending deflections and the total lateral thrust. This choice may be closer to those adopted in engineering practice; it has a possible drawback in the possibility that the lateral expansion of the core, under compression, might cause the core itself to get stuck against the retention profiles. A check for this occurrence has been coded into the implemented software, but in all the examples tested, for "reasonable" values of ε_0, no such problem ever occurred.

Figure 12 shows the dependence of Q_{TOT} on the choice of ξ. As in Figure 5, this variation can be of the order of 100%, and the change of the wave number N is also very significant.

Figure 13 illustrates the dependence of Q_{TOT} on several other parameters, as described for Figure 6. Here the strong dependence on c_ν stands out, while all the other factors seem to follow the same tendency as for the reduced-scale BRB of Figure 6. If one sets $c_\nu = 0$ in the adopted equations, thus ignoring the

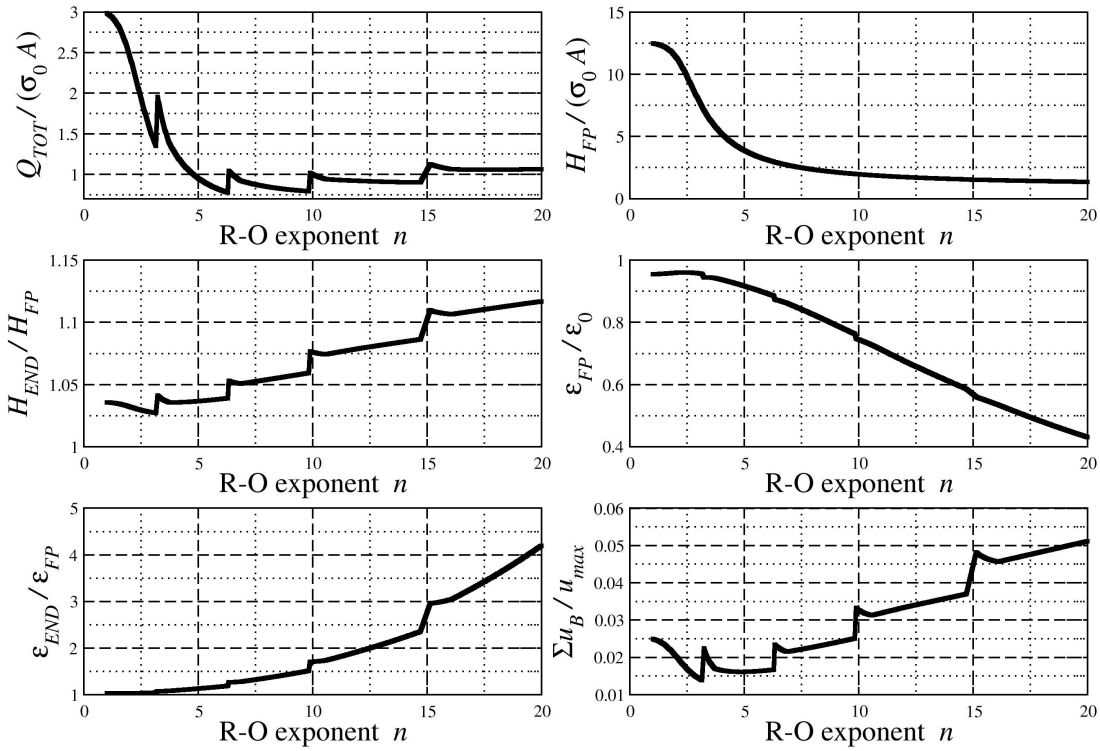

Figure 11. Reduced-scale BRB. Dependence of various mechanical quantities on the Ramberg–Osgood exponent n (5). Results computed adopting $\xi = 3$. Other symbols as explained in the text. The jumps are due to a predicted change in the number N of buckled waves.

contribution of both the Poisson effect and the plastic incompressibility, one obtains a Q_{TOT} value higher by 60% than the "best" one, of the leftmost bar. This effect is due in part to the higher value of the prescribed average strain, here equal to $\varepsilon_0 = 0.03$ instead of $\varepsilon_0 = 0.02$ of the previous case. If one sets $\varepsilon_0 = 0.02$ for this full-scale BRB, one obtains a ratio, between Q_{TOT} with $c_\nu = 0$ and Q_{TOT} with $c_\nu = 1$, equal to 1.22, smaller than the 1.6 shown in Figure 13, yet nonnegligible. The much smaller gap to core thickness ratio, in this last BRB, and the much longer buckled wavelength, might also play a role.

The main reason for this difference, however, is once again that, setting $c_\nu = 0$ for this BRB, the number N of predicted buckled waves increases by one with respect to the case with $c_\nu = 1$. In the case of the reduced-scale BRB of Figure 6, the number N remained the same with $c_\nu = 1$ or $c_\nu = 0$, and the corresponding value of Q_{TOT} did not change much.

Figure 14 illustrates the dependence of the normalized value of Q_{TOT} on the same parameters considered in Figures 7 to 12. In addition, the dependence of Q_{TOT} on μ is plotted for several values of ξ in the bottom right image. The sensitivity to μ is now much lower — almost absent, in fact — than for the reduced-scale BRB, and of a different type, since Q_{TOT} has a maximum for some value of μ. A clear jump of Q_{TOT} across some value of E appears in the left center image, and the same sequence of jumps

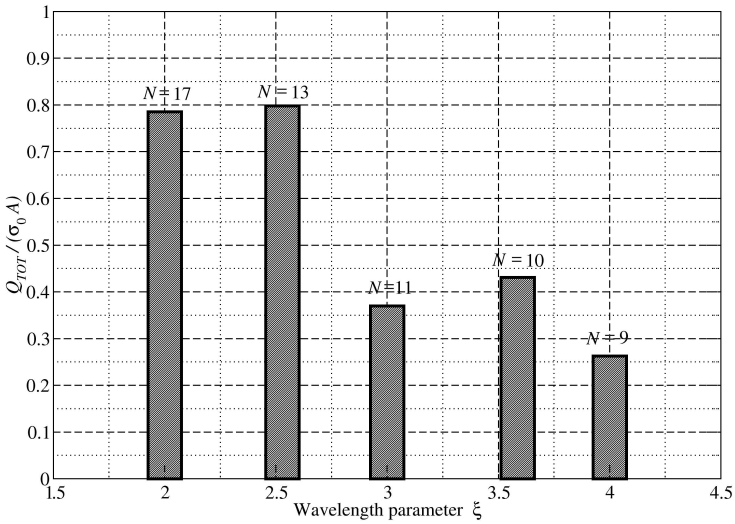

Figure 12. Full-scale BRB example. Variation of the total lateral thrust Q_{TOT} with the choice of parameter ξ of (11). N denotes the predicted total number of buckled waves in the BRB. The result for $\xi = 1.4303$ is missing because of lack of convergence.

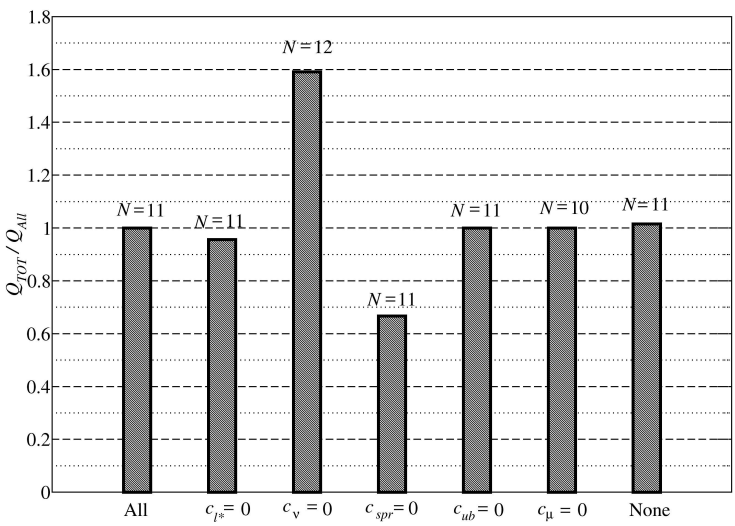

Figure 13. Full-scale BRB. Variation of Q_{TOT} associated to different adopted assumptions. Results computed adopting $\xi = 3$. Symbols as explained in the text.

of Figure 11 is shown in relation to changing n. The relative smallness of the gap g makes almost absent the contribution of $\sum u_B$ to the core shortening (not shown in this figure).

This full-scale BRB, with a proportionally much smaller gap than the reduced-scale one, is "easier" to be solved by means of the adopted scheme, since a failure of convergence did seldom occur. Nevertheless, the strong uncertainties related to the calculation of Q_{TOT} remain unaltered.

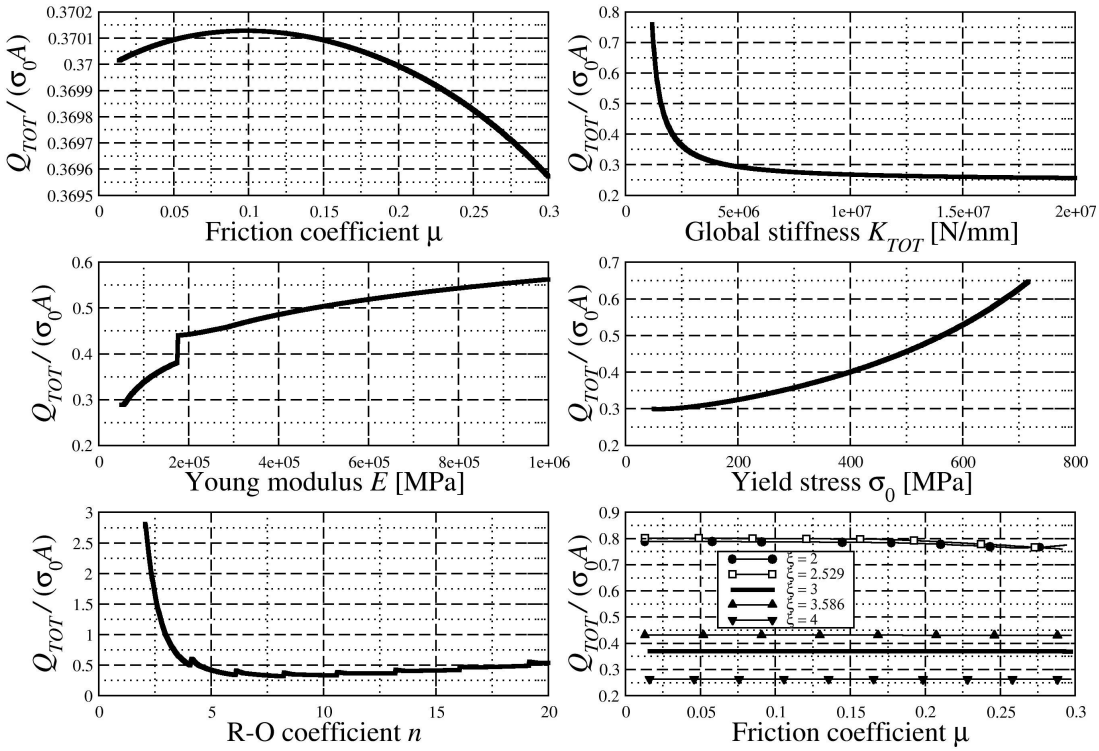

Figure 14. Full-scale BRB. Variation of Q_{TOT} associated to the variation of several analysis parameters. Results obtained with $\xi = 3$ except in the bottom right image. Symbols as explained in the text.

5. Conclusions

The analytical technique illustrated in this work has been developed firstly as an improvement (and a clarification/correction) of a similar one proposed in [Dehghani and Tremblay 2017], secondly as a tool to understand what factors do matter in the calculation of the total lateral thrust Q_{TOT} in BRBs.

The calculations illustrated in this work allow one to conclude what follows, with reference to the calculation of Q_{TOT}.

- The main factor, in this problem, is the number N of waves developed by the BRB buckled core, associated to the value of the parameter ξ of (11). It was shown that a change of ξ produces the largest changes in the lateral thrust Q_{TOT}. Unfortunately, there is no theoretical basis allowing an engineer to select the "correct" value for ξ, among the various equally possible.
- A correct estimate of the stiffness of the restraining profiles is crucial as well. Quite possibly (this was not investigated, here), also the local details of such stiffness may have a high importance.
- A good set of material data for the stress-strain law is also important, including details about the hardening properties under cyclic loading.

- The effect of the tangential frictional contact forces does not seem to be as important as the previous factors. At the light of the uncertainties introduced by the difficulty in selecting ξ, K_{TOT}, and the material parameters, it seems that one may ignore, or treat in the simplest possible way, the contribution due to the friction.
- The lateral expansion of the core can be important, but also this effect appears of a smaller order of magnitude, compared with the first ones.
- Details such as the distinction between l_B and l_B^* in (22), and others discussed above, do not seem to matter, and the simplest calculations could be adopted without a significant loss of accuracy.

It should be kept in mind that Q_{TOT} depends on almost every parameter in a discontinuous way. Therefore, even its limiting — lower and upper — values may be very wrong, if the set of calculation details, including all the data, happens to be defined in the proximity of a jump in the value of Q_{TOT}.

Another very important effect has been ignored in these calculations, as well as in all the ones proposed in the literature. This is the progressive strong increase of Q_{TOT} with the number of loading cycles, even of the same peak amplitude. It is obvious that a correct analytical tool should somehow incorporate also this effect; to the best of this author's knowledge, unfortunately, there is no available theory about this aspect, which might deserve future attention.

When dealing with BRBs, in conclusion, one should always be aware of the uncertainty associated to the calculation of the buckled wavelength, of the discontinuous dependence of Q_{TOT} on the model details, and of the current lack of knowledge about the dependence of Q_{TOT} on the number of loading cycles.

If one is ready to accept these limitations, it seems that a reasonable compromise, for the calculation of Q_{TOT}, might consist in (i) the adoption of a global method, without proceeding one half-wave at a time; (ii) accounting for friction in some simple approximate way, as was done for example in [Bregoli et al. 2016]; (iii) limiting oneself to computing extreme — minimum and maximum — values for Q_{TOT}. Accepting such a procedure, one should then check the lack of discontinuities in the proximity of these extremes for Q_{TOT} (a tedious procedure, obviously), and finally somehow select a statistically significant value to be adopted for the proper design of the BRB restraining profiles and details.

In this author's opinion, in view of much accumulated evidence, BRBs are structural elements whose design has not yet reached a sufficiently acceptable basis. Until, and if ever, a complete understanding of the difficult phenomena involved will be acquired, much attention should be paid in the practical usage of BRBs.

Acknowledgments

This work was done within a research project financed by the Italian Ministry of Education and Research (MIUR).

References

[Bažant and Cedolin 1991] Z. P. Bažant and L. Cedolin, *Stability of structures: elastic, inelastic, fracture and damage theories*, Oxford Engineering Science Series **26**, Oxford University, New York, 1991.

[Bregoli et al. 2016] G. Bregoli, F. Genna, and G. Metelli, "Analytical estimates for the lateral thrust in bolted steel buckling-restrained braces", *J. Mech. Mater. Struct.* **11**:2 (2016), 173–196.

[Dehghani and Tremblay 2017] M. Dehghani and R. Tremblay, "An analytical model for estimating restrainer design forces in bolted buckling-restrained braces", *J. Constr. Steel Res.* **138** (2017), 608–620.

[Dehghani and Tremblay 2018] M. Dehghani and R. Tremblay, "Design and full-scale experimental evaluation of a seismically endurant steel buckling-restrained brace system", *Earthq. Eng. Struct. Dyn.* **47**:1 (2018), 105–129.

[Genna 2019] F. Genna, "On the sensitivity of Finite Element results in the calculation of the lateral thrust for all-steel buckling-restrained braces", *Eng. Struct.* **194** (2019), 66–76.

[Genna 2020] F. Genna, "Lateral thrust in all-steel buckling-restrained braces: experimental and FEM results", *Eng. Struct.* **213** (2020), art. id. 110512.

[Genna and Bregoli 2014] F. Genna and G. Bregoli, "Small amplitude elastic buckling of a beam under monotonic axial loading, with frictionless contact against movable rigid surfaces", *J. Mech. Mater. Struct.* **9**:4 (2014), 441–463.

[Genna and Gelfi 2012] F. Genna and P. Gelfi, "Analysis of the lateral thrust in bolted steel buckling-restrained braces, I: Experimental and numerical results", *J. Struct. Eng.* (*ASCE*) **138**:10 (2012), 1231–1243.

[Jiang et al. 2015] Z. Jiang, Y. Guo, B. Zhang, and X. Zhang, "Influence of design parameters of buckling-restrained brace on its performance", *J. Constr. Steel Res.* **105** (2015), 139–150.

[Metelli et al. 2016] G. Metelli, G. Bregoli, and F. Genna, "Experimental study on the lateral thrust generated by core buckling in bolted-BRBs", *J. Constr. Steel Res.* **122** (2016), 409–420.

[Ramberg and Osgood 1943] W. Ramberg and W. R. Osgood, "Description of stress-strain curves by three parameters", tech. note 902, National Advisory Committee For Aeronautics, Washington, DC, 1943, Available at http://hdl.handle.net/2060/19930081614.

[Takeuchi and Wada 2017] T. Takeuchi and A. Wada (editors), *Buckling-restrained braces and applications*, Japan Society of Seismic Isolation, Tokyo, 2017.

Received 16 Mar 2020. Accepted 29 Apr 2020.

FRANCESCO GENNA: francesco.genna@unibs.it
Department of Civil Engineering, University of Brescia, Brescia, Italy

JOURNAL OF MECHANICS OF MATERIALS AND STRUCTURES
Vol. 15, No. 3, 2020
https://doi.org/10.2140/jomms.2020.15.405

IMPLEMENTATION OF HERMITE–RITZ METHOD AND NAVIER'S TECHNIQUE FOR VIBRATION OF FUNCTIONALLY GRADED POROUS NANOBEAM EMBEDDED IN WINKLER–PASTERNAK ELASTIC FOUNDATION USING BI-HELMHOLTZ NONLOCAL ELASTICITY

SUBRAT KUMAR JENA, SNEHASHISH CHAKRAVERTY,
MOHAMMAD MALIKAN AND HAMID MOHAMMAD-SEDIGHI

The vibration characteristics of functionally graded porous nanobeam embedded in an elastic substrate of Winkler–Pasternak type are investigated. Classical beam theory or Euler–Bernoulli beam theory has been incorporated to address the displacement of the FG nanobeam. bi-Helmholtz type of nonlocal elasticity is being used to capture the small scale effect of the FG nanobeam. Further, the nanobeam is assumed to have porosity, distributed evenly along the thickness throughout the cross-section. Young's modulus and mass density of the nanobeam are considered to vary along the thickness from ceramic to metal constituents in accordance with power-law exponent model. A numerically efficient method, namely the Hermite–Ritz method, is incorporated to compute the natural frequencies of hinged-hinged, clamped-hinged, and clamped-clamped boundary conditions. A closed-form solution is also obtained for hinged-hinged (HH) boundary condition by employing Navier's technique. The advantages of using Hermite polynomials as shape functions are orthogonality, a large domain that makes the method more computationally efficient and avoids ill-conditioning for higher values of polynomials. Additionally, the present results are validated with other existing results in special cases demonstrating excellent agreement. A comprehensive study has been carried out to justify the effectiveness or convergence of the present model or method. Likewise, impacts of various scaling parameters such as Helmholtz and bi-Helmholtz types of nonlocal elasticity, porosity volume fraction index, power-law exponent, and elastic foundation on frequency parameters have been investigated.

1. Introduction

Functionally graded materials (FGMs) are inhomogeneous materials consisting of two or more different materials, and the composition or volume of constituents varies continuously along one or more specific dimensions. As a result, their properties and structure will change steadily along the same dimension. This idea was first used by Japanese researchers [Koizumi 1994]. The gradual and continuous changes in these materials have made them very important and useful properties for application in various industries.

The introduction of FGMs to nano-micro technology has led to the development of devices and tools with better properties and capabilities, such as nano-micro-electro-mechanical systems (NEMS/MEMS), thin shape memory alloys, and atomic light microscopy. Nanotechnology is the study of microscopic objects about 1 to 100 nanometers in size and their applicability in various fields of science, such as

Keywords: FG nanobeam, Hermite–Ritz method, bi-Helmholtz function, porosity, Winkler–Pasternak elastic foundation, vibration.

chemistry, biology, physics, materials science, and engineering. Recently, due to the special mechanical properties of nanostructures, the application of these structures has been developed in engineering, and researchers have been designing high-performance tools such as nanosensors, nano actuators, nanogenerators, etc. to solve new problems. Nanoscale tools are designed using the properties of nanotubes, nanobeams, nano-membranes, and nanosheets, so the discussion of modeling and analysis of nanobeams has attracted the attention of researchers.

Many experiments and computer simulations (molecular simulation) proved that a nanostructure mechanically has different response while it is analyzed in nanoscale size compared with a macroscale investigation. They showed that size is a crucial factor on nanoscale. Among all tools which aid us to predict mechanical response of these materials, the non-classical continuum elasticity approaches are cost and time-effective methods. Accordingly, it has been observed that classical continuum theories do not provide the right answer in predicting the behavior of these small scale structures. In fact, classical continuum theory is unable to account for size effects. The most popular non-classical continuum mechanic theories are: strain gradient theory [Mindlin 1965], nonlocal elasticity theory [Eringen 2002; Jena et al. 2019b; Jena et al. 2020a; Jena et al. 2020b], stress-driven nonlocal elasticity theory [Barretta et al. 2018; Sedighi and Malikan 2020], nonlocal strain gradient theory [Lim et al. 2015; Jena et al. 2019a; Malikan et al. 2020], modified coupled stress theory [Malikan 2017], surface elasticity theory [Ansari et al. 2013], and bi-Helmholtz nonlocal elasticity theory [Lazar et al. 2006; Koutsoumaris and Eptaimeros 2018]. These aforesaid theories, each in turn has small scale parameters. The small scale parameter makes difference between macro scale and nanoscale. Many research approved that these scale parameters are not material constant and vary with variation in natural features and physical characteristics of the nanomaterial. As an example, boundary and edge conditions affect fundamentally the values of small scale parameter. Moreover, as the nano materials except for being size-dependent, are also temperature-dependent, the thermal environment can significantly affect the value of small scale parameter. Thus, a nanostructure in various boundary conditions and different external temperature requires different values for the small scale parameter to give exact results. That is why all the researchers presented amplitude for numerical values of small scale parameters. There are also further examples for factors that affect the amount of a small scale parameter, such as crack specifications in cracked nanomaterials, arrangement of atoms in atomic lattice into some special nanomaterials like graphene and nanotubes with changeable arrangement (chirality effect), etc.

The mechanical behavior of FG nanomaterials with different geometries and various loading and boundary conditions has been extensively investigated by researchers in the current decade. Beams are of great importance due to their wide use in engineering. To date, numerous articles have been written on the study of the dynamics of FGM nanobeams. [Eltaher et al. 2012] based on the finite element method (FEM) analyzed natural frequencies of a nanoscale FGM beam by considering nonlocal continuum mechanics. The beam was modeled according to the Euler–Bernoulli beam theory (EBT) approach. The numerical outputs were calculated for a variety of boundary conditions. [Sharabiania and Yazdi 2013] depicted a nonlinear frequency analysis on FGM nanosize beams in the framework of EBT while the size dependency was investigated on the basis of surface effects. The results were shown for some different edge conditions. [Esmaeili and Beni 2019] investigated buckling and vibration characteristics of flexoelectric smart nanobeam composed of functionally graded materials. [Nazemnezhad and Hosseini-Hashemi 2014] studied nonlocal effects within the framework of nonlinear analysis of vibrations for

FGM nanoscale beams. The immovable ends, such as fixed and pinned conditions were assumed when EBT was employed to give the constitutive equations of frequency. [Hosseini-Hashemi et al. 2014] considered analytically effects of surface and stress nonlocality for pivot-pivot EBT-FGM nanobeam models. [Ansari et al. 2015] examined the excited frequencies nonlinearly for an FGM nanobeam in the body of an exact solution. The influences of the environment, such as temperature differential, were measured as well. The nanosize into the EBT model was investigated utilizing surface elasticity theory, and the Galerkin technique helped to solve the attained equations. [Zeighampour and Beni 2015] developed FGM nanobeams by considering the variation of diameter in the length direction. The strain gradient theory, EBT, and Visco-Pasternak foundation model were combined, which led to the governing equations. The obtained equations were discretized using differential quadrature method (DQM) for pined-pined and clamped-clamped supported and then were solved by eigenvalue solver. Their best results proved the considerable effect of diameter variation on the dynamics behavior of FGM nanobeams. [Ebrahimi and Salari 2015] studied the nonlocal effect on the FGM nanobeams by considering EBT beam model with the presence and absence of the influences of the thermal environment utilizing analytical method based on the Navier method.

[Simsek 2016] discussed the free vibration of an FGM nanoscale beam based on the nonlinear strains and derived mathematical relation by presenting a new Hamiltonian in combining with EBT and nonlocal strain gradient elasticity. [Shafiei et al. 2016] modeled a non-uniform FGM beam taking nanosize effects based on the nonlocal theory of elasticity. The natural frequencies were captured for the beam with the contribution of nonlinear terms. The procedure for solving of the harvested equations was generalized differential quadrature (GDQ) method and Homotopy perturbation method for fixed-fixed, pinned-pinned, and fixed-pinned boundary conditions. [Hosseini and Rahmani 2016] combined thermos-elastic relations to study vibrations of an FGM nanoscale beam when the beam is geometrically curved. The nonlocal elasticity provides the size-dependent behavior, and the numerical results were obtained by analytical solutions. [Khorshidi and Shariati 2016] investigated the vibration characteristics of the sigmoid-type of FGM nanobeams by using the modified couple stress theory. A variety of beam hypotheses such as EBT, first-order shear deformation theory (FSDT) and some higher-order shear deformation theory (HSDT) were investigated with the help of GDQ. [Vosoughi 2016] applied nonlinearity to study free vibration of a FGM nanosize beam embedded on a nonlinear elastic medium. The use of FSDT and nonlocal elasticity addressed the desired equations that were discretized by DQM. [Hamed et al. 2016] compared sigmoid with a nonlinear symmetric power varied along the thickness of EB-FGM nonlocal beams in a vibration study. [Saffari et al. 2017] inspected the stability of an FGM nonlocal FSDT beam by taking surface effects in a dynamical situation. Thermal effects and foundation influences were implemented as well. [Arefi and Zenkour 2017] explored the nonlocal vibration of a Timoshenko FGM nanobeam by taking the Visco-Pasternak matrix into account.

[Vu-Bac et al. 2016] carried out sensitivity analysis for quantifying the influence of uncertain input parameters by using probability density function on uncertain model outputs. The dynamics of three-dimensional inhomogeneities of FGM nanoscale beams was investigated by [Hadi et al. 2018]. [Jouneghani et al. 2018] modeled porosity into the material gradation of FGM nanobeams and examined the structural behavior of the system subjected to variation of environmental parameters such as temperature and humidity. [Mirjavadi et al. 2018] focused on the nonlinear behavior of FGM nanosize beams considering porosities with respect to the EBT and second stress gradient of Eringen. Different end

conditions were taken into consideration by the assistance of GDQM and an iterative technique. [Simsek 2019] performed different closed-form approaches to study a variety of analyses on the FGM nanobeams, namely forced and free vibrations, static bending, and buckling. The nonlocal strain gradient theory was implemented to capture the size dependency influence. Various loading cases were demonstrated in the dynamic analysis of the graded EBT model.

[Aria and Friswell 2019] indicated a finite element analysis in the form of nonlocality to consider free vibration and stability of FGM nanobeams. [Uzun and Yaylı 2019] investigated the free vibration of functionally graded nanobeam for hinged-hinged and clamped-clamped boundary conditions with the help of the finite element model. The nonlocal effect of FG nanobeam was handled by the Eringen's nonlocal theory. [Karami and Janghorban 2019] showed a new shaped function into the higher-order shear deformation theory to study analytically natural frequencies of a FGM nonlocal isotropic/anisotropic beam. Thickness stretching influence was also evaluated by the shape function. The nonlocal strain gradient model determined the nanoscale behavior. [Khaniki 2019] studied vibrations of FGM nanoscale beams based on the two phases nonlocal-local models, and then functionality gradation was derived along length. GDQ helped to obtain numerical results. [Chen et al. 2020] studied thermal buckling behavior of Euler–Bernoulli beam made up of FG material. The transformed-section method was used to investigate the buckling characteristics analytically. [Uzun and Yaylı 2020] in a pioneering work studied free vibration of functionally graded nanobeam for Simply Supported boundary condition using Euler–Bernoulli beam theory and Eringen's nonlocal elasticity by utilizing FEM.

Previous studies, as mentioned above illustrate the fact that the studies involving non-classical theories have rarely used the bi-Helmholtz nonlocal elasticity theory; and have never used the advanced yet simple Hermite–Ritz method for this purpose. In this study, the Euler–Bernoulli theory is applied to find the numerical response of free vibration of FG nanobeams. The numerical solution of the free vibration is obtained, and the response of the rectangular nanobeam is calculated for the bi-Helmholtz nonlocal parameter by employing the Hermite–Ritz method for HH, CH, and CC boundary conditions while closed-form solution is obtained for HH boundary condition by utilizing the Navier's technique. The beam is also embedded on the Winkler–Pasternak elastic bed. Due to the importance of porosity in the structure of functionally graded materials, this argument is included in the present analysis as well. The results of the theory presented are compared with those reported by previous researchers, and a good agreement is observed between the results. A parametric analysis is also carried out to investigate the effect of various scaling parameters such as Helmholtz and bi-Helmholtz types of nonlocal elasticity, porosity volume fraction index, power-law exponent, and elastic foundation on the frequency response of the FG nanobeam.

2. Reviews of Helmholtz and bi-Helmholtz types of nonlocal operators

The bi- Helmholtz type nonlocal modulus, which is the Green's function of bi Helmholtz operator may be stated as [Lazar et al. 2006; Koutsoumaris and Eptaimeros 2018]

$$A^{bH}\left(\left|x-x'\right|\right)=\frac{1}{2}\frac{1}{\xi_1^2-\xi_2^2}\left\{\xi_1 e^{\frac{-|x-x'|}{\xi_1}}-\xi_2 e^{\frac{-|x-x'|}{\xi_2}}\right\} \tag{1}$$

The corresponding bi-Helmholtz operator may be expressed as [Eringen 2002; Lazar et al. 2006; Koutsoumaris and Eptaimeros 2018]

$$\ell^{bH} = \left(1 - \xi_1^2 \frac{d^2}{dx^2}\right)\left(1 - \xi_2^2 \frac{d^2}{dx^2}\right) = 1 - \left(\xi_1^2 + \xi_2^2\right)\frac{d^2}{dx^2} + \xi_1^2\xi_2^2 \frac{d^4}{dx^4} = 1 - \varepsilon^2 \frac{d^2}{dx^2} + \gamma^4 \frac{d^4}{dx^4}, \tag{2}$$

where $\varepsilon^2 = \xi_1^2 + \xi_2^2 = (e_0 a)^2$, $\gamma^4 = \xi_1^2\xi_2^2$ and the constants ξ_1 and ξ_2 are demonstrated as [Eringen 2002; Lazar et al. 2006; Koutsoumaris and Eptaimeros 2018]

$$\xi_1^2 = \frac{\varepsilon^2}{2}\left(1 + \sqrt{1 - 4\frac{\gamma^4}{\varepsilon^4}}\right) \tag{3a}$$

$$\xi_2^2 = \frac{\varepsilon^2}{2}\left(1 - \sqrt{1 - 4\frac{\gamma^4}{\varepsilon^4}}\right) \tag{3b}$$

Here the discriminant $\left(1 - 4\frac{\gamma^4}{\varepsilon^4}\right) \geq 0$, i.e., $\varepsilon \geq \sqrt{2}\gamma$. Considering $\varepsilon = \sqrt{2}\gamma$, we will have $\xi_1 = \xi_2$, where $\xi_1, \xi_2 \in R$ and the parameter γ triumphs over ε. For any other case, i.e., $\varepsilon > \sqrt{2}\gamma$, the effect of ε prevails over γ. From [Lazar et al. 2006], [Koutsoumaris and Eptaimeros 2018], it is evident that that ℓ^{bH} operator matched the Born Karman's model at the end of the Brillouin zone, when $\xi_1 = \xi_2$. Now, the nonlocal modulus is given in (1) maybe stated as [Lazar et al. 2006; Koutsoumaris and Eptaimeros 2018]

$$A^{bH}\left(\left|x - x'\right|, \gamma\right) = \frac{1}{2}\frac{1}{2\gamma^2}\left(\gamma + \left|x - x'\right|\right)e^{\frac{-|x-x'|}{\gamma}} \tag{4}$$

Substituting $\varepsilon = \sqrt{2}\gamma$ or $e_0 a = \sqrt{2}\gamma$, Equation (4) can be expressed as [Lazar et al. 2006; Koutsoumaris and Eptaimeros 2018]

$$A^{bH}\left(\left|x - x'\right|, \frac{e_0 a}{\sqrt{2}}\right) = \frac{1}{2(e_0 a)^2}\left(\frac{e_0 a}{\sqrt{2}} + \left|x - x'\right|\right)e^{-\frac{\sqrt{2}|x-x'|}{e_0 a}} \tag{5}$$

Thus, the bi-Helmholtz operator in differential form may be given as [Lazar et al. 2006; Koutsoumaris and Eptaimeros 2018]

$$\ell^{bH} = 1 - (e_0 a)^2 \frac{d^2}{dx^2} + \frac{(e_0 a)^4}{4}\frac{d^4}{dx^4} \tag{6}$$

Assuming $\xi_1 = e_0 a$ and $\xi_2 = 0$ in (1), the Helmholtz-type nonlocal modulus is given as [Eringen 2002; Koutsoumaris and Eptaimeros 2018]

$$A^{H}\left(\left|x - x'\right|, e_0 a\right) = \frac{1}{2(e_0 a)}e^{\frac{-|x-x'|}{e_0 a}}, \tag{7}$$

and the corresponding Helmholtz operator in differential form is given as [Eringen 2002]

$$\ell^{H} = 1 - (e_0 a)^2 \frac{d^2}{dx^2}. \tag{8}$$

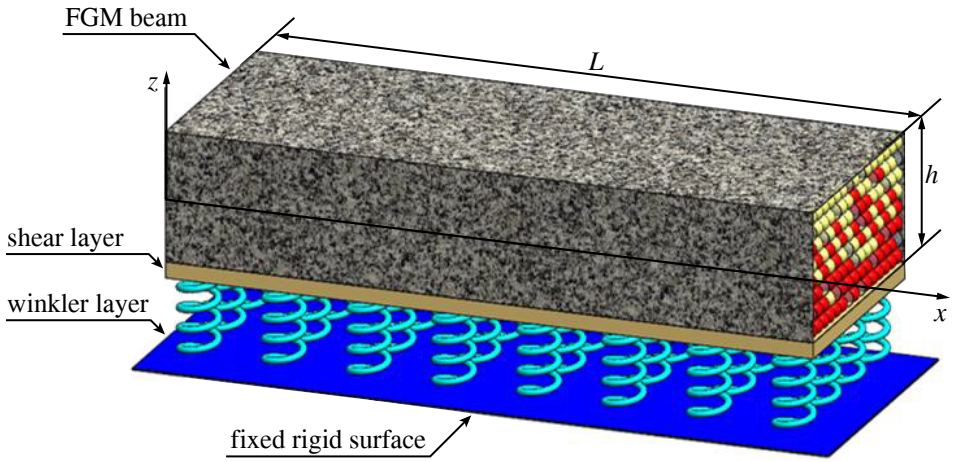

Figure 1a. Schematic diagram of rectangular FG nanobeam embedded in the Winkler–Pasternak elastic foundation.

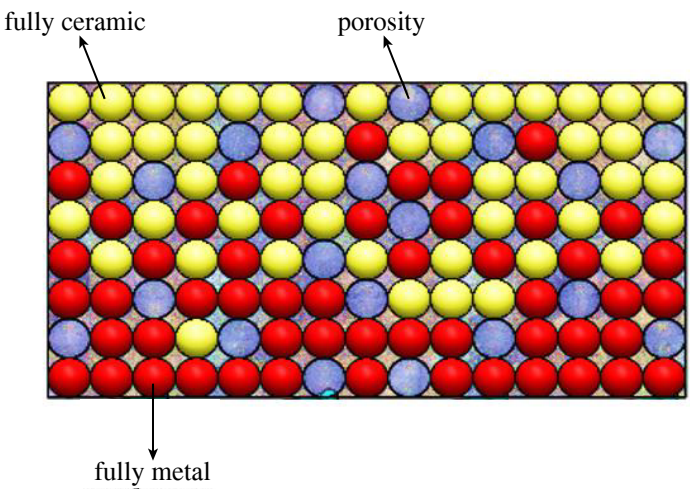

Figure 1b. Graphical representation of the rectangular cross-section of the FG nanobeam with evenly distributed porosity.

3. Mathematical formulation of the proposed model

In this study, a functionally graded porous nanobeam with length (L), breadth (b), thickness (h), and porosity volume fraction ϑ, ($\vartheta < 1$) is taken into consideration, as depicted in Figure 1a. The material composition at the top surface ($z = h/2$) is assumed to be ceramic-rich while the bottom surface ($z = -h/2$) is considered to be metal-rich, and the gradation along thickness from the ceramic-rich surface to metal-rich surface is governed by power-law variation model. The porosity in the nanobeam is assumed as evenly distributed throughout the metal and ceramic constituents, as illustrated in Figure 1b.

Thus, according to the modified rule of the mixture [Wattanasakulpong and Ungbhakorn 2014; Shahsavari et al. 2018]

$$P = P_U V_U + P_L V_L - \frac{\vartheta}{2}(P_U + P_L) \tag{9}$$

Here P denotes the material property FG nanobeam. P_U, V_U is the material property and volume fraction for the ceramic constituent, whereas P_L, V_L symbolize the material property and volume fraction of the metal constituent.

As per the power law variation model, the volume fractions of the ceramic and metal components are expressed as [Wattanasakulpong and Ungbhakorn 2014; Shahsavari et al. 2018]

$$V_U = \left(\frac{z}{h} + \frac{1}{2}\right)^k \tag{10}$$

$$V_L = 1 - \left(\frac{z}{h} + \frac{1}{2}\right)^k \tag{11}$$

Where k is the non-negative parameter, namely power-law exponent, that regulates the distribution of material along the thickness of the nanobeam and z denotes the distance from the mid-plane of the FG nanobeam. Using (9), (10) and (11), the material properties of the FG nanobeam with porosity may be given as [Wattanasakulpong and Ungbhakorn 2014; Shahsavari et al. 2018]

$$P = (P_U - P_L)\left(\frac{z}{h} + \frac{1}{2}\right)^k + P_L - \frac{\vartheta}{2}(P_U + P_L) \tag{12}$$

The Young's modulus $E(z)$, and material density $\rho(z)$ of the FG nanobeam can be demonstrated graphically in Figs. (2–3) and mathematically as [Wattanasakulpong and Ungbhakorn 2014; Shahsavari et al. 2018]

$$E(z) = (E_U - E_L)\left(\frac{z}{h} + \frac{1}{2}\right)^k + E_L - \frac{\vartheta}{2}(E_U + E_L) \tag{13a}$$

$$\rho(z) = (\rho_U - \rho_L)\left(\frac{z}{h} + \frac{1}{2}\right)^k + \rho_L - \frac{\vartheta}{2}(\rho_U + \rho_L) \tag{13b}$$

According to the classical beam theory or Euler–Bernoulli beam theory, the displacement field can be given as [Reddy 2007]

$$u_1(x, z, t) = u\,(x, t) - z\left(\frac{\partial w}{\partial x}\right) \tag{14a}$$

$$u_2(x, z, t) = 0 \tag{14b}$$

$$u_3(x, z, t) = w(x, t) \tag{14c}$$

Where $u(x, t)$, and $w(x, t)$ represent the axial and transverse displacements on the mid-plane of the FG nanobeam, respectively.

The strain-displacement relation of the FG nanobeam is stated as

$$\varepsilon_{xx} = \frac{\partial u_1(x, z, t)}{\partial x} = \frac{\partial u\,(x, t)}{\partial x} - z\frac{\partial^2 w(x, t)}{\partial x^2} \tag{15}$$

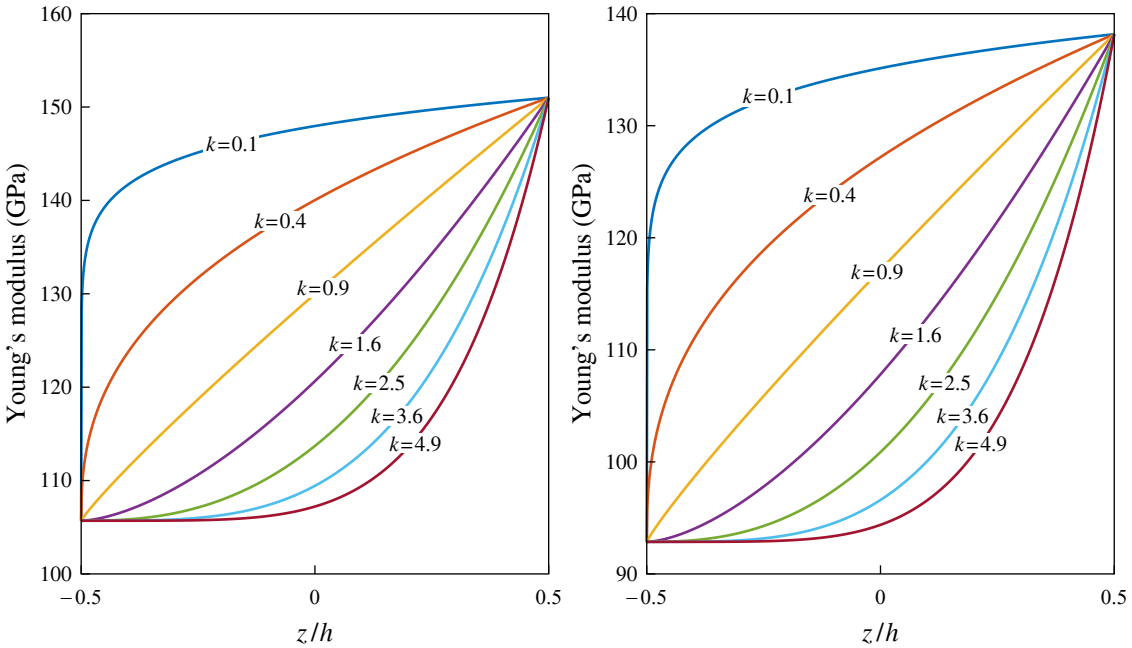

Figure 2. Power-law variation of Young's modulus for FG nanabeam composed of alpha-beta titanium alloy (Ti-6AL-4V) and zirconia (ZrO_2).

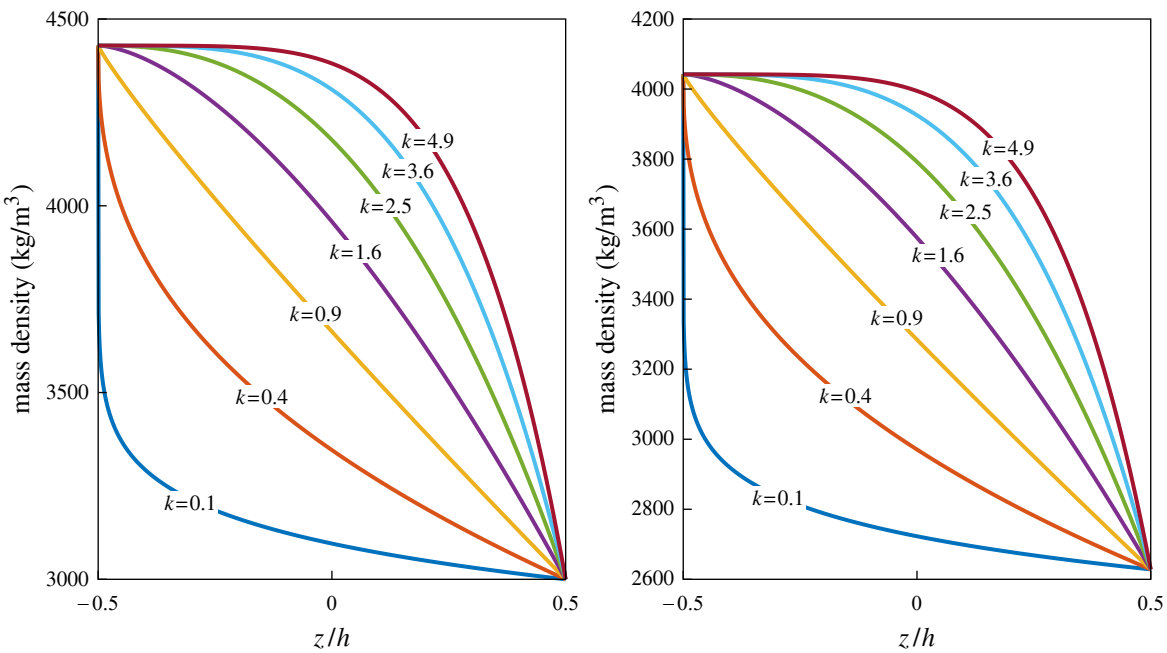

Figure 3. Power-law variation of Mass density for FG nanabeam composed of alpha-beta titanium alloy (Ti-6AL-4V) and zirconia (ZrO_2).

The stress component of the FG nanobeam as generalized Hooke's law may be given as [Pradhan and Chakraverty 2014]

$$\sigma_{xx} = Q_{11}\varepsilon_{xx} = \left(\frac{E(z)}{1-\upsilon^2}\right)\varepsilon_{xx} \tag{16}$$

3.1. ***Energy form of equation for Hermite–Ritz method.*** The strain energy (S) of the FG nanobeam is stated as

$$\begin{aligned} S &= \frac{1}{2}\int_0^L \int_A (\sigma_{xx}\varepsilon_{xx}) dA\, dx = \frac{1}{2}\int_0^L \int_A \left[\sigma_{xx}\left(\frac{\partial u(x,t)}{\partial x} - z\frac{\partial^2 w(x,t)}{\partial x^2}\right)\right] dA\, dx \\ &= \frac{1}{2}\int_0^L \left[N\left(\frac{\partial u(x,t)}{\partial x}\right) - M\left(\frac{\partial^2 w(x,t)}{\partial x^2}\right)\right] dx \end{aligned} \tag{17}$$

Where the stress resultants $(N, M) = \int_A (\sigma_{xx}, z\sigma_{xx}) dA$.

Now, the variation in strain energy (δS) can be given as

$$\begin{aligned} \delta S &= \int_0^L \int_A (\sigma_{xx}\delta\varepsilon_{xx}) dA\, dx \\ &= \int_0^L \int_A \left[\sigma_{xx}\left(\frac{\partial \delta u(x,t)}{\partial x} - z\frac{\partial^2 \delta w(x,t)}{\partial x^2}\right)\right] dA\, dx \\ &= \int_0^L \left[N\left(\frac{\partial \delta u(x,t)}{\partial x}\right) - M\left(\frac{\partial^2 \delta w(x,t)}{\partial x^2}\right)\right] dx \\ &= \int_0^L \left[-\left(\frac{\partial N}{\partial x}\right)\delta u - \left(\frac{\partial^2 M}{\partial x^2}\right)\delta w\right] dx \end{aligned} \tag{18}$$

The kinetic energy (T) of the FG nanobeam can be stated as

$$\begin{aligned} T &= \frac{1}{2}\int_0^L \int_A \rho(z)\left[\left(\frac{\partial u_1}{\partial t}\right)^2 + \left(\frac{\partial u_2}{\partial t}\right)^2 + \left(\frac{\partial u_3}{\partial t}\right)^2\right] dA\, dx \\ &= \frac{1}{2}\int_0^L \int_A \rho(z)\left[\left(\frac{\partial u}{\partial t} - z\left(\frac{\partial^2 w}{\partial x \partial t}\right)\right)^2 + \left(\frac{\partial w}{\partial t}\right)^2\right] dA\, dx \\ &= \frac{1}{2}\int_0^L \left[I_0\left(\left(\frac{\partial u}{\partial t}\right)^2 + \left(\frac{\partial w}{\partial t}\right)^2\right) - 2I_1\left(\frac{\partial u}{\partial t}\right)\left(\frac{\partial^2 w_b}{\partial x \partial t}\right) + I_2\left(\frac{\partial^2 w}{\partial x \partial t}\right)^2\right] dx \end{aligned} \tag{19}$$

In which $(I_0, I_1, I_2) = \int_A \rho(z)(1, z, z^2) dA$ are the mass moment of inertias.

The variation in kinetic energy (δT) can be obtained from (19) as

$$\begin{aligned} \delta T &= \frac{1}{2}\int_0^L \left[I_0\delta\left(\left(\frac{\partial u}{\partial t}\right)^2 + \left(\frac{\partial w}{\partial t}\right)^2\right) - 2I_1\delta\left(\frac{\partial u}{\partial t}\right)\left(\frac{\partial^2 w_b}{\partial x \partial t}\right) + I_2\delta\left(\frac{\partial^2 w}{\partial x \partial t}\right)^2\right] dx \\ &= \int_0^L \left[-I_0\left(\frac{\partial^2 u}{\partial t^2}\right)\delta u - I_0\left(\frac{\partial^2 w}{\partial t^2}\right)\delta w + I_1\left(\frac{\partial^3 w}{\partial x \partial t^2}\right)\delta u - I_1\left(\frac{\partial^3 u}{\partial x \partial t^2}\right)\delta w + I_2\left(\frac{\partial^4 w}{\partial x^2 \partial t^2}\right)\delta w\right] dx \end{aligned} \tag{20}$$

The work done (W) by the Winkler–Pasternak elastic foundation can be expressed as [Uzun and Yaylı 2020]

$$W = -\frac{1}{2}\int_0^L \left[k_w w^2 + k_g\left(\frac{\partial w}{\partial x}\right)^2\right] dx, \tag{21}$$

where k_w and k_g are Winkler and Pasternak elastic constants, respectively.

The variation in external work done (δW) can be derived from (21) as

$$\delta W = -\int_0^L \left[k_w w + k_g\left(\frac{\partial^2 w}{\partial x^2}\right)\right]\delta w dx \tag{22}$$

Using (18), (20) and (22) in the extended Hamilton's principle $\int_0^T (T - S + W)dt = 0$ and collecting the coefficient of δu and δw, the governing equations of motion in terms of stress resultants and displacements can be obtained as

$$\frac{\partial N}{\partial x} = I_0\left(\frac{\partial^2 u}{\partial t^2}\right) - I_1\left(\frac{\partial^3 w}{\partial x \partial t^2}\right) \tag{23a}$$

$$\frac{\partial^2 M}{\partial x^2} = I_0\left(\frac{\partial^2 w}{\partial t^2}\right) + I_1\left(\frac{\partial^3 u}{\partial x \partial t^2}\right) - I_2\left(\frac{\partial^4 w}{\partial x^2 \partial t^2}\right) + k_w w - k_g\left(\frac{\partial^2 w}{\partial x^2}\right) \tag{23b}$$

Multiplying (16) by dA and $z\,dA$ and integrating over the area of cross-section of the FG nanobeam, the local stress resultants can be written as

$$N = A_{11}\left(\frac{\partial u}{\partial x}\right) - B_{11}\left(\frac{\partial^2 w}{\partial x^2}\right), \quad M = B_{11}\left(\frac{\partial u}{\partial x}\right) - D_{11}\left(\frac{\partial^2 w}{\partial x^2}\right), \tag{24}$$

where $(A_{11}, B_{11}, D_{11}) = \int_A Q_{11}(1, z, z^2)dA$, are the stiffness coefficients of FG nanobeam.

Applying bi-Helmholtz operator to (24) and using (23), the nonlocal stress resultant resultants of the FG nanobeam can be obtained as

$$N = A_{11}\left(\frac{\partial u}{\partial x}\right) - B_{11}\left(\frac{\partial^2 w}{\partial x^2}\right) + (e_0 a)^2 \left[\begin{array}{l} \left\{I_0\left(\dfrac{\partial^3 u}{\partial x \partial t^2}\right) - I_1\left(\dfrac{\partial^4 w}{\partial x^2 \partial t^2}\right)\right\} - \dfrac{(e_0 a)^2}{4} \\ \left\{I_0\left(\dfrac{\partial^5 u}{\partial x^3 \partial t^2}\right) - I_1\left(\dfrac{\partial^6 w}{\partial x^4 \partial t^2}\right)\right\} \end{array}\right] \tag{25a}$$

$$M = B_{11}\left(\frac{\partial u}{\partial x}\right) - D_{11}\left(\frac{\partial^2 w}{\partial x^2}\right) + (e_0 a)^2 \left[\begin{array}{l} \left\{\begin{array}{c} I_0\left(\frac{\partial^2 w}{\partial t^2}\right) + I_1\left(\frac{\partial^3 u}{\partial x \partial t^2}\right) - I_2\left(\frac{\partial^4 w}{\partial x^2 \partial t^2}\right) \\ +k_w w - k_g\left(\frac{\partial^2 w}{\partial x^2}\right) \end{array}\right\} \\ -\dfrac{(e_0 a)^2}{4}\left\{\begin{array}{l} I_0\left(\dfrac{\partial^4 w}{\partial x^2 \partial t^2}\right) + I_1\left(\dfrac{\partial^5 u}{\partial x^3 \partial t^2}\right) - \\ I_2\left(\dfrac{\partial^6 w}{\partial x^4 \partial t^2}\right) + k_w\left(\dfrac{\partial^2 w}{\partial x^2}\right) - k_g\left(\dfrac{\partial^4 w}{\partial x^4}\right) \end{array}\right\} \end{array}\right] \tag{25b}$$

Substituting (25) in (17), the strain energy, kinetic energy, and work done by elastic foundation for the FG nanobeam can be depicted as

$$T = \frac{1}{2}\int_0^L \left[I_0\left(\left(\frac{\partial u}{\partial t}\right)^2 + \left(\frac{\partial w}{\partial t}\right)^2\right) - 2I_1\left(\frac{\partial u}{\partial t}\right)\left(\frac{\partial^2 w_b}{\partial x \partial t}\right) + I_2\left(\frac{\partial^2 w}{\partial x \partial t}\right)^2 \right] dx \tag{26}$$

$$W = -\frac{1}{2}\int_0^L \left[k_w w^2 + k_g\left(\frac{\partial w}{\partial x}\right)^2 \right] dx \tag{27}$$

$$S = \frac{1}{2}\int_0^L \left[\begin{array}{l} A_{11}\left(\frac{\partial u}{\partial x}\right)^2 - 2B_{11}\left(\frac{\partial u}{\partial x}\right)\left(\frac{\partial^2 w}{\partial x^2}\right) + D_{11}\left(\frac{\partial^2 w}{\partial x^2}\right)^2 + \\ (e_0a)^2\left(\frac{\partial u}{\partial x}\right)\left\{ I_0\left(\frac{\partial^3 u}{\partial x \partial t^2}\right) - I_1\left(\frac{\partial^4 w}{\partial x^2 \partial t^2}\right)\right\} \\ -\frac{(e_0a)^4}{4}\left(\frac{\partial u}{\partial x}\right)\left\{ I_0\left(\frac{\partial^5 u}{\partial x^3 \partial t^2}\right) - I_1\left(\frac{\partial^6 w}{\partial x^4 \partial t^2}\right)\right\} + (e_0a)^2\left(\frac{\partial^2 w}{\partial x^2}\right) \\ \left\{ I_0\left(\frac{\partial^2 w}{\partial t^2}\right) + I_1\left(\frac{\partial^3 u}{\partial x \partial t^2}\right) - I_2\left(\frac{\partial^4 w}{\partial x^2 \partial t^2}\right) + k_w w - k_g\left(\frac{\partial^2 w}{\partial x^2}\right)\right\} \\ -\frac{(e_0a)^4}{4}\left(\frac{\partial^2 w}{\partial x^2}\right)\left\{ \begin{array}{l} I_0\left(\frac{\partial^4 w}{\partial x^2 \partial t^2}\right) + I_1\left(\frac{\partial^5 u}{\partial x^3 \partial t^2}\right) - I_2\left(\frac{\partial^6 w}{\partial x^4 \partial t^2}\right) \\ + k_w\left(\frac{\partial^2 w}{\partial x^2}\right) - k_g\left(\frac{\partial^4 w}{\partial x^4}\right) \end{array}\right\} \end{array} \right] dx \tag{28}$$

Assuming the motion of the FG nanobeam as sinusoidal i.e., plugging $u(x,t) = U(x)\cos(\omega t)$ and $w(x,t) = W(x)\cos(\omega t)$, the maximum strain energy ($S_{\max}$), kinetic energy ($T_{\max}$), and work done by elastic foundation ($W_{\max}$) for the FG nanobeam can be obtained as

$$S_{\max} = \frac{1}{2}\int_0^L \left[\begin{array}{l} A_{11}\left(\frac{dU}{dx}\right)^2 - 2B_{11}\left(\frac{dU}{dx}\right)\left(\frac{d^2W}{dx^2}\right) + D_{11}\left(\frac{d^2W}{dx^2}\right)^2 - (\omega)^2(e_0a)^2 I_0\left(\frac{dU}{dx}\right)^2 \\ + 2(\omega)^2(e_0a)^2 I_1\left(\frac{dU}{dx}\right)\left(\frac{d^2W}{dx^2}\right) + (\omega)^2\frac{(e_0a)^4}{4} I_0\left(\frac{dU}{dx}\right)\left(\frac{d^3W}{dx^3}\right) + (\omega)^2 \\ \frac{(e_0a)^4}{4} I_1\left(\frac{dU}{dx}\right)\left(\frac{d^4W}{dx^4}\right) + (\omega)^2(e_0a)^2 I_0(W)\left(\frac{d^2W}{dx^2}\right) - (\omega)^2(e_0a)^2 I_2 \\ \left(\frac{d^2W}{dx^2}\right)^2 - (e_0a)^2 k_w(W)\left(\frac{d^2W}{dx^2}\right) + (e_0a)^2 k_g\left(\frac{d^2W}{dx^2}\right)^2 - (\omega)^2\frac{(e_0a)^4}{4} I_0 \\ \left(\frac{d^2W}{dx^2}\right)^2 - (\omega)^2\frac{(e_0a)^4}{4} I_1\left(\frac{d^2W}{dx^2}\right)\left(\frac{d^3U}{dx^3}\right) + (\omega)^2\frac{(e_0a)^4}{4} I_2\left(\frac{d^2W}{dx^2}\right)\left(\frac{d^4W}{dx^4}\right) \\ -\frac{(e_0a)^4}{4} k_g\left(\frac{d^2W}{dx^2}\right)\left(\frac{d^4W}{dx^4}\right) + \frac{(e_0a)^4}{4} k_w\left(\frac{d^2W}{dx^2}\right)^2 \end{array} \right] dx \tag{29}$$

$$T_{\max} = \frac{\omega^2}{2}\int_0^L \left[I_0(U^2 + W^2) - 2I_1(U)\left(\frac{dW}{dx}\right) + I_2\left(\frac{dW}{dx}\right)^2 \right] dx \tag{30}$$

$$W_{\max} = -\frac{1}{2}\int_0^L \left[k_w W^2 + k_g\left(\frac{dW}{dx}\right)^2\right]dx \tag{31}$$

Substituting (29)–(31) into the Lagrangian energy function $\Pi = S_{\max} - W_{\max} - T_{\max}$ and setting $\Pi = 0$, one may get

$$\begin{aligned}
&\int_0^L \left[\begin{array}{l} A_{11}\left(\frac{dU}{dx}\right)^2 - 2B_{11}\left(\frac{d^2W}{dx^2}\right)\left(\frac{dU}{dx}\right) + D_{11}\left(\frac{d^2W}{dx^2}\right)^2 - (e_0a)^2 k_w(W)\left(\frac{d^2W}{dx^2}\right) + (e_0a)^2 \\ k_g\left(\frac{d^2W}{dx^2}\right)^2 + \frac{(e_0a)^4}{4}k_w\left(\frac{d^2W}{dx^2}\right)^2 - \frac{(e_0a)^4}{4}k_g\left(\frac{d^2W}{dx^2}\right)\left(\frac{d^4W}{dx^4}\right) + k_w W^2 + k_g\left(\frac{dW}{dx}\right)^2 \end{array}\right] dx \\
&= \omega^2 \int_0^L \left[\begin{array}{l} I_0(U^2+W^2) - 2I_1(U)\left(\frac{dW}{dx}\right) + I_2\left(\frac{dW}{dx}\right)^2 + (e_0a)^2 I_0\left(\frac{dU}{dx}\right)^2 - (e_0a)^2 I_1 \\ \left(\frac{dU}{dx}\right)\left(\frac{d^2W}{dx^2}\right) - \frac{(e_0a)^4}{4}I_0\left(\frac{d^3U}{dx^3}\right)\left(\frac{dU}{dx}\right) + \frac{(e_0a)^4}{4}I_1\left(\frac{dU}{dx}\right)\left(\frac{d^4W}{dx^4}\right) - (e_0a)^2 \\ I_0(W)\left(\frac{d^2W}{dx^2}\right) - (e_0a)^2 I_1\left(\frac{d^2W}{dx^2}\right)\left(\frac{dU}{dx}\right) + (e_0a)^2 I_2\left(\frac{d^2W}{dx^2}\right)^2 + \frac{(e_0a)^4}{4}I_0\left(\frac{d^2W}{dx^2}\right)^2 \\ + \frac{(e_0a)^4}{4}I_1\left(\frac{d^2W}{dx^2}\right)\left(\frac{d^3U}{dx^3}\right) - \frac{(e_0a)^4}{4}I_2\left(\frac{d^2W}{dx^2}\right)\left(\frac{d^4W}{dx^4}\right) \end{array}\right] dx
\end{aligned} \tag{32}$$

Where;

$$\begin{aligned}
A_{11} &= \frac{bh}{1-\upsilon^2}\left[\frac{(E_U - E_L)}{k+1} + E_L - \left(\frac{\vartheta}{2}\right)(E_U + E_L)\right] \\
B_{11} &= \frac{bh^2 k}{1-\upsilon^2}\left[\frac{(E_U - E_L)}{2(k+1)(k+2)}\right] \\
D_{11} &= \frac{bh^3}{1-\upsilon^2}\left[\frac{(E_U - E_L)(k^2+k+2)}{4(k+1)(k+2)(k+3)} + \frac{E_L}{12} - \left(\frac{\vartheta}{24}\right)(E_U + E_L)\right] \\
I_0 &= bh\left[\frac{(\rho_U - \rho_L)}{k+1} + \rho_L - \left(\frac{\vartheta}{2}\right)(\rho_U + \rho_L)\right] \\
I_1 &= bh^2 k\left[\frac{(\rho_U - \rho_L)}{2(k+1)(k+2)}\right] \\
I_2 &= bh^3\left[\frac{(\rho_U - \rho_L)(k^2+k+2)}{4(k+1)(k+2)(k+3)} + \frac{\rho_L}{12} - \left(\frac{\vartheta}{24}\right)(\rho_U + \rho_L)\right]
\end{aligned}$$

Equation (32) is the Lagrangian energy function of FG porous nanobeam with bi-Helmholtz type of nonlocal elasticity. The Lagrangian energy function for the Helmholtz type of nonlocal elasticity can be

obtained from (32) as

$$\int_0^L \begin{bmatrix} A_{11}\left(\frac{dU}{dx}\right)^2 - 2B_{11}\left(\frac{d^2W}{dx^2}\right)\left(\frac{dU}{dx}\right) + D_{11}\left(\frac{d^2W}{dx^2}\right)^2 - (e_0a)^2k_w \\ (W)\left(\frac{d^2W}{dx^2}\right) + (e_0a)^2k_g\left(\frac{d^2W}{dx^2}\right)^2 + k_wW^2 + k_g\left(\frac{dW}{dx}\right)^2 \end{bmatrix} dx$$

$$= \omega^2 \int_0^L \begin{bmatrix} I_0(U^2+W^2) - 2I_1(U)\left(\frac{dW}{dx}\right) + I_2\left(\frac{dW}{dx}\right)^2 + (e_0a)^2I_0\left(\frac{dU}{dx}\right)^2 - (e_0a)^2I_1\left(\frac{dU}{dx}\right) \\ \left(\frac{d^2W}{dx^2}\right) - (e_0a)^2I_0(W)\left(\frac{d^2W}{dx^2}\right) - (e_0a)^2I_1\left(\frac{d^2W}{dx^2}\right)\left(\frac{dU}{dx}\right) + (e_0a)^2I_2\left(\frac{d^2W}{dx^2}\right)^2 \end{bmatrix} dx \tag{33}$$

3.2. ***Equation of motion for Navier's technique.*** Substituting (25) into (23), the governing equations of motion in terms of displacement can be obtained as

$$A_{11}\left(\frac{\partial^2u}{\partial x^2}\right) - B_{11}\left(\frac{\partial^3w}{\partial x^3}\right) = I_0\left(\frac{\partial^2u}{\partial t^2}\right) - I_1\left(\frac{\partial^3w}{\partial x\partial t^2}\right) - (e_0a)^2 \left\{I_0\left(\frac{\partial^4u}{\partial x^2\partial t^2}\right) - I_1\left(\frac{\partial^5w}{\partial x^3\partial t^2}\right)\right\} + \frac{(e_0a)^4}{4}\left\{I_0\left(\frac{\partial^6u}{\partial x^4\partial t^2}\right) - I_1\left(\frac{\partial^7w}{\partial x^5\partial t^2}\right)\right\} \tag{34a}$$

$$B_{11}\left(\frac{\partial^3u}{\partial x^3}\right) - D_{11}\left(\frac{\partial^4w}{\partial x^4}\right) = I_0\left(\frac{\partial^2w}{\partial t^2}\right) + I_1\left(\frac{\partial^3u}{\partial x\partial t^2}\right) - I_2\left(\frac{\partial^4w}{\partial x^2\partial t^2}\right) + k_ww - k_g\left(\frac{\partial^2w}{\partial x^2}\right) - (e_0a)^2\begin{Bmatrix} I_0\left(\frac{\partial^4w}{\partial x^2\partial t^2}\right) + I_1\left(\frac{\partial^5u}{\partial x^3\partial t^2}\right) - I_2 \\ \left(\frac{\partial^6w}{\partial x^4\partial t^2}\right) + k_w\left(\frac{\partial^2w}{\partial x^2}\right) - k_g\left(\frac{\partial^4w}{\partial x^4}\right) \end{Bmatrix} + \frac{(e_0a)^4}{4}\begin{Bmatrix} I_0\left(\frac{\partial^6w}{\partial x^4\partial t^2}\right) + I_1\left(\frac{\partial^7u}{\partial x^5\partial t^2}\right) - I_2 \\ \left(\frac{\partial^8w}{\partial x^6\partial t^2}\right) + k_w\left(\frac{\partial^4w}{\partial x^4}\right) - k_g\left(\frac{\partial^6w}{\partial x^6}\right) \end{Bmatrix} \tag{34b}$$

The governing equations of motion for the Helmholtz type of nonlocal elasticity can be obtained from (34) as

$$A_{11}\left(\frac{\partial^2u}{\partial x^2}\right) - B_{11}\left(\frac{\partial^3w}{\partial x^3}\right) = I_0\left(\frac{\partial^2u}{\partial t^2}\right) - I_1\left(\frac{\partial^3w}{\partial x\partial t^2}\right) - (e_0a)^2\left\{I_0\left(\frac{\partial^4u}{\partial x^2\partial t^2}\right) - I_1\left(\frac{\partial^5w}{\partial x^3\partial t^2}\right)\right\} \tag{35a}$$

$$B_{11}\left(\frac{\partial^3u}{\partial x^3}\right) - D_{11}\left(\frac{\partial^4w}{\partial x^4}\right) = I_0\left(\frac{\partial^2w}{\partial t^2}\right) + I_1\left(\frac{\partial^3u}{\partial x\partial t^2}\right) - I_2\left(\frac{\partial^4w}{\partial x^2\partial t^2}\right) + k_ww - k_g\left(\frac{\partial^2w}{\partial x^2}\right) - (e_0a)^2\left\{I_0\left(\frac{\partial^4w}{\partial x^2\partial t^2}\right) + I_1\left(\frac{\partial^5u}{\partial x^3\partial t^2}\right) - I_2\left(\frac{\partial^6w}{\partial x^4\partial t^2}\right) + k_w\left(\frac{\partial^2w}{\partial x^2}\right) - k_g\left(\frac{\partial^4w}{\partial x^4}\right)\right\} \tag{35b}$$

4. Solution procedures

In the upcoming subsections, the Hermite–Ritz method and Navier's technique have been described to solve the governing equations of motion for the proposed model.

4.1. ***Application of Hermite–Ritz method.*** Hermite polynomials [Ş. S. Bayın 2018] ($H(n,x)$) are set of orthogonal polynomials with respect to the weight function e^{-x^2} defined over the domain $(-\infty,\infty)$, i.e.,

$$\int_{-\infty}^{\infty} e^{-x^2} H(m,x)H(n,x)dx = \begin{cases} \sqrt{\pi}2^n n!, & n=m \\ 0, & n\neq m \end{cases} \tag{36}$$

First five terms of Hermite polynomials with recurrence relations can be expressed as [Ş. S. Bayın 2018]

$$\begin{aligned} &H(0,x) = 1 \\ &H(1,x) = 2x \\ &H(2,x) = 4x^2 - 2 \\ &H(3,x) = 8x^3 - 12x \\ &H(4,x) = 16x^4 - 48x^2 + 12 \\ &H(n,x) = 2xH(n-1,x) - 2(n-1)H(n-2,x) \text{ and } H'(n,x) = 2nH(n-1,x) \end{aligned} \tag{37}$$

In this investigation, Hermite polynomials are taken as shape functions, i.e., both the axial and transverse displacements of the FG nanobeam are expressed in terms of Hermite polynomials. The main reasons behind choosing the Hermite polynomials as shape functions are;

- Hermite polynomials are the orthogonal polynomials which reduce the computation time.
- Unlike other orthogonal polynomials such as Chebyshev polynomials, Legendre polynomials, etc., the domain is $(-\infty,\infty)$ that offers flexibility in the limit of the Lagrangian energy function.
- It helps to restrict ill-conditioning of the matrix for higher values of polynomials.

The axial displacement $U(X)$, and transverse displacement $W(X)$ can be now expressed as [Pradhan and Chakraverty 2014]

$$U(X) = X^{\eta}(R-X)^{\kappa}\sum_{i=1}^{n} c_i H(i-1,X) \tag{38a}$$

$$W(X) = X^{\eta}(R-X)^{\kappa}\sum_{i=1}^{n} d_i H(i-1,\ X) \tag{38b}$$

Here c_i's, and d_i's are unknown coefficients, $H(n,X)$ is the nth term of Hermite polynomial which is used shape function, $X^{\eta}(R-X)^{\kappa}$ is the admissible functions with exponents η, and κ. For different boundary conditions η, and κ possess different values, as follows:

B.C.	η	κ
H-H	1	1
C-H	2	1
C-C	2	2

Substituting (38) into the Lagrangian energy function of bi-Helmholtz and Helmholtz types of nonlocal elasticity, i.e., (32) and (33) and minimizing Ω^2 with respect to the unknown coefficients c_i's, and d_i's,

$i = 1, 2, 3 \ldots n$, give rise to the generalized eigenvalue problem as

$$[\mathrm{K}]\{X\} = \Omega^2[\mathrm{M}]\{X\} \tag{39}$$

where $\{X\} = [c_1, c_2, c_3, \ldots c_n, d_1, d_2, d_3, \ldots d_n]^T$, [K] represents the stiffness matrix, and [M] denotes the mass matrix.

4.2. ***Application of Navier's technique.*** As per the Navier's technique the axial displacement $u(x,t)$ and transverse the displacement $w(x,t)$ can be expanded in terms of sine and cosine series as [Bekhadda et al. 2019];

$$u(x,t) = \sum_{m=1}^{\infty} u_m \cos\left(\frac{m\pi}{L}x\right)e^{i\omega t} \tag{40a}$$

$$w(x,t) = \sum_{m=1}^{\infty} w_m \sin\left(\frac{m\pi}{L}x\right)e^{i\omega t} \tag{40b}$$

where u_m and w_m are arbitrary parameters and ω is the natural frequency of vibration. Plugging (40) into the (34), and (35), generalized Eigenvalue problem for free vibration of FG nanobeam for bi- Helmholtz and Helmholtz types nonlocal elasticity, respectively, will be obtained as

$$[\mathrm{K}^{bH}]\{X\} = \omega^2[\mathrm{M}^{bH}]\{X\} \tag{41a}$$

$$[\mathrm{K}^{H}]\{X\} = \omega^2[\mathrm{M}^{H}]\{X\} \tag{41b}$$

Here $[K^{bH}] = \begin{bmatrix} k_{11} & k_{12} \\ k_{21} & k_{22} \end{bmatrix}$, $[\mathrm{M}^{bH}] = \begin{bmatrix} m_{11} & m_{12} \\ m_{21} & m_{22} \end{bmatrix}$, $[K^{H}] = \begin{bmatrix} \bar{k}_{11} & \bar{k}_{12} \\ \bar{k}_{21} & \bar{k}_{22} \end{bmatrix}$, $[\mathrm{M}^{H}] = \begin{bmatrix} \bar{m}_{11} & \bar{m}_{12} \\ \bar{m}_{21} & \bar{m}_{22} \end{bmatrix}$ and $\{X\} = [u_m \quad w_m]^T$, where

$$k_{11} = -A_{11}\left(\frac{m\pi}{L}\right)^2, k_{12} = k_{21} = B_{11}\left(\frac{m\pi}{L}\right)^3,$$

$$k_{22} = -D_{11}\left(\frac{m\pi}{L}\right)^4 - (k_w) - (k_g)\left(\frac{m\pi}{L}\right)^2 - (e_0a)^2(k_w)\left(\frac{m\pi}{L}\right)^2$$

$$-(e_0a)^2(k_g)\left(\frac{m\pi}{L}\right)^4 - \frac{(e_0a)^4}{4}(k_w)\left(\frac{m\pi}{L}\right)^4 - \frac{(e_0a)^4}{4}(k_g)\left(\frac{m\pi}{L}\right)^6,$$

$$m_{11} = -I_0 - (e_0a)^2(I_0)\left(\frac{m\pi}{L}\right)^2 - \frac{(e_0a)^4}{4}(I_0)\left(\frac{m\pi}{L}\right)^4,$$

$$m_{12} = m_{21} = I_1\left(\frac{m\pi}{L}\right) + (e_0a)^2(I_1)\left(\frac{m\pi}{L}\right)^3 + \frac{(e_0a)^4}{4}(I_1)\left(\frac{m\pi}{L}\right)^5,$$

$$m_{22} = -I_0 - I_2\left(\frac{m\pi}{L}\right)^2 - I_0(e_0a)^2\left(\frac{m\pi}{L}\right)^2 - I_2(e_0a)^2$$

$$\left(\frac{m\pi}{L}\right)^4 - I_0\frac{(e_0a)^4}{4}\left(\frac{m\pi}{L}\right)^4 - I_2\frac{(e_0a)^4}{4}\left(\frac{m\pi}{L}\right)^6,$$

$$\bar{k}_{11} = -A_{11}\left(\frac{m\pi}{L}\right)^2, \bar{k}_{12} = \bar{k}_{21} = B_{11}\left(\frac{m\pi}{L}\right)^3,$$

$$\bar{k}_{22} = -D_{11}\left(\frac{m\pi}{L}\right)^4 - (k_w) - (k_g)\left(\frac{m\pi}{L}\right)^2 - (e_0a)^2(k_w)\left(\frac{m\pi}{L}\right)^2 - (e_0a)^2(k_g)\left(\frac{m\pi}{L}\right)^4,$$

$$\bar{m}_{11} = -I_0 - (e_0a)^2(I_0)\left(\frac{m\pi}{L}\right)^2, \bar{m}_{12} = \bar{m}_{21} = I_1\left(\frac{m\pi}{L}\right) + (e_0a)^2(I_1)\left(\frac{m\pi}{L}\right)^3,$$

$$\bar{m}_{22} = -I_0 - I_2\left(\frac{m\pi}{L}\right)^2 - I_0(e_0a)^2\left(\frac{m\pi}{L}\right)^2 - I_2(e_0a)^2\left(\frac{m\pi}{L}\right)^4.$$

By solving the eigenvalue problem mentioned in (41), the natural frequencies for the proposed model will be obtained for hinged-hinged (HH) boundary condition.

5. Numerical results and discussions

In this investigation, the FG nanobeam is considered to be composed of metal constituents as alpha-beta titanium alloy or titanium (Ti-6AL-4V) and ceramic constituent as zirconia or zirconium dioxide (ZrO_2). The geometrical properties or dimension of the specimen is taken from [Uzun and Yaylı 2020] as width $(b) = 400\,nm$, thickness $(h) = 100\,nm$, and length $(L) = 8000\,nm$, whereas the mechanical properties [Uzun and Yaylı 2020] are given as; zirconia or zirconium dioxide (ZrO_2): $E_U = 151\,GPa$, $\rho_U = 3000\,Kg.m^{-3}$, and $\upsilon_U = 0.3$ titanium (Ti-6AL-4V): $E_L = 105.7\,GPa$, $\rho_L = 4429\,Kg.m^{-3}$, and $\upsilon_L = 0.298$.

The Young's modulus and mass density are assumed to vary through the thickness in accordance with the power-law exponent model. At the same time, for the sake of convenience, the Poisson's ratio is taken constant throughout the thickness of the FG nanobeam, which is $\upsilon = 0.3$.

5.1. ***Validation.*** In this subsection, the validation of the present model has been conducted with other existing results in special cases. In this regard, the first three natural frequencies of the functionally graded nanobeam of HH boundary condition has been compared with [Uzun and Yaylı 2020], by neglecting the porosity and assuming Helmholtz nonlocal operator. The numerical results are computed for HH boundary condition by using both the Navier's technique (NT) and the Hermite–Ritz method (H-RM), which is demonstrated in Table 1. Likewise, the fundamental frequency parameter $\left(\lambda = \frac{\omega L^2}{h}\sqrt{\frac{\rho_L}{E_L}}\right)$ for HH boundary condition has been compared with [Pradhan and Chakraverty 2014; Aydogdu and Taskin 2007] by neglecting the porosity, nonlocal effect, and elastic foundation. Here the material is considered as Alumina (Al_2O_3), and Aluminum (Al), and the gradation is taken along Young's modulus only with $E_L = 70\,\text{GPa}$, $E_U = 380\,\text{GPa}$ and $\upsilon = 0.3$. The tabular result is depicted in Table 2, with various power-law exponent and aspect ratio. From these results, it is evident that the present model is accurate and copes well with the existing results in special cases.

5.2. ***Convergence.*** Through this subsection, the convergence of the present model has been carried out for first four natural frequencies of FG nanobeam by considering the power-law exponent $(k) = 1$, porosity volume fraction $(\vartheta) = 0.1$, non-dimensional nonlocal parameter $\alpha = e_0/L) = 0.1$, non-dimensional Winkler elastic constant $K_w = k_w L^4/(E_L I) = 40$, and non-dimensional Pasternak elastic constant $K_g =$

(α)	k	ω_1			ω_2			ω_3		
		[A]	Present (NT)	Present (H-RM)	[A]	Present (NT)	Present (H-RM)	[A]	Present (NT)	Present (H-RM)
0	0	10.2084	10.3295	10.3294	26.4247	27.1637	27.1640	51.9523	53.8340	54.5844
	2	8.6973	8.7744	8.7835	21.7885	22.2755	22.2756	42.0585	43.3202	43.9188
	4	8.4672	8.5437	8.5497	21.1040	21.5893	21.5894	40.6136	41.8749	42.4450
	6	8.3682	8.4449	8.4488	20.7909	21.2794	21.2795	39.9342	41.2065	41.7618
	8	8.3116	8.3883	8.3910	20.6024	21.0920	21.0921	39.5165	40.7935	41.3395
0.2	0	9.8519	9.9418	9.9418	21.2306	21.5871	21.5873	33.1951	33.8385	34.2605
	2	8.4376	8.4945	8.5012	17.9078	18.1366	18.1367	27.8374	28.2510	28.6052
	4	8.2208	8.2772	8.2816	17.4076	17.6348	17.6350	27.0354	27.4468	27.7885
	6	8.1285	8.1851	8.1880	17.1877	17.4160	17.4162	26.6971	27.0928	27.4283
	8	8.0763	8.1329	8.1349	17.0597	17.2882	172884	26.4697	26.8839	27.2159
0.4	0	9.4203	9.4710	9.4709	18.6882	18.8290	18.8292	28.0525	28.2723	28.6346
	2	8.1250	8.1568	8.1605	16.0475	16.1355	16.1357	24.0603	24.1955	24.5070
	4	7.9245	7.9559	7.9584	15.6414	15.7285	15.7287	23.4472	23.5814	23.8843
	6	7.8405	7.8721	7.8737	15.4695	15.5570	15.5572	23.1871	23.3220	23.6210
	8	7.7938	7.8253	7.8264	15.3729	15.4603	15.4605	23.0405	23.1754	23.4721

Table 1. Comparison of natural frequencies (in MHz) obtained by present study with [Uzun and Yaylı 2020], in special cases. [A] = [Uzun and Yaylı 2020].

(L/h)	k	0	0.1	1	2	10
5	[C]	6.847	6.499	4.821	4.251	3.737
	[B]	6.847	6.512	5.176	4.752	3.959
	Present	6.8470	6.5120	5.1764	4.7518	3.9597
20	[C]	6.951	6.599	4.907	4.334	3.804
	[B]	6.951	6.612	5.256	4.826	4.021
	Present	6.9516	6.6115	5.2562	4.8258	4.0208

Table 2. Comparison of frequency parameters obtained by present study with [Pradhan and Chakraverty 2014], [Aydogdu and Taskin 2007], in special cases. [B] = [Pradhan and Chakraverty 2014]; [C] = [Aydogdu and Taskin 2007].

$k_g L^2/(E_L I) = 40$. Variations of the first four natural frequencies have studied with no. of terms of the Hermite polynomial for HH, CH, and CC boundary conditions, which are depicted in Fig. 4, Fig. 5, and Fig. 6, respectively. Natural frequencies have also been computed from the closed-form solution by using Navier's technique (NT) for HH boundary condition and compared with the results of the Hermite–Ritz method (HRM) showing good agreement as illustrated in Figure 4. From these graphical results, it is quite evident that the first four natural frequencies of all the boundary conditions are attaining the convergence on or after no. of terms $(n) = 6$. Also, it may be observed that the CC boundary condition is approaching convergence faster than HH and CH boundary conditions.

5.3. ***Effect of bi-Helmholtz nonlocal elasticity.*** In this subsection, the influence of the bi-Helmholtz operator has been studied on natural frequencies of HH, CH, and CC boundary conditions as compared with

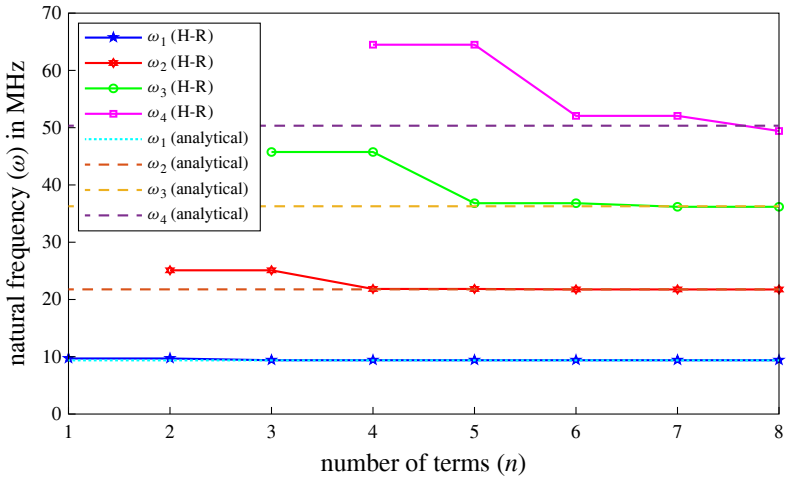

Figure 4. Variation of first four natural frequencies (ω) with no. of terms (n) and comparison with analytical results for HH boundary condition.

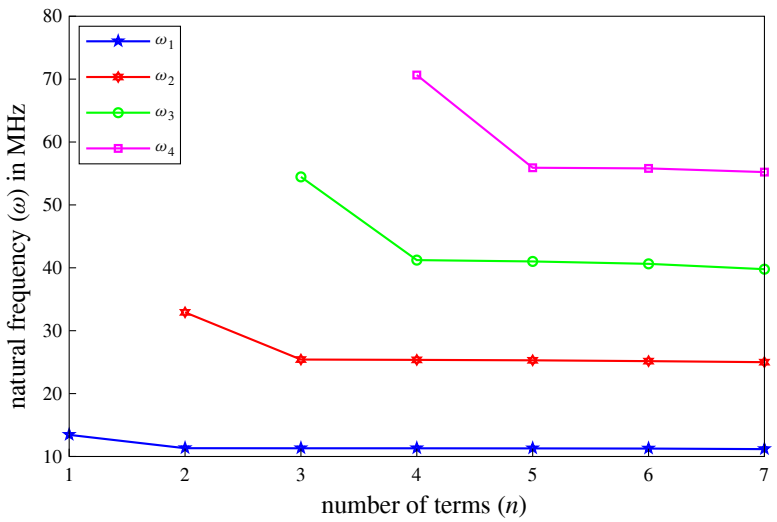

Figure 5. Variation of first four natural frequencies (ω) with no. of terms (n) for CH boundary condition.

the Helmholtz operator. For the computational purpose, power-law exponent $(k) = 1$, porosity volume fraction $(\vartheta) = 0.1$, non-dimensional Winkler elastic constant $(K_w) = 40$, and non-dimensional Winkler elastic constant $(K_g) = 40$ are taken into consideration. The graphical results in Figure 7 represent the variation of first four natural frequencies with respect to the nonlocal parameters (α) for Helmholtz and bi-Helmholtz operators, respectively, for HH boundary condition, and these results are computed by employing Navier's technique. Likewise, Figure 8 and Figure 9 illustrate the graphical results for CH and CC boundary conditions, respectively, which are computed using the Hermite–Ritz method. Here, the nonlocal parameters are assumed to vary from 0 to 0.5 with an increment of 0.1. From these graphical

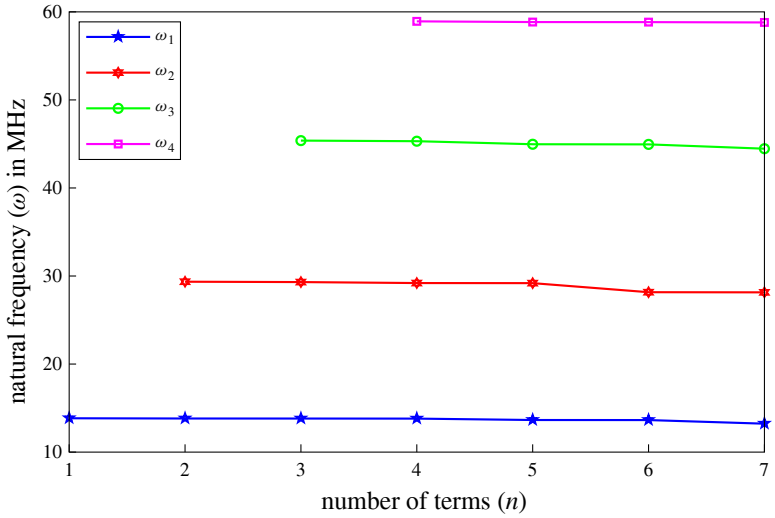

Figure 6. Variation of first four natural frequencies (ω) with no. of terms (n) for CC boundary condition.

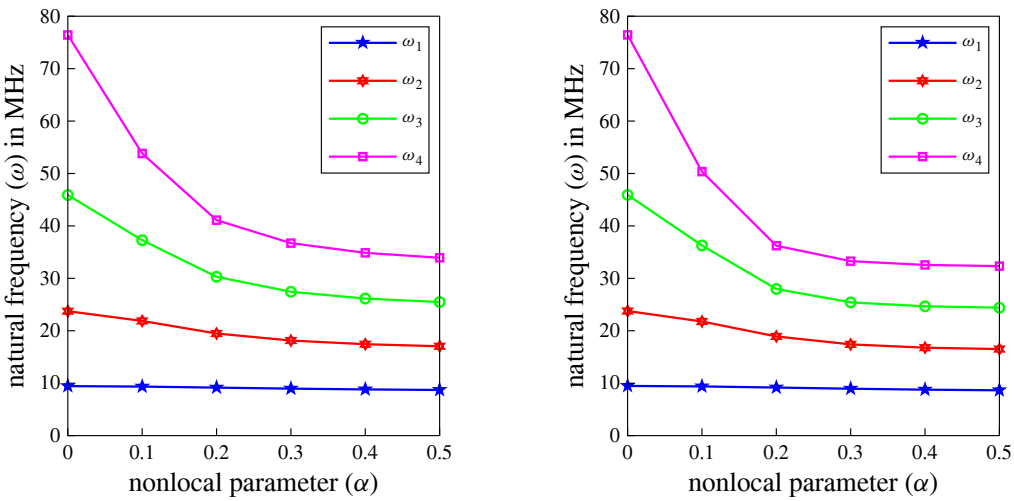

Figure 7. Variation of first four natural frequencies (ω) with nonlocal parameter (α) for HH boundary condition. Left: Helmholtz operator. Right: bi-Helmholtz operator.

results, it may clear that the natural frequencies for all modes and all boundary conditions are decreasing with increase in nonlocal parameters except for the first and second modes of CH and CC boundary conditions with respect to bi-Helmholtz operator. Also, this decrease is very significant in the case of higher modes.

5.4. ***Effect of porosity or porosity volume fraction index.*** This subsection is dedicated to investigating the effect of porosity or porosity volume fraction index (ϑ) on natural frequencies of FG porous nanobeam. Here the porosity volume fraction (ϑ) is varied from 0 to 0.5 with an increase of 0.1, and

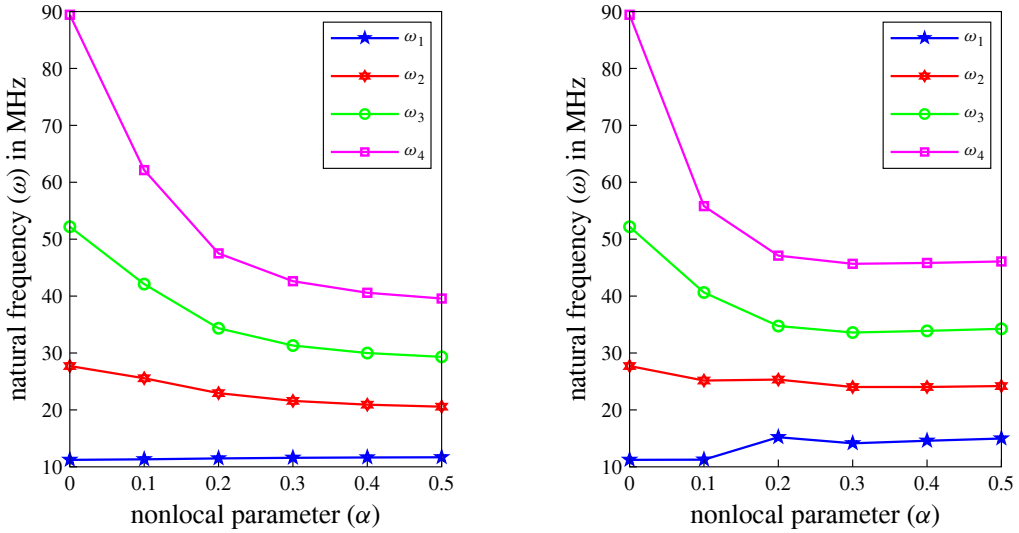

Figure 8. Variation of first four natural frequencies (ω) with nonlocal parameter (α) for CH boundary condition. Left: Helmholtz operator. Right: bi-Helmholtz operator.

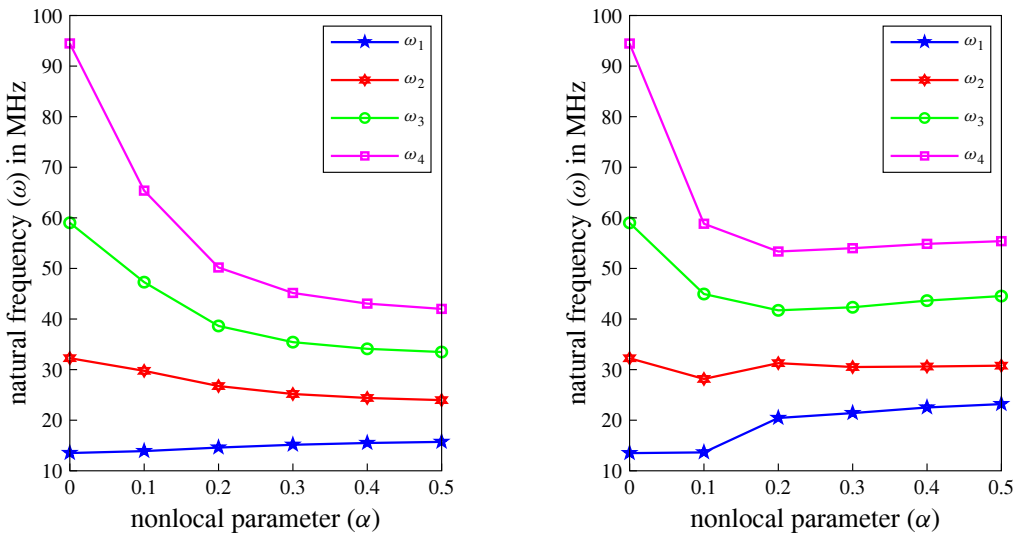

Figure 9. Variation of first four natural frequencies (ω) with nonlocal parameter (α) for CC boundary condition. Left: Helmholtz operator. Right: bi-Helmholtz operator.

other scaling parameters are taken as; power-law exponent (k) = 1, non-dimensional nonlocal parameter (α) = 0.1 non-dimensional Winkler elastic foundation (K_w) = 40, and non-dimensional Pasternak elastic foundation (K_g) = 40. In this regard, graphical and tabular results are given in Table 3 and Figs. 10–12. Natural frequencies of the FG nanobeam increase with the rise in porosity index, which is applicable for all modes, all boundary conditions, and in the case of both the bi-Helmholtz and Helmholtz operators. This is because although with more value of porosity parameter the stiffness of beam becomes lesser and

(a) hinged-hinged (HH) boundary condition

Porosity ϑ	ω_1		ω_2		ω_3		ω_4	
	Ho	**B-Ho**	**Ho**	**B-Ho**	**Ho**	**B-Ho**	**Ho**	**B-Ho**
0	8.9954	8.9933	21.2976	21.1592	36.5307	35.4690	52.9015	49.3444
0.1	9.3787	9.3766	21.8957	21.7614	37.2957	36.2590	53.8264	50.3436
0.2	9.8364	9.8345	22.6194	22.4899	38.2265	37.2193	54.9544	51.5600
0.3	10.3948	10.3930	23.5144	23.3904	39.3847	38.4129	56.3614	53.0744
0.4	11.0950	11.0933	24.6526	24.5353	40.8676	39.9393	58.1674	55.0143
0.5	12.0053	12.0038	26.1546	26.0456	42.8384	41.9655	60.5741	57.5937

(b) clamped-hinged (CH) boundary condition

Porosity ϑ	ω_1		ω_2		ω_3		ω_4	
	Ho	**B-Ho**	**Ho**	**B-Ho**	**Ho**	**B-Ho**	**Ho**	**B-Ho**
0	10.9378	10.8823	24.9546	24.5642	41.3135	39.8005	61.1409	54.8442
0.1	11.3221	11.2586	25.5648	25.1599	42.1072	40.6310	62.1339	55.8055
0.2	11.7839	11.7097	26.3055	25.8800	43.0744	41.6392	63.3464	56.9640
0.3	12.3509	12.2622	27.2248	26.7690	44.2801	42.8905	64.8610	58.3899
0.4	13.0667	12.9572	28.3985	27.8965	45.8267	44.4877	66.8086	60.1930
0.5	14.0039	13.8634	29.9541	29.3777	47.8868	46.6030	69.4088	62.5552

(c) clamped-clamped (CC) boundary condition

Porosity ϑ	ω_1		ω_2		ω_3		ω_4	
	Ho	**B-Ho**	**Ho**	**B-Ho**	**Ho**	**B-Ho**	**Ho**	**B-Ho**
0	13.4994	13.2904	29.1138	27.7048	46.4458	44.1091	64.3550	57.9714
0.1	13.8795	13.6388	29.7438	28.1601	47.2742	44.9480	65.3712	58.8354
0.2	14.3390	14.0564	30.5101	28.6844	48.2846	45.9578	66.6120	59.7990
0.3	14.9070	14.5671	31.4636	29.2890	49.5452	47.1975	68.1620	60.8655
0.4	15.6290	15.2076	32.6841	29.9802	51.1640	48.7578	70.1544	62.0347
0.5	16.5814	16.0379	34.3065	30.7424	53.3224	50.7858	72.8136	63.3195

Table 3. Natural frequencies (MHz) for Helmholtz operator (Ho) and bi-Helmholtz operators (B-Ho) with respect to porosity volume fraction index.

also its cross-sectional moment of inertia reduces, the reduction rate of inertia is more than that of the stiffness in the beam. It should be noted that other types of porosity may have opposite result. Also, it may be noted that the increase in natural frequencies is more significant in higher modes. The results obtained by both the bi-Helmholtz and Helmholtz operators are almost equal in lower modes where it can be clearly distinguished for higher modes, Helmholtz operator possesses more natural frequencies than bi-Helmholtz, and this trend is valid in all the boundary conditions.

5.5. ***Effect of Power-law exponent.*** In this subsection, the influence of the power-law exponent (k) has been studied on the natural frequencies of FG nanobeam. The power-law exponent (k) is taken as 0,

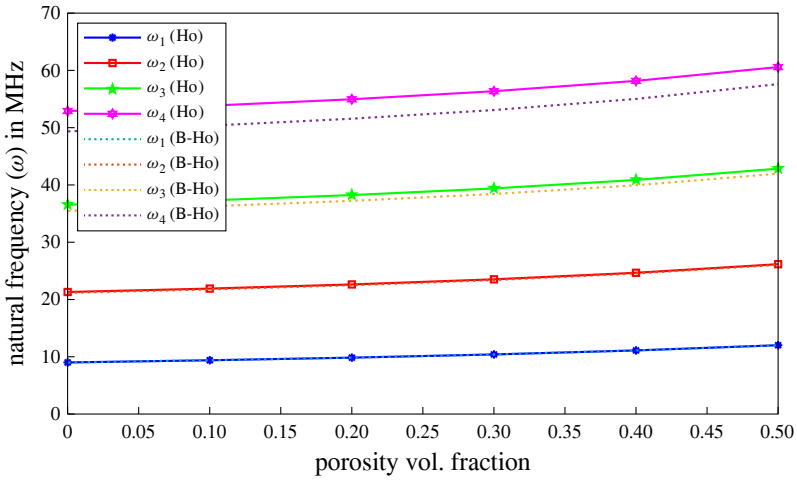

Figure 10. Variation of first four natural frequencies (ω) with porosity volume fraction index (ϑ) for HH boundary condition.

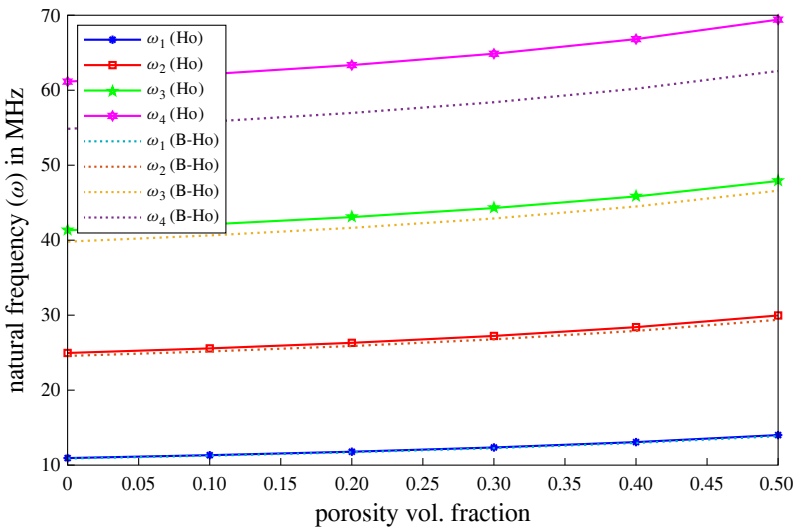

Figure 11. Variation of first four natural frequencies (ω) with porosity volume fraction index (ϑ) for CH boundary condition.

0.2, 0.5, 1, 2, 3, 5, with porosity volume fraction (ϑ) = 0.1, non-dimensional parameter (α) = 0.1, non-dimensional Winkler elastic constant (K_w) = 40, and non-dimensional Pasternak elastic constant (K_g) = 40. Table 4(a–c) and Figs. (13–15) represent the tabular and graphical results for HH, CH, and CC edges with respect to both the bi-Helmholtz and Helmholtz operators. All the computations for HH edge are carried out by using Navier's technique, while the Hermite–Ritz method is used for other boundary conditions. These results clearly reveals that the natural frequencies of all modes and all boundary conditions decrease with an increase in the power-law exponent (k), that means when the beam is purely ceramic i.e., at $k = 0$ possesses the highest natural frequencies and when the beam is

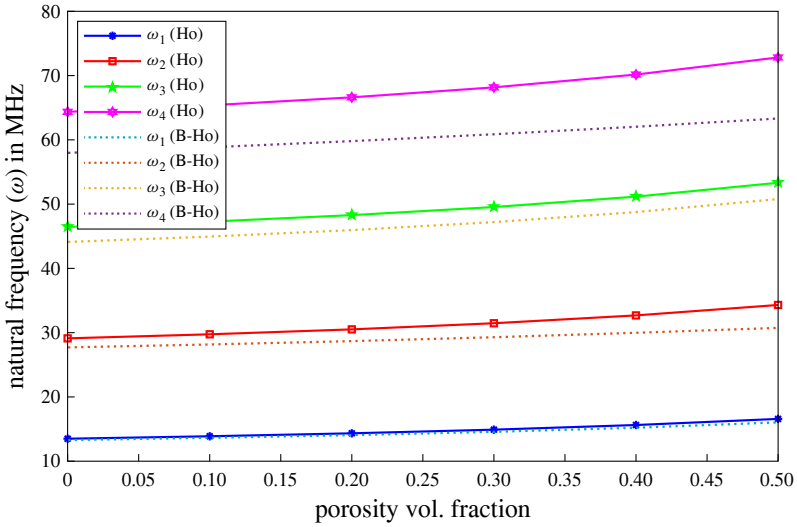

Figure 12. Variation of first four natural frequencies (ω) with porosity volume fraction index (ϑ) for CC boundary condition.

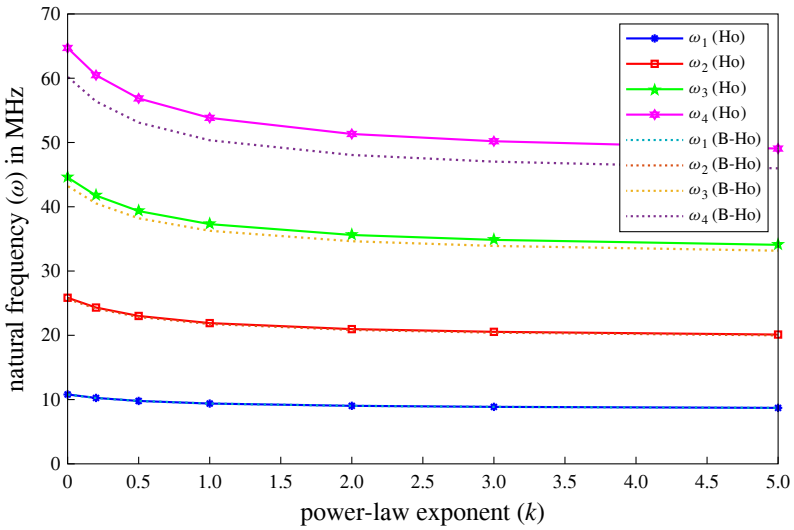

Figure 13. Variation of first four natural frequencies (ω) with power-law index (k) for HH edge.

purely metal i.e., at $k = \infty$ retains the lowest natural frequencies. This reduction is due to the fact that as we go on increasing the power-law exponent (k), the beam becomes more flexible, retaining less natural frequencies. This reduction is more remarkable with higher modes and at $k < 2$.

5.6. ***Effect of elastic foundation.*** This subsection is devoted to analyzing the effect of elastic foundation, i.e., non-dimensional Winkler (K_w), and Pasternak (K_g) elastic parameters on natural frequencies of the FG nanobeam. In this regard, a comprehensive study has been undertaken by varying the elastic

(a) hinged-hinged (HH) boundary condition

k	ω_1		ω_2		ω_3		ω_4	
	Ho	**B-Ho**	**Ho**	**B-Ho**	**Ho**	**B-Ho**	**Ho**	**B-Ho**
0	10.7925	10.7898	25.8422	25.6668	44.5660	43.2276	64.7052	60.2300
0.2	10.2533	10.2509	24.3164	24.1573	41.7427	40.5234	60.4730	56.3892
0.5	9.7849	9.7827	23.0058	22.8605	39.3257	38.2072	56.8548	53.1023
1	9.3787	9.3766	21.8957	21.7614	37.2957	36.2590	53.8264	50.3436
2	9.0255	9.0236	20.9608	20.8352	35.6073	34.6351	51.3214	48.0518
3	8.8637	8.8619	20.5373	20.4155	34.8459	33.9022	50.1941	47.0188
5	8.7060	8.7042	20.1140	19.9962	34.0766	33.1631	49.0495	45.9742

(b) clamped-hinged (CH) boundary condition

k	ω_1		ω_2		ω_3		ω_4	
	Ho	**B-Ho**	**Ho**	**B-Ho**	**Ho**	**B-Ho**	**Ho**	**B-Ho**
0	13.1944	13.1310	30.3566	29.8811	50.4572	48.5432	74.8310	67.0271
0.2	12.4736	12.4098	28.4981	28.0498	47.2095	45.4679	69.8833	62.6547
0.5	11.8530	11.7892	26.9066	26.4819	44.4338	42.8388	65.6618	58.9263
1	11.3221	11.2586	25.5648	25.1599	42.1072	40.6310	62.1339	55.8055
2	10.8668	10.8035	24.4403	24.0509	40.1747	38.7905	59.2147	53.2083
3	10.6584	10.5948	23.9305	23.5472	39.3021	37.9573	57.8970	52.0277
5	10.4516	10.3871	23.4172	23.0390	38.4169	37.1130	56.5535	50.8202

(c) clamped-clamped (CC) boundary condition

k	ω_1		ω_2		ω_3		ω_4	
	Ho	**B-Ho**	**Ho**	**B-Ho**	**Ho**	**B-Ho**	**Ho**	**B-Ho**
0	16.3750	16.1390	35.4890	33.8613	56.7848	53.8613	78.8026	70.9212
0.2	15.4095	15.1707	33.2565	31.6420	53.0834	50.3948	73.5705	66.2187
0.5	14.5811	14.3408	31.3478	29.7477	49.9212	47.4324	69.1034	62.2012
1	13.8795	13.6388	29.7438	28.1601	47.2742	44.9480	65.3712	58.8354
2	13.2872	13.0467	28.4052	26.8338	45.0807	42.8800	62.2886	56.0261
3	13.0181	12.7767	27.7990	26.2265	44.0912	41.9427	60.9000	54.7382
5	12.7484	12.5044	27.1856	25.5997	43.0856	40.9884	59.4853	53.4032

Table 4. Natural frequencies (MHz) for Helmholtz operator and bi-Helmholtz operator with respect to power-law index.

parameters, and the results are noted in tabular form, which can be seen in Table 5. The tabular results are incorporated for HH, CH, and CC boundary conditions with power-law exponent $(k) = 1$, porosity volume fraction $(\vartheta) = 0.1$, and nonlocal parameter $(\alpha) = 0.1$. Different combinations for elastic foundations are considered, and results are noted for the first four natural frequencies by considering both bi-Helmholtz and Helmholtz operators. From these results, it's quite clear that the natural frequencies increase with the increase in elastic constants except the second mode of CC edge, where some irregularities occur with

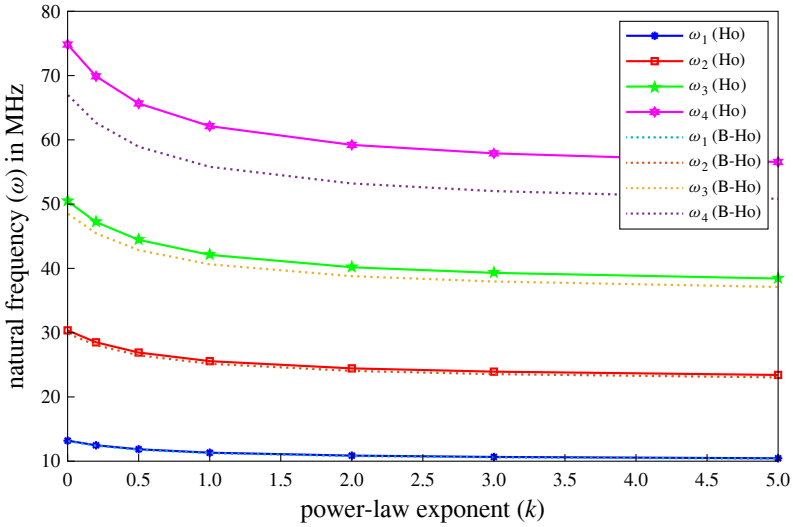

Figure 14. Variation of first four natural frequencies (ω) with power-law index (k) for CH edge.

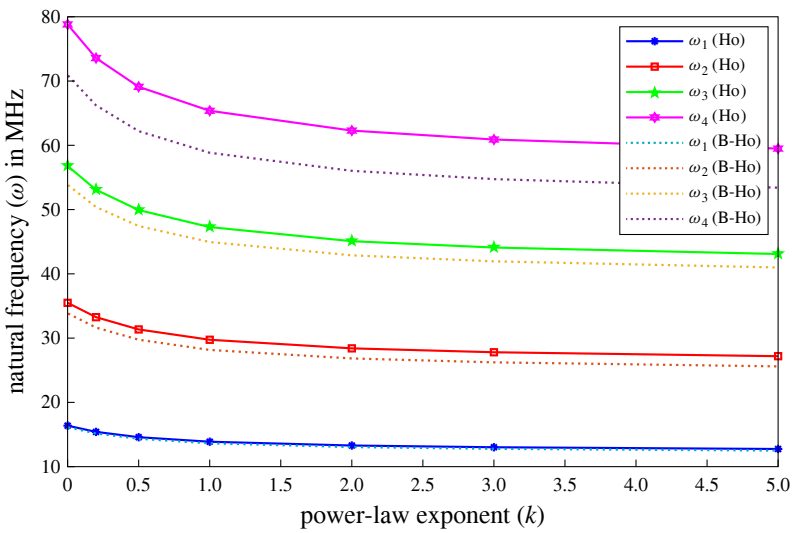

Figure 15. Variation of first four natural frequencies (ω) with power-law index (k) for CC edge.

few combinations for elastic foundations, and these growths are more remarkable with higher modes. The increase in natural frequencies can be explained by the fact that the higher values of elastic parameters make the beam stiffer resulting higher value of natural frequencies.

(a) hinged-hinged (HH) boundary condition

(K_w, K_g)	ω_1		ω_2		ω_3		ω_4	
	Ho	B-Ho	Ho	B-Ho	Ho	B-Ho	Ho	B-Ho
(0, 0)	4.1382	4.1336	14.6881	14.4871	28.3939	27.0178	43.1712	38.7421
(50, 0)	5.0270	5.0232	14.9627	14.7655	28.5369	27.1680	43.2652	38.8469
(100, 0)	5.7807	5.7774	15.2324	15.0387	28.6791	27.3173	43.3591	38.9514
(200, 0)	7.0504	7.0477	15.7579	15.5708	28.9614	27.6136	43.5462	39.1595
(500, 0)	9.9290	9.9270	17.2385	17.0676	29.7924	28.4839	44.1027	39.7774
(700, 0)	11.4529	11.4512	18.1587	17.9965	30.3338	29.0497	44.4698	40.1841
(1000, 0)	13.4180	13.4166	19.4575	19.3063	31.1281	29.8782	45.0149	40.7865
(0, 50)	9.8753	9.8734	23.1776	23.0508	39.1027	38.1152	56.1029	52.7706
(0, 100)	13.3386	13.3372	29.3030	29.2027	47.4534	46.6430	66.5682	63.7849
(0, 200)	18.4042	18.4032	38.7503	38.6746	60.8065	60.1762	83.6594	81.4622
(0, 500)	28.6548	28.6542	58.5692	58.5191	89.6340	89.2076	121.2501	119.7446
(0, 700)	33.8037	33.8031	68.6746	68.6319	104.5250	104.1596	140.8428	139.5489
(0, 1000)	40.3122	40.3118	81.5166	81.4807	123.5406	123.2316	165.9499	164.8531
(50, 50)	10.2795	10.2776	23.3526	23.2267	39.2066	38.2218	56.1753	52.8475
(100, 100)	13.9360	13.9346	29.5795	29.4803	47.6246	46.8171	66.6902	63.9123
(200, 200)	19.2691	19.2681	39.1683	39.0934	61.0736	60.4461	83.8535	81.6615
(500, 500)	30.0426	30.0420	59.2603	59.2108	90.0868	89.6626	121.5849	120.0836
(700, 700)	35.4504	35.4499	69.4996	69.4574	105.0685	104.7050	141.2463	139.9561
$(10^3, 10^3)$	42.2847	42.2842	82.5095	82.4740	124.1976	123.8902	166.4391	165.3455

(b) clamped-hinged (CH) boundary condition

(K_w, K_g)	ω_1		ω_2		ω_3		ω_4	
	Ho	B-Ho	Ho	B-Ho	Ho	B-Ho	Ho	B-Ho
(0, 0)	6.4253	6.4083	18.3745	17.9859	32.9521	30.8534	50.7756	43.9596
(50, 0)	7.0307	7.0151	18.5947	18.2108	33.0753	30.9850	50.8555	44.0520
(100, 0)	7.5879	7.5734	18.8124	18.4330	33.1981	31.1160	50.9354	44.1441
(200, 0)	8.5946	8.5819	19.2403	18.8696	33.4423	31.3764	51.0946	44.3278
(500, 0)	11.0789	11.0690	20.4705	20.1224	34.1643	32.1448	51.5695	44.8743
(700, 0)	12.4629	12.4541	21.2511	20.9160	34.6373	32.6470	51.8837	45.2350
(1000, 0)	14.2898	14.2821	22.3709	22.0528	35.3349	33.3862	52.3514	45.7707
(0, 50)	11.8992	11.8106	26.9144	26.4604	44.0082	42.5950	64.5997	58.1044
(0, 100)	15.5169	15.2826	33.3305	32.5184	52.8007	51.4876	75.9482	68.0455
(0, 200)	20.9356	20.3471	43.4007	41.5228	67.0109	65.4434	94.6476	80.4808
(0, 500)	32.0856	30.2815	64.8135	58.3572	97.9710	93.0027	136.1183	96.3964
(0, 700)	37.7273	35.0532	75.7982	65.7464	114.0332	101.8837	157.8232	111.2155
(0, 1000)	44.8781	40.8570	89.7895	74.2754	134.5788	114.0412	185.6826	130.8656
(50, 50)	12.2367	12.1506	27.0652	26.6138	44.1006	42.6904	64.6625	58.1743
(100, 100)	16.0332	15.8066	33.5739	32.7678	52.9545	51.6454	76.0551	68.1649
(200, 200)	21.6999	21.1326	43.7743	41.9131	67.2533	65.6915	94.8191	80.6828
(500, 500)	33.3308	31.5980	65.4386	59.0508	98.3853	93.4393	136.4165	96.8176
(700, 700)	39.2096	36.6439	76.5464	66.6078	114.5315	102.4415	158.1832	111.7264
$(10^3, 10^3)$	46.6579	42.8044	90.6917	75.3639	135.1820	114.7528	186.1197	131.4858

(c) clamped-clamped (CC) boundary condition

(K_w, K_g)	ω_1		ω_2		ω_3		ω_4	
	Ho	B-Ho	Ho	B-Ho	Ho	B-Ho	Ho	B-Ho
(0, 0)	9.2819	9.2306	22.4127	21.7182	37.7523	34.6837	53.7256	45.8169
(50, 0)	9.7108	9.6618	22.5936	21.9048	37.8598	34.8008	53.8012	45.9054
(100, 0)	10.1215	10.0745	22.7731	22.0898	37.9671	34.9174	53.8766	45.9938
(200, 0)	10.8966	10.8529	23.1278	22.4553	38.1807	35.1496	54.0272	46.1700
(500, 0)	12.9463	12.9096	24.1607	23.5178	38.8145	35.8369	54.4764	46.6946
(700, 0)	14.1488	14.1152	24.8254	24.2002	39.2314	36.2880	54.7738	47.0411
(1000, 0)	15.7816	15.7515	25.7904	25.1892	39.8485	36.9542	55.2170	47.5562
(0, 50)	14.5242	14.1896	31.1770	29.0606	49.2867	46.9236	67.9123	60.6592
(0, 100)	18.2933	17.4110	37.9571	31.6656	58.5964	55.4373	79.6126	65.9577
(0, 200)	24.1051	21.9815	48.7571	27.9550	73.7730	67.9235	98.9483	74.2611
(0, 500)	36.3111	30.8467	72.0062	93.8346	107.0957	100.0219	141.9482	134.5057
(0, 700)	42.5415	35.2581	84.0015	107.3578	124.4489	114.8826	164.4844	155.6561
(0, 1000)	50.4634	40.8676	99.3133	124.8369	146.6785	134.3457	193.4267	182.9408
(50, 50)	14.8019	14.4738	31.3073	29.2003	49.3692	47.0102	67.9720	60.7262
(100, 100)	18.7332	17.8728	38.1710	31.9218	58.7350	55.5839	79.7146	66.0810
(200, 200)	24.7717	22.7106	49.0899	28.5321	73.9932	68.1627	99.1123	74.4800
(500, 500)	37.4159	32.1400	72.5693	94.2673	107.4748	100.4278	142.2341	134.8075
(700, 700)	43.8613	36.8399	84.6772	107.8871	124.9056	115.3773	164.8298	156.0211
$(10^3, 10^3)$	52.0525	42.8145	100.1296	125.4871	147.2320	134.9499	193.8462	183.3844

Table 5. Natural frequencies (MHz) for Helmholtz operator and bi-Helmholtz operator with respect to elastic foundation.

6. Concluding remarks

In this investigation, a computationally efficient method, namely the Hermite–Ritz method has been employed to compute the frequency response of the proposed model. bi-Helmholtz type of nonlocal operator has been incorporated to seizure the effect small scale effect. HH, CH, and CC boundary conditions are considered in this investigation, and closed-form solution is also obtained for HH boundary condition by utilizing Navier's technique. Validation and convergence of the proposed model/and method have been conducted successfully. Conclusions obtained from the parametric study are summarized as follow;

- The natural frequencies are decreasing with the increase in the nonlocal parameters except for the first and second modes of CH and CC boundary conditions concerning bi-Helmholtz operator. Also, this decrease is very significant in the case of higher modes.
- Natural frequencies of the FG nanobeam increase with the rise in porosity volume fraction index and the increase in natural frequencies is more substantial in higher modes.

- The results obtained by both the bi-Helmholtz and Helmholtz operators are almost equal in lower modes. But, in higher modes, the Helmholtz operator possesses more natural frequencies than bi-Helmholtz operator.
- The natural frequencies reduce with the increase in the power-law exponent (k), which means at $k = 0$ the beam possesses the highest natural frequencies and at $k = \infty$ the beam retains the lowest natural frequencies.
- The natural frequencies increase with the increase in elastic parameters except for the second mode of CC edge, where some irregularities occur with few combinations for elastic foundations, and these growths are more remarkable with higher modes.

Acknowledgment

The first two authors are very much thankful to Defence Research & Development Organization (DRDO), New Delhi, India (Sanction Code: DG/TM/ERIPR/GIA/17-18/0129/020) for the funding to carry out the present research work.

References

[Ansari et al. 2013] R. Ansari, V. Mohammadi, M. F. Shojaei, R. Gholami, and S. Sahmani, "Postbuckling characteristics of nanobeams based on the surface elasticity theory", *Compos. B Eng.* **55** (2013), 240–246.

[Ansari et al. 2015] R. Ansari, T. Pourashraf, and R. Gholami, "An exact solution for the nonlinear forced vibration of functionally graded nanobeams in thermal environment based on surface elasticity theory", *Thin-Walled Struct.* **93** (2015), 169–176.

[Arefi and Zenkour 2017] M. Arefi and A. M. Zenkour, "Analysis of wave propagation in a functionally graded nanobeam resting on visco-Pasternak's foundation", *Theoretical and Applied Mechanics Letters* **7** (2017), 145–151.

[Aria and Friswell 2019] A. I. Aria and M. I. Friswell, "A nonlocal finite element model for buckling and vibration of functionally graded nanobeams", *Compos. B Eng.* **166** (2019), 233–246.

[Aydogdu and Taskin 2007] M. Aydogdu and V. Taskin, "Free vibration analysis of functionally graded beams with simply supported edges", *Mater. Des.* **28** (2007), 1651–1656.

[Barretta et al. 2018] R. Barretta, F. Fabbrocino, R. Luciano, and F. M. de Sciarra, "Closed-form solutions in stress-driven two-phase integral elasticity for bending of functionally graded nano-beams", *Physica E* **97** (2018), 13–30.

[Bekhadda et al. 2019] A. Bekhadda, I. Bensaid, A. Cheikh, and B. Kerboua, "Static buckling and vibration analysis of continuously graded ceramic-metal beams using a refined higher order shear deformation theory", *Multidisc. Model. Mater. Struct.* **15**:6 (2019), 1152–1169.

[Chen et al. 2020] W. R. Chen, C. S. Chen, and H. Chang, "Thermal Buckling Analysis of Functionally Graded Euler-Bernoulli Beams with Temperature-dependent Properties", *Journal of Applied and Computational Mechanics* **6** (2020), 457–70.

[Ebrahimi and Salari 2015] F. Ebrahimi and E. Salari, "Nonlocal thermo-mechanical vibration analysis of functionally graded nanobeams in thermal environment", *Acta Astronaut.* **113** (2015), 29–50.

[Eltaher et al. 2012] M. A. Eltaher, S. A. Emam, and F. F. Mahmoud, "Free vibration analysis of functionally graded size-dependent nanobeams", *Appl. Math. Comput.* **218** (2012), 7406–7420.

[Eringen 2002] A. C. Eringen, *Nonlocal continuum field theories*, Springer, 2002.

[Esmaeili and Beni 2019] M. Esmaeili and Y. T. Beni, "Vibration and Buckling Analysis of Functionally Graded Flexoelectric Smart Beam", *Journal of Applied and Computational Mechanics* **5** (2019), 900–17.

[Hadi et al. 2018] A. Hadi, M. Z. Nejad, and M. Hosseini, "Vibrations of three-dimensionally graded nanobeams", *Int. J. Eng. Sci.* **128** (2018), 12–23.

[Hamed et al. 2016] M. A. Hamed, M. A. Eltaher, A. M. Sadoun, and K. H. Almitani, "Free vibration of symmetric and sigmoid functionally graded nanobeams", *Appl. Phys. A Mater. Sci. Process.* **122** (2016), art. id. 829.

[Hosseini and Rahmani 2016] S. A. H. Hosseini and O. Rahmani, "Thermomechanical vibration of curved functionally graded nanobeam based on nonlocal elasticity", *J. Therm. Stresses* **39** (2016), 1252–1267.

[Hosseini-Hashemi et al. 2014] S. Hosseini-Hashemi, R. Nazemnezhad, and M. Bedroud, "Surface effects on nonlinear free vibration of functionally graded nanobeams using nonlocal elasticity", *Appl. Math. Model.* **38** (2014), 3538–3553.

[Jena et al. 2019a] S. K. Jena, S. Chakraverty, and M. Malikan, "Implementation of Haar wavelet, higher order Haar wavelet, and differential quadrature methods on buckling response of strain gradient nonlocal beam embedded in an elastic medium", *Eng. Comput.* (online publication November 2019).

[Jena et al. 2019b] S. K. Jena, S. Chakraverty, M. Malikan, and F. Tornabene, "Stability analysis of single-walled carbon nanotubes embedded in winkler foundation placed in a thermal environment considering the surface effect using a new refined beam theory", *Mech. Based Des. Struct. Mach.* (online publication December 2019).

[Jena et al. 2020a] S. K. Jena, S. Chakraverty, and M. Malikan, "Implementation of non-probabilistic methods for stability analysis of nonlocal beam with structural uncertainties", *Eng. Comput.* (online publication February 2020).

[Jena et al. 2020b] S. K. Jena, S. Chakraverty, and M. Malikan, "Vibration and buckling characteristics of nonlocal beam placed in a magnetic field embedded in Winkler–Pasternak elastic foundation using a new refined beam theory: an analytical approach", *Europ. Phys. J. Plus* **135** (2020), art. id. 164.

[Jouneghani et al. 2018] F. Z. Jouneghani, R. Dimitri, and F. Tornabene, "Structural response of porous FG nanobeams under hygro-thermo-mechanical loadings", *Compos. B Eng.* **152** (2018), 71–78.

[Karami and Janghorban 2019] B. Karami and M. Janghorban, "A new size-dependent shear deformation theory for free vibration analysis of functionally graded/anisotropic nanobeams", *Thin-Walled Struct.* **143** (2019), 106227.

[Khaniki 2019] H. B. Khaniki, "On vibrations of FG nanobeams", *Int. J. Eng. Sci.* **135** (2019), 23–36.

[Khorshidi and Shariati 2016] M. A. Khorshidi and M. Shariati, "Free vibration analysis of sigmoid functionally graded nanobeams based on a modified couple stress theory with general shear deformation theory", *Journal of the Brazilian Society of Mechanical Sciences and Engineering* **38** (2016), 2607–2619.

[Koizumi 1994] M. Koizumi, "The concept of FGM, Ceramic Transactions", *Functionally Gradient Materials* **34** (1994), 3–10.

[Koutsoumaris and Eptaimeros 2018] C. C. Koutsoumaris and K. G. Eptaimeros, "A research into bi-Helmholtz type of nonlocal elasticity and a direct approach to Eringen's nonlocal integral model in a finite body", *Acta Mech.* **229** (2018), 3629–3649.

[Lazar et al. 2006] M. Lazar, G. A. Maugin, and E. C. Aifantis, "On a theory of nonlocal elasticity of bi-Helmholtz type and some applications", *Int. J. Solids Struct.* **43** (2006), 1404–1421.

[Lim et al. 2015] C. W. Lim, G. Zhang, and J. N. Reddy, "A higher-order nonlocal elasticity and strain gradient theory and its applications in wave propagation", *J. Mech. Phys. Solids* **78** (2015), 298–313.

[Malikan 2017] M. Malikan, "Electro-mechanical shear buckling of piezoelectric nanoplate using modified couple stress theory based on simplified first order shear deformation theory", *Appl. Math. Model.* **48** (2017), 196–207.

[Malikan et al. 2020] M. Malikan, M. Krasheninnikov, and V. A. Eremeyev, "Torsional stability capacity of a nano-composite shell based on a nonlocal strain gradient shell model under a three-dimensional magnetic field", *Int. J. Eng. Sci.* **148** (2020), 103210.ss.

[Mindlin 1965] R. D. Mindlin, "Second gradient of strain and surface-tension in linear elasticity", *Int. J. Solids Struct.* **1** (1965), 417–438.

[Mirjavadi et al. 2018] S. S. Mirjavadi, B. M. Afshari, M. Khezel, N. Shafiei, S. Rabby, and M. Kordnejad, "Nonlinear vibration and buckling of functionally graded porous nanoscaled beams", *J. Brazil. Soc. Mech. Sci. Eng.* **40** (2018), art. id. 352.

[Nazemnezhad and Hosseini-Hashemi 2014] R. Nazemnezhad and S. Hosseini-Hashemi, "Nonlocal nonlinear free vibration of functionally graded nanobeams", *Compos. Struct.* **110** (2014), 192–199.

[Pradhan and Chakraverty 2014] K. K. Pradhan and S. Chakraverty, "Effects of different shear deformation theories on free vibration of functionally graded beams", *Int. J. Mech. Sci.* **82** (2014), 149–160.

[Reddy 2007] J. N. Reddy, "Nonlocal theories for bending, buckling and vibration of beams", *Int. J. Eng. Sci.* **45** (2007), 288–307.

[Ş. S. Bayın 2018] Ş. S. Bayın, *Mathematical methods in science and engineering*, 2nd ed., Wiley, 2018.

[Saffari et al. 2017] S. Saffari, M. Hashemian, and D. Toghraie, "Dynamic stability of functionally graded nanobeam based on nonlocal Timoshenko theory considering surface effects", *Physica B: Condensed Matter* **520** (2017), 97–105.

[Sedighi and Malikan 2020] H. M. Sedighi and M. Malikan, "Stress-driven nonlocal elasticity for nonlinear vibration characteristics of carbon/boron-nitride hetero-nanotube subject to magneto-thermal environment", *Physica Scr.* **95** (2020), 055218.

[Shafiei et al. 2016] N. Shafiei, M. Kazemi, M. Safi, and M. Ghadiri, "Nonlinear vibration of axially functionally graded non-uniform nanobeams", *Int. J. Eng. Sci.* **106** (2016), 77–94.

[Shahsavari et al. 2018] D. Shahsavari, M. Shahsavari, L. Li, and B. Karami, "A novel quasi-3D hyperbolic theory for free vibration of FG plates with porosities resting on Winkler/Pasternak/Kerr foundation", *Aerosp. Sci. Technol.* **72** (2018), 134–149.

[Sharabiania and Yazdi 2013] P. A. Sharabiania and M. R. H. Yazdi, "Nonlinear free vibrations of functionally graded nanobeams with surface effects", *Compos. B Eng.* **45** (2013), 581–586.

[Simsek 2016] M. Simsek, "Nonlinear free vibration of a functionally graded nanobeam using nonlocal strain gradient theory and a novel Hamiltonian approach", *Int. J. Eng. Sci.* **105** (2016), 12–27.

[Simsek 2019] M. Simsek, "Some closed-form solutions for static, buckling, free and forced vibration of functionally graded (FG) nanobeams using nonlocal strain gradient theory", *Compos. Struct.* **224** (2019), 11104.

[Uzun and Yaylı 2019] B. Uzun and M. O. Yaylı, "Finite Element Model of Functionally Graded Nanobeam for Free Vibration Analysis", *International Journal of Engineering and Applied Sciences* **11** (2019), 387–400.

[Uzun and Yaylı 2020] B. Uzun and M. O. Yaylı, "Nonlocal vibration analysis of Ti-6Al-4V/ZrO2 functionally graded nanobeam on elastic matrix", *Arabian Journal of Geosciences* **13** (2020), 1–10.

[Vosoughi 2016] A. R. Vosoughi, "Nonlinear Free Vibration of Functionally Graded Nanobeams on Nonlinear Elastic Foundation", *Iranian Journal of Science and Technology, Transactions of Civil Engineering* **40** (2016), 23–32.

[Vu-Bac et al. 2016] N. Vu-Bac, T. Lahmer, X. Zhuang, T. Nguyen-Thoi, and T. Rabczuk, "A software framework for probabilistic sensitivity analysis for computationally expensive models", *Adv. Eng. Softw.* **100** (2016), 19–31.

[Wattanasakulpong and Ungbhakorn 2014] N. Wattanasakulpong and V. Ungbhakorn, "Linear and nonlinear vibration analysis of elastically restrained ends FGM beams with porosities", *Aerosp. Sci. Technol.* **32** (2014), 111–120.

[Zeighampour and Beni 2015] H. Zeighampour and Y. T. Beni, "Free vibration analysis of axially functionally graded nanobeam with radius varies along the length based on strain gradient theory", *Appl. Math. Model.* **39** (2015), 5354–5369.

Received 17 Mar 2020. Revised 10 Apr 2020. Accepted 23 Apr 2020.

SUBRAT KUMAR JENA: sjena430@gmail.com
Department of Mathematics, National Institute of Technology Rourkela, Unit 1, Rourkela, India

SNEHASHISH CHAKRAVERTY: sne_chak@yahoo.com
Department of Mathematics, National Institute of Technology Rourkela, Unit 1, Rourkela, India

MOHAMMAD MALIKAN: mohammad.malikan@pg.edu.pl
Department of Mechanics of Materials and Structures, Gdansk University of Technology, ul. G. Narutowicza 11/12, Gdansk, Poland

HAMID MOHAMMAD-SEDIGHI: h.msedighi@scu.ac.ir
Mechanical Engineering Department, Faculty of Engineering, Shahid Chamran University of Ahvaz, Ahvaz, Iran

and

Drilling Center of Excellence and Research Center, Shahid Chamran University of Ahvaz, Ahvaz, Iran

SUBMISSION GUIDELINES

ORIGINALITY

Authors may submit manuscripts in PDF format online at the Submissions page. Submission of a manuscript acknowledges that the manuscript is original and has neither previously, nor simultaneously, in whole or in part, been submitted elsewhere. Information regarding the preparation of manuscripts is provided below. Correspondence by email is requested for convenience and speed. For further information, write to contact@msp.org.

LANGUAGE

Manuscripts must be in English. A brief abstract of about 150 words or less must be included. The abstract should be self-contained and not make any reference to the bibliography. Also required are keywords and subject classification for the article, and, for each author, postal address, affiliation (if appropriate), and email address if available. A home-page URL is optional.

FORMAT

Authors can use their preferred manuscript-preparation software, including for example Microsoft Word or any variant of TEX. The journal itself is produced in LATEX, so accepted articles prepared using other software will be converted to LATEX at production time. Authors wishing to prepare their document in LATEX can follow the example file at www.jomms.net (but the use of other class files is acceptable). At submission time only a PDF file is required. After acceptance, authors must submit all source material (see especially Figures below).

REFERENCES

Bibliographical references should be complete, including article titles and page ranges. All references in the bibliography should be cited in the text. The use of BibTEX is preferred but not required. Tags will be converted to the house format (see a current issue for examples); however, for submission you may use the format of your choice. Links will be provided to all literature with known web locations; authors can supply their own links in addition to those provided by the editorial process.

FIGURES

Figures must be of publication quality. After acceptance, you will need to submit the original source files in vector format for all diagrams and graphs in your manuscript: vector EPS or vector PDF files are the most useful. (EPS stands for Encapsulated PostScript.)

Most drawing and graphing packages—Mathematica, Adobe Illustrator, Corel Draw, MATLAB, etc.—allow the user to save files in one of these formats. Make sure that what you're saving is vector graphics and not a bitmap. If you need help, please write to graphics@msp.org with as many details as you can about how your graphics were generated.

Please also include the original data for any plots. This is particularly important if you are unable to save Excel-generated plots in vector format. Saving them as bitmaps is not useful; please send the Excel (.xls) spreadsheets instead. Bundle your figure files into a single archive (using zip, tar, rar or other format of your choice) and upload on the link you been given at acceptance time.

Each figure should be captioned and numbered so that it can float. Small figures occupying no more than three lines of vertical space can be kept in the text ("the curve looks like this:"). It is acceptable to submit a manuscript with all figures at the end, if their placement is specified in the text by means of comments such as "Place Figure 1 here". The same considerations apply to tables.

WHITE SPACE

Forced line breaks or page breaks should not be inserted in the document. There is no point in your trying to optimize line and page breaks in the original manuscript. The manuscript will be reformatted to use the journal's preferred fonts and layout.

PROOFS

Page proofs will be made available to authors (or to the designated corresponding author) at a Web site in PDF format. Failure to acknowledge the receipt of proofs or to return corrections within the requested deadline may cause publication to be postponed.

Journal of Mechanics of Materials and Structures

Volume 15, No. 3 May 2020